MATERIALS PROCESSING FUNDAMENTALS 2024

Iron and Steel Production

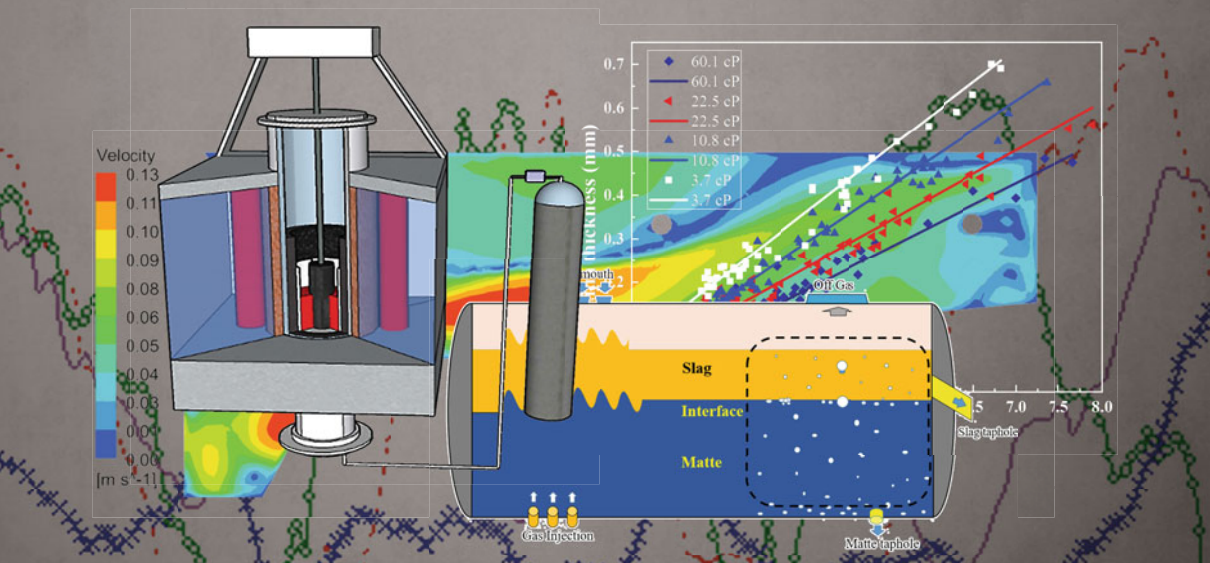

EDITED BY

Samuel Wagstaff
Alexandra Anderson
Adrian S. Sabau
Chukwunwike Iloeje

TMS

Springer

The Minerals, Metals & Materials Series

Samuel Wagstaff · Alexandra Anderson ·
Adrian S. Sabau · Chukwunwike Iloeje
Editors

Materials Processing Fundamentals 2024

Iron and Steel Production

TMS

Springer

Editors
Samuel Wagstaff
Oculatus Consulting
Marietta, GA, USA

Alexandra Anderson
Gopher Resource
Tampa, FL, USA

Adrian S. Sabau
Oak Ridge National Laboratory
Oak Ridge, TN, USA

Chukwunwike Iloeje
Argonne National Laboratory
Lemont, IL, USA

ISSN 2367-1181 ISSN 2367-1696 (electronic)
The Minerals, Metals & Materials Series
ISBN 978-3-031-50183-8 ISBN 978-3-031-50184-5 (eBook)
https://doi.org/10.1007/978-3-031-50184-5

This Springer imprint is published by the registered company Springer Nature Switzerland AG
The registered company address is: Gewerbestrasse 11, 6330 Cham, Switzerland

Paper in this product is recyclable.

Preface

The Materials Processing Fundamentals Symposium is hosted annually at the Annual Meeting of The Minerals, Metals & Materials Society (TMS) as the flagship symposium of the Process Technology and Modeling Committee. It is a unique opportunity for interdisciplinary presentations and discussions about processing, sensing, modeling, multi-physics, computational fluid dynamics, and thermodynamics, among others.

This year the symposium has taken an opportunity to dive into fundamentals and advancements in the field of iron and steel production. As one of the oldest metallurgical domains, and one of the most important materials to human civilization, iron and steel represent immense importance economically and socially on a global scale. Thermodynamic, physical, and computational models of production processes are all key in advancing and developing this domain for this and future generations.

Contributions to this proceedings volume include fundamental studies on slag thermodynamics and behavior, casting phenomena and improvements, as well as novel proposals to improve production efficiency and reduce GHG emissions. Presentations are focused at every length scale from basic thermodynamics to full-scale casting lines and converters illustrating the broad range of interest still found in basic material research.

The engagement of TMS and committee members to chair sessions, review manuscripts, and provide meaningful collaboration is what makes this symposium and its proceedings meaningful and possible. The editor and co-editors acknowledge the invaluable support and contribution of all volunteers as well as TMS staff members without whom, this would not be possible.

Samuel Wagstaff
Alexandra Anderson
Adrian S. Sabau
Chukwunwike Iloeje

Contents

About the Editors

Samuel Wagstaff is currently a partner at Oculatus Consulting, specializing in aluminum processing and product development. He holds degrees in Mechanical Engineering from Cornell University (B.S.) and Materials Science from MIT (M.S., Sc.D.). Previously as the Lead Scientist at Novelis, he led new product and process development for the entire R&D ecosystem across three continents. Currently, Dr. Wagstaff focuses on increasing profitability and productivities of nonferrous products by process improvement and fundamental research. He has helped to design over 1 million tons of recycle capacity in the aluminum sector and is the author of over 35 patents. Dr. Wagstaff is currently serving as the principal investigator on a $1M ReMADE grant to develop technology to improve the recyclability of organic laden aluminum scrap and is involved in much of the industrial expansion of the aluminum sector in North America. In his private life Sam enjoys being with his wife, hunting, fishing, and scuba diving.

Alexandra Anderson Ph.D., PMP, is an R&D manager at Gopher Resource, LLC, an environmental solutions company specializing in lead battery recycling. Her work focuses on driving furnace and refining productivity and efficiency initiatives through computational fluid dynamic (CFD) modeling and implementing novel equipment designs. Currently, she is also the principal investigator for a DOE HPC4Manufacturing partnership between Gopher Resource and Oak Ridge National Lab investigating high-fidelity multi-phase furnace modeling. Alexandra obtained her B.S. in Mechanical Engineering from Gonzaga University and her M.S. and Ph.D. in Metallurgical and Materials Engineering from the Colorado School of Mines. Her dissertation investigated fluid flow and thermal profiles within secondary lead reverberatory furnaces using CFD techniques. Alexandra is active in The Minerals, Metals & Materials Society (TMS), where she serves as the chair of the Process Technology and Modeling Committee; she was also the recipient of the 2021 TMS Extraction and Processing Division (EPD) Young Leader Award. Her scholarly activities include twelve peer-reviewed publications, co-editorships of eight special topics for JOM, as well as several podium presentations both at national conferences and universities.

Adrian S. Sabau received an Engineer Diploma in Mechanical and Materials Processing from the University of Craiova, Romania, and a Ph.D. degree in Mechanical Engineering from Southern Methodist University in 1996. In 1999, Dr. Sabau joined Oak Ridge National Laboratory as a Research Staff Member of Materials Science and Technology, where he worked as a Senior Research Staff Member from 2008. Since 2018, Dr. Sabau has been a Computational Materials Scientist in the Computational Sciences & Engineering Division. Dr. Sabau seeks to advance the materials processing, metal casting, photonic processing, and materials for energy applications through the development of computational fluid dynamics and experimental methodologies for the property measurement, process analysis, and materials behavior in response to conditions experienced in service. Dr. Sabau is an ASME fellow, and ASM fellow, and the recipient of three R&D 100 awards in process sciences. He was granted 9 patents,

released three open-source codes, and has published 170 technical papers.

Chukwunwike Iloeje is a Principal Scientist in the Energy Systems and Infrastructure Analysis Division at Argonne National Laboratory (ANL), a CASE Scientist at the Pritzker School of Molecular Engineering at the University of Chicago, and the Strategic Analysis team Co-lead at ANL.

In his research, Dr. Iloeje uses computational modeling to explore questions at the intersection of sustainable energy conversion, manufacturing, and material transformations, with particular interest in critical materials separations and supply chain optimization, as well as carbon capture and conversion to high-value chemicals.

Dr. Iloeje has a bachelor's degree in mechanical engineering from the University of Nigeria, and an MSc and Ph.D. in Mechanical Engineering from Massachusetts Institute of Technology.

Part I
Numerical Models

Numerical Simulation of the Behavioral Characteristics of Sprayed Water Droplets in a Hot Gas–Solid Fluidized Bed

Xinyong Dai, Liangying Wen, Yan Zhao, and Bo Liu

Abstract The geometric model is set up for a 1:1 three-phase fluidized bed, simulated calculations in the base of the air–tailings–water hot gas–solid–liquid fluidized bed experimental device. The Computational Fluid Dynamics (CFD) model utilizes the Eulerian–Eulerian multiphase modeling method and incorporates the dense discrete-phase (DDPM) model to simulate the flow of water droplets, introduced heat transfer, turbulence, and evaporation models to achieve a coupled solution. The simulation focuses on analyzing the flow, heat transfer, and superheated evaporation of water droplets during the fluidized treatment of tailings. The feasibility of the numerical simulation is verified through visualization experiments. Furthermore, the CFD model is employed to investigate the flow, evaporation, and interaction behaviors of water droplets of different sizes sprayed into a hot gas–solid fluidized bed and their effects on the fluidization state.

Keywords Three-phase fluidized bed · Spray water droplets · Numerical simulation · Superheated evaporation · DDPM

Introduction

Metallurgical production processes generate substantial solid waste resources, including titanium tailings that contain significant amounts of chloride. These tailings are not utilized directly, occupy vast space, and contribute to land occupation and water pollution. Therefore, it is critical to find environmentally friendly and efficient ways to recycle these tailings.

Chlorine-containing tailings currently undergo two main treatment processes. The first involves water washing, which generates significant wastewater and poses challenges for subsequent processing. The second process involves high-temperature calcination. However, the cost of the calcination is high, and the process damages

X. Dai · L. Wen (✉) · Y. Zhao · B. Liu
School of Materials Science and Engineering, Chongqing University, Chongqing 400044, China
e-mail: cquwen@cqu.edu.cn

S. Wagstaff et al. (eds.), *Materials Processing Fundamentals 2024*, The Minerals, Metals & Materials Series, https://doi.org/10.1007/978-3-031-50184-5_1

the glass phase in the tailings, affecting the activity of the tailings, which could be more conducive to subsequent utilization. To improve the treatment and utilization of tailings slag, this work considers using a fluidized bed reactor. The fluidization process uses air as the fluidization gas, and water droplets are sprayed while the gas–solid fluidized bed is heated and fluidized so that the tailings have complete contact with water vapor. Moreover, the resulting products from the process are recycled, reducing the operating costs of the industrial process while ensuring environmental sustainability.

Although research on gas–solid fluidized beds has reached an advanced stage, the addition of a liquid phase to the gas–solid fluidized bed has introduced new complexities due to evolving technological requirements. Technical advancements have made it necessary to consider the introduction of a liquid phase to the bed, and the liquid phase disrupts the original two-phase gas–solid flow equilibrium, which significantly affects the stability and operational safety of the gas–solid fluidized bed. The addition of liquid phase requires further exploration due to its effects, and multiple scholars have pursued research in this area. Boyce [1] uncovered that even small amounts of liquid phase can generate liquid bridging forces between solid-phase particles in the bed, which leads to solid particle bonding and the loss of the fluidized state. Mohagheghi et al. [2] used the capacitance method to study the distribution of liquid phase added to the fluidized bed in the granular phase, and the results showed that adding liquid and then increasing the fluidization gas velocity can improve the fragmentation rate of granular phase agglomerates. Fan et al. [3] demonstrated that when liquid droplets were added to a high-temperature fluidized bed reactor, the liquid droplets would be vaporized in large quantities rapidly, which would have a significant effect on the temperature distribution and gas–solid fluidization state and thus affect the process efficiency and product quality of the production. Li et al. [4] developed a phenomenological model to investigate the momentum exchange, as well as heat and mass transfer, between interacting cold evaporating spray droplets and hot particles. Simulation results revealed an increased spray evaporation rate and a decreased spray evaporation length with an increase in bed temperature, while a wider spray angle also decreased the spray evaporation length. Li et al. [5] employed a three-dimensional non-homogeneous reactor model based on the Eulerian–Eulerian method. The model was used to numerically simulate the effect of nozzle injection velocity on the flow in the injection zone of the lift tube feed under cold mold conditions. The simulation results indicated that the nozzle jet velocity had a significant effect on the two-phase flow in the feed mixing zone, while the nozzle position had less influence on the flow field. The reactor with a nozzle angle greater than 30° is more effective. There are fewer studies related to the influence of different droplet sizes on the gas–solid flow characteristics for the injection of liquid phase sprayed into a hot gas–solid fluidized bed.

Therefore, this work aims to bridge this research gap by investigating the effects of different droplet sizes on the gas–solid flow characteristics in a hot gas–solid fluidized bed during liquid-phase spraying. To better understand the multiphase flow interaction in the fluidized bed of air–tailings–water, this work was conducted using a laboratory multiphase fluidized bed reactor for tailings fluidization. Subsequently,

a 1:1 modeling of the laboratory fluidized bed reactor was performed, and the CFD simulation was used to calculate the tailings fluidization process. This approach allowed the investigation of the influence of water droplets sprayed into the hot gas–solid fluidized bed. The numerical simulation results were compared with the experimental results to validate the feasibility of the numerical model, and the behavior of different sizes of water droplets entering the fluidized bed and their influence on the fluidization state were further investigated.

Model Description

In the numerical simulations, a CFD model [6–8] is constructed to simulate the fluid dynamics using the two-fluid Eulerian–Eulerian approach. This model incorporates the drag model, the turbulence model, the droplet evaporation model, and so on, which is described as follows.

Basic Control Equations

Continuity Equations

$$\frac{\partial}{\partial t}\left(\alpha_{\mathrm{g}}\rho_{\mathrm{g}}\right)+\nabla\cdot\left(\alpha_{\mathrm{g}}\rho_{\mathrm{g}}\vec{v}_{\mathrm{g}}\right)=\left(\dot{m}_{1\mathrm{g}}-\dot{m}_{\mathrm{gs}}\right) \tag{1}$$

$$\frac{\partial}{\partial t}(\alpha_{\mathrm{l}}\rho_{\mathrm{l}})+\nabla\cdot(\alpha_{\mathrm{l}}\rho_{\mathrm{l}}\vec{v}_{\mathrm{l}})=-\dot{m}_{1\mathrm{g}} \tag{2}$$

$$\frac{\partial}{\partial t}(\alpha_{\mathrm{s}}\rho_{\mathrm{s}})+\nabla\cdot(\alpha_{\mathrm{s}}\rho_{\mathrm{s}}\vec{v}_{\mathrm{s}})=\dot{m}_{\mathrm{gs}} \tag{3}$$

$$\alpha_{\mathrm{g}}+\alpha_{\mathrm{l}}+\alpha_{\mathrm{s}}=1 \tag{4}$$

where g, l, and s denote the gas, liquid, and solid phases. α is the volume fraction; ρ is the densities, kg/m^3; $\vec{v}$ is the velocity, m/s; $\dot{m}_{1\mathrm{g}}$, $\dot{m}_{\mathrm{gs}}$ are the mass-transfer rates; and t is the time, s.

Momentum Equations

$$\begin{aligned}\frac{\partial}{\partial t}\left(\alpha_{\mathrm{g}}\rho_{\mathrm{g}}\vec{v}_{\mathrm{g}}\right)+\nabla\cdot\left(\alpha_{\mathrm{g}}\rho_{\mathrm{g}}\vec{v}_{\mathrm{g}}\vec{v}_{\mathrm{g}}\right)&=-\alpha_{\mathrm{g}}\nabla p+\nabla\cdot\left[\alpha_{\mathrm{g}}\mu_{\mathrm{g}}\left(\nabla\vec{v}_{\mathrm{g}}+\nabla\vec{v}_{\mathrm{g}}^{\mathrm{T}}\right)\right]+\dot{m}_{1\mathrm{g}}\vec{v}_{\mathrm{l}}-\dot{m}_{\mathrm{gs}}\vec{v}_{\mathrm{g}}\\&\quad+\vec{K}_{\mathrm{gs}}\left(\vec{v}_{\mathrm{s}}-\vec{v}_{\mathrm{g}}\right)+K_{\mathrm{DPM}}\left(\vec{v}_{\mathrm{DPM}}-\vec{v}_{\mathrm{g}}\right)+\alpha_{\mathrm{p}}\rho_{\mathrm{p}}\vec{g}\end{aligned} \tag{5}$$

$$\frac{\partial}{\partial t}(\alpha_{\mathrm{l}}\rho_{\mathrm{l}}\vec{v}_{\mathrm{l}})+\nabla\cdot(\alpha_{\mathrm{l}}\rho_{\mathrm{l}}\vec{v}_{\mathrm{l}}\vec{v}_{\mathrm{l}})=-\alpha_{\mathrm{l}}\nabla p-\nabla p_{\mathrm{l}}+\nabla\cdot\left[\alpha_{\mathrm{l}}\mu_{\mathrm{l}}\left(\nabla\vec{v}_{\mathrm{l}}+\nabla\vec{v}_{\mathrm{l}}^{\mathrm{T}}\right)\right]-\dot{m}_{1\mathrm{g}}\vec{v}_{\mathrm{l}}$$

$$+ \vec{K}_{\mathrm{ls}}(\vec{v}_{\mathrm{s}} - \vec{v}_{\mathrm{l}}) + K_{\mathrm{DPM}}(\vec{v}_{\mathrm{DPM}} - \vec{v}_{\mathrm{l}}) + \alpha_{\mathrm{l}}\rho_{\mathrm{l}}\vec{g} \tag{6}$$

$$\frac{\partial}{\partial t}(\alpha_{\mathrm{s}}\rho_{\mathrm{s}}\vec{v}_{\mathrm{s}}) + \nabla\cdot(\alpha_{\mathrm{s}}\rho_{\mathrm{s}}\vec{v}_{\mathrm{s}}\vec{v}_{\mathrm{s}}) = -\alpha_{\mathrm{s}}\nabla p - \nabla p_{\mathrm{s}} + \nabla\cdot\left[\alpha_{\mathrm{s}}\mu_{\mathrm{s}}\left(\nabla\vec{v}_{\mathrm{s}} + \nabla\vec{v}_{\mathrm{s}}^{\mathrm{T}}\right)\right] + \dot{m}_{\mathrm{gs}}\vec{v}_{\mathrm{g}}$$
$$+ \vec{K}_{\mathrm{ls}}(\vec{v}_{\mathrm{l}} - \vec{v}_{\mathrm{s}}) + K_{\mathrm{DPM}}(\vec{v}_{\mathrm{DPM}} - \vec{v}_{\mathrm{s}}) + \alpha_{\mathrm{p}}\rho_{\mathrm{p}}\vec{g} \tag{7}$$

where μ is the viscosity, Pa s; p is the pressure, Pa; $\vec{K}_{\mathrm{gs}}$, $\vec{K}_{\mathrm{ls}}$, and K_{DPM} represent the exchange coefficients, kg m^2 s^{-1}; $\vec{v}_{\mathrm{DPM}}$ is the velocity of the particles of the discrete phases, m/s.

Energy Equations

$$\frac{\partial}{\partial t}\left(\phi\rho_{\mathrm{g}}C_{p,\mathrm{g}}T\right) + \nabla\cdot\left(\phi\rho_{\mathrm{g}}C_{p,\mathrm{g}}\vec{v}_{\mathrm{g}}T\right) = \nabla\cdot\left(\phi k_{\mathrm{g}}\nabla T\right) \tag{8}$$

$$\frac{\partial}{\partial t}\left(\phi\rho_{\mathrm{l}}C_{p,\mathrm{l}}T\right) + \nabla\cdot\left(\phi\rho_{l}C_{p,\mathrm{l}}\vec{v}_{\mathrm{l}}T\right) = \nabla\cdot(\phi k_{\mathrm{l}}\nabla T) \tag{9}$$

$$\frac{\partial}{\partial t}\left(\phi\rho_{\mathrm{s}}C_{p,\mathrm{s}}T\right) + \nabla\cdot\left(\phi\rho_{\mathrm{s}}C_{p,\mathrm{s}}\vec{v}_{\mathrm{s}}T\right) = \nabla\cdot(\phi k_{\mathrm{s}}\nabla T) \tag{10}$$

where ϕ is the medium porosity; $C_{p,\mathrm{g}}$, $C_{p,\mathrm{l}}$, and $C_{p,\mathrm{s}}$ are the heat capacities, kJ/(kmol K); T is the temperature, K; k_{g}, k_{l}, and k_{s} are the heat exchange coefficients, W/(m K).

Drag Model

Gas–Solid-Phase-Drag Model

Gidaspow model has been chosen for the gas–solid interphase-drag model, and the equations are described below:

$$K_{\mathrm{sg}} = 150\frac{\alpha_{\mathrm{s}}\left(1-\alpha_{\mathrm{g}}\right)v_{\mathrm{s}}}{\alpha_{\mathrm{g}}d_{\mathrm{s}}^2} + 1.75\frac{\rho_{\mathrm{g}}\alpha_{\mathrm{s}}}{d_{\mathrm{s}}}\left|\vec{v}_{\mathrm{s}} - \vec{v}_{\mathrm{g}}\right|\alpha_{\mathrm{g}} \le 0.8 \tag{11}$$

$$K_{\mathrm{sg}} = \frac{3}{4}C_{D,\mathrm{sg}}\frac{\alpha_{\mathrm{s}}\alpha_{\mathrm{g}}\rho_{\mathrm{g}}}{d_{\mathrm{s}}}\left|\vec{v}_{\mathrm{s}} - \vec{v}_{\mathrm{g}}\right|\alpha_{\mathrm{g}}^{-2.65}\alpha_{\mathrm{g}} > 0.8 \tag{12}$$

$$C_{D,\mathrm{sg}} = \begin{cases} \frac{24}{\alpha_{\mathrm{g}}\mathrm{Re}_{\mathrm{s}}}\left[1 + 0.15\left(\alpha_{\mathrm{g}}\mathrm{Re}_{\mathrm{s}}\right)^{0.687}\right] & \mathrm{Re}_{\mathrm{s}} \le 1000 \\ 0.44 & \mathrm{Re}_{\mathrm{s}} > 1000 \end{cases} \tag{13}$$

$$\mathrm{Re}_\mathrm{s} = \frac{\rho_\mathrm{g} d_\mathrm{s} \left| \vec{v}_\mathrm{s} - \vec{v}_\mathrm{g} \right|}{\mu_\mathrm{g}} \tag{14}$$

where $C_{D,\mathrm{sg}}$ is the gas–solid resistance coefficient; Re_s is the Reynolds number.

Discrete-Phase Resistance Model

The liquid phase is treated as a discrete phase because the liquid is added in the form of a spray and the droplet diameters are small, with sizes ranging from 25 to 100 μm. In the commercial CFD software FLUENT (Ansys Inc., USA), when the DDPM (dense discrete-phase model) model is used, both the gas–liquid interphase-drag coefficients and the solid–liquid interphase-drag coefficients are adopted from the average-discrete-phase-drag model, which is expressed as follows [9, 10]:

$$m_\mathrm{p} \frac{\mathrm{d}\vec{v}_\mathrm{P}}{\mathrm{d}t} = m_\mathrm{p} \frac{\vec{v} - \vec{v}_\mathrm{P}}{\tau_\mathrm{r}} + m_\mathrm{P} \frac{\vec{g}(\rho_\mathrm{P} - \rho)}{\rho_\mathrm{P}} + \vec{F} + \vec{F}_\mathrm{interaction} \tag{15}$$

$$\tau_\mathrm{r} = \frac{\rho_\mathrm{P} d_\mathrm{p}^2}{18\mu} \frac{24}{C_d \mathrm{Re}} \tag{16}$$

$$\mathrm{Re} \equiv \frac{\rho d_\mathrm{p} |\vec{v}_\mathrm{P} - \vec{v}|}{\mu} \tag{17}$$

$$\vec{F}_\mathrm{interaction} = -m_\mathrm{P} \frac{1}{\rho_\mathrm{P}} \nabla \cdot \overline{\overline{\tau_\mathrm{s}}} \tag{18}$$

$$\tau_\mathrm{s} = -\frac{\pi}{6} \sqrt{3} \varphi \frac{\alpha_\mathrm{s}}{\alpha_{\mathrm{s,max}}} \rho_\mathrm{s} g_0 \sqrt{\theta_\mathrm{s}} \overrightarrow{U_\mathrm{s}} \tag{19}$$

$$\theta_\mathrm{s} = \frac{1}{3} u_{\mathrm{s},i} u_{\mathrm{s},i} \tag{20}$$

where p denotes the discrete-phase particle; m_p is the particle mass, kg; d_p is the particle diameter, m; τ_r is the particle relaxation time; $\overline{\overline{\tau_\mathrm{s}}}$ is the shear stress of solid-phase particles; θ_s is the temperature of solid; $\overrightarrow{U_\mathrm{s}}$ is the sliding velocity of solid parallel to the wall; φ is the specularity coefficient between the solid and the wall, which is 0.2 in this case; $\alpha_{\mathrm{s,max}}$ is the maximum stacking volume fraction of the particles, which is 0.63; g_0 is the radial distribution function associated with the model; and $u_{\mathrm{s},i}$ is the component of the solid velocity in the i direction in the Cartesian coordinate system.

Turbulence Model

The gas–solid flow in the fluidized bed belongs to turbulence, the turbulence model is chosen as the Standard k–ε model, and the control equation is expressed as follows:

$$\frac{\partial(\rho k)}{\partial t} + \frac{\partial(\rho k v)}{\partial x_i} = \frac{\partial}{\partial x_j}\left[\left(\mu + \frac{\mu_t}{\sigma_k}\right)\frac{\partial k}{\partial x_j}\right] + G_k - \rho\varepsilon \tag{21}$$

$$\frac{\partial(\rho \varepsilon)}{\partial t} + \frac{\partial(\rho \varepsilon v)}{\partial x_i} = \frac{\partial}{\partial x_j}\left[\left(\mu + \frac{\mu_t}{\sigma_\varepsilon}\right)\frac{\partial \varepsilon}{\partial x_j}\right] + \frac{C_{1\varepsilon}\varepsilon}{k}G_k - C_{2\varepsilon}\rho\frac{\varepsilon^2}{k} \tag{22}$$

where k is the turbulent kinetic energy; ε is the turbulent dissipation rate; $C_{1\varepsilon}$ and $C_{2\varepsilon}$ are constants, 1.44 and 1.92; σ_k and σ_ε are the turbulent Prandtl numbers of turbulent kinetic energy and dissipation rate, 1.00 and 1.30; μ_t is the turbulent kinetic viscosity; and G_k is the velocity gradient caused by the turbulent kinetic energy production term.

Evaporation Model

Since the simulation is carried out in the hot state, the phase change and evaporation need to be considered, and the "thermal-mass coupling solution" is adopted for the droplets. When the evaporated mass is larger than the limiting mass change Δm_p (see Eq. (23)) or the temperature change of the particles is larger than the limiting temperature change ΔT_p (see Eq. (24)), calculations will switch to the coupling algorithm within the integration time step.

$$\Delta m_p = m_p a_m \tag{23}$$

where m_p is the particle mass, kg and a_m is the vaporization limiting factor for this mass.

$$\Delta T_p = \min\left(\left|T_p - T_\infty\right| a_T, T_p a_T\right) \tag{24}$$

where T_p is the particle temperature, K, T_∞ is the volumetric temperature, K, and a_T is the vaporization limiting factor for temperature.

In the numerical simulations, the vaporization limiting factors for mass and heat were set to 0.3 and 0.1, respectively, and the values were determined through systematic testing.

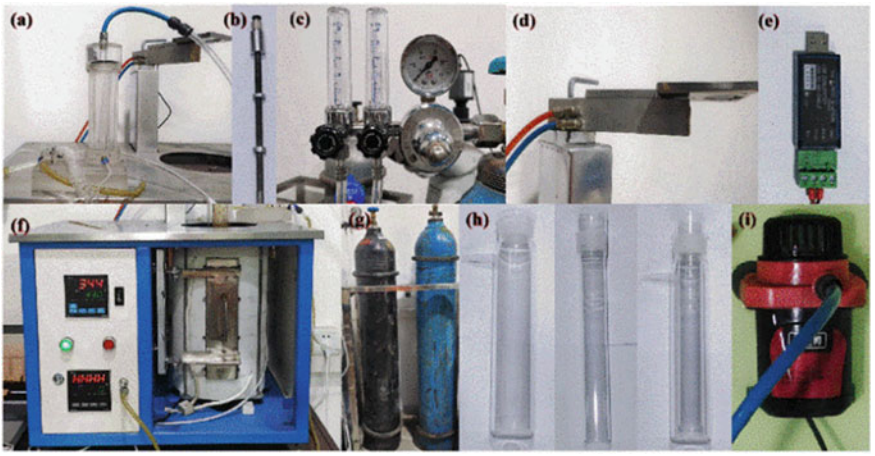

Fig. 1 Actual diagram of the experimental device: **a** liquid storage device; **b** liquid addition device; **c** volumetric displacement meter; **d** sensors; **e** data collector; **f** heating furnace; **g** gas canister; **h** fluidized bed reactor; **i** water-cooled devices

Experiment Device

As shown in Fig. 1, the experimental setup used in this experiment mainly includes a liquid storage device, a liquid addition device, a data collector, a heating furnace, a fluidized bed reactor, and so on.

Geometric Modeling and Mesh Irrelevance Testing

As shown in Fig. 2, (a) is a visual fluidized bed reactor fabricated using quartz glass, (b) and (c) are 2D geometric models modeled and meshing, in which the inlet at the bottom is the inlet of the fluidized gases, and the outlet is provided at the top. The liquid addition tube with an atomization nozzle is inserted 30 mm from the top, and injection is the liquid-phase spray inlet.

Meshing (Ansys Inc., USA) is used to delineate the mesh. In this work, the maximum grid cell sizes of 0.20 mm, 0.37 mm, and 0.80 mm were used for numerical simulations, and total number of grids obtained were 218,966, 64,078, and 13,915, respectively. The fluidization index obtained from the numerical simulation is compared with the experimental results under the same operation conditions. The results are shown in Fig. 3. When the grid size is 0.20 mm and 0.37 mm, these two groups of grid size calculated fluidization index and the experimental results agree, indicating that the simulation results for both are better. Additionally, considering the calculation accuracy and time efficiency, this work adopts the grid size of 0.37 mm to carry out the subsequent calculations.

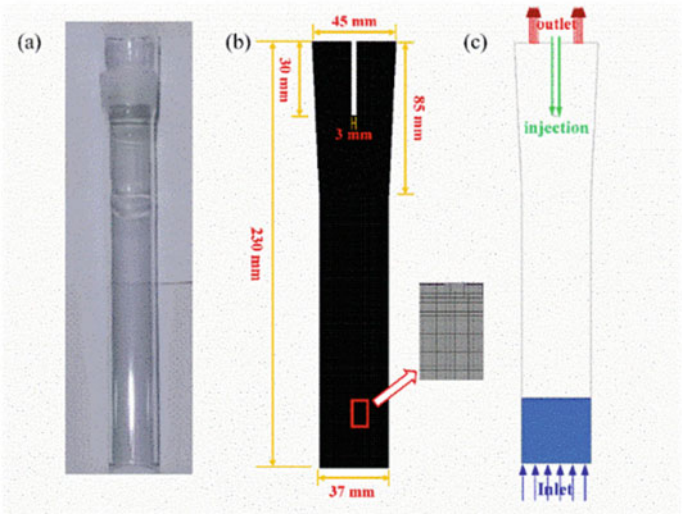

Fig. 2 Geometric model: **a** laboratory fluidized bed reactor, **b** computational modeling, and **c** mesh setup

Fig. 3 Fluidization index for different grid sizes

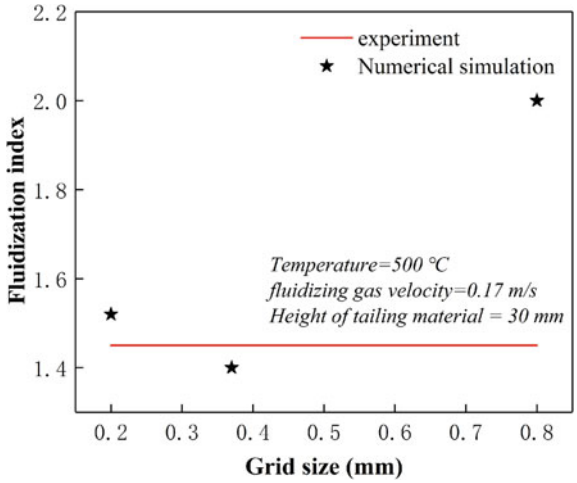

Computational Methods and Boundary Conditions

The commercial software FLUENT (Ansys Inc., USA) was utilized for the iterative solution, and the boundary conditions, gas-phase, solid-phase, and liquid-phase properties are shown in Table 1.

Table 1 Boundary conditions and parameter setting of the simulation

Parameter	Value
Gas-phase viscosity (air)	1.79×10^{-5} kg/(m s)
Solid-phase density (titanium tailings)	2850 kg/m^3
Solid-phase particle diameter	92.40 μm
Water density (liquid phase)	998.20 kg/m^3
Water density (gas phase)	0.55 kg/m^3
Saturation temperature (water)	100 °C
Time step	1×10^{-4} s
Calculation time	21 s

Results and Discussion

Model Validation

The operation conditions used in the numerical simulation were consistent with the experimental operation conditions used in the laboratory, with a reaction temperature of 500 °C, a fluidization gas velocity of 0.17 m/s, a material height of 30 mm, an average particle size of 92.40 μm in the tailings, and a water mist size of 50 μm.

Analysis of Solid-Phase Particle Flow Field Changes

Figure 4 compares simulation and experimental results evaluating the fluidization state of the particle phase during the tailing fluidization treatment process. The numerical simulation displays the velocity vector distribution of the particle phase on the left, while the fluidization state of the tailing captured during the experimental process is shown on the right, with the particle trajectory indicated by a red line.

Figure 4a illustrates the fluidization state of the particle phase in a gas–solid fluidized bed before introducing water droplets. An internally circulating zone is observed inside the bed, attributable to the heterogeneous particle size of the tailings, leading to segregation. Moving onto Fig. 4b, the particles throughout the bed move violently and elutriation. Figure 4c illustrates that the particles reach a stabilized fluidization state as the bed moves smoothly. Some particles adhere to the reactor wall to a certain extent. The movement trend of solid-phase particles during tailings fluidization treatment shows consistency between numerical simulation and experimental observations, and the trajectories correspond nearly.

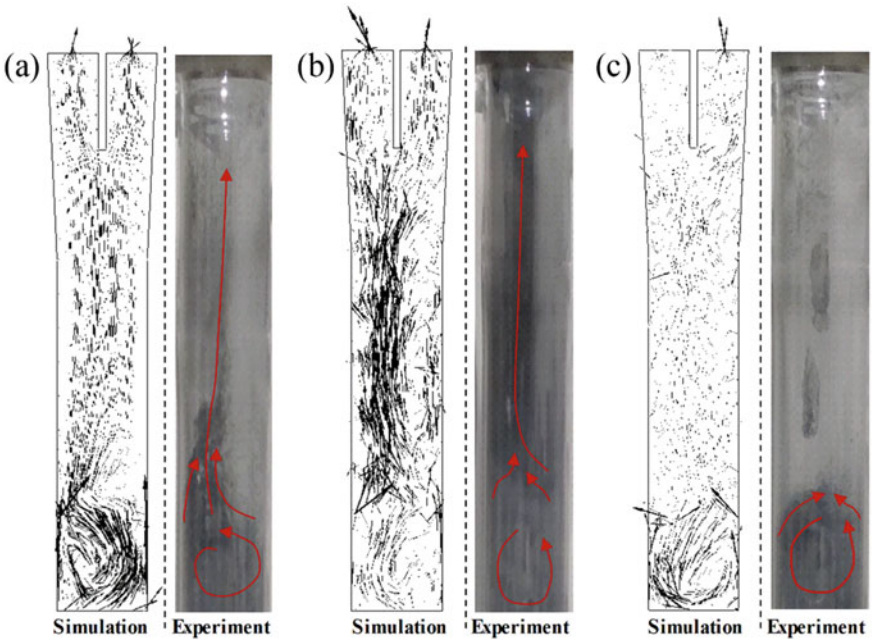

Fig. 4 Comparison between numerical simulation and experiment of fluidization state of the solid-phase particle in three stages of the tailing fluidization process: **a** before spraying water droplets, **b** during spraying water droplets, and **c** after spraying water droplets

Analysis of Pressure Fluctuation

Figure 5 shows the pressure drop with time during the whole tailings fluidization process. Figure 5a shows the pressure drop curve obtained by numerical simulation, while Fig. 5b shows the pressure drop curve obtained by experiment. Initially, the pressure drop experiences some fluctuations during the fluidization process but eventually stabilizes at a relatively constant value within a particular range. During the liquid addition process, the pressure drop curve experiences violent fluctuations. The liquid phase changes from a two-phase flow to a multiphase gas–liquid–solid flow in the reactor, and water droplets undergo a phase transition, producing copious amounts of water vapor. The particles of bed move vigorously, leading to increased pressure drop curve fluctuations. As water evaporates and fluidization persists, the fluctuations in the pressure drop curve gradually decrease until the flow state becomes stable. Although the numerical simulation in this study is based on two-dimensional modeling, resulting in certain dissimilarities in the pressure drop values, the simulation and experimental trends show a high level of consistency.

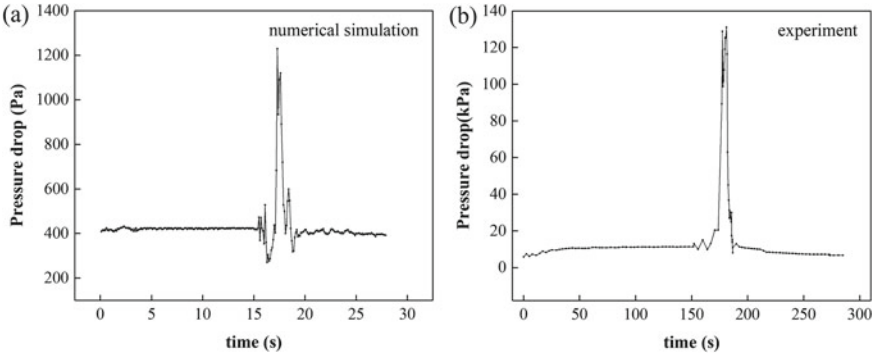

Fig. 5 Variation of pressure drop with time in **a** numerical simulation and **b** experiment during tailing fluidization

Fluidization Quality Analysis

Based on pressure fluctuations, the quality of fluidization is analyzed using the fluidization index (FI), which is calculated by Eq. (25):

$$\mathrm{FI} = \frac{\Delta\overline{p}}{f\overline{p}} \times 10^4 \tag{25}$$

where $\Delta\overline{p}$ is expressed as the average value of pressure pulsation between the pressure point and the atmosphere; f is the frequency of pressure drop fluctuation; and $\overline{p}$ is the average value of pressure drop. It is widely recognized that as the fluidization index (FI) decreases, the average pressure drop pulsation values decrease, and the frequency increases, resulting in an improved fluidization quality.

During the fluidization process of tailings, Fig. 6 shows that the FI values between numerical simulation and experiment have a consistent trend and similar values. Adding water results in a decrease in the value of FI, indicating that the injection of water improves the fluidization quality.

Overall, the numerical simulation results correlate well with the experiment, and the trend has consistency, which shows the feasibility of this numerical model and can provide some reference for the experimental study. In this work, the following simulations utilize the numerical model to simulate the effect of water droplet injection of different sizes on the hot gas–solid fluidized bed as follows.

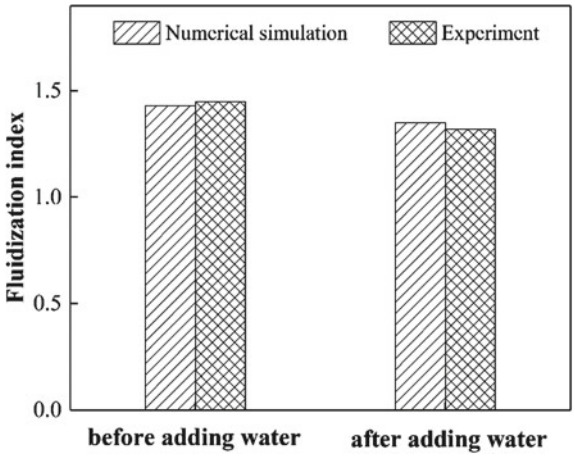

Fig. 6 Fluidization index changes of numerical simulation and experiment before and after adding water

Effect of Different Droplet Sizes

Analysis of Droplets Behavior

As shown in Fig. 7, the H_2O mass fraction and the velocity vector distribution of the water droplets obtained by calculating the 25, 50, 75, and 100 μm diameter water droplets blown into the gas–solid fluidized bed reactor at 500 °C can reflect the distribution of H_2O and the movement path. Overall, smaller water droplet diameters lead to a more diffuse distribution of H_2O in the reactor and less H_2O in the bed. Additionally, due to the downward spraying of water droplets and the upward movement of fluidized gas, the velocity vector diagrams of H_2O show multiple cyclotron zones.

When spraying water droplets with a diameter of 25 μm (Fig. 7a), it is evident that the droplets do not penetrate further into the bed after reaching the scorched

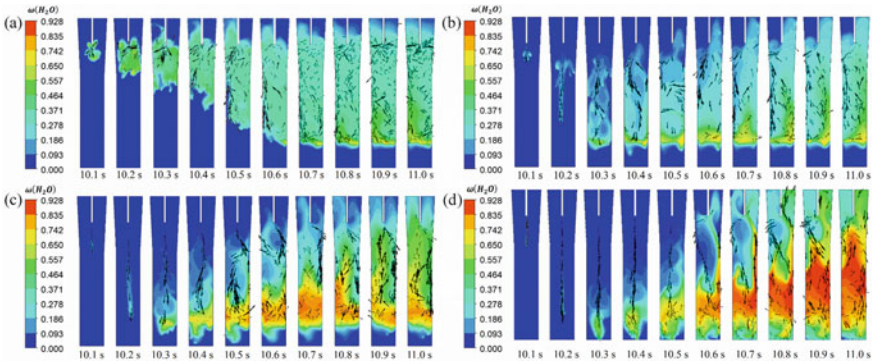

Fig. 7 Mass fraction of H_2O and velocity vector distribution of water droplets in the process of spraying **a** 25, **b** 50, **c** 75, and **d** 100 μm diameter water droplets

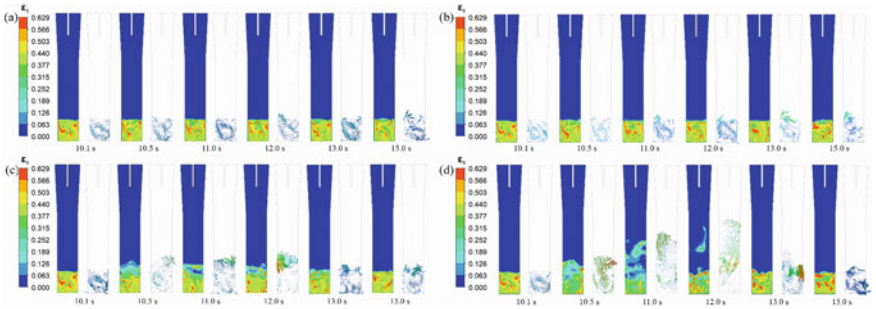

Fig. 8 Volume fraction and velocity vector distribution of solid phase in the process of spraying **a** 25, **b** 50, **c** 75, and **d** 100 μm diameter water droplets

bed surface. The H_2O actively interacts with the particles on the bed surface, and a large amount of H_2O is distributed above the bed during liquid addition. For 50 μm water droplets (Fig. 7b), a small amount of H_2O is observed to enter the bed at 10.4 s. Throughout the liquid addition process, a small amount of H_2O entered the bed in the area against the side wall, and there were interactions between H_2O and the particles near the bed surface. For 75 μm water droplets (Fig. 7c), the water droplets enter the bed after reaching the surface of the bed at 10.2 s. The concentration of H_2O in the bed is higher at 10.4 s and 10.5 s, and then the content of H_2O in the bed decreases due to evaporation and the effect of fluidized gas at the bottom. For 100 μm water droplets (Fig. 7d), more H_2O penetrate the bed, and the interaction between H_2O and particles is enhanced.

Analysis of Particles Behavior

Volume Fraction and Velocity Vector Distribution of Particle

As shown in Fig. 8, the volume fraction of particles and the particle velocity vector distribution of 25, 50, 75, and 100 μm diameter water droplets sprayed into the 500 °C gas–solid fluidized bed reactor during the liquid addition process and stopping the liquid addition for continuous fluidization. The study focuses on the distribution of particles in the bed and their movement paths after the water droplets entered. In general, the movement of particles in the bed will form multiple cyclotron zones, and the beds all tend to expand upward after liquid addition, which state is gradually stabilized with the continuation of fluidization after liquid addition is stopped. Adding water droplets of different diameters makes the bed state and particle distribution different. The larger the droplet size is, the more the amount of entering the bed and the more intense the particle movement.

In the case of 25 μm diameter water droplets, particles exhibit significant differences, and the distribution of materials within the bed depth becomes non-uniform as shown in Fig. 8a, the water droplets do not penetrate the bed. As a result, the droplets

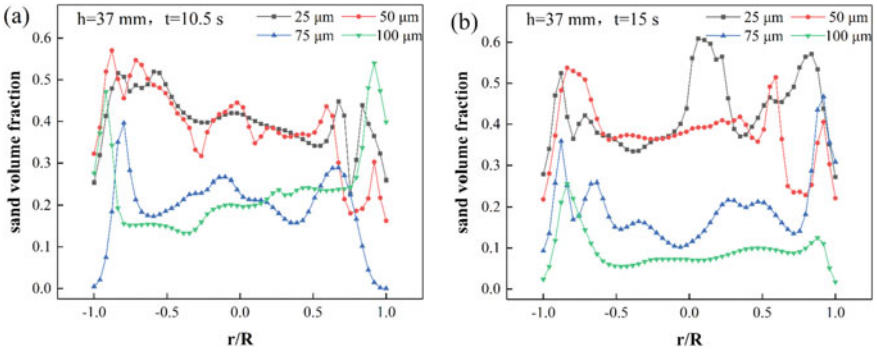

Fig. 9 Radial distribution of solid-phase concentration at 37 mm height for **a** 10.5 s and **b** 15.0 s

only interact with the particles on the bed's surface, having minimal impact on the bed state. The particle concentration distribution remains relatively unchanged, and the particle trajectories in the bed are relatively stable. For 50 μm water droplets (Fig. 8b), a small amount of droplets interacts with the particles near the surface of bed, causing a slight expansion of the bed. For 75 μm water droplets (Fig. 8c), a more pronounced bed expansion is observed. As the water droplets evaporate, the water vapor and fluidized gas carry the particles upward. For 100 μm water droplets (Fig. 8d), a significant amount of droplets enter into the bed. The superheated and evaporated droplets cause a violent expansion of the bed, leading to many particles being carried by the water vapor and fluidized gas. Some particles even break through the bed and are expelled upwards, resulting in a "fault" in the structure. Consequently, the volume fraction of particles exhibits significant differences, and the distribution of materials within the bed depth becomes non-uniform. Eventually, these overweight particles settle back into the bed, and the continuous fluidization restores to be stable.

As shown in Fig. 9, the radial distribution of solid-phase particles at a height of 37 mm from the bottom (converted height-to-diameter ratio of 1.0) is shown at 10.5 s and 15.0 s. During the addition of liquid, the larger the size of the water droplets, the lower the concentration of particles distributed in the bed. After the end of liquid addition, the fluidization continues until the bed is more stable. The concentration of particles is lower than that during the liquid addition process, and the concentration is uniformly distributed in the center area and higher against the walls.

Throughout the process, the radial concentration distribution of particles sprayed into the water droplets with sizes of 25 μm and 50 μm is similar. As displayed in Fig. 7, the water droplets fail to penetrate the bed in these two cases. Instead, they interact solely with some surface particles, and the overall distributions of both particle concentration and velocity vectors remain comparatively identical. These distributions also demonstrated similar trends. The quantity of water droplets entering the bed is considerably different when using 75 μm and 100 μm particles. Therefore,

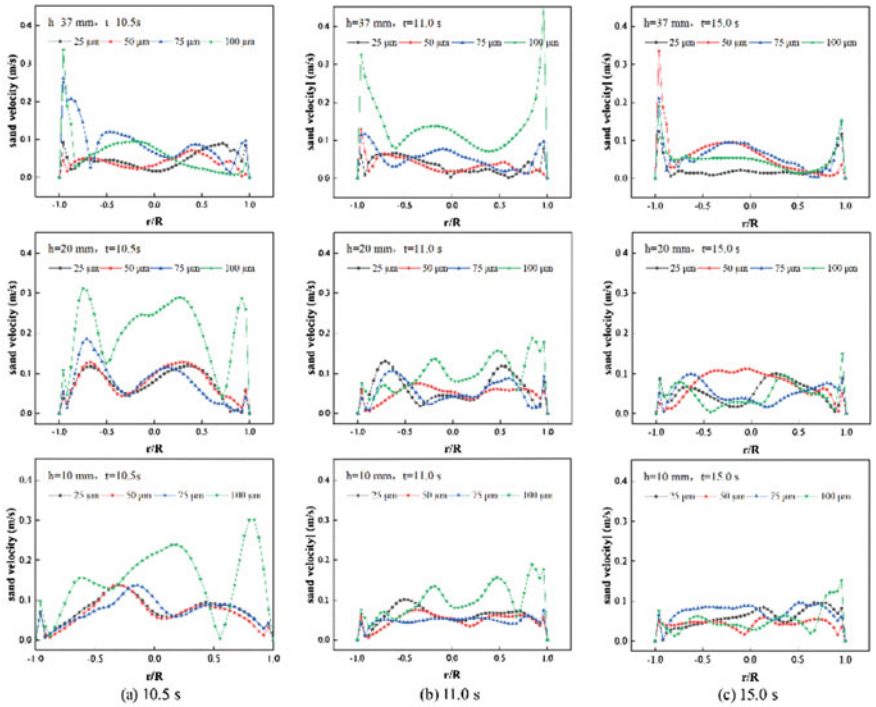

Fig. 10 Velocity radial distribution of solid-phase particles at different horizontal heights at **a** 10.5 s, **b** 11.0 s, and **c** 15.0 s ($h = 10$ mm, 20 mm, 37 mm)

the particle volume fraction distributions are also notably different. At this height, spraying 100 μm water droplets resulted in lower stabilized particle concentrations.

Particle Velocity Distribution

Figure 10 displays the velocity distributions of particles at three depths within the bed during the fluidization process of the tailings at 10.5 s, 11.0 s, and 15.0 s. Particle velocity values fluctuate within the 0–0.45 m/s interval during droplet spray entry into the reactor and fluidization at 15.0 s. The highest velocity values are generally located at the fluidized bed sidewall. As fluidization continues, the liquid phase evaporates, the fluidization state is gradually stabilized, the velocity fluctuation between particles is gradually reduced, and the particle velocity distribution becomes more regular. Table 2 demonstrates the average velocity at various horizontal heights at 15.0 s, which is 0.05 ± 0.01 m/s. The velocities at 10 mm, 20 mm, and 37 mm have near-equal mean values, which shows that the interaction between H_2O, particles, and fluidized gas has achieved a dynamic equilibrium, and the fluidized state is becoming stable.

Table 2 Average velocity of solid-phase particles at different horizontal heights at 15 s ($h = 10$ mm, 20 mm, 37 mm)

Water droplet size	25 μm	50 μm	75 μm	100 μm
High (mm)	Average velocity of solid particles (m/s)			
10	0.06	0.04	0.05	0.05
20	0.05	0.06	0.05	0.05
37	–	0.06	0.05	0.05

Furthermore, the larger the size of the water droplets sprayed, the greater the effect on the activity of the particles in the bed. As mentioned above, the larger the water droplets size is, the greater the amount of water that will enter the bed. As a result, superheated evaporation of more water droplets produces more water vapor, and consequently, gas-phase velocity increases, impacting particle movement. Therefore, water droplets with a size of 100 μm exert a more significant influence on particle velocity.

As the bed height increases from the bottom, the particle velocity value fluctuations become more violent. The droplets interact with the particles, which are thermally vaporized, and they carry the particles upwards with the fluidized gases. The particles experience acceleration as the bubbles burst on the bed's surface, resulting in intensified particle velocity fluctuations in the upper part of the bed. Due to the wall effect, bubbles move upwards along the side walls, creating extreme velocities. Lower-middle regions exhibit less velocity fluctuation, indicating more stable bubble motion and weaker turbulence.

Analysis of Fluidization Quality

As shown in Fig. 11, the fluidization index changes curves after different water droplets are sprayed into the fluidized bed reactor and continuously fluidized until stable. Overall, adding water droplets improves the quality of fluidization in the bed. Notably, in the range of water droplet sizes from 25 to 75 μm, the fluidization index decreases, which means that adding water droplets in this range improves the fluidization quality of the particles. At water droplets of 100 μm, the fluidization index is between 50 and 75 μm values. The reason is that at 100 μm water droplets, excessive water droplets enter the bed, and the large amount of water vapor generated by evaporation leads to a sudden increase in the apparent gas velocity. In this process, the bed layer moves violently and elutriation, which makes the thickness of the material in the bed layer uneven and easy to produce ditch flow, so that the quality of fluidization decreases. Therefore, adding water droplets can improve the fluidization quality of the bed, and the size of the water droplets and the amount of water droplets in the bed impact the fluidization quality.

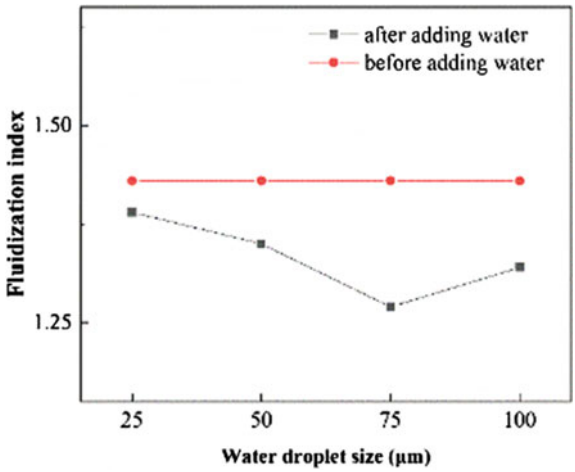

Fig. 11 Changes of fluidization index after adding water droplets of different sizes

Conclusion

This work investigated the behavior of water droplets of different sizes in the fluidized bed and their effects on the fluidization state. The results revealed that 25, 50, 75, and 100 μm diameter water droplets entered the 500 °C gas–solid fluidized bed reactor, forming multiple cyclotron zones due to convection between the sprayed droplets and the incoming fluidized gas. The introduction of liquid led to an upward expansion of the bed; the larger the size of the droplets was, the more the amount of the bed had, and the more intense the bed movement was. Additionally, the fluctuation in particle velocity values increased with the height of the bed from the bottom. As the fluidization continued, the liquid phase evaporated, the fluidization state was stable gradually, and the velocity fluctuation between the particles was reduced. The average velocity values at different horizontal heights were recorded at 0.05 ± 0.01 m/s, exhibiting minimal fluctuation.

Furthermore, an analysis of the fluidization index after the addition of liquid indicated that the value of FI was gradually decreasing in the range of water droplet sizes of 25–75 μm, and the addition of water droplets in this size range improved the fluidization quality of the particles. However, when the water droplet size reached 100 μm, the FI was between the 50 μm and 75 μm droplets. In the case of 100 μm, due to the violent movement and elutriation caused by many water droplets entering the bed, bed thickness was non-uniform, and fluidization quality decreased compared to other water droplet sizes.

Therefore, spraying water droplets in the fluidized bed significantly affects the multiphase behavior and fluidization quality during the tailing process. For the case of this work, 75 μm is the best droplet size, and the proper size selection also supports the subsequent improvement of dechlorination efficiency.

Acknowledgements The work is supported by the National Natural Science Foundation Project of China (51974046).

References

1. Boyce CM (2018) Gas-solid fluidization with liquid bridging: a review from a modeling perspective. Powder Technol 336:12–29. https://doi.org/10.1016/j.powtec.2018.05.027
2. Mohagheghi M, Hamidi M, Berruti F (2013) Study of the effect of local hydrodynamics on liquid distribution in a gas–solid fluidized bed using a capacitance method. Fuel 107:236–245. https://doi.org/10.1016/j.fuel.2013.01.059
3. Fan LS, Lau R, Zhu C (2001) Evaporative liquid jets in gas–liquid–solid flow system. Chem Eng Sci 56(21):5871–5891. https://doi.org/10.1016/S0009-2509(01)00283-4
4. Li T, Pougatch K, Salcudean M (2010) Numerical modeling of an evaporative spray in a riser. Powder Technol 201(3):213–229. https://doi.org/10.1016/j.powtec.2010.03.037
5. Li J, Fan YP, Lu CX (2013) Numerical simulation of influence of feed injection on hydrodynamic behavior and catalytic cracking reactions in a FCC riser under reactive conditions. Ind Eng Chem Res 52(32):11084–11098. https://doi.org/10.1021/ie400250c
6. Pan H, Liang XF, Zhu LT (2019) Computational fluid dynamics simulation of gas–liquid–solid polyethylene fluidized bed reactors incorporating with a dynamic polymerization kinetic model. Asia-Pac J Chem Eng 14(1):e2265. https://doi.org/10.1002/apj.2265
7. Yu J, Wang S, Luo K, Fan J (2023) Discrete element simulation of gas-solid and gas-liquid-solid flows. Ind Eng Chem Res. https://doi.org/10.1021/acs.iecr.3c01173
8. Wang S, Wu F, Di B (2023) Intensification effect of a multi-jet structure on a multiphase flow and desulfurization process in a fluidized bed. ACS Omega 8(6):5861–5876. https://doi.org/10.1021/acsomega.2c07658
9. Koračin N, Zupančič M, Vrečer F (2022) Characterization of the spray droplets and spray pattern by means of innovative optical microscopy measurement method with the high-speed camera. Int J Pharm 629:122412. https://doi.org/10.1016/j.ijpharm.2022.122412
10. Lukas B, Andres C, Hochenauer C (2022) Multi-scale modelling of fluidized bed biomass gasification using a 1D particle model coupled to CFD. Fuel 324:124677. https://doi.org/10.1016/j.fuel.2022.124677

A Novel Electrode Model for Søderberg Electrodes

Kurian J. Vachaparambil, Stein Tore Johansen, Sten Yngve Larsen, Mehdi Kadkhodabeigi, and Torbjørn Pettersen

Abstract Søderberg electrodes, used commonly in submerged arc furnaces for production of ferroalloys and non-ferrous metals, are used to supply AC current into the furnace. These electrodes consists of paste (a mixture of calcined anthracite/petroleum coke and coal tar pitch) that eventually gets baked—a temperature-driven process. With increase in the electrode size and current supplied, safe operation of the electrode requires models that can predict the conditions experienced during operation. In this work, a novel axisymmetric transient Søderberg electrode model is presented. The model is used to simulate an electrode undergoing various slipping sequences, variations in electrode current, casing/briquette addition, and other operational scenarios, such as shut down operation. The model is observed to run much faster than real time, thus enabling its potential use in hybrid digital twin type of applications in industries.

Keywords Søderberg electrodes · Physics-based pragmatic modelling · Electrode operations

K. J. Vachaparambil (✉) · S. T. Johansen · T. Pettersen
Process Technology, SINTEF Industry, 7465 Trondheim, Norway
e-mail: kurian.vachaparambil@sintef.no

S. T. Johansen
e-mail: stein.t.johansen@sintef.no

T. Pettersen
e-mail: torbjorn.pettersen@sintef.no

S. Y. Larsen · M. Kadkhodabeigi
Eramet Norway AS, 7034 Trondheim, Norway
e-mail: sten.yngve.larsen@eramet.com

M. Kadkhodabeigi
e-mail: mehdi.kadkhodabeigi@eramet.com

S. Wagstaff et al. (eds.), *Materials Processing Fundamentals 2024*, The Minerals, Metals & Materials Series, https://doi.org/10.1007/978-3-031-50184-5_2

Introduction

Søderberg electrodes are the dominant electrode systems technology in submerged arc furnaces for production of ferroalloys and non-ferrous metals. These electrodes, made from a paste (mixture of calcined anthracite/petroleum coke and a coal tar pitch) are baked at high temperature to produce a strong, solid, baked, and partially graphitized electrode with high electrical and thermal conductivity. The electrode is used to supply the necessary energy by means of AC current into the furnace. The paste is added from the top of the electrode arrangement, into a steel casing designed to confine the paste. The paste, in the form of large cylinders or briquettes, is pre-heated in the top section of the electrode by a heated airflow in the annulus, surrounding the electrode casing. In the lower part of the electrode, the supplied AC current causes ohmic heating, and some of the heat is extracted via the cooling system coupled to the current clamps. As the paste is heated, it softens (typically between 50 and 100 °C), resulting in the collapse of the overhead bed of briquetted paste and eventually when temperature is high enough (around 500 °C) it becomes baked, see [1]. During operation of the furnace, the electrodes are lowered, by slipping (see [2]), into the furnace at varying rates depending on the estimated consumption of the electrode. As the electrodes are lowered into the furnace and gradually consumed, new casing is welded to the top section of the electrode, and fresh paste is added at regular intervals. As the temperature evolves in the electrode during its operation, they can sometimes undergo breakage (hard and soft) resulting in parts (or entire) baked electrode falls into the furnace which are both highly undesirable (see [1] or [2]). To prevent electrode breakage, the baking isotherm position must be within the current clamp region and regulation of thermal stresses are critical.

With increase in the size of the electrodes and current supplied as well as the use of different pastes (like the PAH free variants), safe operation of the electrode requires mathematical models that can predict the conditions experienced by the electrode during operation. In literature such mathematical models, often referred to as the ‘electrode models’, have predominately been developed by Elkem and is based on temperature and thermal stress modelling [3, 4]. Apart from the models from Elkem, works like [1, 5] have also modelled Søderberg electrodes at various levels of complexity.

In this work, we present a novel axisymmetric transient Søderberg electrode model, developed based on principles of pragmatism. The model includes treatment of the relevant multiphysics along with the ability to model typical operations scenarios like paste addition, electrode slipping, casing addition, electrode consumption, and changes in supplied current. The proposed model is used to predict the position of the baking isotherm in the electrode during various operational scenarios like different current supplied, slipping rate of electrode, and a four hour shutdown.

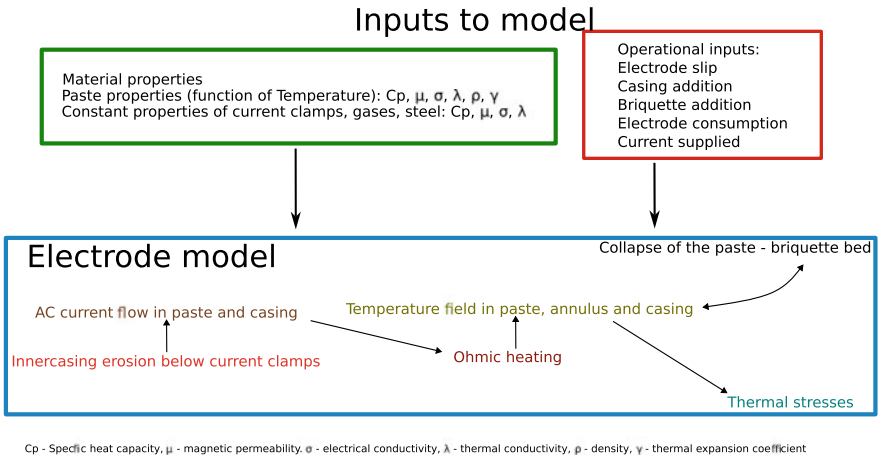

Fig. 1 Schematic of proposed electrode model with the inputs and multiphysics treated

Overview of the Proposed Electrode Model

The electrode model accounts for the multiphysics associated with Søderberg electrodes, i.e., electromagnetism, heat transfer, paste softening, and baking. The overall schematic of the proposed electrode model is illustrated in Fig. 1.

The proposed model uses a axisymmetric assumption with the coordinate system defined with respect to the top of the casing. The computational domain consists of regions that contains paste, fins, casing (inner and outer), and annulus. During operation, the computational domain and the locations of the boundaries (with current clamps, and furnace) are updated as electrode is slipped or new casing is added, see illustration in Fig. 2. Based on the geometry, the model assigns the volume fractions to the different regions (see Fig. 2). This volume fraction definition is used in mixture averaging based definition of the thermo-physical and electromagnetic properties (like ρ, μ, σ, C_p, λ—mixture averaged density, magnetic permeability, electrical conductivity, specific heat capacity, and thermal conductivity).

The electromagnetic model employed is based on solving for magnetic field ($\vec{B}$):

$$\nabla \times \frac{1}{\mu\sigma} \nabla \times \vec{B} = -i\omega\vec{B} \tag{1}$$

where $\omega = 2\pi f$ and f is the frequency of the supplied AC current. The above equation is derived from Maxwell's equations under the assumptions that electromagnetic fields can be expressed as time harmonic fields, no charge source is present in the domain, and the contribution of the electrical displacement term is negligible as the AC current frequencies are low ($f \approx 50\,\text{Hz}$). To solve $\vec{B}$, based on Eq. 1, appropriate boundary condition is implemented such that the current, computed as $\vec{J} = \frac{1}{\mu}\nabla \times \vec{B}$, is physically realistic.

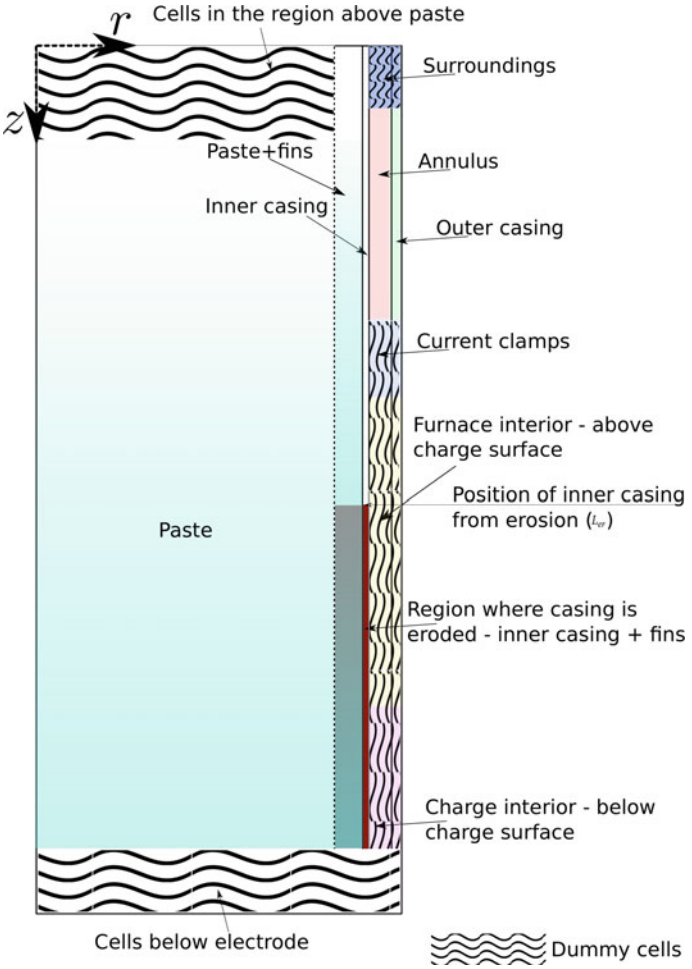

Fig. 2 Schematic of geometry used in the model

Observations during electrode excavations show that at a finite distance below the current clamps the casing gets eroded. And in preliminary simulations, it was observed that the current flows though the inner casing instead of flowing through paste due to the lower electrical resistance of the former. So treating this erosion of casing is critical as it will result in the current to flow in through the electrode—causing it to get baked. This inner casing erosion is treated via a simplified model:

$$\frac{\mathrm{d}L_{\mathrm{er}}}{\mathrm{d}t} = \frac{L_{\mathrm{er,eq}} - L_{\mathrm{er}}}{\tau_{\mathrm{er}}} \tag{2}$$

where τ_{er} is the time scale for erosion of casing and $L_{er,eq}$ is the user defined equilibrium location until which the casing can be eroded. This erosion model is different from the approach used in Elkem model which has been briefly described in [4].

The temperature model of the electrode accounts for the heat added to the paste due to the circulation of warm air in the annulus along with heat transfer into inner and outer casing, ohmic heat due to current flow, heat transfer from electrode end, heat lost due from electrode due to convection and radiation. To save computational cost, a single governing equation for temperature, developed based on mixture model, is employed:

$$\rho \frac{\partial}{\partial t} C_p T + \rho C_p \vec{U}_p \cdot \nabla T = \nabla \cdot \left(\lambda \nabla T\right) + S_T + \Gamma_p \Delta H \tag{3}$$

where T is the mixture temperature in the entire computational domain shown in Fig. 2, $\vec{U}$ is the collapse velocity of the briquette bed, S_T is the source term corresponding to the average ohmic heating in inner casing and paste that is computed based on $\left\langle \vec{J} \cdot \vec{J} \right\rangle_{RMS} / \sigma$, and $\Gamma_p \Delta H$ considers the enthalpy change associated with vaporization and pyrolysis of paste which is endothermic and exothermic, respectively. It should be noted that conjugate heat transfer between inner/outer casing and annular flow is treated within the above equation. The boundary condition on inner casing—current clamps boundary is based on a user defined overall heat transmission coefficient and temperature representing the water cooling of current clamps. The outer casing—surrounding boundary uses a convective heat transfer whereas boundaries at the inner casing—furnace interior employ a convective-radiative heat transfer. It should be noted that the temperature model does not account for the heat transfer due to the transport of volatiles emanating from the paste. Based on the temperature field, a simplified post processing based model for thermal stresses, using linear coefficient of thermal expansion (which is a function temperature), is used.

As the softening of the individual briquette and collapse of the briquette bed is an extremely complex, we use a simplified approach to simulate this phenomena. We assume that the collapse occurs predominately in the axial direction, and the collapse of the briquette is a pure function of temperature which goes from a fixed volume fraction (of 0.5) for fresh briquettes to unity when the briquette has softened. Using this collapse function, which is represented as α_p^*, an artificial 1D momentum equation is constructed to compute $\vec{U}$:

$$\frac{\partial}{\partial z}\left(\rho_p \alpha_p^* \vec{U}\right) = \left(\alpha_p - \alpha_p^*\right) \frac{\partial \rho_p}{\partial t} - \rho_p \frac{\partial \alpha_p^*}{\partial t}, \tag{4}$$

where ρ_p is the density of paste (which is a function of temperature) and α_p is the physical volume fraction of the paste present in the computation domain.

Based on the collapse velocity, computed in Eq. 4, the briquette bed becomes compacted or results in the redistribution of α_p. This is simulated by solving the 1D paste volume fraction conservation equation:

$$\rho_{\mathrm{p}} \frac{\partial \alpha_{\mathrm{p}}}{\partial t} + \frac{\partial}{\partial z}\left(\rho_{\mathrm{p}} \alpha_{\mathrm{p}} \vec{U}\right) = 0. \tag{5}$$

The above equation is solved using numerics to allow for a sharp interfacial advection of the briquette bed. Once the collapse of the briquette, driven by temperature, is simulated, the α_{p} is corrected to account for the electrode consumption and new briquette addition.

The above governing equations is implemented in Python based on the Finite Volume Method (FVM) approach. The descritization of the governing equations is based on first order upwinding scheme. The computational domain is divided into hexahedral cells with flow fields saved as the cell center except for the collapse velocity which is save on the cell faces—staggered arrangement. The time step used by the solver is user specified. The results from the electrode model are visualized using Paraview—an open source visualization software.

Results

In order to showcase the predictive ability of the proposed model, we use it to predict the location of baking zone in an electrode of diameter 1.52 m under various operational scenarios. The baking zone location, which indicates the region when the electrode paste becomes baked, is typically maintained within the current clamps during operation to prevent breakage of the electrode [3]. For simplicity, we consider the 475 °C isotherm to represent the baking zone in the electrode. During the simulation, the electrode is slipped, new briquettes and casing are added to the top apart from its consumption within the furnace. The operation scenarios considered in this work are chosen to be illustrative in nature rather than realistic operational data. Due to the confidentially of the data, the material properties and detailed simulation setting used will not be disclosed.

Impact of Electrode Slip on Baking Isotherm Location

To study the impact of different electrode slipping pattern (for a constant supplied current density of 5×10^4 A/m^2) on baking isotherm position, we consider the following two scenarios: Slip 1—where electrode is slipped by 0.0125 m every 0.5 h, and Slip 2—where electrode is slipped by 0.15 m every 6 h. In these cases, the electrode is slipped by the same amount over the duration of a day.

Figure 3 shows the location of the baking isotherm for the two slipping patterns used. The large slip is seen to abruptly lower the position of the baking isotherm when compared to shorter slip at the instance on the slip. Once the electrode is slipped, then the 'new' paste experiences higher temperature along with the impact of casing erosion—eventually baking it. The baking isotherm location, in the case

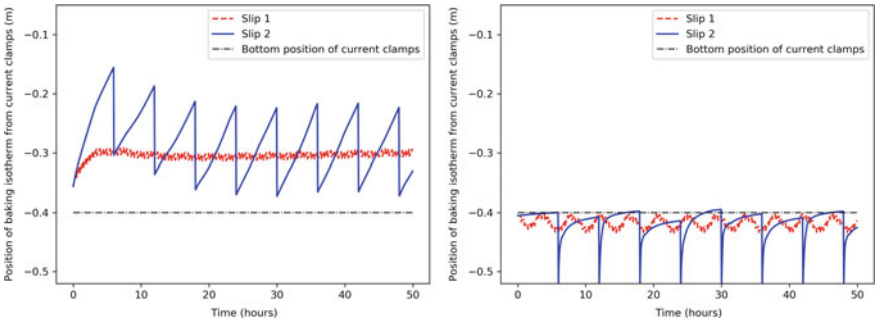

Fig. 3 Axial location of baking isotherm for two different slipping patterns (Slip 1—0.0125 m every 0.5 h, and Slip 2—0.15 m every 6 h): on axisymmetric line (left) and on electrode surface (right). Note the coordinate system used in these plots is such that $z = 0$ is at the center of the current clamps and larger negative values indicate positions further below the current clamp center

of the electrode undergoing Slip 1, is clearly seen to reach an asymptotic value after the slip (close to the behaviour observed using a shorter slips). The difference in the asymptotic behaviour of baking isotherm is related to the addition of fresh briquette to the top of the electrode which subsequently get heated up and then collapses. The collapse velocity of the bed alters the temperature distribution and thereby the location of the baking isotherm. Interestingly, in the case of the electrode undergoing Slip 1, the slips are not large enough to cause large changes to the system resulting a slow transition of paste into baked state. Interestingly, in the case of Slip 1, baking isotherm location is also seen to exhibit an oscillating pattern over the span of few hours which cannot be explained by the slipping rate used. It should be noted that the transient behaviour observed in the beginning of Fig. 3 is due to the initial conditions used by the simulations.

Effect of Current Supplied on Baking Isotherm Location

The impact of the current supplied to the electrode on the baking isotherm location is investigated for two current densities: 5×10^4 A/m^2 and 6×10^4 A/m^2. Due to the larger ohmic heating associated with higher supplied current, the baking isotherm moves further into the current clamps as seen in Fig. 4. It should be mentioned in both these simulation, the electrode was slipped 0.0125 m every 0.5 h.

Thermal Stresses During a 4 h Shutdown Operation

In order to simulate a 4 h shutdown of current to the electrode, we assume that the current (rather the current density) supplied to the electrode varies as a function

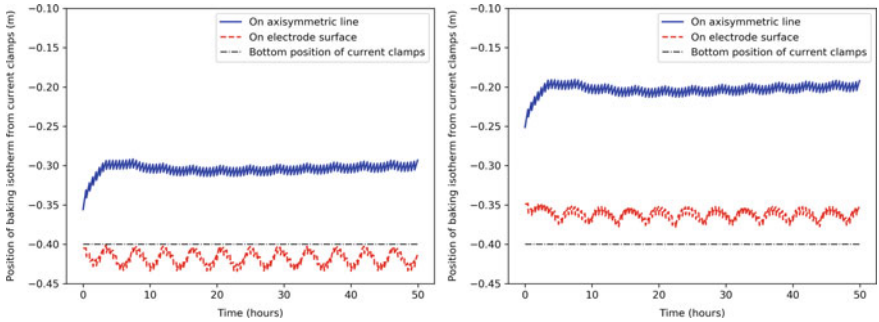

Fig. 4 Axial location of baking isotherm on axisymmetric line and electrode surface for the two scenarios of current density supplied to electrode: 5×10^4 A/m^2 (left) and 6×10^4 A/m^2 (right). Note the coordinate system used in these plots is such that $z = 0$ is at the center of the current clamps and larger negative values indicate positions further away (below) from the current clamp center

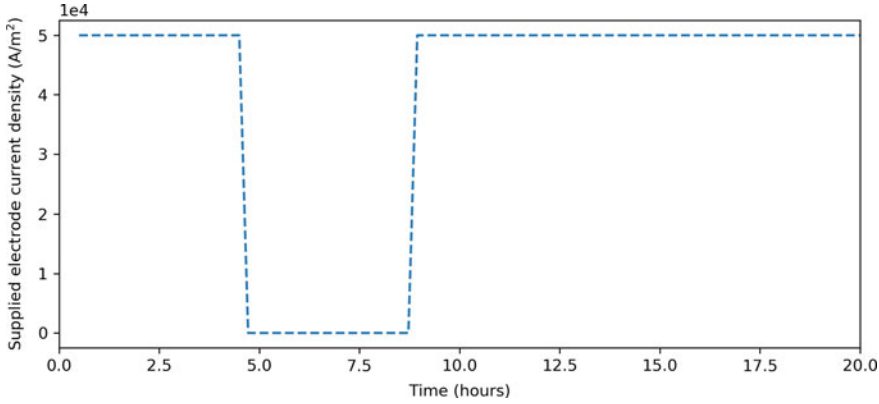

Fig. 5 Variation of the current density supplied to electrode during shutdown operation

of time based on Fig. 5. It should be noted that during the shutdown operation, the thermal boundary conditions are not changed and no operations are performed on the electrode. The stress predicted by the model before shutdown and during the recovery (or once current is provided after shutdown) is shown in Fig. 6. As the baked paste, contract at temperature below 1000 °C and thereafter it expands [5], the stress experienced by the electrode sections can be either compression (when values are smaller than zero) or tension (when values are larger than zero) [3]. The contours show that during recovery, the both compressive and tension stresses are acting on the electrode both radially and axially. Further, studies are required to identify the risk of breakage from these model predictions.

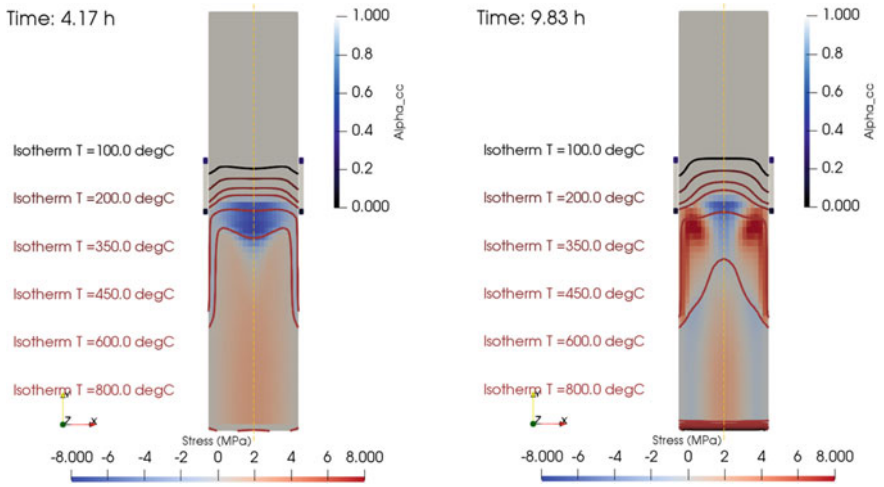

Fig. 6 Thermal stress distribution and temperature isotherms (coloured lines), within the paste region in the computational domain (dashed vertical line represents $r = 0$), during shutdown of current for 4 h to the electrode: before current is shutdown (left) and after almost an one hour recovery (right)

Conclusion

A novel framework to simulate the conditions experienced by Søderberg electrode during operation is presented in this work. The model is demonstrated for a hypothetical electrode to investigate the position of the baking zone under various operating scenarios (like current and slipping rate) and thermal stresses (during a 4h shutdown). The model can be potentially used as a hybrid digital twin as it run relatively quickly—it ran about 65 times faster than real time.

Future works in this topic should consider implementing a non-reversible change in the paste's properties as it is heated up, more realistic boundary conditions which are representative of operational conditions, and model validation using industrial data.

Acknowledgements The current work has been funded by Eramet and The Research Council of Norway (IPN—Project number 313864). The authors would like to thank Eramet for the detailed discussions and for the approval to publish this work.

References

1. Van Gorder RA, Kamilova A, Birkeland RG, Krause AL (2021) Locating the baking isotherm in a Søderberg electrode: analysis of a moving thermistor model. SIAM J Appl Math 81(4):1691–1716

2. Innvaer R, Fidje K, Kalgraf K (1995) Expert system for Soderberg electrodes. Proc INFACON 7:555–564
3. Larsen B (2012) Electrode models for Søderberg electrodes. In: The proceedings of fifth international platinum conference, pp 494–500
4. Innvaer R, Fidje K (1986) Effect of current variations on material properties and thermal stresses in Soderberg electrodes. Proc INFACON 4:321–330
5. Dougall IM, Smith CFR, Olmstead O, Gericke WA (2004) A finite element model of a Søderberg electrode with an application in casing design. Proc INFACON 10:575–584

Development of the KR Desulfurization Process Model Centered on Production Rhythm

Guosen Zhu, Pan Gao, Jianping Yang, Bin Chen, and Xiaodong Zhao

Abstract Nowadays, most steelmaking plants still rely on manual experience to perform Kambara Reactor (KR) desulfurization, which makes it difficult to accurately control the endpoint [S] content for different steel grades, and can easily cause the waste of resources. To achieve cost reduction and efficiency increase, a KR desulfurization process model with production rhythm as the core was developed. The model included three desulfurization modes based on different requirements, namely process priority, time priority, and desulfurizer priority. The self-learning function to regress historical data of past heats was used in the modes of time priority and desulfurizer priority to obtain process parameters, while the process priority mode calculated process parameters just in the dependence of working conditions of current heat. After applying the developed model in a steelmaking plant, the average consumption of desulfurizer decreases from 6.41 to 5.27 kg/t. The one-time hit ratio of desulfurization pretreatment increases from 96.47 to 98.63%.

Keywords KR desulfurization · Process model · Production rhythm · Process priority · Time priority · Desulfurizer priority

Introduction

With an increasing demand for high-quality steel with low sulfur, Kambara Reactor (KR) has gradually become a widely used desulfurization pretreatment process for molten iron in long steelmaking processes, due to its low cost, good dynamic conditions, and high desulfurization efficiency [1, 2]. The KR desulfurization process is invented by Nippon Steel in 1963 and applied for industrial production in 1965. The KR desulfurization process mainly involves immersing a cross shaped stirring head

G. Zhu · P. Gao (✉) · J. Yang · B. Chen
Shougang Research Institute of Technology, Beijing 100043, China
e-mail: glpon@163.com

G. Zhu · X. Zhao
Beijing Shougang Co., Ltd, Beijing 100041, China

S. Wagstaff et al. (eds.), *Materials Processing Fundamentals 2024*, The Minerals, Metals & Materials Series, https://doi.org/10.1007/978-3-031-50184-5_3

into a certain depth of the ladle filled with molten iron. In detailed, the desulfurizer, such as calcium oxide, is added to the surface of the molten iron by the feeder, and then is fully contacted and reacted with the molten iron by the vortex generated from the stirring head rotating, achieving the goal of desulfurization [3].

As the main raw material consumption of the KR desulfurization process, the amount of desulfurizer directly affects the smelting cost of the desulfurization process. At the same time, high consumption of desulfurizer can cause a large slag amount, a long slag removal time with high iron loss, directly leading to an increase in iron consumption in the steelmaking process [4]. Based on existing technological means, adopting an economical amount of desulfurizer is an important strategy to reduce the production cost of KR desulfurization without modifying the equipment and making large-scale adjustments to the operator personnel [5]. Many steel enterprises have conducted lots of research and obtained significant results, such as Angang, and Wisco [6–8].

Based on the actual situation in the studied steelmaking plant, different steel grades have completely different control requirements for sulfur content. Some varieties, such as oriented silicon steel, require very low sulfur content in the molten steel, and the casting times of some cast plans are also tight for control. At the same time, there are also conventional products in some heats that have relatively loose requirements for sulfur content. Based on such a practical condition, a desulfurization process model with production rhythm as the core was developed according to different molten iron conditions, to meet the production rhythm and quality requirement.

Concept of Desulfurization Process Model Centered on Production Rhythm

The desulfurization process model centered on production rhythm mainly includes three desulfurization process modes, namely process priority, time priority, and desulfurizer priority.

The modes of time and desulfurizer priorities mainly use self-learning functions to regress based on historical data of past heats, to obtain the processing data of the heats closest to the current processing heat, and to determine the desulfurization process mode. Among them, the self-learning formula for stirring time mainly considers 5 heat data with initial [S] content deviation within $\pm 0.01\%$ and temperature deviation within ± 10 °C and then takes the average value for desulfurization treatment.

The process priority mode does not refer to data from previous heats, and each heat is recalculated based on the process model. The modes of time and desulfurizer priorities are mainly based on the implementation of the self-learning function.

The design concept of the desulfurization process model centered on production rhythm is as follows: the default mode is the process priority process. If there is a surplus processing time, the desulfurizer priority mode can be selected to achieve low desulfurizer consumption. If high-level steel grades such as silicon steel are

produced, and the time priority mode is adopted since the production rhythm is very tight. Based on historical heat, increasing desulfurizer consumption is adopted to achieve a rapid desulfurization effect, ultimately meeting the need for production rhythm.

Parameter Design of Time Priority and Desulfurizer Priority Modes

The desulfurization process model in this paper is divided into three modes: process priority, time priority, and desulfurizer priority, and the specific meanings of each mode are as follows:

(1) Process priority: Based on the initial conditions and the set process model, calculate the required desulfurizer consumption, stirring time, and other parameters.
(2) Time priority: Analyze historical heat data to obtain the minimum stirring time for heats with similar initial [S] content and temperature as current heat, and set it as the stirring time for the current heat.
(3) Desulfurizer priority: Analyze historical heat data to obtain the maximum stirring time for heats with similar initial [S] content and temperature as current heat, and set it as the stirring time for the current heat.

Parameter Design of Time Priority Mode

The analysis steps for the historical heats used in the time priority mode are as follows:

(1) Select 5 historical heats without secondary stirring, whose initial [S] content and temperature are closest to those of the current heat, and the shortest stirring time for them is selected as the stirring time for the current heat;
(2) Based on process priority as the mode, select 3 historical heats without secondary stirring, whose initial [S] content and temperature are closest to those of the current heat;
(3) Based on time priority as the mode, select 3 historical heats without secondary stirring, whose initial [S] content and temperature are closest to those of the current heat;
(4) Take the average actual consumption of desulfurizer for the 6 heats selected above as the set value of desulfurizer for the current heat.

In the method, 3 historical heats are selected to avoid serious deviation of the calculation results from operational practice due to special circumstances of a single heat.

In this method, the selected historical data are all actual production data, which means that the historical heats are considered as a large number of industrial experiments, and the model selects the optimal experimental results as control parameters for the current heat. Through this method, it is possible to steadily reduce the consumption of desulfurizers while ensuring the effectiveness of desulfurization.

Parameter Design of Desulfurizer Priority Mode

The desulfurizer priority mode will increase the desulfurization processing time, and the analysis steps for its historical heat are as follows:

(1) Select 5 historical heats without secondary stirring, whose initial [S] content and temperature are closest to those of the current heat, and the longest stirring time for them is selected as the stirring time for the current heat;
(2) Based on desulfurizer priority as the mode, select 6 historical heats without secondary stirring, whose initial [S] content and temperature are closest to those of the current heat;
(3) Take the average actual consumption of desulfurizer for 6 heats selected above as the set value of desulfurizer for the current heat.

This method aims to reduce the consumption of desulfurizer by extending the stirring time. At the same time, this process can achieve a low-cost effect. The process achieves a reduction in desulfurizer consumption by assuming 3 existing heats as shown in Fig. 1: the time priority mode is selected for the first heat with shorter time consumption and more desulfurizer consumption; the process priority mode is selected for the second heat with common time consumption and desulfurizer consumption; the desulfurizer priority mode is selected for the third heat with the least desulfurizer consumption and longer time consumption. Assuming that the model starts learning based on previous heats, if the fourth heat adopts the time priority mode, and the difference in processing time between the first and second heats is not significant, then the set desulfurizer consumption in the fourth heat will be the average value of desulfurizer consumption in the first and second heats (the third heat was not considered due to the significant difference in time with the first heat). In this case, the desulfurizer consumption in the fourth heat will be reduced compared to the first heat while ensuring the desulfurization effect, eventually reaching the level of the second heat. That is to say, the desulfurizer consumptions calculated by the time priority and the process priority modes are equivalent after a certain period of learning. At this point, the technical engineers will adjust the model parameters of the process priority mode to further reduce the desulfurizer consumption.

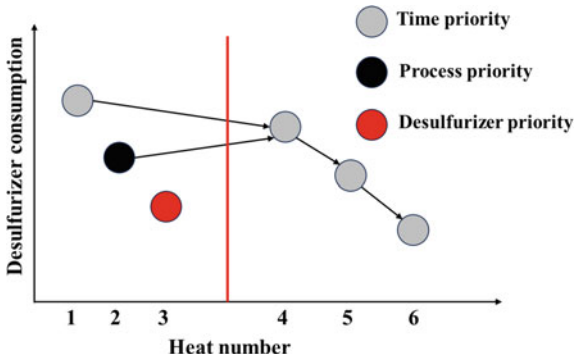

Fig. 1 Design concept of desulfurization process model based on cost reduction

Parameters Design of Process Priority Mode

Calculation of Desulfurizer Consumption

Among the factors that affect desulfurizer consumption, quantifiable ones include initial molten iron temperature, weight, sulfur content, and silicon content. The effective content and apparent utilization rate of desulfurizers can be estimated through certain methods.

The calculation of desulfurizer consumption is based on the initial [S] of molten iron, fitting the calculation formula, and then making corrections based on the initial temperature of molten iron, silicon, weight, effective content, and utilization rate of desulfurizer:

$$W_{\mathrm{DeS}} = \frac{a * [\%\mathrm{S}] + b + k * ([\%\mathrm{Si}] - [\%\mathrm{Si}]_0) + m * (T - T_0)}{\eta \times \omega \times W_0 / W} \tag{1}$$

where a, b: the linear parameters obtained through fitting; k: silicon correction coefficient, increased desulfurizer consumption when the initial silicon content is greater than the standard one; $[\%\mathrm{Si}]_0$: the standard value of initial silicon content; m: temperature correction coefficient, increase desulfurizer consumption when the initial temperature is greater than the standard one; T_0: the standard value of initial temperature; W_0: the standard weight of molten iron for one heat, and W is the weight of molten iron in the current heat; ω: the effective content of desulfurize, namely 85%; η: the apparent utilization coefficient of desulfurizer, namely 60%.

Calculation of Benchmark Parameters a and b

Heat Statistics with Target Sulfur of 0.005%

The relationship between the initial [S] content of molten iron and desulfurizer consumption is shown in Fig. 2, corresponding to heats with a target [S] of 0.005%.

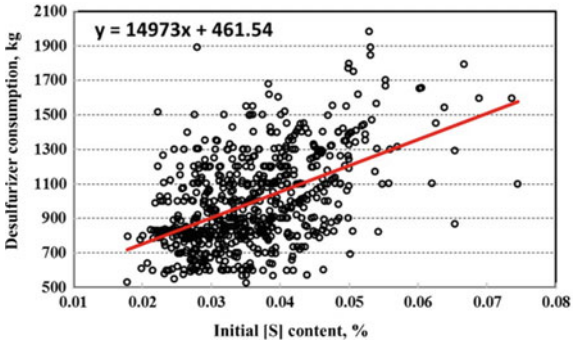

Fig. 2 Relationship between initial [S] content of molten iron and desulfurizer consumption (A target [S] of 0.005%)

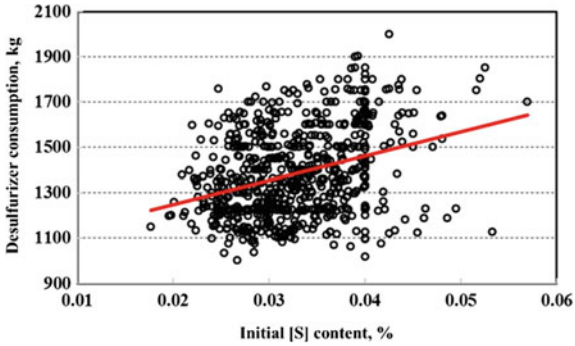

Fig. 3 Relationship between initial [S] content of molten iron and desulfurizer consumption (A target [S] of 0.001%)

Heat Statistics with Target Sulfur of 0.001%

The relationship between the initial [S] content of molten iron and desulfurizer consumption is shown in Fig. 3, corresponding to heats with a target [S] of 0.001%.

Parameter Selection and Calculation Formula

The relationships between the initial [S] content of heats with the target [S] values of 0.001% and 0.005% and the desulfurizer consumption are similar in slope (about 5% difference). The relationship for heats with the target [S] value of 0.001% is treated as the calculation basis, and then making corresponding corrections on this basis serves as the calculation formula for the target [S] value of 0.005%.

$$\text{Calculation parameter: } a = 15848 \times 0.85 \times 0.6 = 8082;$$
$$b = 878 \times 0.85 \times 0.6 = 447.$$

The calculation formula for heats with the target [S] value of 0.001% is as follows:

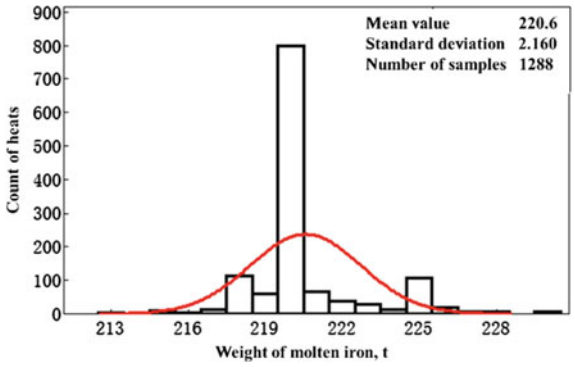

Fig. 4 Weight distribution of molten iron

$$W_{\mathrm{DeS}} = \frac{8082 \times [\%\mathrm{S}] + 447 + k \times ([\%\mathrm{Si}] - [\%\mathrm{Si}]_0) + m \times (T - T_0)}{0.85 \times 0.6 \times 220/W} \quad (2)$$

Selection of Standard Molten Iron Weight

The weight distribution of molten iron is as shown in Fig. 4.

From Fig. 4, it can be seen that the average weight of molten iron is 220.6 t, with a normal distribution and a standard deviation of 2.16 t. Therefore, the standard weight of molten iron for one heat is determined as 220.6 t, with a minimum value of 215 t and a maximum value of 225 t.

Silicon Correlation Coefficient

The distribution of initial [Si] content in molten iron is as shown in Fig. 5:

The average [Si] content of 0.33% is treated as the standard [Si] content, meanwhile 0.15% and 0.55% are treated as the lowest and highest [Si] contents respectively.

If the maximum influence of [Si] content is 100 kg in desulfurizer consumption, the influence coefficient of initial [Si] content is as follows.

$$k = 100 \div (0.55 - 0.33) \times 0.85 \times 0.6 = 231.8 \quad (3)$$

$$W_{\mathrm{DeS}} = \frac{8082 \times [\%\ \mathrm{S}] + 447 + 231 \times ([\%\ \mathrm{Si}] - [\%\ \mathrm{Si}]_0) + m \times (T - T_0)}{0.85 \times 0.6 \times 220/W} \quad (4)$$

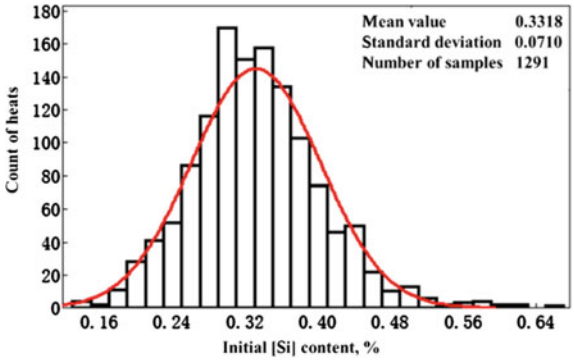

Fig. 5 Distribution of initial [Si] content in molten iron

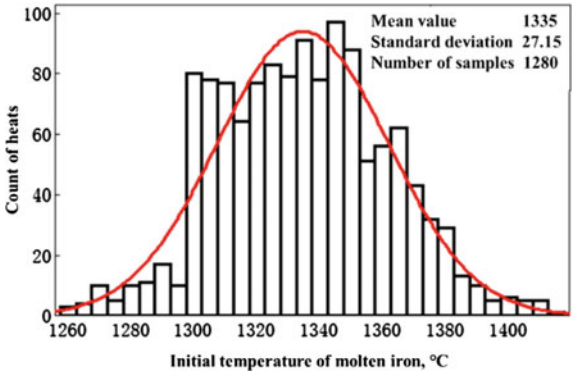

Fig. 6 Temperature distribution of molten iron entering the station

Temperature Correlation Coefficient

The initial temperature distribution of molten iron is as shown in Fig. 6.

The average temperature of 1335 °C is treated as the initial standard temperature, meanwhile, 1260 °C and 1400 °C are treated as the lowest and highest temperature respectively. If the maximum influence of temperature is 100 kg in desulfurizer consumption, the initial temperature influence coefficient is as follows:

$$m = 100 \div (1335 - 1250) \times 0.85 \times 0.6 = 0.61;$$

For heats with the target [S] of 0.001%, the desulfurizer calculation formula:

$$W_{\mathrm{DeS}} = \frac{8082 \times [\%\mathrm{S}] + 447 + 231 \times ([\%\mathrm{Si}] - [\%\mathrm{Si}]_0) + 0.61 \times (T - T_0)}{0.85 \times 0.6 \times 220/W} \quad (5)$$

For heats with the target [S] of 0.005%, the desulfurizer calculation formula:

$$W_{\mathrm{DeS}} = \frac{8082 \times [\%\mathrm{S}] + 243 + 231 \times ([\%\mathrm{Si}] - [\%\mathrm{Si}]_0) + 0.61 \times (T - T_0)}{0.85 \times 0.6 \times 220/W} \quad (6)$$

Table 1 Division of stirring stage

Stirring stage	1	2	3	4
Method analysis	Fixed time	Percentage of remaining time	Percentage of remaining time	Percentage of remaining time
Stirring time	150 s	30%	30%	40%
Notes	Adopting a fixed time of 150 s	Allocate the remaining time as a percentage to stage 2/3/4		

Stirring Time Control Method

Based on the control characteristics of the KR desulfurization process and the principle of optimal stirring dynamics conditions, the KR smelting process is controlled in stages, and the speed and stirring time of different stages are adjusted to ensure uniform stirring of molten iron. The stirring stage is divided into: stirring head descending stage, stirring speed increasing stage, adding the first batch of materials stage, stirring stage 1, stirring stage 2, stirring stage 3, stirring stage 4, and stirring head ascending stage. Each stage corresponds to different stirring speeds and times. In the early stage, it mainly involves the acceleration of the stirring head, batch feeding, and slag melting process, while in the middle and later stages, it is the stage of full stirring, desulfurization slag floating, and removal.

To flexibly adjust the time ratio of each stage and ensure that there is enough time required for the acceleration stage, the following time allocation modes are designed for 4 stirring stages (Table 1).

The allocation method for each time period is optional: each time period can be in the form of fixed values and percentages. At the same time, considering the possibility of a calculation time of 0 for a certain stage, at least two stages are calculated in percentage form.

Insertion Depth Control Method

Due to KR being a typical interfacial reaction, the desulfurization reaction only occurs on the surface of the desulfurizer. Therefore, it is necessary to maximize the contact area between the desulfurizer and molten iron to achieve good desulfurization results. Therefore, in the design of insertion depth, it is necessary to consider the dynamic factors of desulfurization and optimize the insertion depth.

Since the insertion depth cannot be adjusted during the stirring process, the insertion depth for heats is set at the beginning of the stirring process. During the stirring process, the system will automatically execute control actions such as lowering the stirring head to the processing position, stirring, and lifting the stirring head to the waiting position.

Under the condition of enabling self-learning of insertion depth, the system will use the insertion depth set in the previous heat as the set value for the current heat when initializing the heat data.

Application Effect

The desulfurization process model centered on production rhythm has been applied in the studied steelmaking plant, achieving a reduction in worker labor intensity, and a significant increase in labor productivity. After the application of the desulfurization process, remote slag removal control is achieved, and one-key desulfurization control is achieved. The desulfurization operation for each heat is optimized from 83 to 14 steps (Fig. 7).

After optimization, the desulfurizer consumption in the studied steelmaking plant has steadily decreased from the monthly average of 6.41 kg/t (the minimum of 5.91 kg/t, maximum of 6.99 kg/t) to 5.27 kg/t (the minimum of 4.96 kg/t, maximum of 5.82 kg/t), achieving a reduction in desulfurization cost and resource consumption (Fig. 8).

After the application of the developed model, the average one-time hit rate of desulfurization has significantly improved from 96.47 to 98.63% (Fig. 9). Meanwhile, the stability has greatly improved with a minimum of 97.37% and a maximum of 99.20%.

	Enter the station		During processing				After processing	
Operation:	Slagging	Sample	Model calculation	Stirring head descending	Stirring process: speed, time, depth	Stirring head ascending	Sample	Slagging
Before optimization:	2	5	5	7	54	3	5	2
After optimization:	1	2	7	1	0	0	2	1

Fig. 7 Changes in KR operation steps before and after process improvement

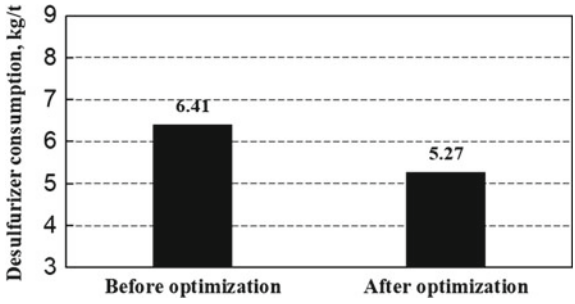

Fig. 8 Changes in KR desulfurizer consumption before and after optimization

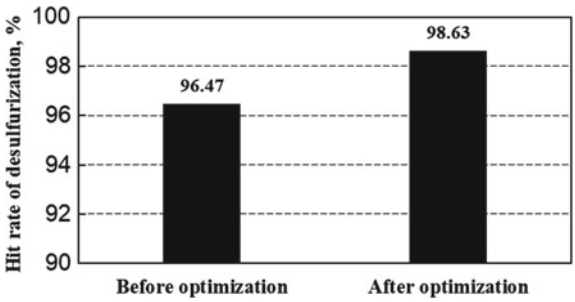

Fig. 9 Changes in one-time hit rate of desulfurization before and after optimization

Conclusions

(1) The KR desulfurization process model with production rhythm as the core was developed, including three desulfurization modes based on different requirements, namely process priority, time priority, and desulfurizer priority.
(2) The self-learning function to regress historical data of past heats was used in the modes of time priority and desulfurizer priority to obtain process parameters, while the process priority mode calculated process parameters just in the dependence of working conditions of current heat.
(3) After the application of the developed model, remote slag removal and one-key desulfurization is achieved, and the desulfurization operation for each heat is simplified from 83 to 14 steps.
(4) After applying the developed model, the average consumption of desulfurizer decreases from 6.41 kg/tFe to 5.27 kg/tFe, and the average one-time hit ratio of desulfurization pretreatment increases from 96.47 to 98.63%.

References

1. Zhao W (2013) Comparison of desulphurization processes of injection and KR method. Metall Equip 204:86–88
2. Ji JH, Liang RQ, Feng YT et al (2012) Study on the characteristics of fluid flow in stirring vessels of new type stirring of KR desulphurization. J Iron Steel Res S1:171–174
3. Wang XH (2007) Iron and steel metallurgy–steelmaking. Higher Education Press, Beijing
4. Qin ZH, Chen XL (2017) Production practice of reducing KR desulfurizing agent consumption in steel. Wisco Technol 55(2):16–18
5. Yan XB, Zhao XD, Zhang LG et al (2017) The study of economical desulphurizer consumption computational model utilized on KR desulfurization process. In: Proceedings of the 11th China steel annual conference, Beijing
6. Song JS, He HL, Liu PF et al (2019) Development of model with deep immersion for desulphurization by KR method in Ansteel and application of the model. Angang Technol 3:22–25

7. Xu CC, Wang AJ, Liao LH et al (2013) Application of KR hot metal desulfurization technology and one key desulfurization. Wisco Technol 51(2):17–20
8. Zhou JF, Peng JY, Cheng ZQ et al (2022) Study on water model test of KR stirred hot metal desulfurization. Steelmaking 38(5):10–15

Evolution of the Tundish Flux Microstructure During Continuous Casting Process: A Molecular Dynamics Simulation Study

Hao Hu, Xianyang Wang, Peng Shi, Xin Xie, Chenhui Wu, Mujun Long, and Dengfu Chen

Abstract Following the absorption of inclusions, alterations occur in the microstructure of the tundish flux, thereby affecting its performance and diminishing the quality of continuous casting blanks. In this study, molecular dynamics simulations were employed to analyze the influence of varying levels of absorbed inclusions on the flux microstructure. The results indicate that the flux continuously absorbs inclusions, such as Al_2O_3 and SiO_2, during the continuous casting process, leading to an increase in the degree of microstructural polymerization. In the later stages of continuous casting, the proportion of bridging oxygen and tricluster oxygen in the tundish flux increased by 3.7% and 5.1%, respectively, while the average bond length of Al-O increased by 0.033 Å. The complexity of the microstructure leads to the deterioration of the physical and chemical properties of the coating, such as melting point and viscosity, and further reduces its ability to absorb inclusions.

Keywords Tundish flux · Microstructure · Inclusions · Molecular dynamics

Introduction

As a commonly reactor in metallurgical processes, the tundish plays a crucial role in homogenizing the temperature and composition of molten steel, as well as promoting the floating and removal of inclusions [1, 2]. Initially, the primary purpose of adding flux to tundish is only to prevent cooling of molten steel. In recent years, with the

H. Hu · X. Wang · M. Long (✉) · D. Chen
Laboratory of Materials and Metallurgy, College of Materials Science and Engineering, Chongqing University, Chongqing 400044, China
e-mail: longmujun@cqu.edu.cn

P. Shi · X. Xie · C. Wu
Pangang Group Research Institute Co, Ltd., Panzhihua 617000, China

M. Long
National Key Laboratory of Advanced Casting Technologies, Shenyang 110000, China

S. Wagstaff et al. (eds.), *Materials Processing Fundamentals 2024*, The Minerals, Metals & Materials Series, https://doi.org/10.1007/978-3-031-50184-5_4

development of high-quality steel, the metallurgical functions of tundish fluxes have multiplied [3]. Among these functions, one of the most important is to absorb and remove the inclusions in the liquid steel, with the physicochemical properties and microstructure serving as essential indicators to evaluate the flux's ability to absorb inclusions.

At present, a significant number of scholars have extensively studied the physicochemical properties of tundish fluxes. Zheng et al. [4] optimized the composition of tundish fluxes from the thermodynamics point of view, and they conjectured that increasing alkalinity and reducing the content of SiO_2 in tundish fluxes were conducive to absorbing inclusions in steel and thus purifying liquid steel with lower oxidation. Wu et al. [5] pointed out that the ability of tundish fluxes to dissolve and absorb inclusions was directly related to its chemical composition. As the flux absorbed a large amount of inclusions in the later stage of use, the ability to capture and dissolve inclusions reduced. Liu et al. [6] conjectured that the inclusion absorption process of tundish fluxes was mainly affected by viscosity and inclusion capacity. Chen et al. [7] showed that tundish fluxes should maintain proper melting point, viscosity and surface tension, so as to provide suitable dynamic conditions for its effective absorption of inclusions. However, the performance of tundish fluxes often deteriorates significantly at the end of use.

However, at present, the microscopic mechanisms of the continuous absorption of inclusions by the flux during the continuous casting process are actively studied, and the microstructure evolution of the flux after absorbing inclusions requires further research. The molecular dynamics (MD) method is a crucial technique for calculating and simulating the microstructure of materials. It can be used to simulate the dynamic properties and microstructure of slags at high temperature [8]. In this paper, we conducted MD simulations to simulate the microstructures of molten slags at high temperatures at the atomic and molecular levels. We analyzed the impact of absorbing inclusions on the flux's structure, providing guidance for uncovering the degradation mechanisms of flux performance after absorbing inclusions and enhancing flux performance. This research is of great significance for improving the quality of continuous casting billets.

Experimental Procedures

Sampling Scheme

This article investigates the tundish fluxes used for a certain high aluminum steel (Al alloy deoxidation). After the refining of molten steel in the ladle is completed, it flows into the tundish through the ladle nozzle and begins casting. A tundish can be used to cast multiple molten steel, and a total of 6 heats of molten steel are cast in the same tundish. Tundish fluxes at the middle stage of casting is collected in each heat. The content of the flux is determined by XRF, and the results are shown in Table 1.

Table 1 Content of each component

Heat	Analysis result (%)							
	CaO	FeO	MgO	SiO_2	Al_2O_3	Cr_2O_3	F	TiO_2
2	37.47	2.44	10.42	9.15	31.75	0.38	1.13	4.48
3	34.42	2.83	11.62	10.3	31.04	0.21	1.09	5.7
4	32.54	2.32	11.61	11.63	31.16	0.33	0.89	6.38
5	26.1	2.83	11.54	12	31.12	4.65	0.64	7.04
6	23.83	2.3	10.09	11.04	35.96	3.1	0.69	8.88

Molecular Dynamics Simulation Scheme

In the MD simulation of slag, selecting the right potential function and potential parameters is the key to the success of the simulation. Born–Mayer–Higgins potential (BMH) is one of the most widely used potential functions in slag systems in recent years.

$$U_{ij} = \frac{q_i q_j}{r_{ij}} + A_{ij} \exp(-B_{IJ} r) - \frac{C_{IJ}}{r_{ij}^6} \tag{1}$$

In the formula above, $U_{ij}(r)$ is the interatomic potential; q_i and q_j is the charge of the atom; r_{ij} is the distance between atoms i and j; A_{ij}, $B_{ij,}$ and C_{ij} are energy parameters for ij that describe repulsive and van der Waals forces, respectively.

The molten layer of tundish flux is in contact with liquid steel, it is completely melted into liquid state, meeting the simulation conditions. To enhance calculation accuracy, the simulation components were simplified appropriately, and the main component of the tundish flux "CaO–Al_2O_3–MgO–SiO_2–TiO_2" was selected for calculation [9]. The atomic numbers of Al, Ca, Mg, O, Si, and Ti were calculated according to the component content of each component, as shown in Table 2.

The parameters of BMH interaction between various particles in the slag are shown in Table 3 [4].

In this study, a square model box is used as the primary cell form of high-temperature molten slag. The initial conception was random conformation, 4000 atoms were randomly distributed in the cube box of the protocell by Material Studio.

Table 2 Atomic quantity table

Heat	Al	Ca	Mg	O	Si	Ti
2	617	663	256	2257	151	55
3	600	606	284	2270	169	70
4	598	569	282	2283	190	78
5	627	479	294	2304	205	90
6	705	426	282	2324	184	111

Table 3 BMH potential parameter

Atom1	Atom2	A_{ij}(eV)	B_{ij}(1/Å)	C_{ij}(eV Å^6)
Si	O	62,794.37	0.165	0
Ca	O	717,827	0.165	8.67
O	O	1,497,049	0.17	17.34
O	Al	86,057.58	0.165	0
O	Mg	154,984.6	0.165	1.7347
O	Ti	242,696.3	0.165	0

In the calculation of atomic force, the truncation radius is selected to 8.0 Å, the truncation radius is set to 10 Å, and the truncation diameter is less than the side length of any system cell. The calculation time step is set to 1 fs, output and save data every 10 steps, and run 180,000 steps in total. First, set the initial temperature 4727 °C (5000 K), run 10,000 steps to verify the stability of the system, and fully mix to eliminate the initial distribution of atoms, and then reduce the temperature to 1550 °C (1823 K) through 50,000 steps. Finally, the structure information such as RDF are obtained by further relaxation for 50,000 steps at 1550 °C.

After reaching the equilibrium state in the calculation, the three-dimensional space coordinates of each particle are obtained. The position coordinates of each atom are analyzed using self-programmed Matlab software to determine the bonding state of each atom and calculate the proportion and distribution of each atom type.

Results and Discussion

Evolution of RDFs Between Atoms of Tundish Flux During Casting Process

The radial distribution function (RDF) curve represents the statistical analysis of the positional distance between two types of atoms, effectively characterizing the bonding state between different atoms. At 1550 °C, RDF of different ion pairs in the melt are shown in Fig. 1. As can be seen from Fig. 1, the horizontal coordinate corresponding to the RDF peak value of Si–O, Al–O, Ca–O, Mg–O, and Ti–O ion pairs, that is, the average bond length, is about 1.61 Å, 1.74 Å, 2.35 Å, 1.97 Å, and 1.87 Å, respectively. These values closely align with measurements reported in the literature [10].

Al_2O_3 and SiO_2 are the highest content of acidic substances in the slag system, and are the skeleton elements in the tundish flux solution [11, 12]. As can be seen from Fig. 1, the first wave peak values corresponding to $g_{Al–O}(r)$ and $g_{Si–O}(r)$ are about 1.61 Å and 1.74 Å, respectively, indicating that the probability of O atom existing on the shell of 1.61 Å and 1.74 Å radius from Si and A1 is the largest.

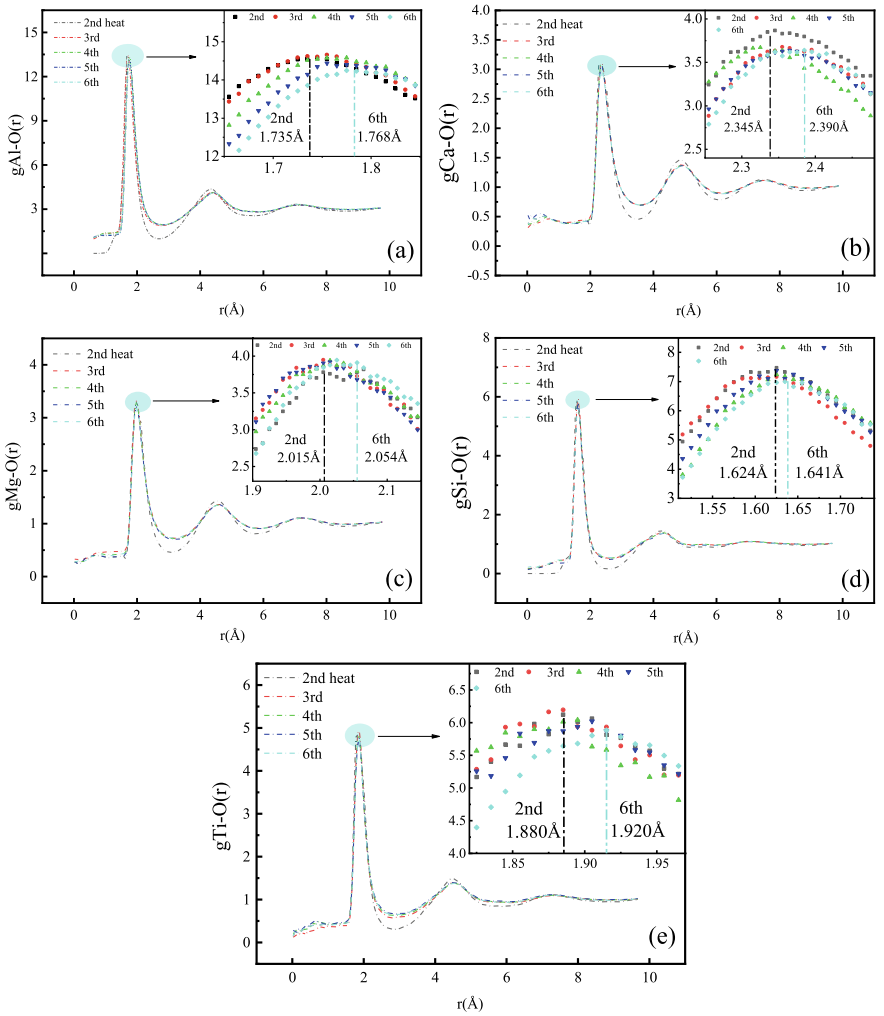

Fig. 1 RDF curve between atomic pairs: **a** Al–O, **b** Ca–O, **c** Mg–O, **d** Si–O, **e** Ti–O

The average bond length of Al–O and Si–O is 1.61 Å and 1.74 Å, respectively, which is in good agreement with the experimental values reported in literature [10]. Because the Al–O average bond length is longer than the Si–O average bond length, the Al–O bond is less stable than the Si–O bond. In addition, there are second peaks in the $g_{\mathrm{Al–O}}(r)$ and $g_{\mathrm{Si–O}}(r)$ curves, indicating the existence of long-range ordered structures. Since the first trough values corresponding to $g_{\mathrm{Si–O}}(r)$ and $g_{\mathrm{Al–O}}(r)$ are 2.0 Å and 2.5 Å, respectively, it means that the probability of the existence of O atom is 0 on the shell with 2.0 Å and 2.5 Å radii from Si and Al, respectively. 2.0 Å and 2.5 Å are defined as the truncation radius of melt structure information of Al–O bond

less than Si–O bond in Matlab statistical analysis, respectively. The O atom within the truncation radius is the first coordination with Si and Al.

For alkaline metal elements, CaO and MgO are the main alkaline substances in the slags. As can be seen from the figure, the bond length between Ca–O and Mg–O is relatively long, and the bond length gradually becomes longer with the increase of the heat times, respectively, from to. This is because alkali metal or alkaline earth metal ions play a dual role in the aluminate structure [13].

All the above studies show that the proportion of complex bridgy-oxygen structure in slags is increasing, and further statistics on the type distribution of various oxygen atoms are needed.

Evolution of Oxygen Atom Types in Tundish Flux During Casting Process

As can be seen from Fig. 2, in the flux high-temperature slag system, O_b content increases significantly, O_{nb} content decreases sharply, and O_t content increases only slightly with the increase of heat times. This is because CaO acts as a network destroyer in the system. With the decrease O_f CaO content, the O ion dissociated by CaO decreases, resulting in the polymerization of O_{nb} or O_f to form O_b or O_t, which makes the melt structure complicated. The difference between the simulated and experimental values of oxygen concentration distribution is less than 12%. In particular, there is tricluster oxygen, that is, oxygen cluster O_t, in the flux melt. The presence of O_t balances the negative charge excess of the corresponding $[AlO_4]^{5-}$ tetrahedron. In the flux system, with the decrease of CaO content, O_b or O_t is formed by polymerization, which makes the melt structure simple.

Further, each oxygen atom is further subdivided according to the different types of oxygen-like atom connecting atoms, and the statistical results are shown in Fig. 3. For free oxygen and non-bridging oxygen, the concentration of free oxygen and OA (O–Al) gradually decreases, and changes to complex bridging oxygen, while

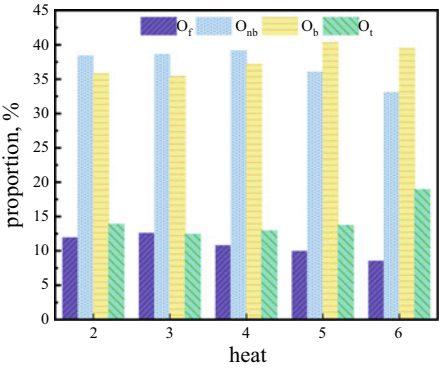

Fig. 2 Evolution law of oxygen atom types

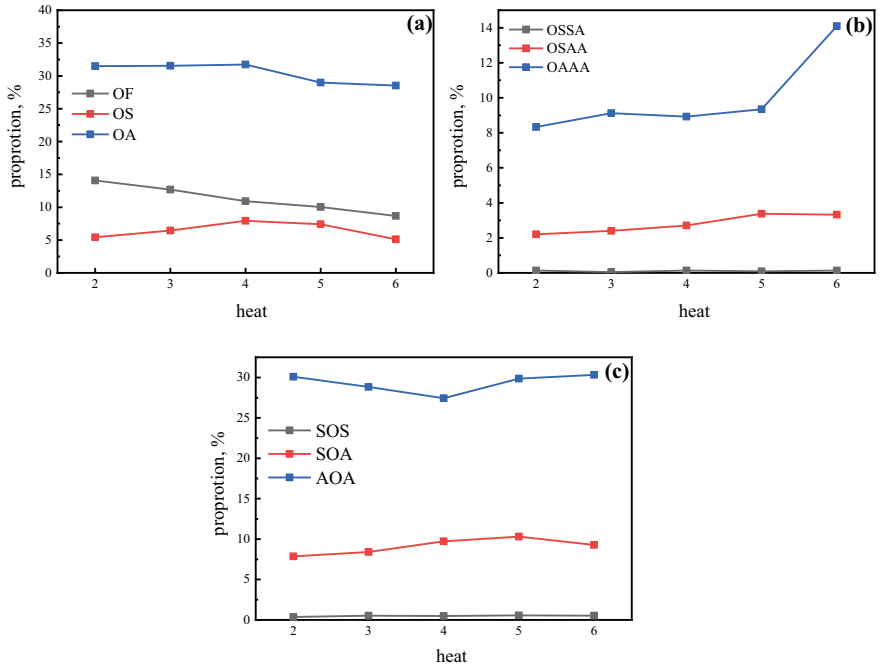

Fig. 3 Evolution of oxygen types: **a** Non-bridging oxygen, **b** bridging oxygen, **c** tricluster oxygen

the concentration of OS (O–Si) increases slightly at first, and then decreases after reaching the maximum value in the fourth heat. The reason is that the initial SiO_2 content in the tundish flux is very low, and the SiO_2 content rises rapidly during the use of the tundish flux.

The proportion of OS also increased, and in the later period, due to the overall transformation of the flux to a complex structure, the overall non-bridging oxygen content decreased, resulting in a decrease in O–Si concentration. Most of the bridge oxygen is mainly AOA (Al–O–Al), and the concentration is always high. The concentrations of OAAA and OSAA both increase significantly, which significantly increases the complexity of the melt structure.

Figure 4 shows the Q^i distribution of Si atoms. In traditional silicate melt, there are five different silica tetrahedrons, represented by Q^0, Q^1, Q^2, Q^3, and Q^4, corresponding to island, dimer, ring or chain, sheet or layer, and three-dimensional frame or network tetrahedrons in geology, respectively, [14]. With the decrease of CaO content, the concentration of structural units Q^0, Q^1, and Q^2 decreased, and the concentration of Q^3 and Q^4 increased. This is because as the CaO content of the network depolymerizer decreases, simple network structure units Q^0 and Q^1 are aggregated to form a complex network structure.

In particular, in the flux melt, Al atoms appear Q^5 structural units, as shown in Fig. 5. This is due to the formation of highly coordinated (penta-coordinated)

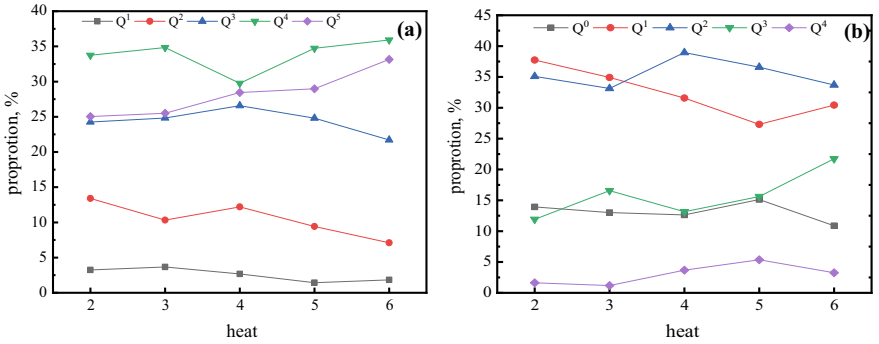

Fig. 4 The evolution of Q^i: **a** Al, **b** Si

aluminum in order to balance the excess charge of $[AlO_4]^{5-}$, the possible presence of Q^5 structural units. In the flux calcium aluminate system, the increase of CaO content makes the complex network structure unit and Q^5 depolymerize to form the simple network structure unit Q^1 and Q^2. The simple structural unit has a lower viscosity and melting point, which is conducive to the inclusion absorption of the flux. Because the content of Ti atom is very small, it has little influence on the evolution of oxygen atom, so the discussion of Ti atom is omitted.

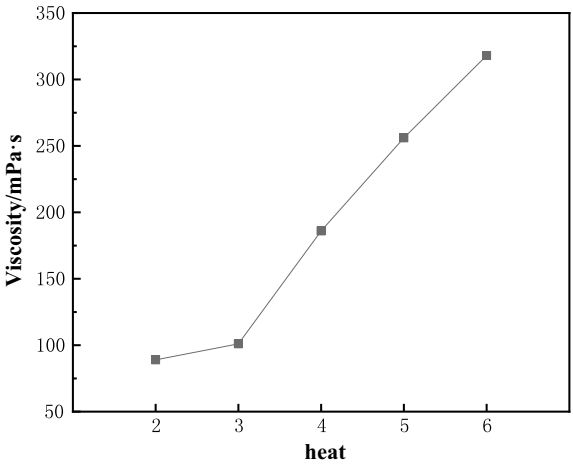

Fig. 5 Evolution law of viscosity of tundish flux (1550 °C)

The Influence of Microstructural Evolution of Tundish Flux on the Ability to Absorb Inclusions

The greater the degree of molecular polymerization in the slags, the worse the flow performance of the slag and the worse the kinetic conditions for absorbing inclusions [7]. In the experiment, an inner cylinder rotating viscometer was used to test the viscosity curve of flux at 1550 °C, as shown in Fig. 5.

With the increase of the number of casting heats, the ratio of SiO_2 and CaO/Al_2O_3 decreases, and the viscosity increases gradually, which is mainly due to: CaO can provide the coating with O^{2-}, which can promote the disintegration of complex silica ions into simple silica ions. With the reduction of CaO content, the slag structure gradually becomes more complex, and the viscosity of the flux is reduced.

The ratio of the amount of non-bridged oxygen (NBO) to temperature, O_{nb}/T, is a parameter to characterize the concentration of slags. The larger the O_{nb}/T ratio is, the more the amount of non-bridged oxygen is, the greater the damage degree of the network chain is. According to the relationship between slag structure parameter Q and O_{nb}/T proposed by Mills [15], as shown in Eq. 2, the specific expression of O_{nb}/T of the flux system is as follows:

$$Q = 4 - \left(O_{nb} + O_f\right)/T, \tag{2}$$

where T is the absolute temperature, K; The slag structure parameter Q is the amount of non-bridged oxygen.

The viscosity data are all the viscosity values tested by rotation method, and the data of Q in the table is calculated by the formula, and its size represents the complexity of the slag structure. By analyzing the viscosity value and the microstructure parameter Q value, the relationship between viscosity and microstructure is attempted to be established. The calculation results show that there is a strong linear relationship between Q and viscosity, as shown in Fig. 6.

Figure 6 shows the linear fitting relationship between viscosity values and Q. The size of Q represents the complexity of silicon-oxygen ion clusters and phosphorus-oxygen ion clusters in the slag structure. Through statistical fitting and comparison of the data, it is found that the fitting degree between the measured viscosity value and the microstructure parameter Q at 1823 K is high, R^2 reaches 0.93, and its linear relationship is as follows:

$$\eta = 40.41Q - 160.39 \tag{3}$$

With the increase of the viscosity of the flux, the residence time of the solid inclusion at the steel-slag interface will be extended. After the flux is poured into the third heat, the microstructure of the flux tends to form molecular groups with large polymerization degree, and the viscosity rises. By adding a higher alkaline modifier at the later stage of casting, the content of inclusions in the billet can be kept at a low level during stable continuous casting.

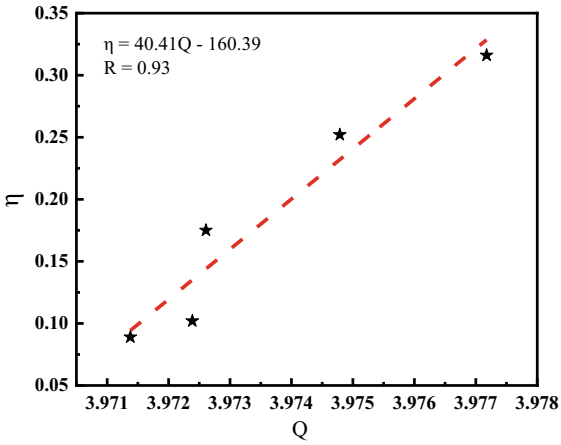

Fig. 6 Degree of polymerization-viscosity regression analysis function

Conclusions

1. The bond length between the atomic pairs in the flux increased with the increase of the content of adsorbed inclusions, and the Al–O bond length was the most obvious change. The Al–O bond length was 1.735 Å at the second heat, and increased to 1.768 Å at the sixth heat, and the average Si–O bond length was not significantly changed.
2. As the number of heat cycles increased, both free oxygen and non-bridged oxygen decreased significantly. From the first heat to the last heat, the non-bridged oxygen decreased from 38 to 32%. Most of the oxygen atoms become bridging oxygen or polymerized oxygen, which increases the degree of melt polymerization and reduces the ability of the flux to absorb inclusions.
3. As the number of heats increased, the slag structure becomes complicated, and the increase of bridge oxygen and cluster oxygen has a strong correlation with the increase of viscosity. The increase of basic oxides is beneficial to the dissociation of the complex melt structure, and further enhance the quality of the continuous casting billet.

Acknowledgements The authors gratefully acknowledge the financial support provided by the National Natural Science Foundation of China, project No. 51874059, 52074053, 52274320 and 52274321.

References

1. Wei Z, Ruimin WU, Wang Y (2019) Robotic system for adding tundish-covering flux based on machine vision. Baosteel Tech Res 13(03):37–42

2. Li JL, Shu QF, Liu YA (2014) Dissolution rate of Al_2O_3 into molten CaO–Al_2O_3–CaF_2 flux. Ironmaking Steelmaking 41(10):732–740
3. Yuan Z, Yan WU, Zhao H (2013) Wettability between Molten slag and MgO-C refractories for the slag splashing process. ISIJ Int 53(4):598–602
4. Zheng K, Liao J, Wang X (2013) Raman spectroscopic study of the structural properties of CaO-MgO-SiO_2-TiO_2 slags. J Non-Cryst Solids 376
5. Wu T, Wang Q, Yu C, He S (2016) Structural and viscosity properties of CaO-SiO_2-Al_2O_3-FeO slags based on molecular dynamic simulation. J Non-Cryst Solids 450:23–31
6. Gao J, Wen G, Huang T, Tang P, Liu Q (2016) Effects of the composition on the structure and viscosity of the CaO-SiO_2-based mold flux. J Non-Cryst Solids 435
7. Chen Z, Wang H, Sun Y (2019) Insight into the relationship between viscosity and structure of CaO-SiO2-MgO-Al2O3 Molten slags. Metall Mater Trans B 50(6)
8. Fan G, Diao J, Jiang L, Zhang Z, Xie B (2015) Molecular dynamics analysis of the microstructure of the CaO-P_2O_5-SiO_2 slag system with varying $P2O_5/SiO_2$ ratios. Mater Trans 56:655–660
9. Diao J, Fan G, Liu X, Xie B (2014) Computer simulation of anionic structures of Molten CaO-SiO_2-P_2O_5 system. Metall Mater Trans 45B(5):1942–1947
10. Fan G, He S, Wu T (2015) Effect of Fluorine on the structure of high Al_2O_3-bearing system by molecular dynamics simulation. Metall Mater Trans B 46(4):2005–2013
11. Wang Z, Sun Y, Sridhar S, Zhang M, Guo M, Zhang Z (2015) Effect of Al_2O_3 on the viscosity and structure of CaO-SiO_2-MgO-Al_2O_3-FetO slags. Metall Mater Trans 46B(2):537–541
12. Liu Y, Bai C, Lv X (2015) Molecular dynamics simulation on the influence of Al_2O_3 on the slag structure at 1873 K. Mater Today Proceedings 2:453–459
13. Liu Y, Xuewei LV, Bai C (2014) Density of the blast furnace slag bearing TiO_2 at 1673 K. ISIJ Int 54(9):2017–2024
14. Shimoda K, Saito K (2007) Detailed structure elucidation of the blast furnace slag by molecular dynamics simulation. ISIJ Int 47(9):1275–1279
15. Mills KC, Sridhar S (1999) Viscosities of ironmaking and steelmaking slags. Ironmaking Steelmaking 26(4):262–268

Part II
Thermodynamics and Slag Behavior

Dissolution Behavior of AlN in $CaO–Al_2O_3$-Based Slag

Xufeng Wang, Zaihui Xi, Qiangqiang Wang, Shengping He, and Xubin Zhang

Abstract Fe–Mn–Al–C steel can form AlN particles because of its high [Al] content (w[Al] = 8–12 wt%), which can affect the properties of slag during continuous casting. In this study, the dissolution behavior of AlN in a new $CaO–Al_2O_3$-based slag without SiO_2 was investigated by a static experiment method. Results demonstrated AlN rod could be dissolved in the liquid slag and it only reacted with Li_2O, which caused the increase of Al_2O_3 and the decrease of Li_2O in the slag. The interface between slag and AlN was examined by scanning electron microscopy, and the products near the slag side were $Al_2O_3–CaO–BaO–CaF_2$ complexes, while individual Al_2O_3 and $AlN–Al_2O_3$ complexes were dispersed near AlN side. Additionally, the viscosity and break temperature of the slag increased greatly with the increase of AlN. XRD showed the primary crystalline phase in the slag was $11CaO·7Al_2O_3·CaF_2$. This work provided theoretical guidance for future application of the slag for high-Al steel.

Keywords Fe–Mn–Al–C steel · $CaO–Al_2O_3$-based slag · AlN · Dissolution behavior · Physical and chemical properties

Introduction

Fe–Mn–Al–C steel with high-Mn and high-Al contents ([Mn] = 20–30%, [Al] = 5–12%) has been widely used in the automobile field in recent years, due to its excellent weight loss and high strength properties field [1, 2]. However, the [Al] in steel reacts with the oxidizing components in slag would lead to the composition change and performance deterioration of the slag. Thereby restricting the production of high-Al steel by continuous casting (CC) process.

To settle the issue of steel-slag reaction to realize the CC production of high-Al steel, a new type of $CaO–Al_2O_3–BaO–CaF_2–Li_2O$ non-reactive mold flux which

X. Wang · Z. Xi · Q. Wang (✉) · S. He · X. Zhang
College of Materials Science and Engineering, and Chongqing Key Laboratory of Vanadium–Titanium Metallurgy and Advanced Materials, Chongqing University, Chongqing 400044, China
e-mail: wtfwawj@163.com

S. Wagstaff et al. (eds.), *Materials Processing Fundamentals 2024*, The Minerals, Metals & Materials Series, https://doi.org/10.1007/978-3-031-50184-5_5

Table 1 Compositions of mold flux

Slag samples	CaO	Al_2O_3	CaF_2	Li_2O	BaO
wt%	30.12	29.02	17.54	7.64	15.68

discarded all the oxides was proposed [3, 4]. The network structure of the slag system was mainly $[AlO_4]^-$ tetrahedron [5] with simple chain and layer structure [6]. In addition, compared with the traditional CaO–SiO_2-based slag, the slag system had better wettability with high-Mn high-Al steel, which was beneficial for the performance of lubricating shell by the slag melt [7]. According to the excellent properties of the CaO–Al_2O_3–BaO–CaF_2–Li_2O non-reactive slag, the slag system has a good potential application prospect for the CC production of high-Al steel.

In the high-Al steel with [Al] content up to 5–12 wt%, AlN was the main inclusion[8]. In the CC process, AlN would float into the slag, increasing viscosity, break temperature, and melting temperature [8, 9], further leading to surface defects. Therefore, to improve the absorption capacity of AlN inclusions by mold flux, it is necessary to explore the dissolution behavior of AlN inclusions in mold flux. In this work, the dissolution behavior of AlN inclusions in CaO–Al_2O_3–BaO–CaF_2–Li_2O slag was investigated by the static experimental method, and the effect of AlN on the properties of slag was studied. This work could lay a theoretical value and reference basis for the design of non-reactive slag for high-Al steel.

Experimental Procedure and Methods

Preparation of Slag Samples and AlN Rods

The composition of the slag used in the experiment is shown in Table 1. The slag samples were prepared using analytical grade chemical reagents, in which Li_2O was prepared in the form of Li_2CO_3. The diameter of AlN rods had a size of Φ10 mm × H10 mm, a density of 95%, and a purity of 99.9%. The AlN powder used in the experiment was an analytical grade chemical reagent with a purity of 99.98%, its oxygen content was less than 0.1 wt%.

Experimental Equipment and Methods

To prevent the AlN rod from being oxidized by the air at high temperatures, the static experiment method which immersed the AlN rods in the slag and isolated them from air was used to explore the dissolution behavior of AlN in the slag, as shown in Fig. 1. 250 g slag sample in Table 2 was prepared and pre-melted at 1300 °C for 20 min in a $MoSi_2$ furnace to uniform the slag composition. Meanwhile, two small graphite

crucibles with AlN rods fixed at the bottom were prepared, and the small graphite crucibles were covered with a large graphite crucible. Subsequently, the pre-melted slag was quickly poured into the small graphite crucibles to completely submerge the AlN rods, and the liquid slag with a height of about 10 mm lower than the top of the small graphite crucibles was poured into the large graphite crucible. The slag in the large graphite crucible did not contact with AlN rods. Besides, a graphite lid was placed on the top of the large graphite crucible to further reduce the oxygen partial pressure in the crucible, and then the large graphite crucible was placed in the furnace at 1400 °C for 1 h and then taken out for air-cooling. Argon was introduced into the experiment to prevent AlN from being oxidized by the oxygen in the air. After that, the slags in the large graphite crucible and the small graphite crucibles were ground through a 200-mesh for XRD detection. The AlN rods after the experiment were cut longitudinally by a diamond wire cutting machine, and then the interface between AlN and slag was analyzed by field emission scanning electron microscope (FE-SEM) after grinding and polishing.

The effects of different AlN additions on the viscosity and melting temperature of slag were tested by rotary viscometer and hemispherical point method, respectively. The experimental equipment and detailed operation process could be found in our previous papers [10–12]. 250 g slag samples were prepared and pre-melted at 1300 °C for 20 min in the furnace to uniform the composition, and then AlN powders were weighed according to 0 wt%, 2 wt%, 4 wt%, 6 wt%, and 8 wt% of the slag sample weight. Thereafter, AlN was added to the surface of the liquid slag utilizing a graphite

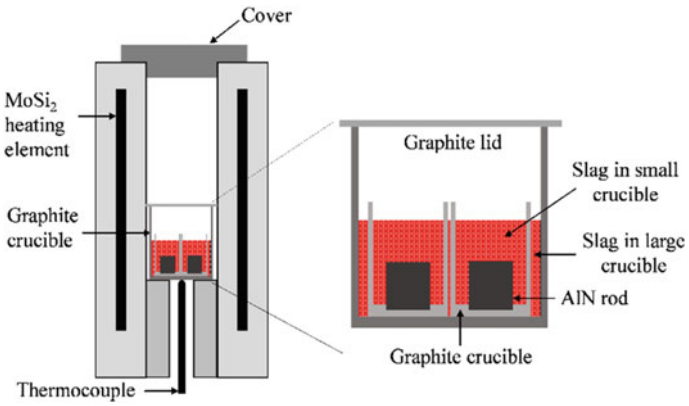

Fig. 1 Schematic of the static slag-AlN rod contacting experiment

Table 2 Compositions of slags after slag-AlN rod contacting experiment (wt%)

Slag samples	CaO	Al_2O_3	CaF_2	Li_2O	BaO
NL	30.52	28.29	17.94	7.22	16.03
NS	29.66	32.62	17.30	5.44	14.98

tube. The slag sample was stirred every five minutes to make the added AlN fully react with the fused sample and held at 1300 °C for 0.5 h. Then the furnace was cooled at 6 °C/min to obtain the viscosity and break temperature of the slag. The slag after the viscosity test was ground for melting temperature test. The melting temperature was defined as the temperature at which the height of the slag sample decreased to half of the original height during the test. Each group of samples was tested more than three times, and the mean value of the three groups of test differences not exceeding 10 °C was selected as the melting temperature of the slag. Argon was introduced into the experiment to prevent AlN from being oxidized by the oxygen in the air.

Dissolution Behavior of AlN in the Slag

The Shape Change of the AlN Rod and the Composition Change of the Slag

The longitudinal section shape of the AlN rod stripped from the slag after the dissolution experiments is shown in Fig. 2. It could be noted that the size of the AlN rod was reduced from an initial 10 mm to 7.90 mm, indicating that the slag had a certain ability to dissolve AlN.

The composition of the slag samples in the large graphite crucible and small graphite crucibles is shown in Table 2. The slag was not in contact with the AlN rod in the large crucible and the slag in contact with AlN in the small crucibles was defined as slag NL and NS, respectively. Compared with the original slag, the composition of the slag NL varied from 0.35 to 0.73 wt%, and the contents of CaO, CaF_2, and BaO in the slag NS varied from 0.24 to 0.70 wt%. But remarkably, Al_2O_3 increased by 3.60 wt% and Li_2O decreased by 2.20 wt%. The increase of Al_2O_3 and the decrease of Li_2O in slag NS might be due to the chemical reaction between the slag and AlN rod.

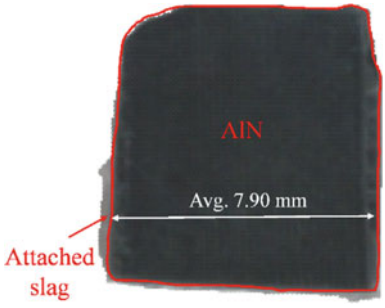

Fig. 2 Shape of AlN rod after experiment

Optical Microscopes and Electrons Microscopic Analysis of Slag-AlN Interface

The slag-AlN interface morphology observed by the optical microscope is shown in Fig. 3. The upper gray part was the slag, and the lower black and white part was AlN. It was evident there was a bright white area at the interface, whose color could be differentiated from that of solidified slags and AlN rods, which may be caused by the reaction between slag and AlN. This part was defined as the interface transition layer between the slag and AlN.

The interface morphology and element surface scanning results of the slag-AlN interface obtained by SEM are shown in Fig. 4, and the element line scanning results of the slag and AlN rod interface are shown in Fig. 5. It can be seen that the AlN rod was in close contact with the slag, and there was obvious mutual penetration of elements at the interface. Al was mainly distributed on the AlN side, Ca and Ba were mainly distributed on the slag side, and there was a small amount of distribution on the AlN side. From the slag side to the AlN side, the concentration of Al increased rapidly, and the concentration of O, Ca, Ba, and F decreased gradually. In general, the N concentration gradually increased from the slag side to the AlN side, although it was higher in some areas of the slag side, which indicated that the reaction occurred at the interface and led to the penetration of the N element at the interface. In addition, the products at the interface near the slag side were $Al_2O_3–CaO–BaO–CaF_2$ complexes, and the products near the AlN side were individual AlN, Al_2O_3, and $AlN–Al_2O_3$ complexes.

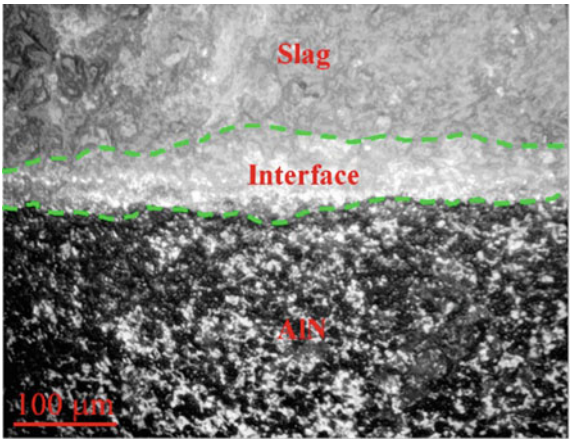

Fig. 3 Interface between slags and AlN rods by optical microscope

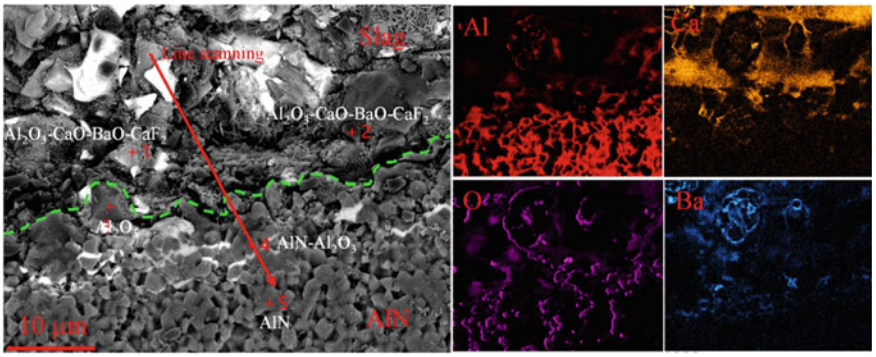

Fig. 4 Interface morphology and elemental mapping of slag and AlN rod

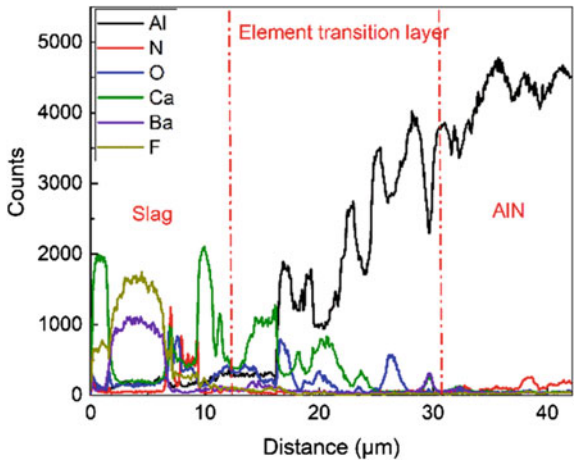

Fig. 5 Line scanning of interface between slag and AlN rod

Reactivity Between Slag and AlN

Reactions (1)–(4) are the reactions between AlN and each component, and the Gibbs free energy change formulas of them at 1400 °C calculated by FactSage thermodynamic software are shown in Table 3. It could be seen that AlN only reacted with Li_2O and did not react with others. Therefore, it was reasonable that Al_2O_3 at the interface was formed by the reaction of AlN and Li_2O. AlN or reacted directly with [O] provided by Li_2O to form Al_2O_3, as shown in Reaction (7), or decomposed into [Al] and then reacted with [O] provided by Li_2O to form Al_2O_3 as shown in Eqs. (5), (6) and (8) [13–16]. This was also the reason for the increase of Al_2O_3 and the decrease of Li_2O in the slag which was in contact with the AlN rod after the dissolution experiment.

$$2/3\mathrm{AlN} + \mathrm{CaO} = 1/3\mathrm{Al_2O_3} + \mathrm{Ca} + 1/3\mathrm{N_{2(g)}} \quad (1)$$

Table 3 Activity of each component in slags at 1400 °C

Slag samples	ΔG_{CaO}	ΔG_{BaO}	ΔG_{Li_2O}	ΔG_{CaF_2}
J/mol	159,392.52	160,804.54	−23,076.96	285,645.01

$$2/3AlN + BaO = 1/3Al_2O_3 + Ba + 1/3N_{2(g)} \quad (2)$$

$$2/3AlN + Li_2O = 1/3Al_2O_3 + 2Li_{(g)} + 1/3N_{2(g)} \quad (3)$$

$$2/3AlN + CaF_2 = 2/3AlF_{3(g)} + Ca + 1/3N_{2(g)} \quad (4)$$

$$AlN = [Al] + 1/2N_2 \quad \Delta G = 282689 - 173T \quad (5)$$

$$AlN = [Al] + 2[N] \quad \Delta G = 303500 - 134.6T \quad (6)$$

$$2AlN + 3[O] = Al_2O_3 + N_2 \quad \Delta G = -679607.5 + 42.5T \quad (7)$$

$$2[Al] + 3[O] = Al_2O_3 \quad \Delta G = -1225000 + 393.8T \quad (8)$$

Effect of AlN on the Properties of the Slag

Effect of AlN on Viscosity, Melting Temperature, and Break Temperature of Slag

Figure 6 shows the variation of viscosity, break temperature, and melting temperature of slag with different AlN additions. It can be seen that as the AlN increased, the viscosity of the slag gradually increased from the initial 0.089 to 0.099 Pa s, 0.130 Pa s, 0.176 Pa s, and 0.253 Pa s when 2 wt%, 4 wt%, 6 wt%, and 8 wt% AlN were added. However, the viscosity of the slag was still within the allowable range of CC process. The break temperature (the temperature at which the viscosity of the slag raised sharply during the cooling process) of the slag increased from the initial 1102 to 1145 °C and 1225 °C when 2 wt% and 4 wt% AlN were added. When the amount of AlN added was 6 wt% and 8 wt%, the break temperature decreased by 23 °C and 33 °C, respectively. After absorbing AlN, the break temperature of the slag was too high, which easily led to a decrease in slag consumption, and in turn, caused slab sticking and sticking leakage [17]. In addition, the melting temperature of the slag gradually increased from the initial 1084 to 1159 °C when 6 wt% AlN

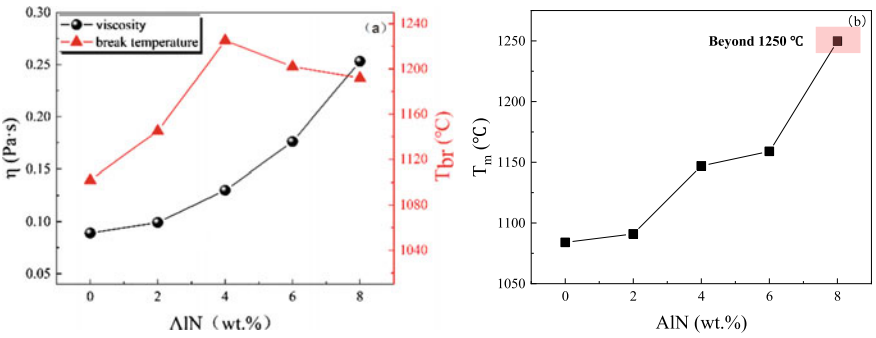

(a) viscosity and break temperature (b) melting temperature

Fig. 6 Basic properties of slag with various AlN additions

was added. When the addition amount of AlN was 8 wt%, the melting temperature of the mold flux exceeded the maximum measured value of 1250 °C allowed by the equipment, which may be due to the formation of high melting temperature phases and gas generation in the slag sample.

Solidification Phase Analyses of Mold Flux

The XRD analysis of the slag samples with varying AlN additions after air-cooling was carried out, as shown in Fig. 7. The initial slag was mainly glass phase with a small amount of $LiBaF_3$. With the addition of AlN in the slag, the precipitated phase in the slag became complicated, in which $11CaO{\cdot}7Al_2O_3{\cdot}CaF_2$ was the main phase. The melting temperature of $11CaO{\cdot}7Al_2O_3{\cdot}CaF_2$ was 1577 °C, which would deteriorate the heat transfer controlling and lubrication tasks of solid slag film, it still needs further research

The above experiments on the dissolution of AlN in the slag and the effect of AlN on the properties of slag showed that $CaO–Al_2O_3$-based slag had a certain solubility of AlN, and AlN floated into the slag would deteriorate the slag performance. Under the condition of slag-metal reaction, the performance stability of mold flux was faced with more problems, which required further research on the change of performance of slag after absorbing AlN and its control method.

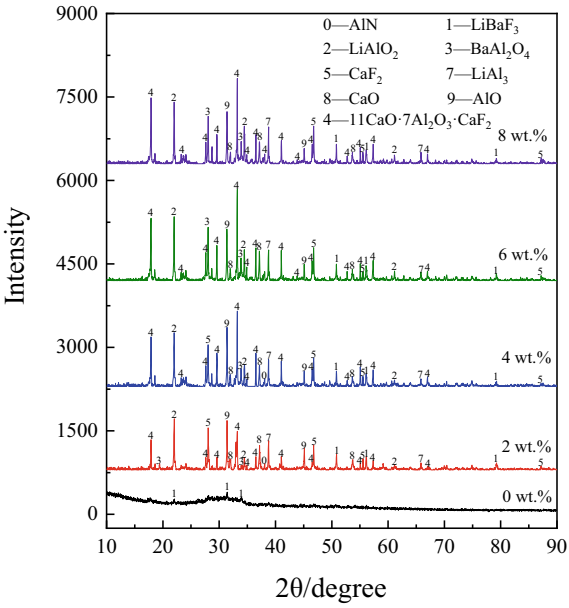

Fig. 7 XRD analysis of slag with different AlN contents

Conclusion

In this study, the dissolution behavior of AlN inclusion in $CaO–Al_2O_3$-based non-reactive mold fluxes was explored by SEM–EDS and thermodynamic calculation, and its effect on properties of $CaO–Al_2O_3$-based mold flux was also explored. The following conclusions were obtained.

(1) After the dissolution experiment, the content of Al_2O_3 in the slag contacted with the AlN rod increased by 3.60 wt%, and the content of Li_2O decreased by 2.20 wt%.

(2) The results of SEM showed that the product at the slag-AlN interface near the slag side were Al_2O_3–CaO–BaO–CaF_2 complexes, and near the AlN side were individual AlN, Al_2O_3, and AlN–Al_2O_3 complexes.

(3) Thermodynamic calculation showed that AlN only reacted with Li_2O in slag to produce Al_2O_3. The dissolution process of AlN inclusions in the slag was inferred as that AlN decomposed to produce [Al] and then reacted with [O] provided by Li_2O to produce Al_2O_3 or AlN directly reacted with [O] provided by Li_2O to produce Al_2O_3.

(4) With the content of AlN in the slag increased from 0 to 8 wt%, the viscosity of the slag increased from 0.089 to 0.253 Pa s, the break temperature increased from 1102 to 1192 °C, and the melting temperature increased from 1084 to 1159 °C when the addition of 6 wt%. When the addition of AlN was 8 wt%, the melting point exceeded 1250 °C.

(5) The XRD result showed that the original slag was mainly glass phase, with the increase of AlN addition, $11CaO{\cdot}7Al_2O_3{\cdot}CaF_2$ became the main crystalline phase in the slag.

References

1. Tang D, Zhen-Li MI, Chen YL (2005) Technology and research and development of advanced automobile steel abroad. Iron and Steel 40(6):1–5
2. Neu RW (2013) Performance and characterization of TWIP steels for automotive applications. ASTM Int 2(1):20130009
3. Li ZR (2019) Study on reactivity control of mold flux and basic structure and properties of slag for high manganese and high aluminum steel. Chongqing University
4. Wu T, He SP, Guo YT, Wang Q (2014) Study on reactivity between mould fluxes and high-Al molten steel. In: Characterization of minerals, metals, and materials 2014. TMS, San Diego, pp 265–270
5. Chen Y, He SP, Li ZR, Zhang XB, Wang QQ, Wang Q (2022) Properties and structure of a new non-reactive mold flux for high-Al steel. J Iron Steel Res Int 29(1):61–70
6. Chen Y, Pan WJ, Wang QQ, He SP (2022) Study on structure and properties of mold flux for non-reactive high aluminum steel continuous casting. In: The 13th China iron and steel annual conference, Chongqing, China, pp 292–296
7. Yuan HZ, Dan ZK, Wang QQ, He SP (2020) Contact angle and adhesion of $CaO–SiO_2$- and $CaO–Al_2O_3$-based mold slags on solid steel of various compositions. J Market Res 9(4):7828–7837
8. Wang X, Liu H, Zhao M, Wang Q, Zhang X, He S (2023) Effect of AlN on properties of non-reactive $CaO\text{-}Al_2O_3$-based mold flux for high-Al steel. Mater Today Commun 34:105432
9. Wang XF, Wang QQ, Zhang XB, Wang Q, He SP (2022) Effect of AlN on properties of $CaO–SiO_2$ based mold flux for high aluminum steel. Iron and Steel 57(05):64–71
10. Li ZR, You XC, Li M, Wang QQ, He SP, Wang QQ (2019) Effect of substituting CaO with BaO and CaO/Al_2O_3 ratio on the viscosity of $CaO–BaO–Al_2O_3–CaF_2–Li_2O$ mold flux system. Metals 9(2):1–13
11. Long X, He SP, Xu JF, Huo XL, Wang Q (2012) Properties of high basicity mold fluxes for peritectic steel slab casting. J Iron Steel Res Int 19(7):39–45
12. Chen Z, Du WT, Zhang M, Wang Q, He SP (2021) Effects of substituting SiO_2 with oxidisers on the reaction performance and physical properties of mould flux for high Ti-bearing steel. ISIJ Int 61(3):814–823
13. Amadeh A, Labbe JC, Laiemeche A, Quintard P (1996) Influence of boron nitride and carbon additives on the behaviour of sintered AlN in a steel-making environment. J Eur Ceram Soc 16(4):403–408
14. Labbe JC, Laïmeche A (1996) Study of the behaviour of aluminium nitride in the iron and steel industry. J Eur Ceram Soc 16(8):893–898
15. Amadeh A, Heshmati-Manesh S, Labbe JC, Laimeche A, Quintard P (2001) Wettability and corrosion of TiN, TiN–BN and TiN–AlN by liquid steel. J Eur Ceram Soc 21(3):277–282
16. Luo Y, Li M, Scheller PR, Sridhar S, Zhang L (2019) Interaction between liquid steel and AlN substrate containing Al-Y-oxides. Metall and Mater Trans B 50(5):2459–2470
17. Mills KC, Fox AB (2003) The role of mould fluxes in continuous casting-so simple yet so complex. ISIJ Int 43(10):1479–1486

Equilibrium Between Yttrium and Oxygen in Molten Iron

Jian Kang, Hongpo Wang, and Yu Wang

Abstract Rare earth is an important additive to improve the comprehensive properties of steel products. To precisely control the amount of rare earth in the molten steel and rare earth inclusions is a fundamental issue that has not been effectively solved due to the lack of accurate thermodynamic data. The equilibrium between yttrium and oxygen in the liquid iron was investigated using pure Y_2O_3 crucibles for smelting experiments, and accurate thermodynamic data were obtained in the range of 1600–1700 °C. The results show that the deoxygenation product of yttrium was Y_2O_3 and the equilibrium constant of the reaction $Y_2O_3(s) = 2[Y] + 3[O]$ can be expressed as follows:

$$\log K_Y\left(K_Y = a_Y^2 a_O^3 / a_{Y_2O_3}\right) = -60065/T + 18.92 \quad 1600 - 1700\ ^\circ C$$

While the deoxidation product, $K'_Y(= [\%Y]^2[\%O]^3)$, was expressed as follows:

$$\log K'_Y = \log K_Y - (-19591/T + 1.72) \times (3[\%Y] + 11.1[\%O])$$
$$0.006 < [\%Y] < 0.21$$

By the use of the interaction parameter $e_O^Y = -19591/T + 1.72$.

Keywords Deoxidation equilibrium · Yttrium · Deoxidation product · Interaction parameter · Iron

J. Kang · H. Wang (✉) · Y. Wang
College of Materials Science and Engineering, Chongqing University, Chongqing 400044, China
e-mail: wanghp@cqu.edu.cn

H. Wang
The State Key Laboratory of Mechanical Transmissions, Chongqing University, Chongqing 400044, China

S. Wagstaff et al. (eds.), *Materials Processing Fundamentals 2024*, The Minerals, Metals & Materials Series, https://doi.org/10.1007/978-3-031-50184-5_6

Introduction

The quality and performance of steel products are affected by the cleanliness of molten steel [1]. The ways to control the cleanliness of molten steel include stabilizing chemical composition [2], reducing the content of impurity elements in steel [3], and improving inclusions [4]. The relationship between alloy elements and molten steel composition is one of the major focuses for metallurgists.

Rare earths (RE) have been widely used in the iron and steel industry field [5–7]. The role of rare earth elements (REEs) in steel includes molten steel purification [8], inclusion modification [9], solidification structure refinement [10], and micro-alloying [11]. Given the advantageous role of RE in steel, the application of REEs in steel has been continuously expanding in recent years. Although there have been many studies on the application of heavy rare earth element yttrium in steel, they have focused on the modification of inclusions [12], the effect on the mechanical properties [13], and the corrosion resistance of steel [14]. However, the instability of RE in steel and the difficulty in controlling their additive amount limit the application field of RE [15]. It is closely related to the limited thermodynamic data of RE deoxygenation and desulfurization. To better study the modification effect of yttrium (Y) on inclusions in molten steel, more accurate thermodynamic data is needed. In addition, metallurgical processes aimed at saving costs and improving the quality of steel products also need to determine the consumption of Y during the deoxidation process. Therefore, further exploring RE's behavior in steel is necessary.

Based on comparing previous experimental data [16, 17], this study explored the equilibrium thermodynamics of Y deoxidation through experimental sampling and thermodynamic calculations. Based on the experimental results, the equilibrium constant of Y saturation deoxygenation reaction and the effect of Y on oxygen activity in molten iron were determined and optimized. It is hoped to provide basic data for the comprehensive utilization of rare earth resources and the application of Y in metallurgy and to create conditions for the accurate prediction and control of RE-inclusions in steel production.

Experimental Methods

The industrial pure iron was used as raw material, and the smelting experiments of Fe–Y–O were conducted in a 15 kW medium frequency induction furnace under argon protection with a purity of 99.999% and a flow rate of 0.5 mL/min. The thermodynamic data is measured by adding Y–Fe alloy with an equal gradient. The experimental raw materials and alloy chemical composition are shown in Table 1.

The crucible used in the smelting experiment is the high-purity Y_2O_3 crucible, and its purity is 99.3% after XRF detection. The melting crucible with 600 g of industrial pure iron was put into a graphite crucible moved to the furnace chamber and then evacuated to 2.5 Pa. The furnace was washed twice with 99.999% argon

Table 1 Chemical composition of experimental materials and alloys (wt%)

Number	C	Si	Mn	S	O	Y	La	Ce	Fe
4N–Fe	< 0.0004	< 0.0005	< 0.0001	< 0.0004	< 0.0060	–	–	–	99.99
Fe–Y	–	–	–	–	0.002	64.73	< 0.02	< 0.02	Balance

gas and started to raise the temperature. The smelting temperatures are 1600 °C, 1650 °C, and 1700 °C, respectively. Before adding Y–Fe alloy, the actual temperature is measured by directly inserting a thermocouple into the center of the molten steel. After reaching the target temperature and holding it for 10 min, the quartz tubes with an inner diameter of 6 mm were used to extract about 10 g of liquid steel from the center of the molten pool, followed by water-quenching within 2 s. Control the temperature based on the thermocouple at the bottom of the crucible. During sampling, the argon flow rate increased to 1 mL/min. After sampling, the liquid steel was cooled to room temperature, and some other samples were taken from the bar and ingots.

The N and O analyzer was used to detect the oxygen content in the samples. The samples' Y concentrations were determined by Optima 8000 inductively coupled plasma optical emission spectrometry. The process samples and ingot samples were observed using Sunny XD30M optical microscopy and JEOL 7800F scanning electron microscopy. The compositions of deoxidation products were analyzed using an energy-dispersive spectrometer.

Experimental Results and Discussion

Equilibration Time

The thermal kinetic equilibrium time of Y-deoxygenation was obtained through the method of equal gradient time sampling. After adding 0.4 wt% Y, the variation of Y content in molten iron with smelting time is shown in Fig. 1. Within 20 min, the content of [Y] gradually decreases with the increase of melting time. When the smelting time exceeds 20 min, the [Y] content remains constant, indicating that [Y] and [O] reached dynamic equilibrium. Therefore, the time for establishing equilibrium was determined to be 20 min, which is similar to the experiment of Ishii et al. [17] (10–15 min). To ensure the ideal kinetic conditions in the experiment, the equilibrium time after adding Y was controlled at 30 min, and the sampling time in Ishii et al.'s experiment was 20 min after adding the RE-alloy.

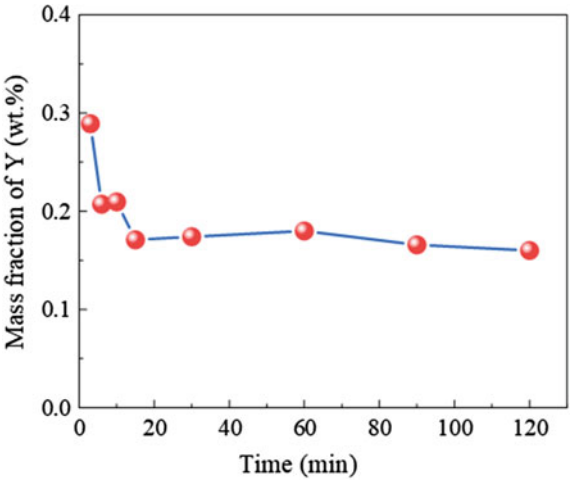

Fig. 1 Changes of Y in molten iron with time

Deoxidation Product

Figure 2 shows the statistical results of EDS and EPMA of deoxygenated products. The EDS in the figure contains 50 points, while EPMA contains 25 points. EDS analysis shows that the deoxygenation product of Y in molten iron is distributed near Y_2O_3. EPMA further determined that the atomic ratio of Y and O in the molten iron is 2:3, so the stable phase of the deoxygenation product is Y_2O_3. This indicates that when the smelting temperature is 1600, 1650, and 1700 °C, the deoxygenation product of Y in liquid iron is Y_2O_3.

The distribution of Y deoxygenation products in the ingot is shown in Fig. 3. As shown in the figure, the deoxygenation products are mainly distributed on the top surface of the ingot and exist in the form of Y_2O_3. This result is the same as the

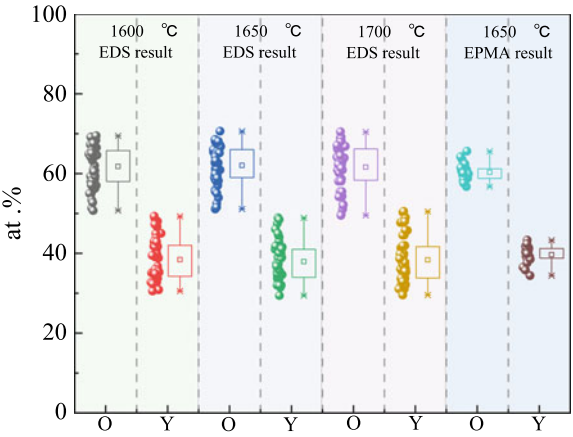

Fig. 2 Deoxygenation products of yttrium in molten iron at different temperatures

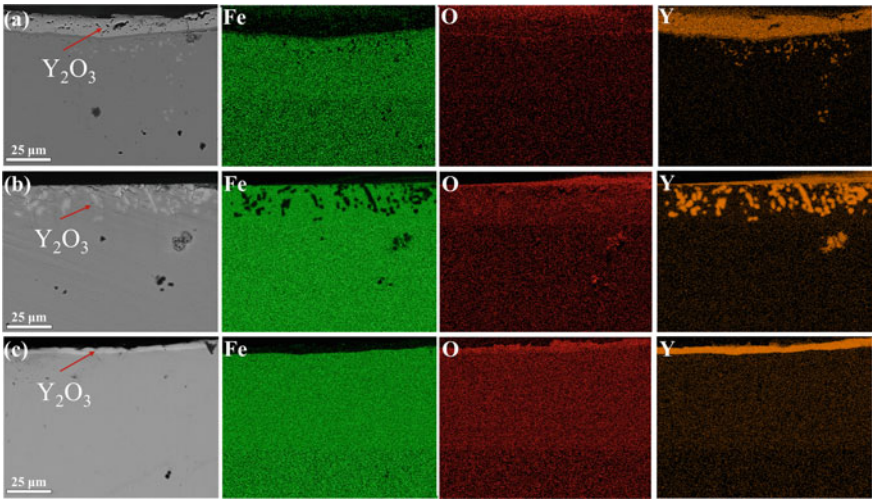

Fig. 3 Distribution of deoxygenation products in ingots: **a** 1600 °C; **b** 1650 °C; **c** 1700 °C

product type in the process sample, indicating that the dynamic conditions during the melting process promote the deoxygenation product to float up to the surface of the molten steel. The undissolved Y–Fe phase was not observed in the ingot, indicating that the Y–Fe alloy added during the melting process fully dissolved and reached equilibrium within 30 min.

Thermodynamics of Y Deoxidation in Molten Iron

The deoxidation reaction of Y in liquid iron can be expressed as:

$$Y_2O_3(s) = 2Y + 3O \tag{1}$$

The equilibrium constant of Y deoxygenation can be expressed as:

$$K_Y = a_Y^2 \times a_O^3 / a_{Y_2O_3} \tag{2}$$

During the deoxygenation reaction, a_Y and a_O are taken to the infinitely diluted solutions of yttrium and oxygen elements in pure liquid metal, with a composition of 1 wt%. Y_2O_3 is a solid state, and its activity can be regarded as 1. Activity can be expressed as the product of activity coefficient and composition, and Eqs. (2) can be expressed as

$$K_Y = a_Y^2 \times a_O^3 = f_Y^2[\%\ Y]^2 \times f_O^3[\%\ O]^3 \tag{3}$$

In the formula, f_Y and f_O are the activity coefficients of yttrium and oxygen in the liquid iron. Therefore, the deoxygenation products of yttrium can be expressed as:

$$K'_Y = [\%\ Y]^2 \times [\%\ O]^3 \tag{4}$$

According to 3.2, the deoxygenation product of Y in molten iron is Y_2O_3.

Incorporation Eqs. (3) and (4) substituting $e_Y^O = M_Y/M_O \cdot e_O^Y = 5.55e_O^Y$, log K'_Y can be expressed as

$$\begin{aligned}\log K'_Y &= \log K_Y - 2\log f_Y - 3\log f_O \\ &= \log K_Y - \left(2e_Y^Y + 3e_O^Y\right)[\%Y] - \left(2e_Y^O + 3e_O^O\right)[\%O] \\ &= \log K_Y - e_O^Y(2[\%Y] + 11.1[\%O]) - \left(2e_Y^Y[\%Y] + 3e_O^O[\%O]\right)\end{aligned} \tag{5}$$

At the temperature of this experiment, due to the oxygen content being much lower than 0.05 wt%, The value of f_Y^O in Eq. (5) can be considered as 1. The value of e_Y^O reported in the literature of Buzek et al. [18] at 1600 °C is 0.03. The value of e_Y^O at 1700 °C is assumed to be 1, as the range of [Y] is also much smaller than 0.3 wt%. Considering the relationship between e_Y^Y and e_O^O, the value of $(2e_O^O[\%Y + 3e_O^O[\%O])$ is also very small. Therefore, Eq. (5) can approximate as Eq. (6). Obviously, log K'_Y and (3[% Y + 11.1 [% O]) are linear functions, so the slope is considered as the interaction coefficient e_O^Y.

$$\log K'_Y = \log K_Y - e_O^Y(3[\%Y] + 11.1[\%O]) \tag{6}$$

The relationship between log K'_Y and (3 [% Y + 11.1 [% O]) in liquid iron is shown in Fig. 4a. As shown in the figure, log K'_Y increases linearly at different temperatures. Due to the difficulty in determining the oxygen content in liquid iron, the experimental values have dispersibility. Compared with the results reported by Ishii et al. [17], the range of log K'_Y and (3[% Y + 11.1 [% O]) has been expanded. Based on the least squares analysis of the data, log K'_Y can be expressed as

$$\begin{aligned}\log K'_Y &= \log K_Y - (-19591/T + 1.72) \times (3[\%Y] + 11.1[\%O]) \\ &\quad 0.006 < [Y] < 0.21\end{aligned} \tag{7}$$

The equilibrium constant depends on temperature, and log K'_Y can be expressed as

$$\log K'_Y = -60065/T + 18.92 \tag{8}$$

Due to the complexity of high-temperature experiments, there are differences in the Gibbs free energy and chemical equilibrium constant results of Y deoxidation obtained by different researchers, as shown in Table 2. However, selecting the appropriate equilibrium constant is the foundation of thermodynamic calculations. The

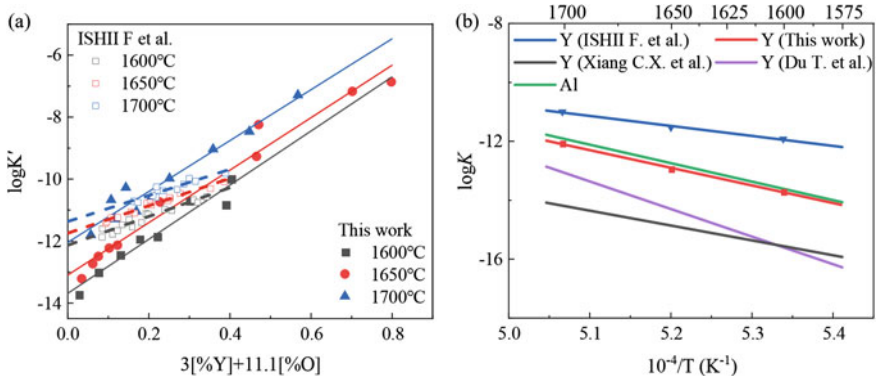

Fig. 4 Plot of log $K'_{Y(Fe)}$ versus (3[%Y + 11.1[%O]) in liquid iron

equilibrium constants at different temperatures are labeled in Fig. 4b and compared with previous research results. The equilibrium constant of Y deoxygenation is lower than Al in the range of 1600–1700 °C, which is consistent with the experimental results of Xiang et al. [19] and Du et al. [16, 20].

The interaction coefficient in Eq. 7 is obtained from the slope in Fig. 4a. The values of the interaction coefficient at 1600, 1650, and 1700 °C can be determined as −8.74, −8.46, and −8.21, as shown in Fig. 5. Due to the temperature dependence of the values of the interaction parameters e_O^Y, they can be expressed as:

$$e_O^Y = -19591/T + 1.72 \quad 0.006 < [Y] < 0.21 \tag{9}$$

Figure 6 shows the equilibrium between yttrium and oxygen in molten iron calculated according to Eqs. (8) and (9), where the value of yttrium content at the lowest point of the curve is approximately 0.023 wt%. The experimental values are much smaller than the values reported by Ishii et al. [17]. At 1600 °C, the deoxygenation

Table 2 Gibbs free energy and chemical equilibrium constant of Y deoxidation

Reaction	Log $K = -A/T + B$		$\triangle G = -(X - YT)$ (J mol^{-1})		K at 1600°C	Liquid	Crucible	Ref.
	$10^{-4}A$	B	$10^{-5}X$	Y				
$Y_2O_3 = 2Y + 3O$	4.257	7.74	8.149	148.16	1.0×10^{-15}	Ni	–	[16]
	3.616	7.33	6.923	140.34	1.6×10^{-12}	Fe	Y_2O_3	[17]
	5.074	11.39	9.715	218.08	2.75×10^{-15}	Fe	MgO	[19]
	9.365	34.4	17.926	658.00	2.5×10^{-16}	Fe	MgO	[20]

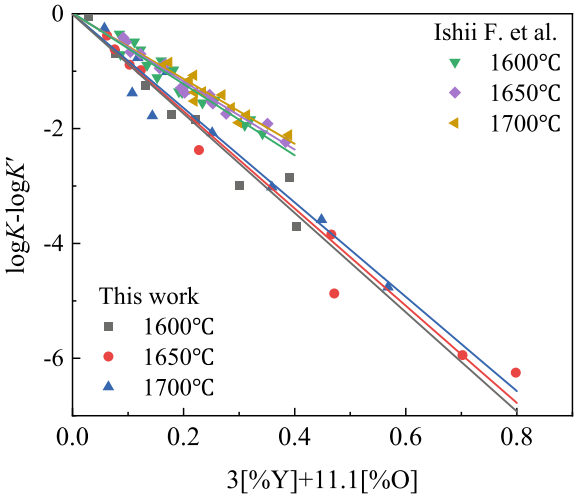

Fig. 5 Relation of (log K_Y – log K'_Y) against (3[%Y] + 11.1[%O]) in liquid iron

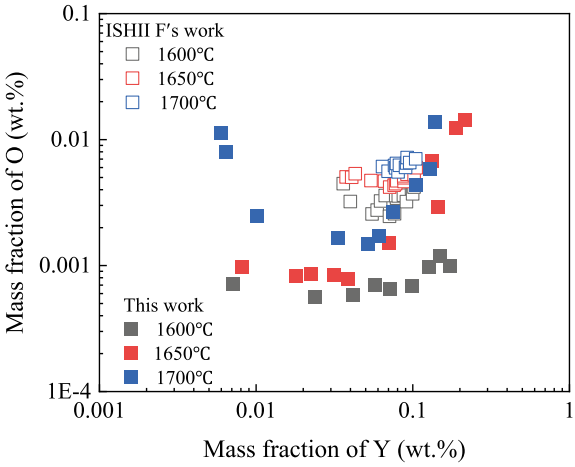

Fig. 6 Equilibrium between Y and O in liquid iron: **a** 1600–1650–1700 °C; **b** 1600 °C

efficiency of Y in this study was significantly higher than the values in the literature, mainly due to the purity of the crucible being greater than 99%, effectively avoiding the reaction between Y and the crucible.

Factors Affecting the Measurement Results

There are three main factors affecting the deoxygenation of Y in liquid iron: First, Y reacts with the crucible to form a compound that consumes [Y] in the molten iron. Xiang et al. [19] reported in their study that [Y] undergoes significant chemical

reactions with MgO and CaO, resulting in the actual [Y] concentration in the molten iron being lower than the equilibrium [Y] concentration. In their experiment, they used MgO crucibles to achieve Y–O equilibrium by extending the equilibrium time. However, the reaction between [Y] and MgO crucibles is inevitable [8]. Second, [Y] reacts with [O] to form Y_2O_3 and float up to the surface of the molten iron. The distribution of deoxygenation products affects the determination of [Y] content in the molten iron. If the quality of the molten iron is too low, the products cannot be separated from the molten iron during melting, which increases the sampling error. In addition, another important factor affecting the content of [Y] is the equilibrium time of Y in molten iron, which in turn affects the determination of the equilibrium constant. Ishii et al. [17] used Y_2O_3 crucibles as the melting crucible, and the measured [Y] and [O] contents were significantly higher than those in this study. The possible reason for this is that the equilibrium time is too short, which affects the equilibrium concentration of [Y] in the molten iron. However, in this work, the mass of molten iron increased to around 600 g, and melting in an induction furnace can provide good kinetic conditions to promote the full flotation of deoxygenated products. Due to the increase in the mass and equilibrium time of molten iron, the influence of non-equilibrium and product heterogeneity on the equilibrium constant is effectively reduced, significantly reducing the experimental error caused by the latter two. The analysis of the above research results indicates that the thermodynamic data obtained in this work has more reference significance.

Conclusion

Experimental studies were conducted on the deoxygenation equilibrium of yttrium in liquid iron using sampling methods within the temperature range of 1600 to 1700 °C, and the conclusion of this work is as follows:

1. The deoxygenation product of Y in liquid iron is Y_2O_3. Based on experimental methods, the equilibrium constant of deoxidation and the relationship between deoxygenation products and temperature were determined when the yttrium content in molten iron ranged from 0.006 to 0.21 wt% as follows:

$$\log K_{\mathrm{Y}} = -60065/T + 18.92$$

$$\log K'_{\mathrm{Y}} = \log K_{\mathrm{Y}} - (-19591/T + 1.72) \times (3[\%\mathrm{Y}] + 11.1[\%\mathrm{O}])$$
$$0.006 < [\mathrm{Y}] < 0.21$$

At 1600, 1650, and 1700 °C, the values are −8.74, −8.46, and −8.21, respectively.

2. The reaction between rare earth elements and crucibles, the floating of inclusions, and the quality of molten iron are important factors that affect experimental research. In this study, the purity of the Y_2O_3 crucible was greater than 99%, effectively reducing the consumption of Y and crucible, with Y deoxidation as the main link in the molten iron. The increase in the mass of molten iron to 600 g provides good dynamic conditions for Y deoxidation and inclusion floatation, avoiding systematic errors caused by the uniformity of inclusions and Y in the molten iron, and making the experimental data more accurate.

Acknowledgements This work was sponsored by the National Natural Science Foundation of China (grant number 52374326) and the Natural Science Foundation of Chongqing, China (grant number cstc2021jcyj-msxmX0988). Thanks to Chao Deng, from the Electron Microscopy Center of Chongqing University, for his help with SEM observations.

References

1. Van Ende M-A, Guo M, Rob D et al (2009) Formation and evolution of Al-Ti oxide inclusions during secondary steel refining. ISIJ Int 49:1133–1140
2. Cui X, Song B, Mao J (2022) Effect of Al and S on the evolution of inclusion and formation of acicular ferrite in the Mg-RE-Ti-treated Steel. Trans Indian Inst Met 75(9):2221–2230
3. Kang J, Yu YC, Zhang JL et al (2021) Effect of rare earth on inclusion evolution in industrial production of HRB500E steel. Metall Res Technol 118(2):220
4. Li H, Yu Y, Ren X et al (2017) Evolution of Al_2O_3 inclusions by cerium treatment in low carbon high manganese steel. J Iron Steel Res Int 24(9):9
5. Luo DQ, Yu YH, Zhang ZM et al (2021) Development of high impact toughness offshore engineering steel by yttrium-based rare earth addition. Ironmaking Steelmaking 48(10):1247–1253
6. Bai GJ, Yang JC, Liang WJ (2023) Effect of lanthanum–cerium mixed rare earth on inclusions in U76CrRe heavy rail steel. Can Metall Q, 1–14
7. Jiang XY, Li G, Tan HY et al (2023) Modification of inclusions by rare earth elements in a high-strength oil casing steel for improved sulfur resistance. Materials 16(2):675
8. Han QY, Liu SW, Niu HB et al (1982) Determination of equilibrium constant of Ce-O and Nb-O in liquid iron. Acta Metallurgical Sinica 18(2):176–186
9. Wang Y, Li CR, Zhu WL et al (2021) Effect of yttrium treatment on alumina inclusions in high carbon steel. J Iron Steel Res Int, 633
10. Zhang HH, Xiong HH, Qin J et al (2023) Mechanism of ferrite nucleation induced by Y_2O_2S inclusion in low carbon steel. J Iron Steel Res Int 30(6):1291–1299
11. Guo Z, Liu P, Zheng Y et al (2023) Effect of cold-rolling deformation and rare earth yttrium on microstructure and texture of oriented silicon steel. High Temp Mater Processes (London) 42(1):20220258
12. Zhang J, Zhang LF, Ren Y (2021) Effect of yttrium content on the transformation of inclusions in a Si-Mn-killed stainless steel. Metall Mater Trans B 52(4):2659–2675
13. Qiu GX, Zhan DP, Li CS et al (2020) Effects of electroslag remelting process and Y on the inclusions and mechanical properties of the CLAM steel. Nucl Eng Technol 52(4):811–818
14. Shi WN, Yang SF, Li JS (2018) Correlation between evolution of inclusions and pitting corrosion in 304 stainless steel with yttrium addition. Sci Rep 8(1):4830
15. Li DZ, Wang P, Chen XQ et al (2022) Low-oxygen rare earth steels. Nat Mater 21(10):1137–1143

16. Du T, Wang LM, Liu AS et al (1993) Thermodynamics and phase equilibria for cerium and yttrium in the presence of oxygen and sulphur in nickel-base solution. J Alloy Compd 193:38–40
17. Ishii F, Ban-Ya S (1995) Equilibrium between yttrium and oxygen in liquid iron and nickel. ISIJ Int 35(3):5
18. Buzek Z (1971) Chemical metallurgy of Iron and steel. In: International symposium on metallurgical chemistry, p 173
19. Xiang CX, Yang SF, Han QY (1987) Equibibria of Y-O and Y-S in molten iron. J Beijing Univ Iron Steel Technol 9(2):78–86
20. Du T, Wang LM (1985) Thermodynamics of Fe-Y-O, Fe-Y-S, Fe-Y-O-S metallic solutions. J Less-Common Met 110:179–785

Influence of a Rising Bubble on the Behavior of the Slag-Steel Interface

Yong Liu, Shusen Cheng, and Wenxuan Xu

Abstract The interfacial contact area between molten steel and slag is one of the key factors influencing the efficiency of chemical reactions. This study reconstructs the phenomenon of gas bubbles traversing the slag-steel interface by constructing a physical model of the water–oil system and employing image processing techniques. The study focuses on the effects of bubble size, slag density, viscosity, and interfacial tension on the entrainment volume of steel and the slag-steel interface area. The entrainment volume increases with the increase of bubble size or slag density, but decreases with the increase of slag viscosity. The interface area shows a trend of first increasing and then decreasing with the increase of bubble size, and increases with the increase of slag density or the decrease of slag viscosity. As the oil-air interfacial tension increases, the water–air interfacial tension decreases, or the water–oil interfacial tension decreases, the liquid–liquid interface area increases.

Keywords Physical model · Mathematical simulation · Steel-slag interface · Rising bubble · Carried volume · Interfacial area

Introduction

In metallurgical reaction processes, molten metal is often covered by a certain thickness of slag and accompanied by a gas stirring and mixing process. Consequently, the rising of bubbles from the metal to the slag is an inevitable process [1–3]. The passage of bubbles through the slag-steel interface effectively increases the interface area [3]. Also, this phenomenon can affect the efficiency of the slag-steel interface reaction [4–6].

Y. Liu (✉) · S. Cheng
School of Metallurgical and Ecological Engineering, University of Science and Technology, Beijing, Beijing 100083, China
e-mail: liuyong_ustb@126.com

W. Xu
Research Institute of Technology, Shougang Group Co., Ltd., Beijing 100043, China

S. Wagstaff et al. (eds.), *Materials Processing Fundamentals 2024*, The Minerals, Metals & Materials Series, https://doi.org/10.1007/978-3-031-50184-5_7

In the 1960s, researchers [7] notice the phenomenon of bubbles at the slag-steel interface and conducted exploratory work. Han et al. [8–10] used X-ray transmission techniques to study the phenomenon of single bubbles passing through the slag-iron interface. The findings revealed that the entrainment of iron droplets increased with larger bubble sizes and decreased with rising interfacial tension and higher slag viscosity. Besides, researchers have indirectly studied the phenomenon of bubbles at the interface of immiscible liquid phases using physical simulation based on the principle of similarity. The factors such as bubble diameter [11–13], interfacial tension [11], fluid viscosity, and density [14–17] are considered to analyze their effects on the interface phenomenon. Díaz et al. [13] discovered that with the increase in bubble size, the volume of entrained heavier liquid phase also increases [12]. Tanno et al. [17] demonstrated that the amount of entrained heavier liquid phase decreases with the increase in density of the heavier liquid phase. The research conducted at the liquid-bubble interface, a liquid film carrying the heavier liquid phase is formed, and the flow rate of the liquid film around the bubble depends on viscosity, interfacial tension, and buoyancy effects between the liquids [18, 19].

In summary, the majority of research efforts have concentrated on analyzing the liquid column of the heavier liquid phase carried by bubbles and the volume of entrained liquid. Nevertheless, there is a scarcity of research addressing the alterations in interface area resulting from the process of bubble traversal. The purpose of this study is to investigate the motion behavior of bubbles at the liquid–liquid interface, reproduce the phenomenon of bubbles crossing the liquid–liquid interface, and specifically analyze the changes in interface area when bubbles of different sizes cross different upper liquid phases.

Physics and Mathematical Models

Clod Model

The physical experiments were conducted in a rectangular organic glass container with inner dimensions of 220 mm × 80 mm × 500 mm, as shown in Fig. 1. A planar light source is placed on one side of the organic glass container. The experimental recordings were captured using a high-speed color camera with a frame rate of 200 frames per second. The size of the bubbles during the experiment was controlled by a rotating axis connected to a circular holder. A specified volume of bubble was injected into the circular holder using a syringe, and then released by the rotating axis bearing.

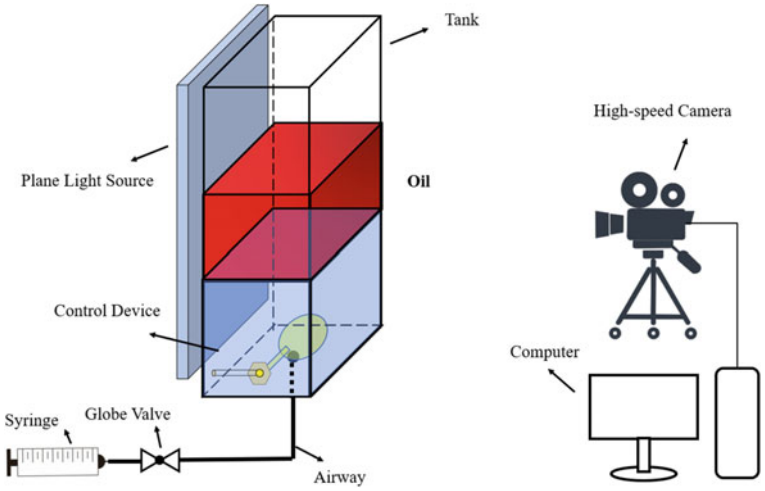

Fig. 1 Experimental setup

Table 1 Physical experimental fluid properties parameters

Parameter	Water	3# oil	Paraffin oil	100# oil	200# oil
Density/(g cm^{-3})	0.98	0.76	0.84	0.80	0.81
Viscosity/(mPa s)	3	8.9	9.6	93.3	193.5
Surface tension/(N m^{-1})	0.07	0.033	0.030	0.035	0.034
Water–oil interfacial tension/(N m^{-1})	–	0.040	0.040	0.042	0.047

Experimental Method

During the experiment, the water level was kept constant, and the main focus was on the influence of the initial bubble diameter on the entrainment volume and the steel-sludge interface area when different types of oil simulated the slag layer. The key physical parameters are given in Table 1. In the experiment, each test group was repeated 5 times to reduce the accidental error in the experimental data.

Numerical Simulation

In physical simulation experiments, although the phenomenon of bubbles passing through the slag metal interface can be reproduced, due to the properties of the experimental material, the effects of single factors such as fluid density, viscosity, and interfacial tension on the entrainment volume and slag metal interface area cannot be accurately determined. Therefore, numerical simulation methods are used

to analyze the impact of individual parameters. The assumptions and detailed control equations underlying the numerical simulation can be found in references [20, 21], which have been validated through physical models of water oil systems.

Interface Area Analysis Method

As bubbles enter the slag phase from the metal solution, the steel-slag interface bulges upwards, forming peaks that can be tall, short, wide, or thin. To analyze this phenomenon, a rectangular coordinate system, as illustrated in Fig. 2a, was established. Coordinates at the liquid–liquid interface boundary were then extracted using GetData software, as depicted in Fig. 2b. This process enabled the derivation of the data relationship governing the liquid–liquid interface boundary, which was subsequently fitted to reconstruct the entrainment phenomenon.

In this study, the growth rate of the interface area is a crucial parameter used to assess changes in the interface area. The calculation of the interface area growth rate is denoted as λ and is determined using Eq. (1).

$$\lambda = (S_h - S_f)/S_f \tag{1}$$

where S_h and S_f represent the surface area of the bulging and initial liquid–liquid interface, respectively.

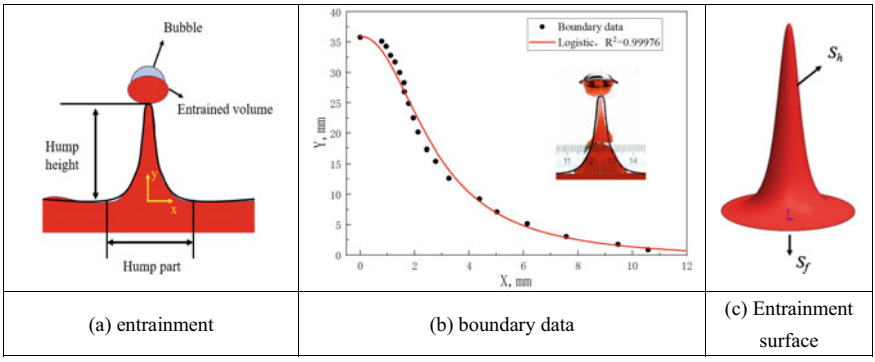

(a) entrainment | (b) boundary data | (c) Entrainment surface

Fig. 2 Schematic diagram for extracting the interfacial area of a liquid–liquid interface

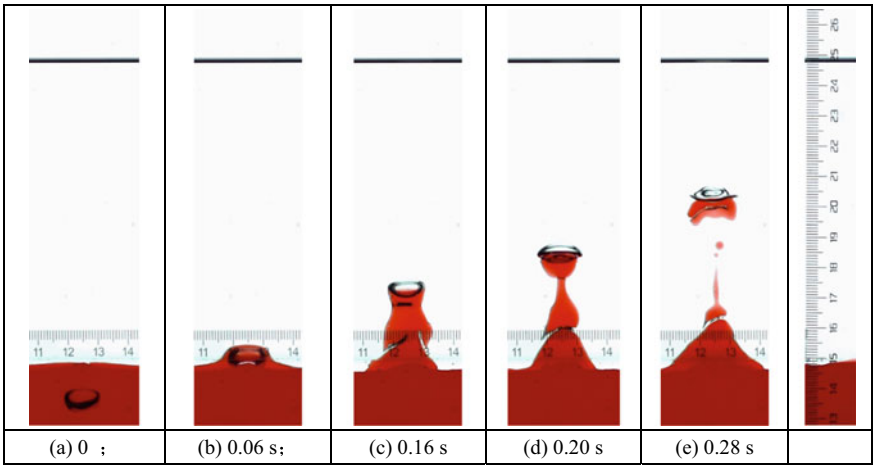

Fig. 3 Phenomenon of bubble ascent and entrainment process

Results

The Entrainment Phenomenon

The process of a bubble rising in a water-paraffin oil solution is depicted in Fig. 3. To emphasize the liquid–liquid interface, a water-soluble red dye was introduced into the water, enhancing the contrast between the two phases and making the evolving shapes between them during the ascent of the bubble more discernible. As evident in Fig. 3, the bubble is released in a static state. During its ascent, the bubble experiences deformation due to varying pressures in its vicinity. It continues to rise at a specific velocity until it reaches the interface between the liquid phases. Upon crossing this interface, a column of water forms beneath the bubble due to the wake effect. After reaching a certain height, this entrained water column detaches from the interface, breaking into two portions. One portion continues to ascend with the bubble, while the other descends back to the lower region.

Analysis of the Influence of the Entrainment Volume

Figure 4 illustrates the relationship between entrainment volume and bubble size in various oil–water systems. The entrainment volume increases as the bubble diameter increases, but this relationship is nonlinear. In the 10# white oil–water system, with a 5 mm bubble size, the entrainment volume is 180 mm3. When the bubble size increases to 10, 15, 20, and 25 mm, the entrainment volume increases by 255.56%, 733.33%, 1866.67%, and 3611.11%, respectively, compared to the 5 mm bubble. Moreover,

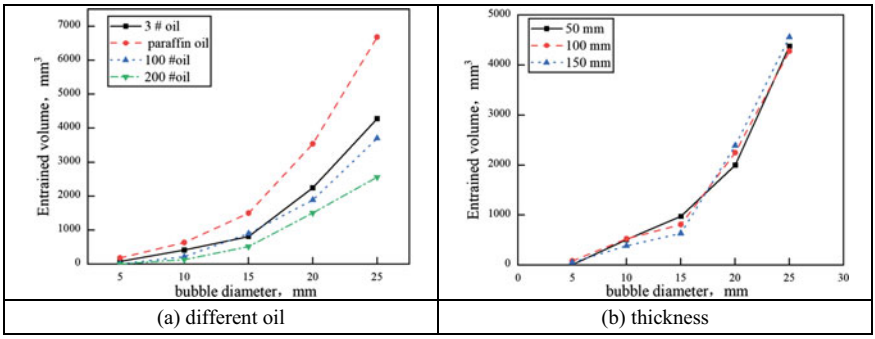

(a) different oil (b) thickness

Fig. 4 Relationship between bubbles of different sizes and entrained volume

the entrainment volume decreases as viscosity increases. For instance, with a 10 mm bubble size, the entrainment volume decreases by 65.63% and 78.91% as the oil phase viscosity increases from 9.6 to 93.3 mPa s and 193.5 mPa s, respectively. Furthermore, Fig. 4a indicates that within the range of studied oil layer thicknesses, there is no significant impact on the entrainment volume with varying oil layer thicknesses.

Analysis of the Influence of Slag-Steel Interface Area

Physical simulation experiments were conducted to investigate the changes in the water–oil interface area induced by bubbles of different sizes, as depicted in Fig. 5. It is apparent from Fig. 5 that the alteration in the liquid–liquid interface area follows a pattern of initial increase followed by a subsequent decrease as the bubble diameter increases. Taking the paraffin oil–water system as an example, when the bubble size escalates from 5 mm to 10, 15, 20, and 25 mm, the growth rates of the liquid–liquid interface area increase by 81.80%, 312.98%, 130.00%, and 113.44%, respectively.

Figure 5a illustrates the influence of oil phase density and bubble diameter on the growth exponent of the interface area. As the oil phase density increases, the growth exponent of the interface area begins to decline. This reduction is attributed to the increased buoyancy as the water phase begins to penetrate the oil phase. Figure 5b presents the impact of oil phase viscosity on the interface area. As the oil phase viscosity decreases, the growth exponent of the interface area increases. For instance, when the initial bubble diameter is 15 mm, the growth rates of the interface area decrease by 10.99% and 31.39% as the oil phase viscosity increases from 9.6 to 93.3 mPa s and 193.5 mPa s, respectively.

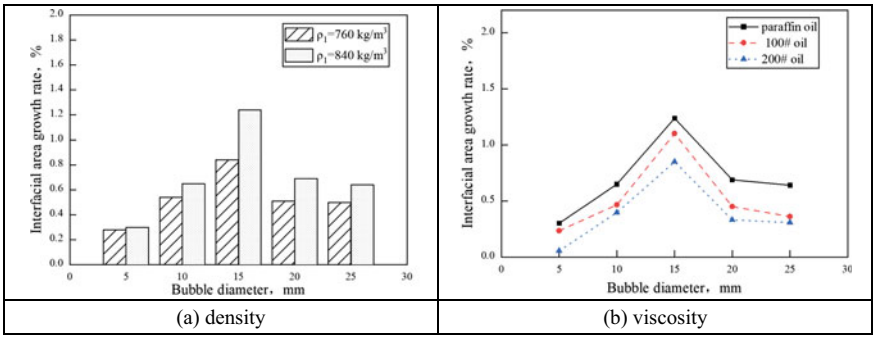

(a) density (b) viscosity

Fig. 5 Impact of light phase density and viscosity on interfacial area

Influence of the Interfacial Tension on the Interfacial Area of Slag-Steel

In the numerical simulation scheme, the initial size of the bubble is 10 mm, and the parameters for the water phase and paraffin oil are described in Table 1. The numerical simulation results are shown in Fig. 6. The schematic diagram of the three-phase interface (water–oil–gas) during the bubble crossing process is shown in Fig. 6a–e. The three-dimensional display of the bubble rising process is shown in Fig. 6f. A comparison between physical and numerical simulations shows that the results are similar.

The variation in the liquid–liquid interface area during the bubble crossing process is depicted in Fig. 7, with a focus on the influence of interfacial tension. Observing Fig. 7a–c, it is evident that as the surface tension of the oil phase increases, leading to a reduction in the surface tension of water and consequently a decrease in the interfacial

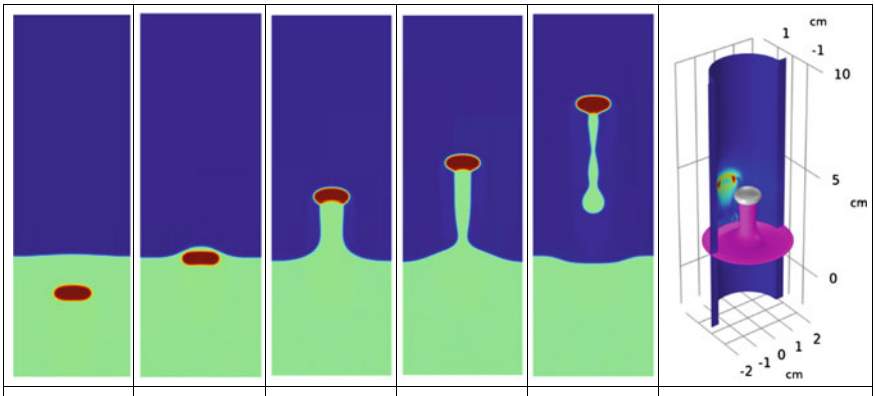

(a) 0 s (b) 0.068 s (c) 0.165 s (d) 0.214 s (e) 0.295 s (f) Bubble rise

Fig. 6 Mathematical results

tension between water and oil, the interface area expands. Specifically, when the surface tension of the oil phase increases from 0.03 N/m to 0.04, 0.05, and 0.06 N/m, the maximum interface area increases by 0.59%, 1.78%, and 2.96%, respectively, compared to the base value of 0.03 N/m. Conversely, when the surface tension of water increases from 0.03 N/m to 0.04, 0.05, and 0. N/m, the maximum interface area decreases by 1.62%, 3.86%, and 6.05%, respectively. Figure 7c highlights the impact of oil–water interfacial tension on the interface area. As the oil–water interfacial tension increases, the resistance to bubble motion during the crossing of the liquid–liquid interface intensifies, leading to a reduction in the interface area. Specifically, when the oil–water interfacial tension increases by 33.33%, 66.67%, and 100.00% relative to the base value of 0.03 N/m, the maximum interface area decreases by 2.86%, 5.14%, and 9.14%, respectively.

The analysis above reveals that the interfacial tensions between water–oil-gas phases affect the water–oil interface area during the process of bubble crossing, with the degree of influence ranked as follows: water–oil interfacial tension, water–air interfacial tension, and oil-air interfacial tension.

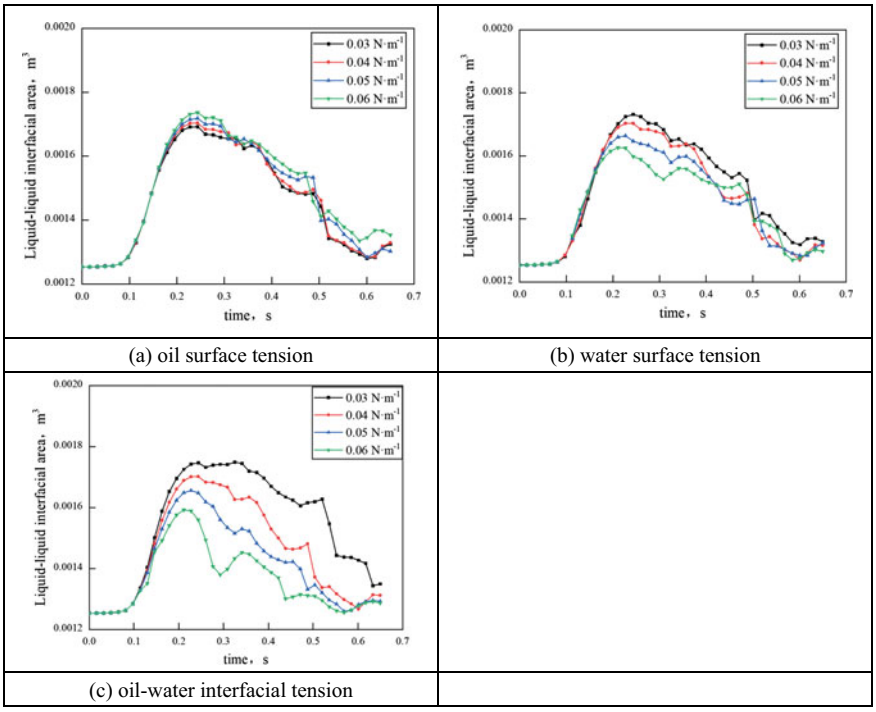

Fig. 7 Effect of interfacial tension on the interfacial area

Conclusions

(1) There is a nonlinear relationship between bubble size growth and entrainment, and as the bubble size increases, the rate of entrainment also increases sharply. Furthermore, the entrainment volume increases with the increase of oil density or the decrease of oil viscosity. However, within the studied range of oil layer thickness, the impact on entrainment is relatively small.
(2) The interface area between the liquid–liquid phases shows a trend of increasing first and then decreasing as the bubble size increases. Meanwhile, when the density of the oil phase decreases or the viscosity increases, it has an inhibitory effect on the upward bulging of the liquid–liquid interface, restricting the growth rate of the interface area.
(3) The interface area between the liquid–liquid phases increases as the surface tension of the oil phase increases, the surface tension of the water phase decreases, or the interfacial tension between water and oil decreases. The degree of influence on the interface area is ranked as follows: water–oil interfacial tension, water–air interfacial tension, and oil-air interfacial tension.

References

1. Fabritius T, Riipi J, Järvinen M, Mattila O, Heikkinen E-P, Kärnä A, Kurikkala J, Sulasalmi P, Härkki J (2010) Interfacial phenomena in metal–slag–gas system during AOD process. ISIJ Int 50(6):797–803
2. Beskow K, Dayal P, Björkvall J, Nzotta M, Sichen D (2006) A new approach for the study of slag–metal interface in steelmaking. Ironmaking Steelmaking 33(1):74–80
3. Ekengård J, Andersson AMT, Jönsson PG (2008) Distribution of metal droplets in top slags during ladle treatment. Ironmaking Steelmaking 35(8):575–588
4. Yoshida H, Liu J, Kim S-J, Gao X, Ueda S, Kitamura S (2016) Influence of the interfacial tension on the droplet formation by bubble rupture in Sn(Te) and salt system. ISIJ Int 56(11):1902–1909
5. Kitamura S, Zeze M, Nakashima J (2016) Multi-phase flow of liquid/liquid system in steelmaking process. Jpn J Multiphase Flow 30(3):266–273
6. Song D-Y, Maruoka N, Maeyama T, Shibata H, Kitamura S (2010) Influence of bottom bubbling condition on metal emulsion formation in lead-salt system. ISIJ Int 50(11):1539–1545
7. Poggi D, Minto R, Davenport WG (1969) Mechanisms of metal entrapment in slags. JOM 21(11):40–45
8. Han Z, Holappa L (2003) Mechanisms of iron entrainment into slag due to rising gas bubbles. ISIJ Int 43(3):292–297
9. Han Z, Holappa L (2003) Bubble bursting phenomenon in gas/metal/slag systems. Metall and Mater Trans B 34(5):525–532
10. Han Z, Holappa L (2003) Characteristics of iron entrainment into slag due to rising gas bubbles. ISIJ Int 43(11):1698–1704
11. Greene GA, Chen JC, Conlin MT (1988) Onset of entrainment between immiscible liquid layers due to rising gas bubbles. Int J Heat Mass Transf 31(6):1309–1317
12. Mercier JL, da Cunha FM, Teixeira JC, Scofield MP (1974) Influence of enveloping water layer on the rise of air bubbles in Newtonian fluids. J Appl Mech 41(1):29–34
13. Díaz-Damacillo L, Ruiz-Angulo A, Zenit R (2016) Drift by air bubbles crossing an interface of a stratified medium at moderate Reynolds number. Int J Multiph Flow 85:258–266

14. Choi K, Park H (2021) Interfacial phenomena of the interaction between a liquid–liquid interface and rising bubble. Exp Fluids 62(6):1–21
15. Pierson J-L, Magnaudet J (2018) Inertial settling of a sphere through an interface. Part 1. From sphere flotation to wake fragmentation. J Fluid Mech 835:762–807
16. Zhao H, Wang J, Zhang W, Xie M, Liu F, Cao X (2019) Bubble motion and interfacial phenomena during bubbles crossing liquid–liquid interfaces. Processes 7(10), Article 10
17. Tanno M, Liu J, Gao X, Kim S-J, Ueda S, Kitamura S (2017) Influence of the physical properties of liquids and diameter of bubble on the formation of liquid column at the interface of two liquid phases by the rising bubble. Metall and Mater Trans B 48(6):2913–2921
18. Mao N, Kang C, Teng S, Mulbah C (2020) Formation and detachment of the enclosing water film as a bubble passes through the water-oil interface. Colloids Surf, A 586:124236
19. Rozario A, Viswanathan NN, Basu S (2019) Rise of gas bubbles across the interface between two liquids. Metall and Mater Trans B 50(1):10–15
20. Zhou XB, Zhao ZS, Wang WX, Xu JG, Yue Q (2023) Physical and mathematical simulation on the bubble entrainment behavior at slag-metal interface. Acta Metallurgica Sinica Online First, 1–12
21. Farhadi J, Sattari A, Hanafizadeh P (2022) Passage of a rising bubble through a liquid-liquid interface: a flow map for different regimes. Can J Chem Eng 100(2):375–390

Influence of Slag Viscosity on Copper Matte Entrainment Volume by a Rising Bubble Through Immiscible Liquids Interface

Xiangfeng Cheng, Mao Chen, Fuming Zhang, Gele Qing, and Jianlong Wu

Abstract In the settlement zone of the copper smelting furnace, SO_2 bubbles will be generated due to the insufficient oxidization of copper matte concentrate by injected oxygen-rich air in the reaction zone, entailing mass transfer in the liquid–liquid system by a rising bubble penetrating through the liquid–liquid interface. Different operating conditions between the bottom blown furnace and side blown furnace lead to different slag and matte viscosity. To investigate the copper smelting slag viscosity effect on the matte entrainment volume, cold model experiments using high-speed imaging techniques and high-temperature experiments were carried out. Results show that the lower liquid entrainment volume increases with the decreasing upper liquid viscosity and increasing bubble size. Higher slag viscosity and more SO_2 bubbles generated in the side blown furnace probably deteriorate the matte entrainment in the slag phase, while matte viscosity exerts slight influences due to the stable viscosity variation.

Keywords Copper smelting · SO_2 bubbles · Slag viscosity · Matte entrainment

X. Cheng · G. Qing · J. Wu
Shougang Research Institute of Technology, Beijing 100043, China

Beijing Key Laboratory of Green Recyclable Process for Iron & Steel Production Technology, Beijing 100043, China

M. Chen (✉)
State Key Laboratory of Vanadium and Titanium Resources Comprehensive Utilization, Panzhihua 617000, Sichuan, China
e-mail: ptchenmao@163.com

F. Zhang
Shougang Group, Beijing 100041, China

S. Wagstaff et al. (eds.), *Materials Processing Fundamentals 2024*, The Minerals, Metals & Materials Series, https://doi.org/10.1007/978-3-031-50184-5_8

Introduction

The demand for copper has been increasing for the last decades with an increase of exploitation quantity, while a significant loss of copper in the slags happens in the smelting process simultaneously. Generally, the copper loss can be classified into physical entrainment, e.g., entrained matte droplets and chemical entrainment, e.g., Cu^{+} ions with O^{2-} or S^{2-} ions. Several sources of entrained matte in slags are reported in the previous studies [1, 2]. The slag chemistry studies of bottom blown furnace (BBF) and side blown furnace, e.g., Teniente Converter (TC) indicate that the majority of the copper losses to the slag are the mechanically entrapped matte droplets.

In the relatively static environment of settlement zone in bath smelting furnace, numerous SO_2 gas bubbles are generated from the further oxidization of copper matte in the matte phase, leading to a significant mass transfer when penetrating matte-slag interface, as shown in Eq. 1.

$$CuFeS_2(s) + O_2(g) + SiO_2(s) \rightarrow (Cu, Fe, S)(l) + FeO - SiO_2(l) + SO_2(g) \quad (1)$$

Numerous SO_2 bubbles penetration process through the immiscible matte-slag interface is expected to cause matte entrainment in the slag phase. The matte and bubble size distributions in industrial slag samples in bottom blown furnace and Teniente Converter have been analyzed, while the copper losses in two furnaces are different with about 3% in bottom blown furnace and up to 12% in the Teniente Converter [2, 3] (Fig. 1).

Single bubble rising behaviours through the liquid–liquid interface are highly dynamic processes applied in numerous industrial applications, e.g., metallurgical processes, nuclear reactor safety, etc. [2, 4–8]. Gas bubbles rising across a liquid–liquid interface could carry a surface coating of the lower liquid into the upper phase and scatter small droplets into the slag phase. The film stability was described through

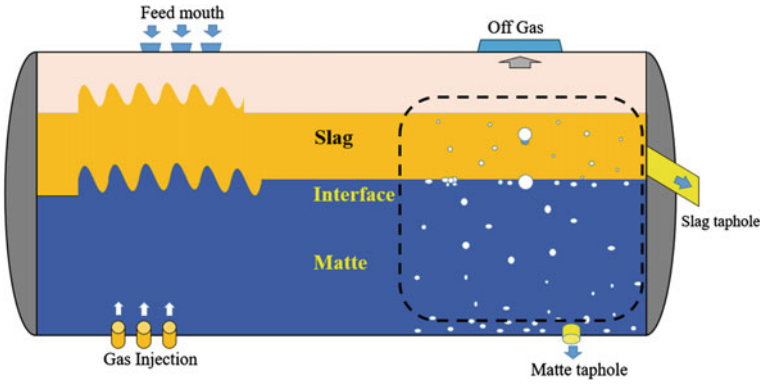

Fig. 1 Rising bubbles generated in the settlement zone of the smelting furnace

floatation coefficient and spreading coefficient by considering the interfacial energies of the bottom blown furnace and side blown furnace (e.g., Teniente Converter (TC)) [1]. The settlement time of matte droplets entrained in the slag phase was estimated, and results showed that the majority of copper matte droplets observed in slags were difficult to settle down during periodic discharging time [2].

Many experimental and numerical studies have been carried out on bubble passage through the immiscible liquids interface [4, 9–11]. The passage of bubble rise in fluids and at the interface was followed, and the dynamic behaviour of the interface was investigated by the bubble's position and the corresponding retention time at the interface. Moreover, many researchers have reported the film enveloping the bubble or the column between the bubble and the lower interface caused by rising bubbles at the interface in several combinations of liquid–liquid systems [12].

The viscosity of smelting slags is an important process variable to reflect the flow behaviours in most pyrometallurgical smelting operations and has a strong influence on rates of mixing of mass transfer, metal and slag separation, etc. The copper matte is a combination of copper sulphide, a small amount of iron sulphide and some heavy metals, of which copper sulphide makes up 80–95%. The temperature and composition of slags have great effects on slag viscosity [13]. Due to the limited varying range of matte viscosity, the temperature has little impact on the dynamic viscosity of the pure compounds Cu_2S, FeS, and also the pseudo-binary systems of FeS–Cu_2S. The dynamic viscosity of melts in the Cu_2S–FeS system is less affected by temperature, varying slightly from 0.002 to 0.004 Pa s. Thus, the operating temperature in the smelting furnace mainly depends on the molten slag requirement. Besides, the matte grade in the bottom blown furnace is similar to that in the Teniente Converter at approximately more than 70%, while the oxygen enrichment is far higher in bottom blown smelting furnace at 72–73% than in side blown smelting furnace typically at 35–42%.

This paper aims to explore the copper matte and smelting slag viscosity effects on the copper matte entrainment volume in the slags with cold model experiments and high-temperature validation experiments.

Experimental

Experimental Setup

Copper matte transport process from the matte phase to upper slag phase through immiscible matte-slag interface at high temperatures is difficult to be observed directly. To simulate and visualize the whole transporting process at the interface and quantify the lower liquid entrainment volume by rising bubbles when passing through the interface, cold model experimental setup was used to capture bubble penetration behaviours through the liquid–liquid interface, as shown in Fig. 2a. Cold model experimental setup consisted of a transparent glass container (80 mm * 80 mm * 600

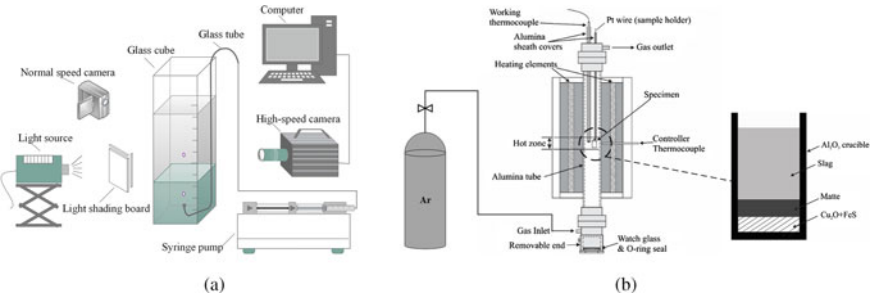

Fig. 2 Schematic diagram of an experimental device in **a** cold model experiments and **b** high-temperature experiments

mm), and a high-speed camera to capture the bubble penetration behaviours and measure the lower liquid entrainment volume at 500 fps. A light source (XGY-II, Zhejiang Xinguangyang Lighting Co., Ltd.) at the opposite direction of the high-speed camera was used to provide dispersed light through a light shading board to illuminate liquids in the glass cube. Air was fed from a syringe pushed by an infusion pump (Kd Scientific 780100, ALT) to control the air flow rate precisely.

High-temperature experiments in the laboratory were carried out to verify the attachment between matte droplets and SO_2 bubbles and further explore the slag viscosity influence on matte entrainment. Scanning Electron Microscope (SEM) was used to determine the microstructures of the quenched laboratory slags. The schematic diagram of the furnace inner structure and experimental setup are displayed in Fig. 2b. High-temperature experiments were conducted in a vertical tube furnace using alumina crucibles (inner dimensions: 2 cm diameter, 5 cm high). Samples were prepared in three layers (Fig. 2b): a slag layer at the top, a matte layer in the middle, and a mixture of Cu_2O and FeS at the bottom. The bottom layer with Cu_2O and FeS mixture is to generate SO_2 bubbles in the melts.

Materials

In the cold model experiments, solutions of glycerol with different concentrations in the water and silicone oils with different viscosities were used to investigate the lower liquid and upper liquid viscosity effects on the lower liquid entrainment volume, respectively, as given in Table 1.

It should be noted that upper liquid entrainment volume was defined as the total lower liquid droplets volume transporting into upper liquid by a rising gas bubble.

The synthetic slags were also used to observe the slag viscosity effects on bubble penetration behaviours at the matte-slag interface. The slag physical properties are given in Table 2.

Table 1 Physical properties of liquid–liquid combination systems

Lower phase				Upper phase			
Material	Viscosity (cP)	Density (g/cm^3)	Surface tension (mN/m)	Material	Viscosity (cP)	Density (g/cm^3)	Surface tension (mN/m)
Glycerol 80%	60.1	1.21	48.06	10 cP silicone	10	930	20.1
Glycerol 70%	22.5	1.19	48.26	50 cP silicone	50	959	20.7
Glycerol 60%	10.8	1.16	48.11	200 cP silicone	200	970	21.1
Glycerol 40%	3.72	1.10	48.66	500 cP silicone	500	970	21.1

Table 2 Physical properties of synthetic slag samples in high-temperature experiments

Samples	Synthetic slags (wt%)				Melting point (°C)	Viscosity (Pa s)
	CaO (g)	Fe (g)	Fe_2O_3 (g)	SiO_2 (g)		
No. I	3.4888	3.9801	10.3379	0	1141	0.022
No. II	2.6168	2.2389	5.815	6.9781	1117	0.273

In Experiment No. I, approximately 20% CaO and 80% FeO were mixed to form slags with lower viscosity, while more SiO_2 (40%) and less FeO (45%) were mixed with CaO to generate slag with higher viscosity in Experiment No. II. The chemicals Cu_2O (≥99.99%) and FeS (≥99.9%; both Sigma-Aldrich, USA) were mixed to generate SO_2 bubbles at the bottom of the Al_2O_3 crucible. The pelletized Cu_2O and FeS mixture was placed at the bottom of the crucible to generate SO_2 bubbles to simulate the bubble transportation process in the smelting furnace.

Experimental Procedures

Immiscible glycerol solution and silicone oil systems in the cold model experiments were used to simulate the matte and slag systems in the copper smelting furnace. In different glycerol-silicone oil systems, air was fed by a syringe pump at different injection flow rates and glass nozzle sizes to control bubble size. The bubble size could be controlled through some specially made glasses which are replaceable in the notch of gas injection tube. Seven specially made glass nozzles (inner diameters: 0.5 mm, 3 mm, 4 mm, 5 mm, 6 mm, 7 mm, 9 mm) were used to generate bubbles varying from 2 to 10 mm in diameter. All experiments were carried out at 25 °C. The bubble size and lower liquid entrainment volume in the upper phase can be measured by Image J with high-speed imaging techniques.

High-temperature experiments were conducted in a vertical tube furnace in the Ar atmosphere (99.999%). The specimen was heated to 600 °C at 15 °C/min and placed in the furnace at 600 °C to dry for 30 min firstly. Then, samples were heated to 900 °C at 5 °C/min. Two three-layer samples were heated to 1200 °C. The specimen was kept at 1200 °C for 10 min to release as many bubbles as possible, and then lowered rapidly to the cold end of the furnace. The crucible was fast-quenched by the high-purity Ar gas.

Results and Discussion

Bubble size plays a significant role in the distinct bubble penetration regimes through immiscible liquids interface. Small bubbles, generally 2.5–4.5 mm in diameter, referred to those which cannot penetrate the interface directly due to the interfacial resistance at the first impact. Large gas bubble, generally larger than 4.5 mm in diameter, can penetrate liquid–liquid interface directly with a long liquid column due to the large momentum. However, lower liquid column dragged by rising gas bubble in the upper phase tend to detach from the bubble before it ruptures into small droplets. The threshold for small and large bubbles depends on the fluids physical properties in different immiscible liquid–liquid systems [1, 4].

Lower Liquid Entrainment Volume by a Small Rising Gas Bubble

Bubble passage through two immiscible liquids interface shows a strong correlation with bubble size and fluids physical properties. Fine bubbles in the millimeter or submillimeter range tend to induce a barely perceptible lower liquid film to surround a gas bubble or scattered fine lower liquid droplets to be attached to the bubble surfaces [2]. However, for small bubbles with diameters more than 2.5 mm shown in Fig. 3a–d, a stable attachment between a thick lower liquid layer and a rising gas bubble tends to be formed in silicone oils at different viscosities although it may not inevitably happen in different immiscible liquid–liquid systems, which can lead to the detachment height as high as 500 mm. Moreover, it was found that a long thin column or tail tends to be formed in the 10 cP silicone oil as shown in Fig. 3a and caused more scattered lower liquid droplets when it ruptured behind the rising bubble. The reason for this type of behaviour can be attributed to the larger silicone oil viscosity as an equivalent bubble requires only a smaller buoyancy force to overcome the viscous force from the silicone oil to penetrate the interface and enable bubble passage by greater kinetic energy. Thus, for bubbles in Fig. 3d, silicone oil with a viscosity of 500 cP will make it difficult for small bubbles to pass through the interface and possess sufficient momentum to induce the long tail. Thus, a larger

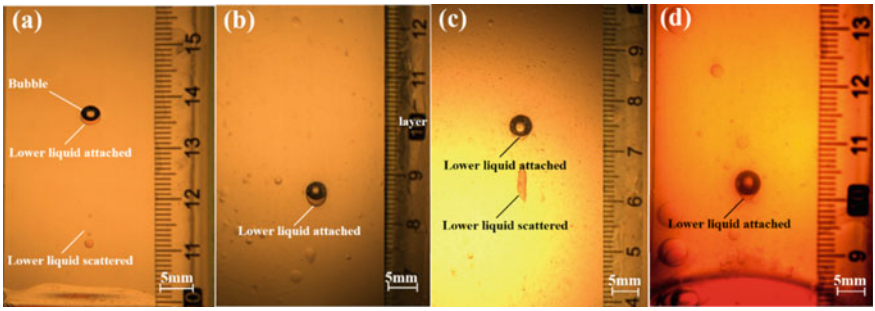

Fig. 3 Medium bubble and lower liquid attachment at different upper liquid viscosities of **a** 10 cP, **b** 50 cP, **c** 200 cP, and **d** 500 cP

upper liquid viscosity will inhibit the total entrainment volume of lower liquid in the upper liquid phase.

Lower Liquid Entrainment Volume by a Larger Rising Gas Bubble

As the bubble size increases, flow regimes during the passage of a rising bubble through a liquid–liquid interface will be different. Figure 4a–d shows the bubbles with diameters of 6.3 mm, 6.1 mm, 6.0 mm, and 5.9 mm in 10 cP, 50 cP, 200 cP, and 500 cP silicone oil, respectively. In Fig. 4a, the bubble shows an irregular shape and experiences severe deformation due to the smaller silicone oil viscosity at 50 cP. However, with the increase of silicone oil viscosity in Fig. 4b–d, the bubble present regular shapes, i.e., a spherical cap, ellipsoidal, and nearly spherical shape, respectively. In Fig. 4a and b, a large lower water droplet from the ruptured water column was observed to rise behind a rising bubble, which size was comparable to the rising bubble. In Fig. 4c and d, a long tail tends to be formed behind the rising bubble due to the larger upper liquid viscosity, while an obvious lower liquid layer was attached at the rear of the bubble in Fig. 4d. This is probably because the larger silicone oil viscosity favors the stability of the bubble shape and therefore a more stable attachment of the lower liquid layer to the bubble surface.

Attachment Between SO_2 Bubble and Matte in Copper Smelting Slags

To investigate the slag viscosity effect on the attachment volume of copper matte by the numbers of SO_2 bubbles in smelting slags, high-temperature experiments were carried out. Figure 5 shows the attachment between SO_2 bubbles and copper matte

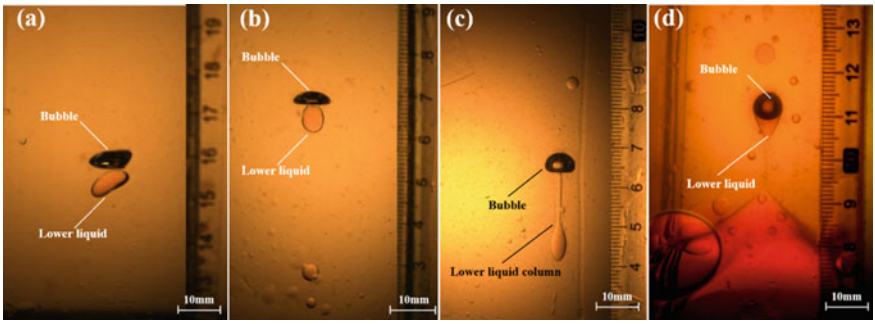

Fig. 4 Large bubble and lower liquid attachment at different upper liquid viscosities **a** 10 cP, **b** 50 cP, **c** 200 cP, and **d** 500 cP

in different smelting slags with slag viscosity of 0.022 Pa s in Fig. 5a and 0.273 Pa s in Fig. 5b. From SEM photographs, it was found that SO_2 bubbles in the smelting slags in both Fig. 5a and b ranged from 50 to 500 μm. A larger number of SO_2 bubbles were observed to distribute in the smelting slags in Fig. 5a compared with the number of bubbles in Fig. 5b, while the average bubble size is comparatively smaller than that in Fig. 5b. This is probably because higher slag viscosity inhibits the small bubble penetration through the matte-slag interface, leading to a smaller number of but larger SO_2 bubbles in the slags. It should be noted that the volume ratio between matte droplets and gas bubbles in Fig. 5a presents a larger value than that in Fig. 5b, meaning more matte droplets tend to be carried into smelting slags with lower viscosities for SO_2 bubbles at an equivalent size. Therefore, the ascending slag viscosity can significantly increase the matte entrainment volume for a rising SO_2 bubble through the immiscible matte-slag interface, which was in good agreement with the results shown in cold model experiments.

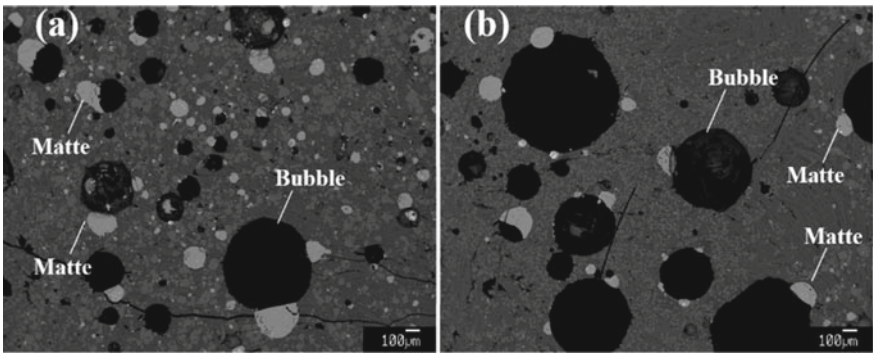

Fig. 5 SO_2 bubble and matte attachment in slags at different viscosities: **a** slag viscosity: 0.022 Pa s; **b** slag viscosity: 0.273 Pa s

Discussion

The lower liquid film thickness was derived by the total lower liquid entrainment volume and bubble size, which assumes the lower liquid droplets spread on the bubble surfaces evenly.

Figure 6 shows the effects of silicone oil viscosity (10 cP, 50 cP, 200 cP, 500 cP) effects on water entrainment volume for different sized bubbles. The interfacial tension between water and silicone oils was controlled at approximately 50 mN/m. The entrained water thickness on the bubble surface shows a good correlation with the bubble size assuming the water droplets were evenly spreading on the spherical bubble surface. The lower liquid layer thickness increases with the increase of bubble size and decrease of silicone oil viscosities from 500 to 10 cP. Besides, the difference of water film thickness becomes more significant with the increase of the bubble size.

Figure 7 shows the lower liquid viscosity effects on lower liquid thickness at a rising bubble. It can be found that with the increasing lower liquid viscosity, the lower liquid thickness on the bubble surfaces decreases. However, the lower liquid thickness showed not much difference when the lower liquid viscosity reached above 22.5 cP.

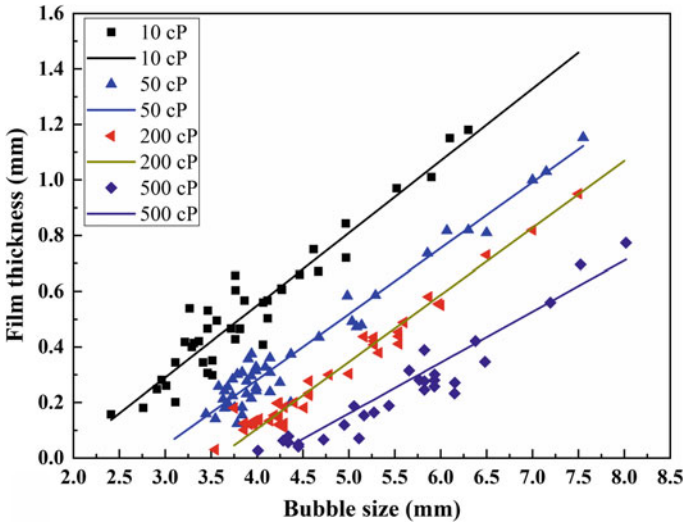

Fig. 6 Upper liquid viscosity effects on lower liquid thickness at a rising bubble

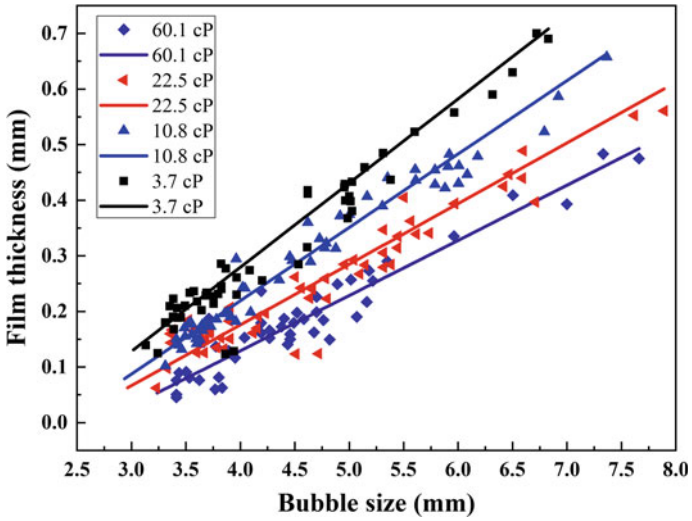

Fig. 7 Lower liquid viscosity effects on lower liquid thickness at a rising bubble

Conclusions

Copper matte and smelting slags viscosity effect on the matte entrainment volume has been carried out. Experimental results show that the water entrainment volume increases with decreasing silicone viscosity and increasing bubble size. High-temperature experimental results show a good agreement with the cold model experiments that the smelting slag with higher viscosity can inhibit the matte entrainment in the slags in terms of the number of SO_2 bubbles and matte entrainment volume.

From the perspective of industrial application, lower oxygen enrichment in the side blown furnace (35–42%) than that in bottom blown furnace (72–73%) facilitates the generation of more SO_2 bubbles ranging from millimeters to microns in the settlement zone of the smelting furnace, thus leading to more copper matte entrainment in the slags. Besides, the dynamic viscosity of matte, i.e., Cu_2S–FeS system, is less affected by temperature, varying slightly from 0.002 to 0.004 Pa s. However, the slag viscosity μ_{slag} in Teniente Converter (0.124 Pa s) is smaller than that in a bottom blown furnace (0.180 Pa s) due to the higher temperature (TC: 1250 °C; BBF: 1170 °C) and lower SiO_2, Fe_3O_4 contents. The lower slag viscosity contributes to the copper matte entrainment in the side blown furnace.

References

1. Greene GA, Chen JC, Conlin MT (1991) Bubble induced entrainment between stratified liquid layers. Int J Heat Mass Tran 34(1):149–157
2. Cheng XF, Cui ZX, Contreras L, Chen M, Nguyen VA, Zhao BJ (2019) Matte entrainment by SO_2 bubbles in copper smelting slag. JOM 71(5):1897–1903
3. Cheng, XF, Contreras L, Chen M et al (2017) Introduction of matte droplets in copper smelting slag. Paper presented at the 8th international symposium on high-temperature metallurgical processing, TMS 2017
4. Emery TS, Raghupathi AP, Kandlikar GS (2018) Flow regimes and transition criteria during passage of bubbles through a liquid-liquid interface. Langmuir 34(23):6766–6776
5. Shi WB, Yang XG, Sommerfeld M et al (2019) Modelling of mass transfer for gas-liquid two-phase flow in bubble column reactor with a bubble breakage model considering bubble-induced turbulence. Chem Eng J 371:470–485
6. Kapusta JPT (2017) Submerged gas jet penetration: a study of bubbling versus jetting and side versus bottom blowing in copper bath smelting. JOM 69(6):970–979
7. Saito T, Toriu M (2015) Effects of a bubble and the surrounding liquid motions on the instantaneous mass transfer across the gas–liquid interface. Chem Eng J 265:164–175
8. Singh KK, Bart HJ (2019) Passage of a bubble through the interface between a shear-thinning heavier liquid and a Newtonian lighter liquid. Chem Eng Commun, 1–18
9. Mao N, Teng S, Mulbah C (2020) Formation and detachment of the enclosing water film as a bubble passes through the water-oil interface. Colloids Surf A Physicochem Eng Asp 586:124236
10. Singh KK, Gebauer F, Bart HJ (2017) Bouncing of a bubble at a liquid–liquid interface. AIChE J 63(7):3150–3157
11. Singh KK, Bart HJ (2015) Passage of a single bubble through a liquid–liquid interface. Ind Eng Chem Res 54(38):9478–9493
12. Farhadi J, Sattari A, Hanafizadeh P (2022) Passage of a rising bubble through a liquid-liquid interface: a flow map for different regimes. Can J Chem Eng 100(2):375–390
13. Chen M, Raghunath S, Zhao B (2014) Viscosity measurements of SiO_2-"FeO"-MgO system in equilibrium with metallic Fe. Metall Mater Trans B 45(1):58–65

Part III
Processing

Effect of MgO on Crystallization Properties of Mold Flux for Ultra-wide Slab Peritectic Steel

Gang Li, Qiangqiang Wang, Shengping He, and Xubin Zhang

Abstract Controlling the heat flux at meniscus is one of the key aspects to prevent the formation of cracks during the continuous casting of crack-sensitive steel. This study investigated the influence of MgO addition on the performance of mold slag in the production of ultra-wide strand with a cross-section of 3000 mm × 150 mm. The main results indicated that when MgO increased from 0 to 8 wt%, the crystallization of slag film gradually decreased to 0% and then gradually increased. The break temperature and melting point also have the same change rule. When MgO was below 6 wt%, the O^{2-} ionized from MgO destroyed the silicon-oxygen tetrahedron structure of the flux and inhibited crystallization. Conversely, magnesia alumina spinel would form in the flux. XRD results also confirmed these results. This study provided a new idea for the composition optimization of mold flux for continuous casting of large cross-section peritectic steel.

Keywords Peritectic slab · Mold flux · MgO · Crystallization property · Break temperature

Introduction

Peritectic steel slab is prone to longitudinal cracks on the surface of slab due to peritectic reaction during continuous casting. At present, for this problem, the selection of protective slag with appropriate performance is undoubtedly the most cost-effective solution. The mold flux for peritectic steel needs to fulfill two requirements: provide lubrication for the slab and possess strong crystallization ability to enhance its heat transfer control capabilities [1–3]. However, increasing the solidification temperature to thicken the solid slag film can lead to insufficient liquid slag inflow, resulting in a thin liquid slag film and deteriorating the lubrication conditions for the slab. This, in

G. Li · Q. Wang (✉) · S. He · X. Zhang
College of Materials Science and Engineering, and Chongqing Key Laboratory of Vanadium–Titanium Metallurgy and Advanced Materials, Chongqing University, Chongqing 400044, China
e-mail: wtfwawj@163.com

S. Wagstaff et al. (eds.), *Materials Processing Fundamentals 2024*, The Minerals, Metals & Materials Series, https://doi.org/10.1007/978-3-031-50184-5_9

turn, can cause bonding and breakout. Therefore, the key to designing a mold flux for peritectic steel lies in ensuring uniform heat transfer control while avoiding surface longitudinal cracks, all while ensuring the smooth operation of continuous casting.

Adding a small amount of MgO to the mold flux can reduce the break temperature and improve the chemical stability of the slag. However, if the MgO content in CaO–SiO_2–Al_2O_3 slag was too high, it reacted with SiO_2 and Al_2O_3 to form magnesia alumina spinel or magnesia pyroxene, which impaired the fluidity of the slag [4]. Additionally, Wang [5, 6] studied non-reactive mold fluxes for high-aluminum steel using the single hot thermocouple technique (SHTT) and heat flux simulator of mold slag film. The results showed that with an increased MgO content, the crystallization time of the mold flux increased, the crystallization ratio decreased, the heat transfer characteristic time of the slag film increased, and the maximum heat flux density and average heat flux density increased. In other words, the addition of MgO inhibits crystallization. However, Daniel [7, 8] studied the CaO–SiO_2–Al_2O_3–MgO–TiO_2 slag system using SHTT. The results showed that as the MgO content in the slag increased, the corresponding initial crystallization temperature and critical cooling rate also increased, indicating that the increase in MgO content promoted the crystallization of the mold flux.

The role of MgO in different slag systems may be different, especially in high-basicity mold fluxes, scholars have not yet reached a consensus. In this study, the CaO–SiO_2-based mold flux for ultra-wide slab peritectic steel is taken as the research object. The effect of MgO content on the melting and crystallization properties of the mold flux was studied by changing the MgO content, and the mechanism of performance change was analyzed. This research provided valuable insights for the development and improved application of CaO–SiO_2-based mold fluxes for ultra-wide slab peritectic steel.

Experimental Methodology

Composition of the Mold Flux

The base slag was derived from the CaO–SiO_2-based peritectic steel industrial mold flux used in continuous casting. The slab section measured 150 mm × (2600–3200 mm), and the working casting speed was 1.1–1.2 m/min. The raw materials used in each component of the mold flux were chemically pure, and Na_2O was replaced by Na_2CO_3. The flux design followed a single factor variable method, where the comprehensive basicity and other components in the flux remained fixed, and only the content of MgO was changed. The specific content and label of each component during the experiment are shown in Table 1.

$$R = \left(w_{CaO} + 56/78 \times w_{CaF_2}\right) / w_{SiO_2}. \quad (1)$$

Table 1 Composition and content of mold flux (wt%)

Sample number	R	CaO	SiO_2	Al_2O_3	MgO	Na_2O	CaF_2	Fe_2O_3	MnO
M1	1.35	34.92	34.95	3.97	0.00	8.21	17.29	0.60	0.06
M2	1.35	45.82	33.94	3.97	2.00	8.21	17.29	0.60	0.06
M3	1.35	44.46	32.93	3.97	4.00	8.21	17.29	0.60	0.06
M4	1.35	43.09	31.92	3.97	6.00	8.21	17.29	0.60	0.06
M5	1.35	42.41	31.42	3.97	7.00	8.21	17.29	0.60	0.06
M6	1.35	41.73	30.91	3.97	8.00	8.21	17.29	0.60	0.06

Experimental Process

In this study, the slag sample was first melted at 1300 °C and kept for 30 min and then poured into the prepared iron crucible and cooled to room temperature. The crystal and glass distribution of the fracture were observed. Subsequently, the slag block was ground and passed through a 200-mesh sieve for melting point and phase testing. The melting point of mold powder was measured by hemispherical point method. The hemispherical point of mold powder was measured by CQKJ-II slag melting temperature characteristic tester. Each group of samples was tested three times or more. Three groups of hemispherical point values with a difference of no more than 10 °C were selected, and the average value was taken as the melting point of mold powder.

The crystallization performance of mold flux was tested by an improved full-field high-temperature laser confocal tester (Fig. 1). Firstly, the temperature was raised to 1300 °C according to the preset heating rate and kept for 1 min to ensure that the sample was melted evenly and the gas produced by carbonate decomposition was removed. Subsequently, different cooling rates were set to cool down, and the crystallization process of the slag sample was observed and recorded. The crystallization photos at different times were statistically processed by Adobe Photoshop software, and the ratio of the crystalline pixel to the entire field of view was approximately regarded as the area ratio, which was used as the proportion of the slag crystallization process. In general, when the crystalline area in the slag accounted for 5% that the total field of view, the corresponding temperature was defined as the initial crystallization temperature (T_C) of the mold flux, and when the crystalline area reached 90% of it, the crystallization was considered to be complete.

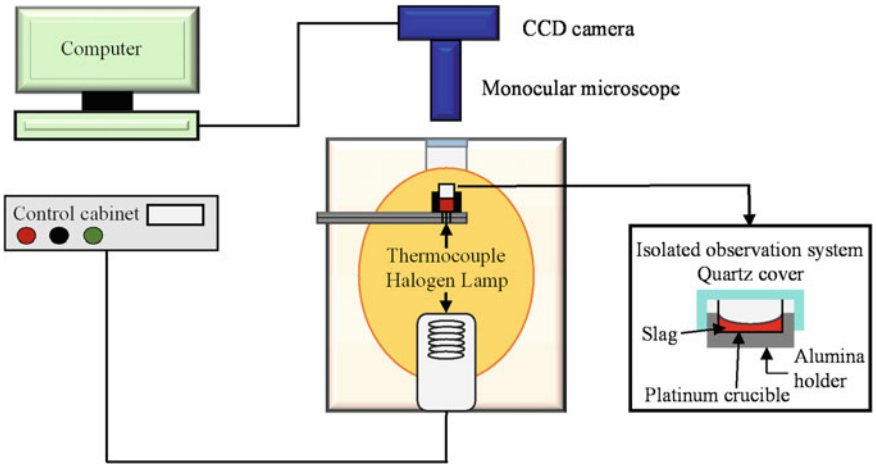

Fig. 1 Schematics of experimental apparatus for crystallization

Results and Discussion

Effect of MgO on Melting and Solidification Properties

Figure 2 shows the cooling section of mold flux with different MgO content. Without MgO, the cooling section was basically a fully crystalline phase. As the MgO content increased from 0 to 6 wt%, the crystallization ratio of the cooling section decreased rapidly from more than 95% to less than 5%, indicating that MgO has a strong effect on inhibiting crystallization. However, as the MgO exceeds 6 wt%, the cross-sectional crystallization ratio increased with the increase of MgO. At the same time, there was an obvious transition zone between the crystal phase and the glass phase (the area between the two dashed lines). In addition, with the MgO increased, the color of the crystal phase in the slag film section gradually changed from light to dark, which may be related to the change of the main precipitated crystal phase in the slag film.

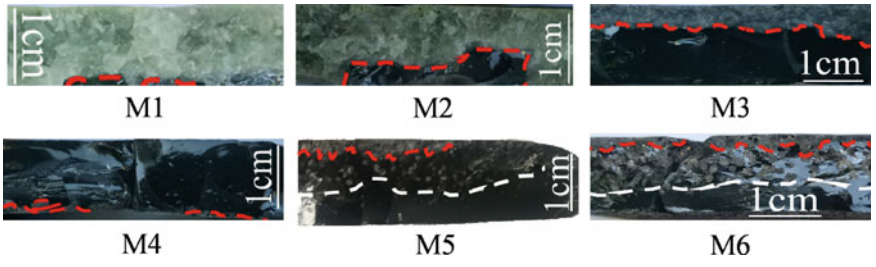

Fig. 2 Effect of MgO on the cooling cross-sectional

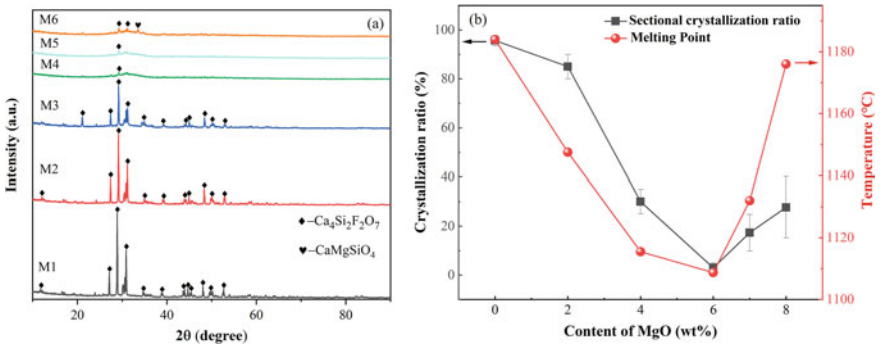

Fig. 3 Effect of MgO on **a** phase, **b** melting point and crystallization ratio

Figure 3a shows the XRD analysis results of the composition of each solid slag film in Fig. 2, and the main mineral phase was cuspidine ($Ca_4Si_2F_2O_7$). With the MgO increased, the peak intensity showed a downward trend. While MgO exceeded 4 wt%, the peak intensity of cuspidine decreased significantly, and the crystallization ability of mold flux was greatly weakened. In addition, a new crystalline phase $CaMgSiO_4$ was detected when the MgO content was 8 wt%, which verified the previous analysis.

The crystalline phase in the mold flux usually had a high melting point, and the melting point of the high-basicity mold flux had a great relationship with the crystallization ratio of the slag film. Therefore, the melting point and crystallization ratio of the mold flux had the same change trend (Fig. 3b). With the increase of MgO from 0 to 6 wt%, the melting point decreased rapidly from 1184 to 1108.7 °C. As the MgO exceeded 6 wt%, the melting point increased with the increase of the cross-sectional crystallization ratio. Especially because of the precipitation of Mg-containing mineral phases in the slag, the melting point increased very rapidly.

Effect of MgO on Crystallization Properties

Figure 4 shows the effect of MgO on the initial crystallization position and crystallization direction of slag. When MgO did not exceed 6 wt%, the slag began to precipitate the crystal phase from one side of the Pt crucible, and then spread to the other side until the slag was completely crystallized. As MgO exceeded 6 wt%, the slag began to crystallize from the edge of the crucible and then crystallized to the middle. At the same time, the crystal began to precipitate in the middle of the crucible and grew rapidly. This was related to the appearance of different crystal phases in the slag

Figure 5 shows the effect of MgO on the T_C and crystallization rate at a cooling rate of 1 °C/s. With the MgO increased, the T_C always maintained a downward trend, while the crystallization rate showed a trend of decreasing first and then increasing, which was consistent with the results reported in the literature [9]. With the increase

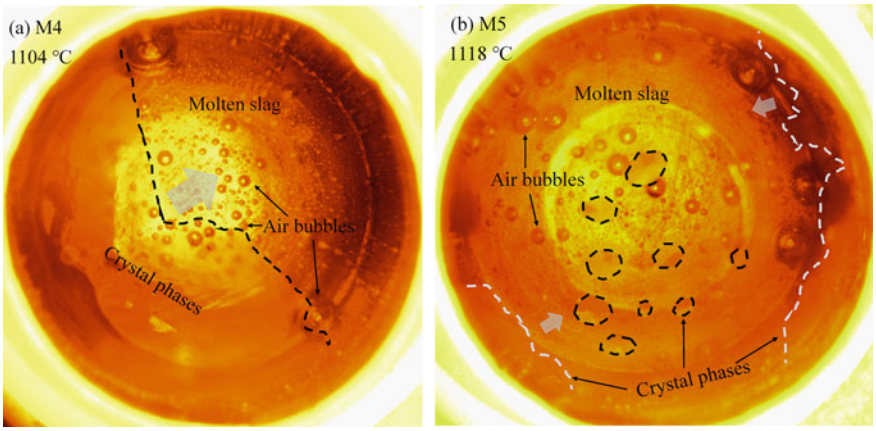

Fig. 4 Effect of MgO on the initial crystallization position and direction

of MgO from 0 to 6 wt%, the crystallization rate of the slag decreased rapidly from 0.021 to 0.0085 s^{-1}. As MgO exceeded 6 wt%, the crystallization rate of the slag increased rapidly and then remained basically unchanged. This again proved that MgO mainly played a role in inhibiting crystallization in the $CaO–SiO_2$-based mold flux.

The effect of MgO on the crystallization properties could be analyzed from two perspectives [10]. On the one hand, the O^{2-} ionized by MgO destroyed the structure of the silicon-oxygen tetrahedral network in the flux, which reduced the degree of polymerization and inhibited crystallization. On the other hand, the small radius of

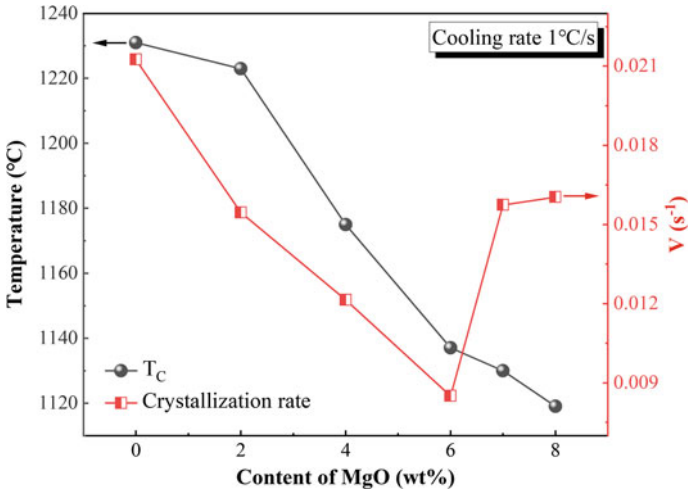

Fig. 5 Effect of MgO on the T_C and crystallization rate

Mg^{2+} had a large electrostatic potential, and it could grab the O^{2-} in the flux to aggregate the silicon-oxygen tetrahedron, causing them to aggregate and increase the polymerization degree of the flux. While MgO was less than 6 wt%, the O^{2-} ionized from MgO destroyed the slag network to form a structure dominated, thereby inhibiting the crystallization of cuspidine. As the MgO exceeded 6 wt%, the effect of Mg^{2+} on improving the degree of polymerization gradually increased, so that the crystallization rate of the slag stopped decreasing and began to rise. Therefore, the effect of MgO on the crystallization properties of mold flux depended on the comprehensive results of the two.

In summary, MgO has the tendency to impede the precipitation of cuspidine and reduce its proportion within slag film, which may weaken the mold flux's ability to regulate heat transfer. In addition, as the MgO content was too high, the high melting point phases containing Mg would precipitate in the slag, which may lead to the deterioration of the lubrication performance. Therefore, to determine the optimal range of MgO content in the mold flux, the actual use effect should be referred. For ultra-wide slab peritectic steel continuous casting, MgO content should not be too high.

Conclusions

In this study, the effect of MgO content on the melting and crystallization properties of high-basicity CaO–SiO_2-based mold flux was studied by controlling the basicity of mold fluxes by single factor variable method. The main conclusions are as follows:

1. MgO had a strong effect on inhibiting crystallization. Therefore, it had a great influence on the crystallization ratio and melting point of the solid slag film.
2. As the MgO was less than 6 wt%, the slag began to crystallize from one side of the crucible edge and spread to the other side. As the MgO exceeded 6 wt%, the crystallization of the slag began almost simultaneously from the edge and the middle of the crucible.
3. With the increase of MgO, the initial crystallization temperature always maintained a downward trend, while the crystallization rate showed a trend of decreasing first and then increasing.

References

1. Zhu LL, Wang Q, Wang QQ, Zhang SD, He SP (2019) In-situ observation of crystallization of mold slag using a digital optical microscope in an infrared furnace. J Am Ceram Soc 102(1):104–108
2. Zhu LL, Wang Q, Zhang SD et al (2017) Volatilisation problems in the measurement of mold fluxes crystallisation by hot thermocouple technique. Ironmaking Steelmaking

3. Madias J, Cicutti C, Castella A et al (1999) Study of breakouts, implementation of a detection system and plant results. Steelmaking Conf Proc 7:51–58
4. Brandaleze E, Gresia GD, Santini L et al (2012) Mold fluxes in the steel continuous casting process
5. Wang H, Tang P, Wen G, Yu X (2010) Effect of MgO on physicochemical properties of non-reactive mold fluxes used for high Al steel. Chin J Process Eng 10(5):905–910
6. Chen J, He F, Zhang B, Xie JL and Liu XQ (2019) Effect of MgO on microstructure and crystalline morphology of mold fluxes in continuous casting. Bull Chin Ceramic Soc 38(2):501–507
7. Silva DR, Vilela ACF, Heck NC, Heller H-P, Volkova O (2018) Solidification behavior of CaO–SiO_2–Al_2O_3 mold fluxes containing MgO and low TiO_2 content using single hot thermocouple technique (SHTT): continuous-cooling-transformation (CCT) and viscosity analysis. Steel Res Int 89(2):8
8. Yang J, Zhang J, Sasaki Y et al (2018) Effect of MgO on crystallization and heat transfer of fluoride-free mold fluxes. Metall and Mater Trans B 49(6):3097–3106
9. Hanao M, Kawamoto M, Watanabe T (2004) Influence of Na_2O on phase relation between mold flux composition and cuspidine. ISIJ Int 44(5):827–835
10. Pang ZD, Lv XW, Yan ZM, Liang D, Dang J (2019) Transition of blast furnace slag from silicate based to aluminate based: electrical conductivity. Metall and Mater Trans B 50:385–394

Study on Solidification Shrinkage Behavior of Beam Blank Based on a High Temperature Strain Model

Zhidan Huang, Xinhua Yang, Leilei Zhang, Mujun Long, and Dengfu Chen

Abstract The solidification shrinkage behavior of beam blank is critical for the mold design. In this study, a three-dimensional high temperature strain model was developed, with which the deformation trends of the Q235 steel 435 mm × 320 mm × 90 mm section beam blank were obtained. The results showed that the complex geometry led to significant differences in shrinkage behaviors in various regions. The maximum deformation occurred at the outer corner of flange reaching 1.9 mm, while the minimum occurred at the web was merely 0.1 mm. Besides, the shrinkage of the narrow face would generate a disturbance on flange-tip causing it to bend outwards to the narrow face. The shrinkage rate at the narrow face and flange gradually increased in the range of 100 mm below meniscus and gradually decreased beyond 100 mm. Results provide fundamental data for the control and improvement of the surface quality of beam blanks.

Keywords Beam blank · Solidification · Q235 · Deformation · Numerical simulation

Introduction

Beam blank is an important variant of the near-final shape continuous casting process. It primarily refers to continuous cast billets with non-standard cross-sectional shapes, excluding regular shapes such as square, slab, round, and rectangular billets. The steel grades produced through the continuous casting of shaped billets mainly include plain carbon steels, low-alloy structural steels, carbon structural steels, structural steels for bridges, and structural steels for shipbuilding. These steel grades, which are categorized by carbon content, often fall within the range of fully killed steel and semi-killed steel which exhibit a significant susceptibility to cracking [1].

Z. Huang · X. Yang · L. Zhang · M. Long · D. Chen (✉)
Laboratory of Materials and Metallurgy, College of Materials Science and Engineering, Chongqing University, Chongqing 400044, China
e-mail: chendfu@cqu.edu.cn

S. Wagstaff et al. (eds.), *Materials Processing Fundamentals 2024*, The Minerals, Metals & Materials Series, https://doi.org/10.1007/978-3-031-50184-5_10

Compared to traditional section cast billets, beam blanks have more boundary variations, including eight convex corners (flange angles), four concave corners (R corner), and twelve independent straight segments. Beam blanks have a larger specific surface area, which improves heat dissipation during the continuous casting process and results in faster cooling of the billet [2]. Additionally, the unique shape of the molten pool and the presence of more angular regions in beam blanks lead to non-uniform steel flow patterns and cooling conditions on the solidified shell surface inside the mold, making it more prone to surface cracks [3]. Therefore, to ensure high-quality final products, it is essential to focus on the uniform temperature distribution along the billet section and the uniformity of the solidified shell throughout the solidification process [4]. The design of the mold for beam blanks directly determines the uniformity of internal shell solidification during cooling. The solidification and contraction behavior of the billet inside the mold plays a crucial role in optimizing the mold design and are particularly important for improving the quality of beam blank products [5].

Due to the difficulty of directly measuring the solidification behavior inside the mold during the production process, this study employs a high temperature strain mathematical model for beam blank. It comprehensively analyzes the shrinkage behaviors and characteristics of the solidified shell, laying a theoretical foundation for optimizing the heat transfer behavior during the continuous casting process of beam blank and obtaining high-quality beam blank products.

Modeling Methods

This study employs a high temperature strain model for the molten steel inside the mold of beam blanks to obtain temperature field distribution and solidified shell distribution. It conducts research on the strain behavior of the solidifying shell based on the flow and heat transfer behavior.

Geometric Model

This study neglects the curvature of the CC machine and establishes a 1/4 model based on symmetry. In order to consider the influence of the second cooling zones on the solidification of the billet inside the mold, the length of the molten steel portion in the casting direction is 1.5 m. The cross-sectional dimensions of the mold are 443.0 $\times$ 328.5 $\times$ 92.0 mm.The main parameters used in the model are shown in Table 1.

Table 1 Properties and conditions of the simulations

Parameter	Value
Casting speed (m/min)	1.2
Mold length (mm)	800
Effective mold length (mm)	700
SEN inner diameter (mm)	30
SEN thickness (mm)	10
Grid size (mm)	5
Superheat (°C)	25
SEN submergence depth (mm)	70

Basic Assumptions and Governing Equations

In the present investigation, several assumptions are made in the numerical model to simplify the analysis and facilitate the study of specific phenomena. These assumptions include:

(1) The billet is treated as a continuous medium. (2) The billet material is assumed to be isotropic and uniform, with nonlinear mechanical properties. (3) The melting heat absorption of the slag on the upper part of the meniscus is neglected. (4) The influence of vibrations in the mold on the heat transfer process is neglected. (5) The metal material follows the Von Mises yield criterion [6].

The governing equations for mass and momentum conservation can be expressed as:

$$\nabla \cdot (\rho \vec{v}) = 0 \tag{1}$$

$$\rho \frac{\partial\left(\vec{V}\right)}{\partial t} + \rho\left[\vec{V} \cdot \nabla\right]\vec{V} = -\nabla P + \nabla \cdot \left[\mu_{\text{eff}}\left(\nabla \vec{V} + (\nabla \vec{V})^{\text{T}}\right)\right] + \rho g \tag{2}$$

$$\mu_{\text{eff}} = \mu + \mu_t \tag{3}$$

$$\mu_t = \rho c_\mu \frac{k^2}{\varepsilon}. \tag{4}$$

The turbulence equation can be expressed as:

$$\frac{\partial(\rho k u_i)}{\partial x_i} = \frac{\partial}{\partial x_i}\left[\left(\mu + \frac{\mu_t}{\sigma_k}\right)\frac{\partial k}{\partial x_i}\right] + G_k - \rho\varepsilon \tag{5}$$

$$\frac{\partial(\rho \varepsilon u_i)}{\partial x_i} = \frac{\partial}{\partial x_i}\left[\left(\mu + \frac{\mu_\varepsilon}{\sigma_\varepsilon}\right)\frac{\partial \varepsilon}{\partial x_\varepsilon}\right] + \frac{C_{1\varepsilon}}{k} G_k - C_{2\varepsilon}\rho\frac{\varepsilon^2}{k}. \tag{6}$$

The energy equation can be expressed as:

$$\frac{\partial}{\partial t}(\rho T) + \frac{\partial(\rho u_i T)}{\partial x_i} = \frac{\partial}{\partial x_i}\left[\Gamma_{\text{eff}}\frac{\partial T}{\partial x_i}\right] + S_r. \tag{7}$$

The plastic behavior equation can be expressed as [7]:

$$d\varepsilon_{ij} = d\varepsilon_{ij}^{e} + d\varepsilon_{ij}^{P} + d\varepsilon_{ij}^{T}. \tag{8}$$

Boundary Conditions and Material Properties

The SEN is set as velocity inlet, and the turbulent kinetic energy k and turbulent kinetic energy dissipation rate ε are calculated using Eqs. (9) and (10), respectively [8].

$$k = 0.01v^2 \tag{9}$$

$$\varepsilon = 2k^{1.5}/D. \tag{10}$$

The thermal boundary conditions for heat transfer on the surface of the mold can be specified by the heat flux. The expression for the heat flux applied in the model for the mold is given as [9]:

$$q = \alpha - \beta\sqrt{L/v}. \tag{11}$$

The heat transfer process on the surface of the billet in the secondary cooling zones is described by the heat transfer coefficient, h [10]:

$$q = h(\phi_b - \phi_w). \tag{12}$$

The physical parameters used are as shown in Table 2 [11–13].

Results and Discussion

Analysis of Solidification Shell Distribution

The distribution of the solidified shell obtained from the simulation is shown in Fig. 1. The circumferential distribution of the solidified shell at a distance of 500 mm below the meniscus is extracted and displayed in Fig. 2, where A represents the midpoint of

Table 2 Physical properties

Parameter	Value
Density (kg/m^3)	$(7.81324 - 3.4421 \times 10^{-4}) \times t) \times 1000$
Specific heat (J/kg °C)	$(0.108498 + 4.882 \times 10^{-5}) \times t) \times 4184$
Thermal conductivity (W/m °C)	$(0.55950 - 1.6500 \times 10^{-4}) \times t) \times 100$
Latent heat of solidification (kJ/kg)	264.5
Liquidus temperature (°C)	1517
Solidus temperature (°C)	1450
Viscosity (kg/m s)	0.0067
Young's modulus (MPa)	$986 - 2.33T + 1.9 \times 10^{-3}T - 5.18 \times 10^{-7}T^3$
Poisson's ratio	0.33
Coefficient of thermal expansion	1.395×10^{-5}

the web, B represents the midpoint of the R corner, C represents the inner corner of the flange, D represents the outer corner of the flange, and E represents the midpoint of the narrow side. Comparing the circumferential distribution of the solidified shell at a distance of 500 mm below the curved surface with the actual industrial data measured in the literature [12], simulation results are in agreement with the measured values of the shell thickness distribution.

At point D, which is the flange outer corner, the simulated solidified shell is the thickest in the circumferential direction, reaching a maximum of 24 mm. At point C, which is the inner corner of the flange tip, the thickness of the solidified shell is less than that at the outer flange corner D. This is because the angle at point D is a

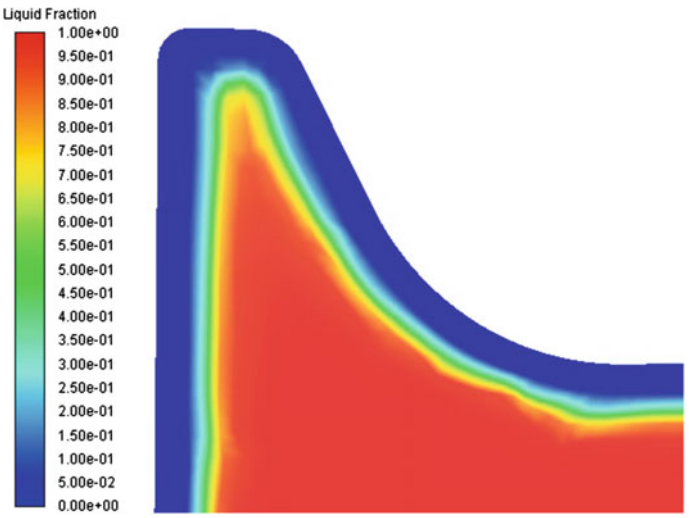

Fig. 1 Contour of liquid fraction of beam blank

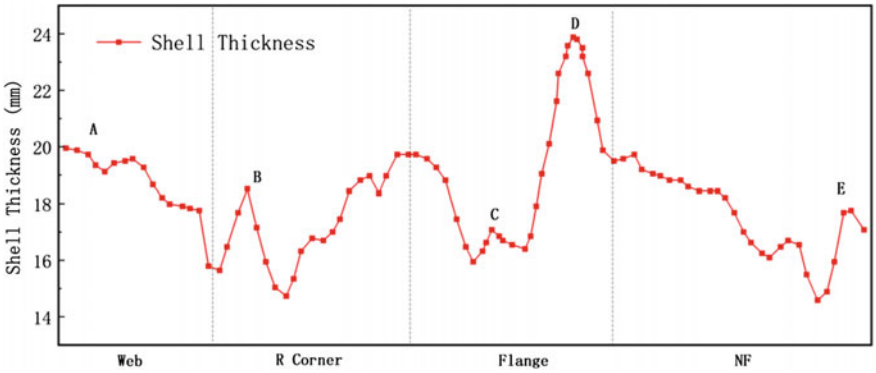

Fig. 2 Circumferential pattern of solidified shell

right angle, while the angle at point C is obtuse, giving the point D a longer effective heat transfer boundary. Additionally, the position of point D is subjected to cooling from both the wide side and narrow side water slots in the mold, whereas point C is only cooled by the wide side water gap. The remaining areas of the shell have relatively uniform thicknesses ranging from 15 to 20 mm. The thinnest locations occur at the R corner and the narrow side endpoint. This is because the R corner has an obtuse angle, resulting in concentrated heat flow that is difficult to dissipate, and the midpoint of the narrow side is impacted by the steel jet from the SEN, causing slower growth of the shell compared to other regions.

Analysis of Solidification Shell Deformation Behaviors

Due to the complex geometry of the beam blank, the solidification process varies in different regions. To further investigate the shrinkage behavior of different regions during the solidification process, this study analyzed the deformation characteristics at 12 characteristic points on the beam blank surface. The numbering and locations of the characteristic points are shown in Fig. 3.

Figure 4 shows the shrinkage of each characteristic point on the narrow face of the beam blank. Within the range of 0–100 mm from the meniscus, the billet experiences the highest shrinkage rate. Subsequently, as the solidifying shell thickness increases and the shell temperature decreases, the deformation of the shell continues to increase. Among the different characteristic points, the points closer to the flange corner exhibit greater shrinkage. This corresponds to the thicker solidified shell near the flange corner. Additionally, near the vicinity of the mold outlet, the displacement along the X direction decreases for characteristic point 3#. This is due to an outward bending disturbance caused by increased shrinkage in the Y direction of the solidified shell, resulting in curvature of the flange tip towards the outer side of the narrow face, thereby offsetting some X direction displacement.

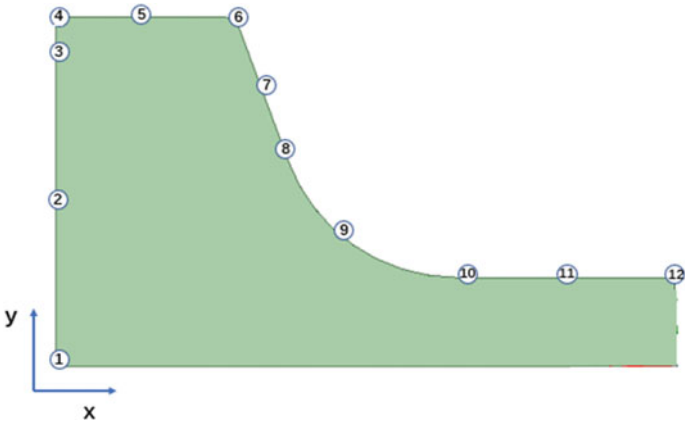

Fig. 3 Positions of various characteristic points on the beam blank

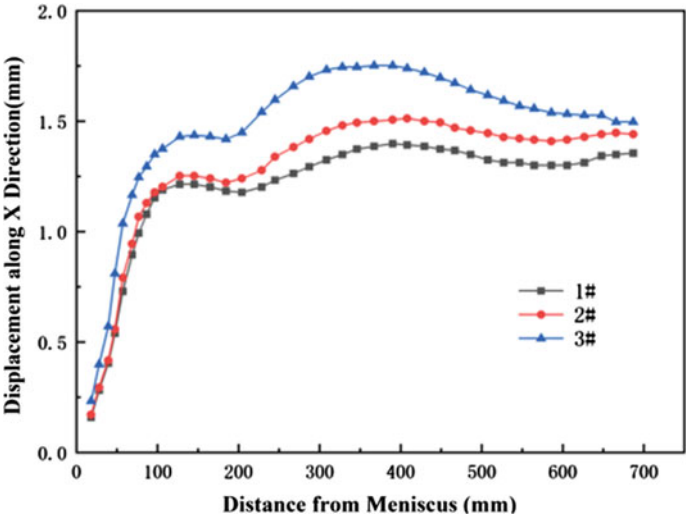

Fig. 4 Displacement of positions in the narrow face

Figure 5 illustrates the shrinkage in the Y direction of each characteristic point at the flange tip. As depicted in Fig. 5, the billet exhibits a higher shrinkage rate within 0–100 mm below the meniscus, and the shrinkage rate slows down after 100 mm. At the mold outlet, the characteristic point 4#, which is closer to the flange outer corner, experiences the largest shrinkage of up to 2 mm. The next is the center point 5# at the flange tip, while the flange inner corner point 6 shows the smallest shrinkage. This pattern does not align with the circumferential distribution of the solidified shell as indicated in the previous section, where the sequence of shell thickness goes as 4# > 6# > 5#. Hence, it can be concluded that in the complex cross-sectional structure of

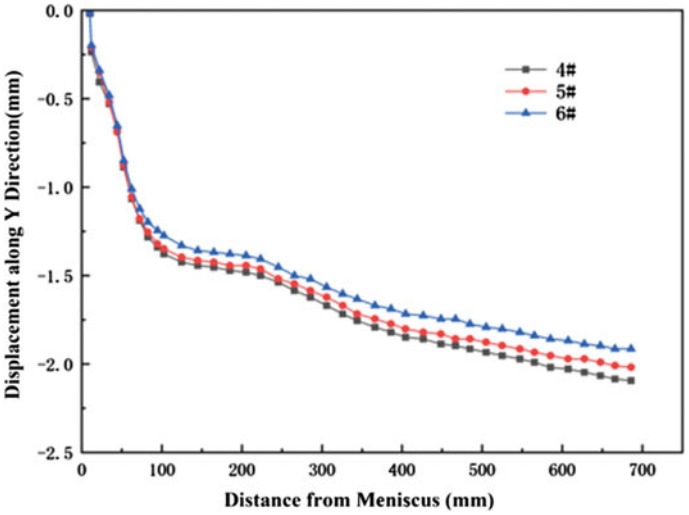

Fig. 5 Displacement of the positions in flange tip

the beam blank, the shrinkage level of a specific region cannot be solely determined based on the shell thickness.

Figure 6 presents the displacement of characteristic points on the inner side and R corner of the billet. Due to the presence of an inclined surface on the inner side of the flange, the displacement of the billet is decomposed into two directions for comparison. The displacement in the X direction is similar among the characteristic points, with the maximum displacement occurring at point 8#, reaching 1.5 mm. However, there is a significant difference in the Y direction displacement. In point 7#, there is almost no shrinkage displacement in the Y direction, while at point 8#, the maximum displacement in the Y direction reaches 1 mm. The shrinkage in the Y direction of the billet is smaller compared to the X direction. At the mold outlet, the maximum displacement in the Y direction is merely 0.6 mm, whereas it reaches a maximum of 1.5 mm in the X direction. Additionally, a transition point of the billet's shrinkage rate, similar to the narrow side and the flange tip, is observed in the vicinity of 100 mm below the meniscus.

Figure 7 displays the deformation of the billet's web in the Y direction. There is a more fluctuating pattern of shell shrinkage observed on the web. These fluctuations are the result of the combined effects of the deformation due to the R corner, the traction from the solidified shell, the hydrostatic pressure of the molten steel, and the gradually increasing thickness of the solidified shell. In the distance range of 0–400 mm from the meniscus, the traction force and the hydrostatic pressure of the molten steel cause a positive displacement in the Y direction on the web. Below 400 mm from the meniscus, as the solidified shell thickness increases and becomes capable of supporting the hydrostatic pressure of the molten steel, the shell surface undergoes deformation in the negative Y direction.

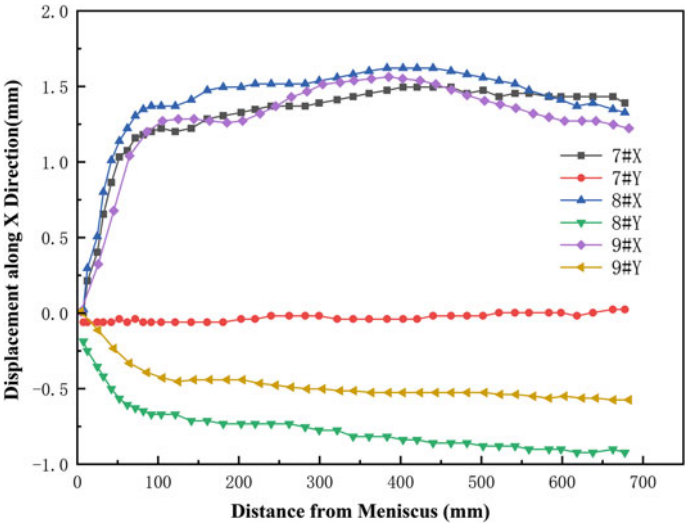

Fig. 6 Displacement of positions in flange

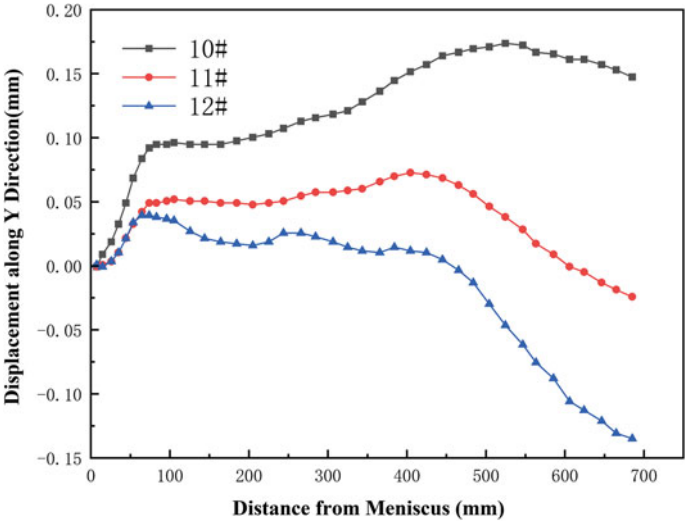

Fig. 7 Displacement of positions in the web

Conclusions

This study developed a high temperature strain model for beam blank inside the mold and obtained the deformation characteristics at various positions of a Q235 steel billet with a cross-section of 435 mm × 320 mm × 90 mm. The study investigated the

billet deformation characteristics considering 3D forced flow in the solidified shell and concluded the following:

(1) The solidified shell at the outer corner of the flange is the thickest in the circumferential direction, reaching a maximum thickness of 24 mm. The thinnest sections occur at the R corner and the midpoint of the narrow face. This is because the outer corner of the wingtip experiences simultaneous cooling from the wide and narrow sides of the mold, while the R corner has an obtuse angle and the midpoint of the narrow face is influenced by the SEN jet flow, leading to a more concentrated heat flow in these two regions. The shell thickness in the remaining areas is relatively uniform, ranging from 15 to 20 mm.
(2) Due to the complex geometry of the beam blank, there are significant differences in the shrinkage behavior at different characteristic points. At the flange tip, where it experiences heat transfer from three sides, exhibits the largest amount of solidification shrinkage, reaching a maximum displacement of 2 mm. On the other hand, the center of the web undergoes the least amount of shrinkage, with a displacement value of only 0.1 mm.
(3) The characteristic points on the billet, except for the web, exhibit a relatively rapid shrinkage rate within a range of 100 mm below the meniscus. After 100 mm, the shrinkage rate begins to slow down. Due to the hydrostatic pressure from the molten steel, the web starts to show minimal displacement below 400 mm from the meniscus.

Acknowledgements The authors gratefully acknowledge the financial support provided by the National Natural Science Foundation of China, projects No. 52274320 and 52074053.

References

1. Yang G, Zhu L, Chen W, Yu X, Guo G (2019) Propagation of surface cracks on beam blank in the mold during continuous casting. Ironmaking Steelmaking 46:809–818
2. Chen W (2008) Thermomechanical analysis and optimisation for beam blank continuous casting. Ironmaking Steelmaking 35:129–136
3. Yang G, Zhu L, Chen W, Guo G, He B (2018) Simulation of crack initiation and propagation in the crystals of a beam blank. Metals 8:905
4. Santis MD, Cristallini A, Rinaldi M, Sgrò A (2014) Modelling-based innovative feeding strategy for beam blanks mold casting aimed at as-cast surface quality improvement. ISIJ Int 54:496–503
5. Chen W (2019) Mold taper optimization for continuous casting of H-beam blanks. Metall Res Technol 116:505
6. Chen W (2012) Three-dimensional FEM study of fluid flow in mold for beam blank continuous casting: influence of straight through conduit type SEN. Ironmaking Steelmaking
7. Luo W, Yan B, Lu X, Wen G (2013) Improvement of water slot design for beam blank casting mold. Ironmaking Steelmaking 40:582–589
8. Sheng D, Jonsson L (1999) Investigation of transient fluid flow and heat transfer in a continuous casting tundish by numerical analysis verified with nonisothermal water model experiments. Metall Mater Trans B 30:979–985

9. Yun C, Zhang J (2021) Development and application of a dynamic secondary cooling control model for beam blanks based on finite element method. Chin J Eng 33:418–422
10. Zhao Y, Chen DF, Long MJ, Shen J, Qin R (2014) Two-dimensional heat transfer model for secondary cooling of continuously cast beam blanks. Ironmaking Steelmaking 41:377–386
11. Ha J, Cho J, Lee B, Ha M (2001) Numerical analysis of secondary cooling and bulging in the continuous casting of slabs. J Mater Process Technol 113:257–261
12. Koric S (2006) Efficient thermo-mechanical model for solidification processes and its applications in steel continuous casting. Int J Numer Methods Eng 66:1955–1989
13. Jiao M, Xie Z, Jia G (2008) Applying of real-time heat transfer and solidification model on the dynamic control system of billet continuous casting. ISIJ Int 48:1722–1727

In-Situ Observation of Melting and Solidification Process of CuCr Alloy by High Temperature Confocal Microscope

Jin-Ru Han, Zhi-He Dou, and Ting-An Zhang

Abstract In this paper, the melting process of CuCr alloy is observed in-situ by high temperature confocal microscope, followed by process solidification at a solidification rate of 1 °C/s. It is found that the melting process of CuCr alloy is mainly divided into two steps: the first step is the complete melting of Cu-rich phase matrix, and the second step is that Cr phase is gradually dissolved in molten Cu matrix. The solidification process of CuCr alloy can be divided into three stages: initial solidification stage, stable solidification stage, and final solidification stage. The temperature range of stable solidification stage is 1400 °C–1250 °C, at which time the solidification rate of the alloy is the fastest, and the solidification structure with uniform distribution of Cr-rich phase is obtained. Finally, the model of CuCr alloy is firstly established by Materials studio based on heterostructure theory.

Keywords CuCr alloy · High temperature confocal microscope · Melting and solidification · Heterostructure

Introduction

The process of liquid phase separation and the mechanism of second phase coarsening are some of the key points in the study of immiscible alloys. As an immiscible alloy, the process of two-phase separation of CuCr alloy can be summarized as three stages (as shown in Fig. 1): the first stage is the nucleation of a small amount of Cr phase. In the second stage, nuclei grow up by various means of material transport (diffusion, Ostwald maturation, Marangoni motion, convection) and coarsen by collision and aggregation between nuclei. In the third stage, when Cr particles reach a certain size, under the action of the density difference between Cu and Cr components and

J.-R. Han · Z.-H. Dou (✉) · T.-A. Zhang
Key Laboratory of Ecological Metallurgy of Multi-metal Intergrowth Ores of Ministry of Education, Northern University, Shenyang 110819, Liaoning, China
e-mail: douzh@smm.neu.edu.cn

School of Metallurgy, Northern University, Shenyang 110819, Liaoning, China

S. Wagstaff et al. (eds.), *Materials Processing Fundamentals 2024*, The Minerals, Metals & Materials Series, https://doi.org/10.1007/978-3-031-50184-5_11

Marangoni motion, the second phase droplets begin to deposit or float, and the smaller droplets are continuously captured during the motion, that is, gravity coagulation and Marangoni coagulation occur, which eventually leads to the stratification of the melt [1]. At the same stage, many coarsening mechanisms work at the same time, especially the Marangoni motion of the second phase droplets in microgravity [2]. Therefore, the segregation of the Cr phase depends on its kinetic processes such as growth, collision, coarsening, settling or uplift, whereas when there is a temperature gradient in the melt, the second phase droplets undergo a Marangoni motion from the cold end to the hot end, and thus if the cooling rate is sufficiently fast that the alloy solidifies through the immiscible zone very quickly without the second phase having enough time to undergo coarsening and deposition, the CuCr alloys with a diffuse distribution of the Cr phase can be obtained.

The preparation technology of homogeneous immiscible alloys has always been the research hotspot and difficulty of immiscible alloys. The industrial preparation methods of CuCr alloys include powder metallurgy, infiltration, and vacuum consumable melting [3–5], but powder metallurgy mostly adopts solid phase sintering and does not involve the solidification process of liquid phase, whereas the infiltration method firstly sintered the Cr powder to the skeleton, and therefore does not involve the process of solidification of the second phase either.

Zhang has put forward a new idea of preparing large-size homogeneous CuCr immiscible alloy based on aluminothermic reduction, that is, firstly, copper oxide and chromium oxide are used as raw materials, and the miscible high temperature CuCr melt is obtained by aluminothermic self-propagation, at which time the theoretical adiabatic temperature can reach 2848 K, and then refined under the high-frequency magnetic field and subsequent solidification [6–9], so it is a liquid solidification

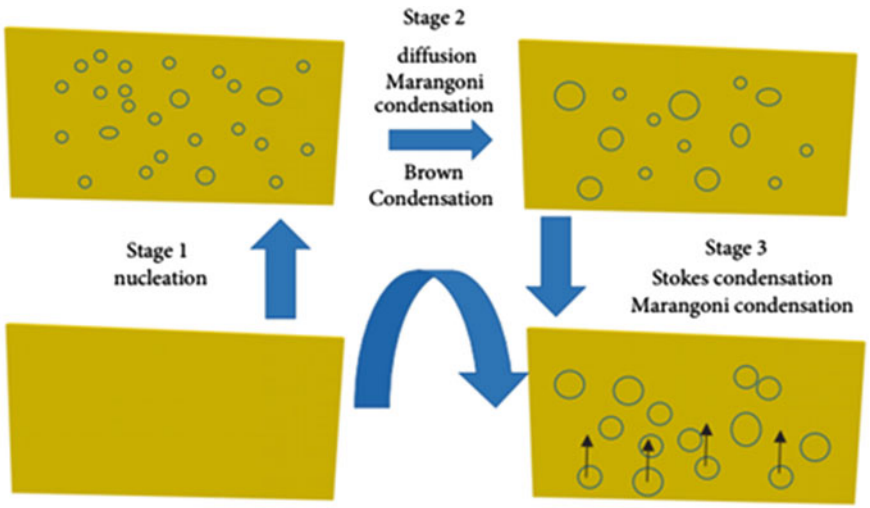

Fig. 1 Process of two-phase separation of CuCr alloy [1]

process, but the characterization of the actual solidification process of CuCr alloy is rarely mentioned at present. The heating furnace in the high temperature confocal microscope has good temperature control ability, with the heating rate ranging from 0 °C/s to 30 °C/s and the cooling rate ranging from 0 °C/s to 100 °C/s, which can accurately control the cooling rate of its samples [10, 11], which lays a foundation for the characterization of the solidification process of CuCr alloy. Therefore, the melting and solidification process of CuCr alloy is observed by high temperature confocal microscope, and the solidification curve is fitted to analyze the microstructure of CuCr alloy after solidification.

Experiment

The CuCr alloy used in this study is prepared by aluminothermic reduction-induction melting. Aluminothermic reduction is based on CuO, Cr_2O_3 as raw materials, Al as reducing agent, and add CaO as slagging agent, $KClO_3$ as heat generator, through the reduction reaction quickly obtained CuCr alloy melt, and the generation of by-products of Al_2O_3 leads to the solidification of the as-cast alloy internal holes and inclusions, so the induction refining is in order to strengthen the effect of slag-alloy separation, to solve the internal defects of the alloy, aluminothermic reduction and induction refining of the process flow is shown in Fig. 2. The chemical composition (mass fraction, %) of CuCr alloy is listed in Table 1. The sample is machined into a cylindrical shape (7 mm in diameter and 3 mm in height). Before in-situ observation, the sample is polished and placed in an alumina crucible, which is placed in the heating position of a metallurgical furnace with thermocouples. After evacuating the gas in the furnace with a vacuum pump, ultra-pure argon (99.99%) is continuously blown into the furnace to avoid oxidation of the sample surface.

The purpose of this study is to explore the melting and solidification process of CuCr alloy, so the phase diagram of CuCr alloy (as shown in Fig. 2) is analyzed. When the content of Cr in the CuCr alloy is 25.6%, CuCr25 alloy belongs to hyper-eutectic alloy, the melting point of the CuCr25 alloy is about 1600 °C, and there is no immiscible zone between two liquid phases in the solidification process. Thus the solidification process of the CuCr25 alloy starts with the transformation of $L \rightarrow Cr + L_{Cu}$, that is, the primary crystal Cr crystallizes from the Cr-rich liquid phase, and the liquid phase transforms to Cu-rich phase. If the solidification rate is slow, it will easily lead to alloy segregation phenomenon, so it is beneficial to obtain homogeneous CuCr alloy if the rapid solidification technology can be applied to the solidification process of CuCr alloy [12, 13]. Therefore, the CuCr25 sample is heated to 1640 °C within 672 s by high temperature confocal, kept at 1640 °C for 30 s, then cooled to about 1100 °C at a solidification rate of 1 °C/s, and the furnace power supply is turned off at 1100 °C to cool the sample to room temperature. The heating and solidification process curve is shown in Figs. 3 and 4.

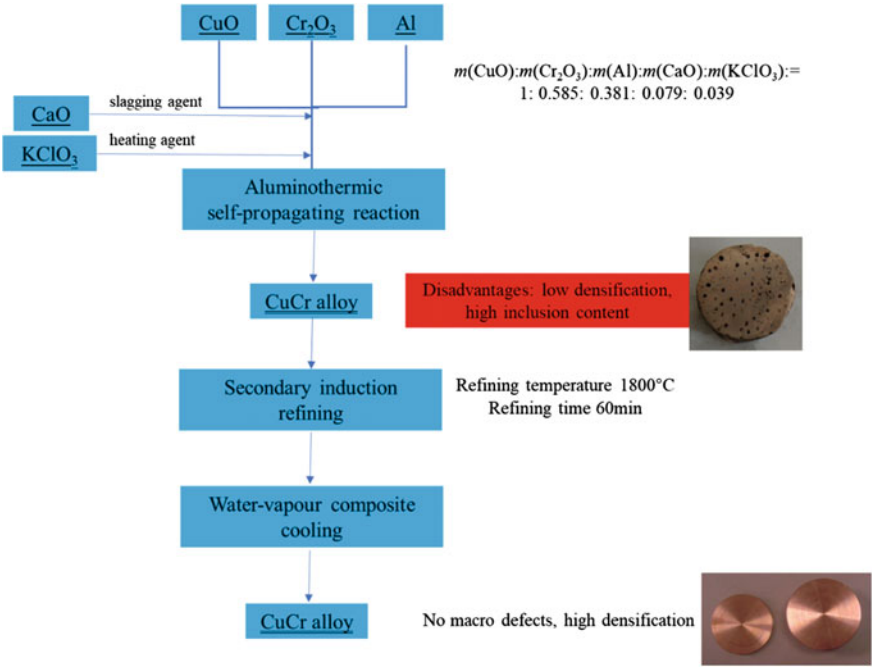

Fig. 2 The process flow of aluminothermic reduction-induction refining

Table 1 Composition of CuCr alloy prepared by aluminothermic reduction-induction refining

Sample	Cu%	Cr%	Al%
CuCr25	Bal	25.6	0.23

Results and Discussion

High Temperature Confocal In-Situ Observation of Melting Process of CuCr Alloy

Figure 5 shows the melting process of CuCr alloy observed in-situ by high temperature confocal microscope. When the temperature reaches 1177.1 °C, it is observed that the Cu matrix begins to melt, and when the temperature gradually rises to 1397.4 °C, it can be observed that the Cu-rich matrix melts completely, and the Cr phase exists in the initial state. With the temperature rising further, but not reaching the melting point of the alloy, the Cr phase has begun to dissolve in the Cu matrix gradually, with the proportion of Cr phases gradually decreases, and when the temperature rises to 1640.3 °C, it has completely appeared in the state of melt. Therefore, by observing the melting process of CuCr alloy in-situ, it is determined that the melting

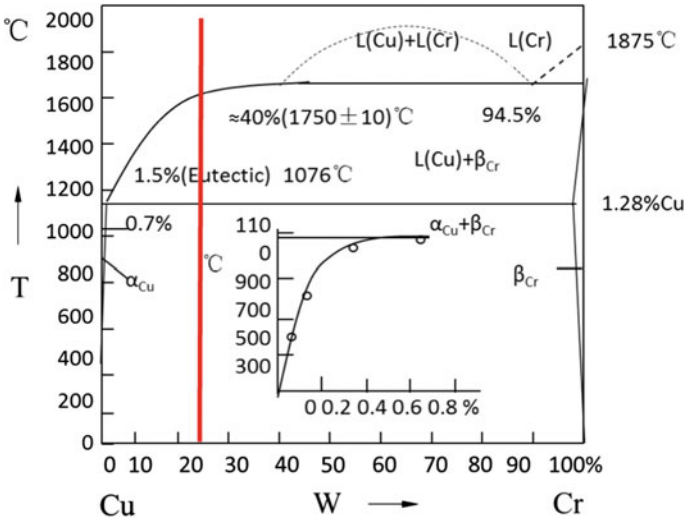

Fig. 3 Binary phase diagram of CuCr alloy

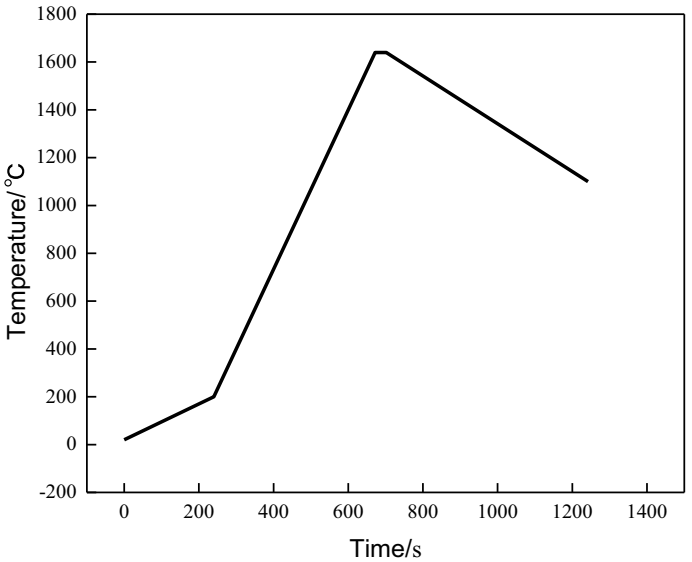

Fig. 4 Curve of heating and cooling process system of high temperature confocal microscope

process is mainly divided into two steps: The first step: Melting of Cu-rich matrix, when Cr phase exists alone; The second step: With the increase of temperature, Cr phase dissolves gradually in Cu matrix, and finally homogeneous alloy melt is obtained.

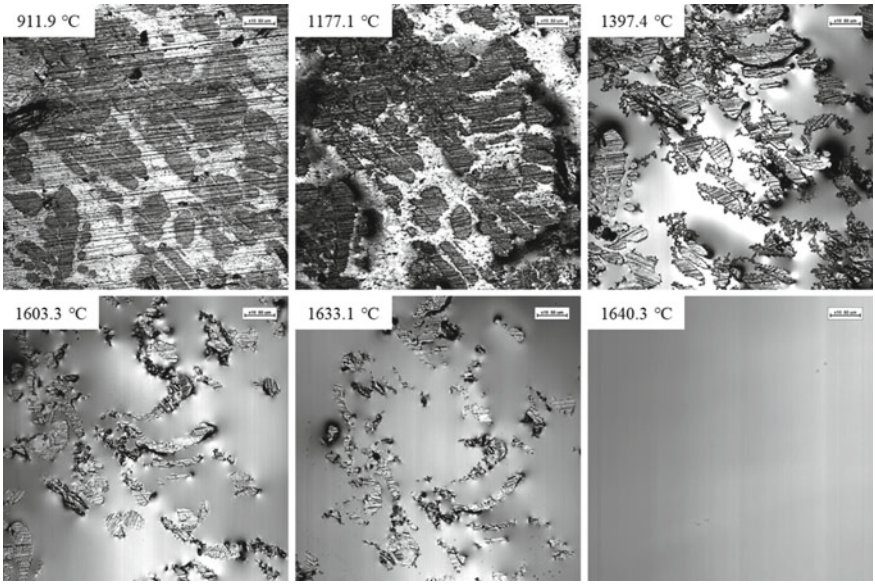

Fig. 5 In-situ observation of the melting process of CuCr alloy by high temperature confocal microscope

High Temperature Confocal In-Situ Observation of the Solidification Process of CuCr Alloy

Figure 6 shows the solidification process of CuCr25 alloy observed in-situ by high temperature confocal microscope, and the solidification rate of the alloy is 1 °C/s. It can be found from the figure that the initial solidification of CuCr25 alloy is found at 1550.2 °C. With the further decrease of temperature, the early solidified Cr phase nucleates and grows gradually. The growth of Cr-rich phase is completed at 1400.4 °C, because the Cr-rich phase is closer to a bright grain. In the subsequent solidification process, there are black areas wrapping bright Cr-rich phase. With the decrease of temperature, the liquid phase gradually decreases and the black solidification area increases, and the liquid phase in the alloy disappears completely at 1030 °C. At this time, after observing the solidified structure, it is inferred that the bright area is Cr-rich phase and the black area is Cu-rich phase. The microstructure of CuCr alloy after solidification is found to be 25.1~26.2% of the Cr phase area, combined with the liquid phase fraction in Fig. 6, it is found to verify this conjecture, which indicates that after the solidification of CuCr alloy, after the nucleation and growth of the Cr-rich phase, the Cr-rich phase edges of the Cu melt solidifies first, to achieve the wrapping of the Cr-rich phase. This is conducive to the inhibition of the growth and growth of the Cr-rich phase with the further reduction of the temperature until the Cu melt is completely solidified.

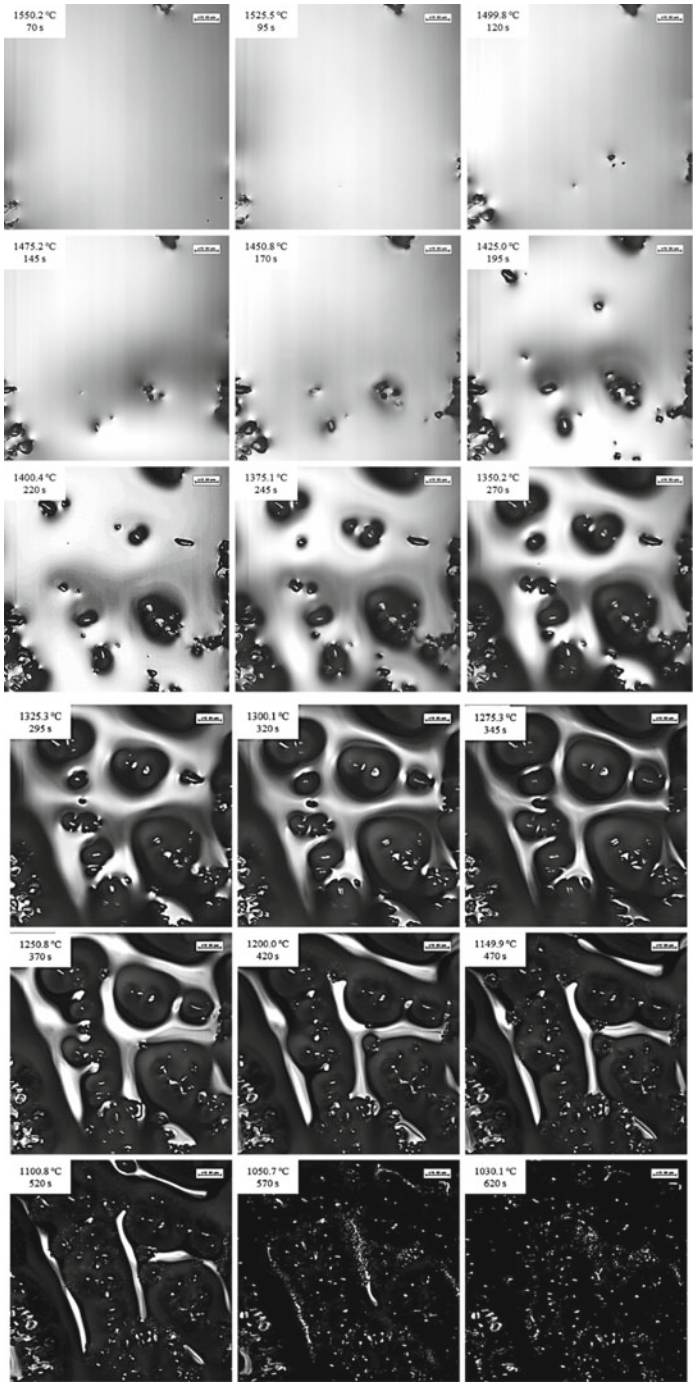

Fig. 6 In-situ observation of solidification process and solidification structure of CuCr alloy by high temperature confocal microscope

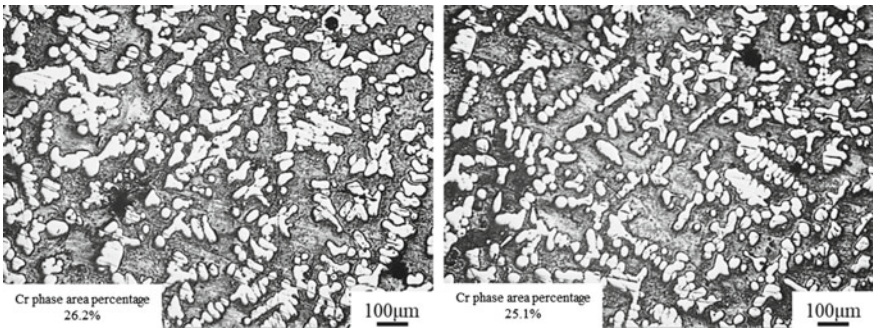

Fig. 6 (continued)

Figure 7 shows the relationship between liquid phase fraction and temperature during solidification of CuCr alloy. From the relationship between liquid fraction and solidification temperature, it is found that the solidification process can be divided into three stages: initial solidification stage, stable solidification stage, and final solidification stage. The temperature interval of the initial solidification stage is 1600 °C–1400°C, which is supposed to be the stage of Cr phase nucleation, and the temperature interval of the stable solidification stage is 1400–1250°C, which occurs the growth of the Cr phase and the solidification of the Cu matrix at the edge after the growth of the Cr phase, and at this time, the solidified Cu phase wraps around the Cr-rich phase, and the temperature interval of the final solidification stage is 1250–1030 °C, which should be all the solidification of the Cu substrate.

The fitted liquid fraction (f_L) as a function of temperature (T °C) [14]:

$$f_L = 1 - \frac{0.97}{1 + \exp(\frac{T-1323.1}{50.1})} \tag{1}$$

Crystal Structure Characterization of CuCr Alloy

Zhou [15] clearly pointed out that monotectic alloys are heterostructures, so CuCr alloys are also typical heterostructures. According to the theory of heterostructure, the structure model of CuCr alloy was established for the first time by Materials studio, as shown in Fig. 8. The specific steps include the introduction of Cu and Cr crystal model, the tangent surface of (100) plane of Cu and Cr crystal, and the cell expansion according to the lattice constant, and finally the crystal layer is constructed.

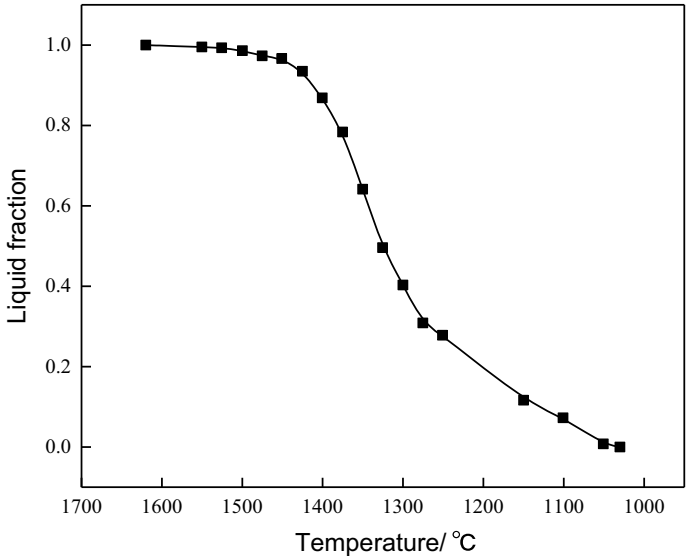

Fig. 7 Liquid phase fraction of solidification process of CuCr alloy

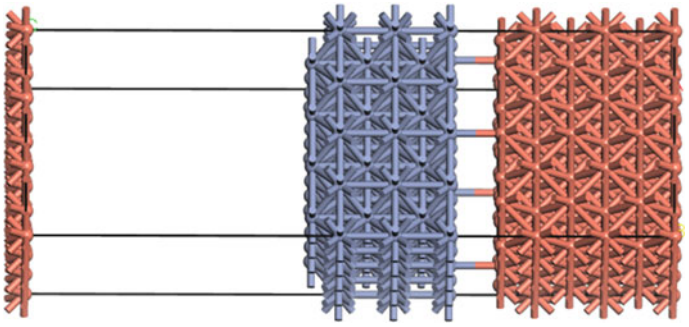

Fig. 8 Structural model of CuCr alloy established by materials studio

Conclusion

(1) The melting process of CuCr alloy is observed by high temperature confocal microscope. It is found that with the increase of temperature, the melting process of CuCr alloy was mainly divided into two steps. The first step is the melting of Cu-rich matrix, in which Cr phase existed alone; The second step is the gradual dissolution of Cr phase in Cu matrix with the increase of temperature, and finally the homogeneous alloy melt is obtained.

(2) The solidification process of CuCr alloy can be divided into three stages: initial solidification stage, stable solidification stage, and final solidification stage. The temperature range of stable solidification stage is 1400–1250 °C, and the solidification rate of the alloy is the fastest. Finally, the solidification curve of CuCr alloy is fitted, and the heterostructure model of CuCr alloy is established.

References

1. Han JR, Dou ZH, Zhang TA, An W (2022) Progress in the preparation of large-size high-performance CuCr alloys. Adv Mater Sci Eng 2022. https://doi.org/10.1155/2022/1333985
2. Liu S, Jie J, Dong B (2018) Novel insight into evolution mechanism of second liquid-liquid phase separation in metastable immissible Cu-Fe alloy. Mater Des 156:71–81
3. Cao WC, Liang SH, Zhang X (2011) Effect of Fe on microstructures and vacuum arc characteristics of CuCr alloys. Int J Refract Met H 29(2):237–243
4. Cao WC, Liang SH, Zhang X (2011) Effect of Mo addition on microstructure and vacuum arc characteristics of CuCr50 alloy. Vacuum 85(10):943–948
5. Ma YQ, Lin HJ, Song DD (2014) Microstructure evolution and thermal physical properties of CuCr alloy after high pressure treatment. Rare Met 33(3):293–298
6. Han JR, Dou ZH, Zhang TA, An W (2023) Fe microalloying during the in-situ synthesis of homogeneous CuCrFe alloys by aluminothermic Self-propagating. J Mater Res Technol 25:95–106
7. An W, Dou ZH, Han JR, Zhang TA (2022) Microstructure uniformity control of CuCr alloy prepared in-situ by aluminothermic reduction coupled with permanent magnetic stirring. J Alloy Compd 96:170797
8. An W, Dou ZH, Han JR, Zhang TA (2022) Microstructure evolution and property strengthening of CuCr50 prepared by thermite reduction-electromagnetic casting during the heat treatment process. J Mater Res Technol 24:6533–6544
9. Han JR, Dou ZH, Zhang TA, An W (2022) Effect of reduction-slagging coupling of Cr_2O_3 during in-situ preparation of homogenic CuCr50 alloy by self-propagating high temperature synthesis metallurgy. J Mater Res Technol 19:3658–3669
10. Shen Y, Wang C (2019) In Situ observation of martensite lath growth behaviors in the coarse grained heat-affected zone of 12.5Cr-0.5Mo heat-resistant steel during simulated welding. Metall Mater Trans A 50(11):4955–4960
11. Zou X, Sun J, Matsuura H (2018) In Situ Observation of the nucleation and growth of ferrite laths in the heat-affected zone of EH36-Mg shipbuilding steel subjected to different heat inputs. Metall Mater Trans B 49(5):2168–2173
12. Xie M, Liu JL, Lu XY (2001) Investigation on the Cu-Cr-RE alloys by rapid solidification. Metall Mater Trans A 304–306:529–533
13. Wang YP, Zhang RL, You YM (2011) Review of the preparation of fine-grain and superfine-grain Cu-Cr alloys via rapid solidification. Gaoya Dianqi/High Voltage Apparatus 47(12):80–85
14. Miao ZJ, Shan AD, Wang W (2011) Solidification process of conventional superalloy by confocal scanning laser microscope. T Nonferr Metal Soc 21:236–242
15. Zhou SF, Xie M, Wu CY (2022) Selective laser melting of bulk immiscible alloy with enhanced strength: heterogeneous microstructure and deformation mechanisms. J Mater Sci Technol 14:81–87

Research on Fluid Flow Characteristics in Converter Tapping Process

Xuan Liu, Anjun Xu, and Fei Yuan

Abstract In the process of converter tapping, the process parameters of the tapping hole are essential for the flow characteristics of molten steel and the tapping time. ANSYS FLUENT19.3 software is used to establish a three-dimensional model of a 200t converter and ladle and investigate the distribution law of molten steel flow field during the tapping process of the converter under different tapping parameters by volume of fluid model. The molten steel flow rate is more uniform and stable, and the turbulence is significantly reduced when the shape of the tapping hole is a segmented variable diameter type, the diameter is 180–160 mm, and the angle to the horizontal direction is 10°, thereby reducing the degree of erosion at the tapping hole. The error between the simulation and the actual tapping time is within 5%, which verifies the accuracy of the model. It provides theoretical support for optimizing the process parameters of the converter tapping hole and studying the temperature drop law of the tapping process.

Keywords Converter tapping · Flow characteristics of molten steel · Tapping hole · Tapping time · Numerical simulation

Introduction

The steel slag separation is realized in the converter tapping process, which can reduce the molten steel pollution caused by the steel slag flowing into the ladle. At the same time, the tapping flow strongly stirs the molten steel in the ladle, which promotes the floating of slag inclusions and deoxidized products, which not only affects the production efficiency of molten steel smelting but also affects the quality of molten steel [1–3].

The tapping time of the converter is an important factor affecting the temperature drop, production efficiency, and production cost of the converter [4, 5]. The tapping

X. Liu · A. Xu (✉) · F. Yuan
School of Metallurgical and Ecological Engineering, University of Science and Technology, Beijing 100083, China
e-mail: anjunxu@126.com

S. Wagstaff et al. (eds.), *Materials Processing Fundamentals 2024*, The Minerals, Metals & Materials Series, https://doi.org/10.1007/978-3-031-50184-5_12

time not only depends on the diameter of the tapping hole but also is closely related to the shape of the tapping hole and its flow field [6]. Due to the high tapping temperature of the converter reaching 1600 °C, it is impossible to study the flow characteristics of molten steel during the tapping process using physical methods. The current research mainly focuses on water modeling and numerical simulation to study the flow characteristics of fluids and optimize process parameters [7–9]. Among them, Zhang et al. [10] found that the steel flow velocity is relatively stable and the tapping time can be shortened when the shape of the inlet of the tapping port is circular by the water model experimental; Li [11] reduced the tap turbulence by changing the diameter of the tapping hole of the 120t converter and increasing the taper of the inner hole of the tapping hole, and the tapping time was shortened to 3.5–5 min, the water model can describe the characteristics of the local model well, but it is difficult to monitor the flow situation of the entire converter tapping process [12–14]. However, computational fluid dynamics (CFD) has been widely applied to multiphase flow in high-temperature metallurgical processes, which can clearly describe the flow state of molten steel. Therefore, numerical simulations are used to study black box operation in high-temperature furnaces, and they play a vital role in the design and operation of metallurgical furnaces [15–17]. Dider [18] studied the flow characteristics of the molten steel in the cylindrical, conical, and segmented variable diameter type tapping hole by numerical simulation: Due to the gradual decrease of the inner diameter of the tap hole of the sectional variable diameter type, the velocity distribution of the molten steel at the end of the tap hole is more uniform. In addition, some scholars [19] indicated that the angle of the tapping hole also affects the dispersion state of molten steel during the tapping process.

In summary, the tapping hole's diameter, shape, and angle are essential for the velocity distribution and tapping time of the tapping process. However, there are few research reports on the influence of tapping process parameters on the distribution of molten steel flow field in the converter tapping process. The present study uses a 200 t converter in a domestic steel plant as an example to investigate the effects of the diameter, shape, and angle of the tapping hole on the flow characteristics of molten steel during the tapping process of the converter through numerical simulations. The numerical simulation results are verified by using the field data.

Numerical Modelling

In this study, ANSYS FLUENT19.3 commercial software is used to investigate the tapping process of the 200t converter by numerical simulation.

Basic Assumptions

(1) The converter shell and ladle wall are ignored, and only the molten pool part in the inner wall is reserved as the calculation domain, and all walls are smooth and there is no slippage on walls;
(2) It is assumed that the converter is stationary when tapping;
(3) The slag layer on the top layer of molten steel in the molten pool when tapping is ignored;
(4) The molten steel in the converter is regarded as an incompressible Newton fluid, and the physical parameters (density, viscosity, etc.) of the molten steel do not change with temperature.

Governing Equations

(1) VOF (Volume of Fluid) modelling

The VOF model was used to study the flow characteristics of molten steel in the converter. In this model, different fluid components shared a set of momentum equations, and the phase interface of each calculation unit was tracked by introducing the phase volume fraction.

$$\frac{\partial \alpha_q \rho_q}{\partial_t} + \vec{v} \cdot \nabla \alpha_q \rho_q = 0 \tag{1}$$

where α_q is the value of the volume fraction of the q phase, ρ_q is the volume fraction density of the q phase, and $\vec{v}$ is the velocity.

The momentum equation is shown below, where ρ and μ depend on the volume fraction of Ar and molten steel phases in the grid:

$$\frac{\partial}{\partial t}(\rho \vec{v}) + \nabla \cdot (\rho \vec{v} \vec{v}) = -\nabla p + \nabla \cdot \left[\mu\left(\nabla \vec{v} + \nabla \vec{v}^T\right)\right] + p\vec{g} + \vec{F} \tag{2}$$

where p is the static pressure, $p\vec{g}$ is the gravity, and F is the external force and is defined as the force of the DPM (Discrete Particle Models) on the continuous phase.

ρ and μ are computed as follows, respectively:

$$\rho = \rho_g \alpha_g + \rho_1 \alpha_1 \tag{3}$$

$$\mu = \mu_g \alpha_g + \mu_1 \alpha_1 \tag{4}$$

where α is the volume fraction of the phase in each unit, ρ is the phase density, and subscripts ρ and l represent the gas and liquid phases, respectively.

(2) Turbulence modelling

The standard low Reynolds number k–ε model was used to characterize the turbulent behaviour of the gas–liquid two-phase flow in the molten pool of the top–bottom combined blowing converter.

$$\frac{\partial(\rho_m k)}{\partial t} + \frac{\partial(\rho_m \mathrm{ku}_i)}{\partial x_i} + \rho_m \varepsilon = \frac{\partial}{\partial_j}\left[\left(\mu_{\mathrm{eff}} + \frac{\mu_t}{\sigma_k}\right)\frac{\partial k}{\partial x_j}\right] + G_k \tag{5}$$

where μ_{eff} is the turbulent effective viscosity coefficient expressed as

$$\frac{\partial(\rho_m \varepsilon)}{\partial t} + \frac{\partial(\rho_m u_i \varepsilon)}{\partial x} = \frac{\partial}{\partial x_j}\left[\left(\mu_{eff} + \frac{\mu_t}{\sigma_\varepsilon}\right)\frac{\partial \varepsilon}{\partial x_j}\right] + \frac{1}{k}\left(\varepsilon C_{1\varepsilon} G_k - \varepsilon^2 C_{2\varepsilon}\rho_m\right) \tag{6}$$

$$\mu_{\mathrm{eff}} = \mu_m + \rho_m C_\mu \frac{k^2}{\varepsilon} \tag{7}$$

where μ_m is the fluid molecule viscosity and $C_{1\varepsilon}$, $C_{2\varepsilon}$, C_μ, σ_k, and σ_ε are constants whose values are 1.44, 1.92, 0.09, 1.3, and 1.0, respectively.

Computation Methodology

Figure 1 is a schematic diagram of the converter and ladle. Table 1 lists the key parameters of the experiment. The physical properties of the fluid are shown in Table 2.

The computational domain of the converter tapping process simulation includes five parts: the converter molten pool (only half of the molten pool of molten steel), the tapping pipe, the ladle molten pool, the air domain between the end of the tapping hole, and the top surface of the ladle. Orthogonal hexahedral meshes were used in

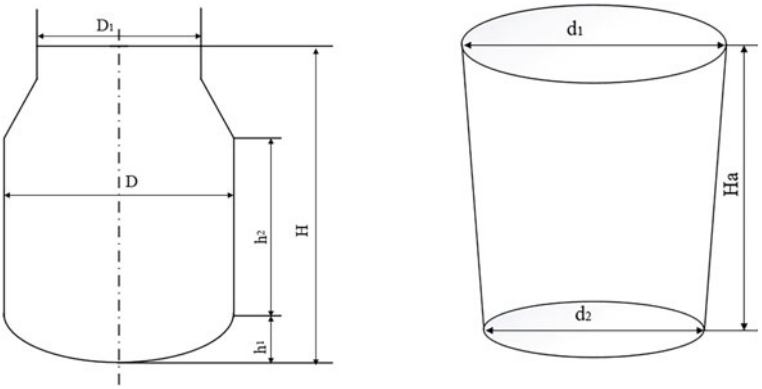

Fig.1 Schematic diagram of 200t converter and ladle

Table 1 Main parameters of converter and ladle model mm

	Ladle			Converter					
	d_1	d_2	H_a	H	D	D_1	h_1	h_2	Tapping pipe length
Model size	4010	3360	4412	8700	5800	3220	1650	4414	2250

Table 2 Physical properties of the fluid

Item	Steel(1923 K)	Air(300 K)
Density, kg/m^3	7200	Compressible
Viscosity, kg/m·s	0.005	1.789×10^{-5}
Thermal conductivity, W/ m·K	23.26	0.0242
Specific heat, J/ kg·K	879	1006.43

the calculation area to ensure the convergence of the calculation results and avoid numerical diffusion. The schematic diagram of molten steel injection and grid division is shown in Fig. 2. The total number of grids in the entire computing area is about 2 million.

Five groups of experiments were designed for the numerical simulation are shown in Table 3.

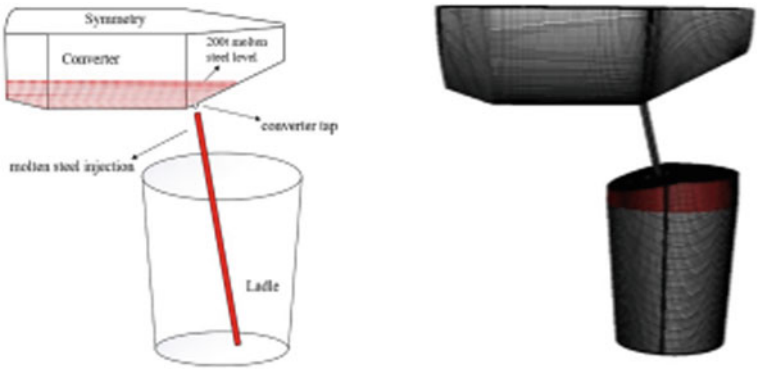

Fig. 2 Schematic diagram of molten steel injection and meshing

Table3 Experimental schemes

	Scheme				
	1	2	3	4	5
Converter tap shape	Segmented variable diameter type, Cylindrical				
Converter tap diameter/mm	180–160, 180, 160				
Converter tap angle/°	10, 15				

Among them, 160 and 180 represent the diameter when the shape of the tapping hole is cylindrical; 180–160 represents the diameter at both ends of the tapping hole when the shape of the tapping hole is a segmented variable diameter type; 10° and 15° represent the angle between the tapping hole and the horizontal direction. For example, in the experiment represented by 180–160-10: The shape of the tapping hole is a segmented variable diameter type, with diameters of 180 mm and 160 mm at both ends, and the angle between the tapping hole and the horizontal direction is 10°. Five sets of experiments are 160–10, 180–10, 180–10, 180–160-10, and 180–160-15, respectively.

The initial operating pressure and velocity are 101 kPa and 0 m/s, respectively.

The boundary condition of the converter furnace mouth is the pressure inlet and the gauge pressure at the inlet is 0 Pa. The boundary conditions of the edge of the air domain above the ladle are the pressure outlet, and the gauge pressure at the outlet is 0 Pa. The boundary conditions of the inner wall surface of the converter, the inner wall surface of the tap pipe, and the inner wall surface of the ladle are all thermal insulation walls. In addition, the Enhanced Wall Treatment method, which can flexibly judge the density of grids at different positions, to calculate the flow state of molten steel at different walls.

The calculation process was based on the pressure solver. The pressure and the velocity were coupled by the Pressure-Implicit with Splitting of Operators algorithm. The Patch command was used to define the initial volume region of the two phases. The calculation time step was 1.0×10^{-3}. The convergence criterion is as follows: The dimensionless residual curve of the energy variable is less than 1.0×10^{-6}, and the residuals of the other variables are less than 1.0×10^{-3}.

Verification of Numerical Simulation

Comparing and verifying the tapping time data of a steel plant with the numerical simulation results, when the diameter of the tapping hole is 160 mm, the shortest tapping time at a steel plant is 240 s, while the numerical simulation's tapping time is 250.8 s. The error between the actual value of the molten steel tapping time and the simulated value is within 5%, which verifies the accuracy of the simulation.

Results and Discussion

Distribution of Molten Steel Flow Field in the Converter Tapping Process

In this study, through the calculation of the molten steel flow field in the converter tapping process, the molten steel phase distribution, velocity changes, turbulent kinetic energy changes, the erosion of the ladle bottom, and the ladle mixing characteristics are analyzed during the converter tapping process.

Distribution of Molten Steel Phase in the Converter Tapping Process

Since the molten steel injection is affected by gravity and surface tension, the diameter of the molten steel injection gradually decreases during the converter tapping process shown in Fig. 3. In addition, it can be concluded that the degree of air entrainment by the molten steel in the ladle is different under different tapping process parameters.

From Fig. 4, the cylindrical tap has the characteristics of a large amount of entrained air and small bubbles, while the tap of the segmented diameter type has a small amount of entrained air, but the bubbles are relatively large. At the same time, Li et al. [20] found that air entrainment is the main reason for reducing steel quality during the converter's tapping process. Therefore, if the alloy is added on the opposite side of the impact direction of molten steel, the contact between the alloy and the entrained air can be effectively reduced, thereby reducing the secondary oxidation degree of the molten steel.

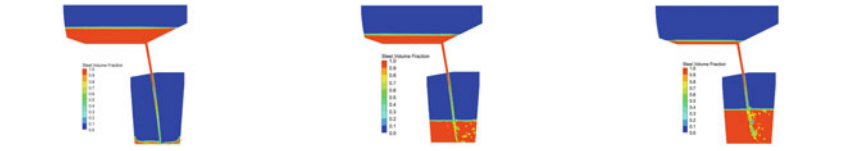

Fig. 3 Distribution of molten steel phase: 180–160-10

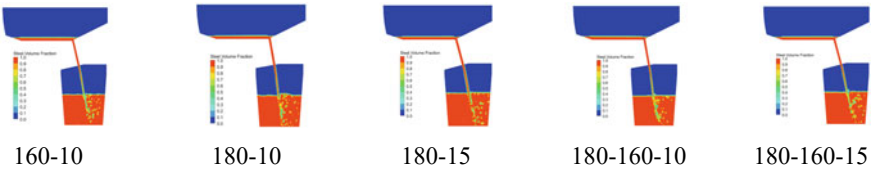

Fig. 4 Late stage of converter tapping: distribution of molten steel phase

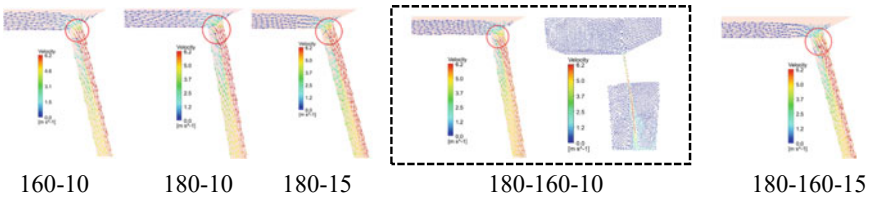

Fig. 5 Late stage of converter tapping: the vector diagram of the velocity

Velocity Distribution in the Converter Tapping Process

The gradual reduction of the inner diameter of the segmented variable diameter tap leads to less interference between the molten steel and the tap, thereby achieving a more stable and uniform velocity distribution near the tap. When the angle between the tapping hole and the horizontal direction is 10°, the erosion wear between the molten steel and the inner wall of the tapping hole can be reduced shown in Fig. 5.

From Fig. 6, it can be concluded that the trend of average flow rate and mass flow rate of molten steel remains consistent. In the process of converter tapping, as the molten steel level in the converter decreases, the flow rate and flow of molten steel will also decrease. At the end of the converter tapping stage, due to the excessive air entrainment into the molten steel (if the slag is not ignored, the slag will begin to fall), the velocity and mass flow curve of the tapping port will oscillate irregularly and then drop sharply. When the process parameters of the tapping hole are 180–10, 180–15, 160–10, 180–160-10, 180–160-15, the average velocity of the tapping hole is 5.61 m/s, 5.74 m/s, 5.71 m/s, 6.34 m/s, 6.22 m/s, respectively, the average mass flow of the tapping hole is 983.07 kg/s, 1013.39 kg/s, 797.5 kg/s, 881.5 kg/s, 868.43 kg/s, respectively, the tapping time is 203.4 s, 197.4 s, 250.8 s, 226.9 s, and 230.3 s, respectively. The shape and diameter of the tapping hole have a greater impact on the tapping time, while the angle has a lesser effect. However, the reasonable process parameters of the tapping hole also depend on the turbulent kinetic energy of the tapping hole, the impact characteristics of the molten steel on the ladle, and the mixing effect of the ladle.

Turbulent Kinetic Energy Distribution During Converter Tapping

From Fig. 7, during the tapping process of the converter, the turbulence of the tapping pipe is reduced accordingly over time. The average values of turbulent flow in the tap pipeline in the early, middle, and late stages of converter tapping are 2.05 m^2/s^2, 1.99 m^2/s^2, and 1.69 m^2/s^2, respectively. Smaller turbulent flow reduces the wear of the molten steel on the wall of the tapping pipe.

From Fig. 8, it can be concluded that intuitively the tapping pipes with different process parameters will show different turbulent kinetic energy distribution sizes and states.

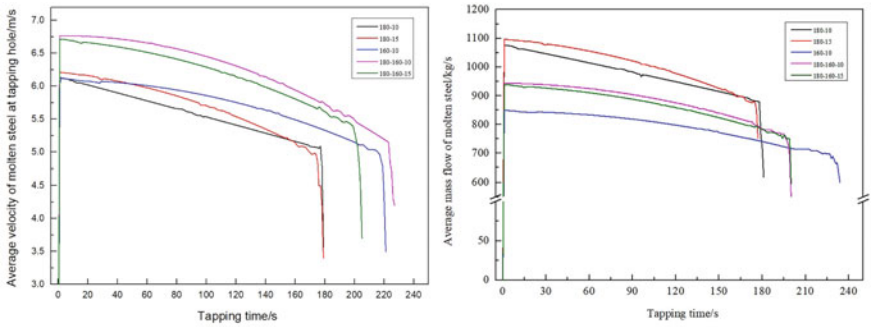

Fig. 6 Flow characteristics of molten steel at tapping hole with different process parameters

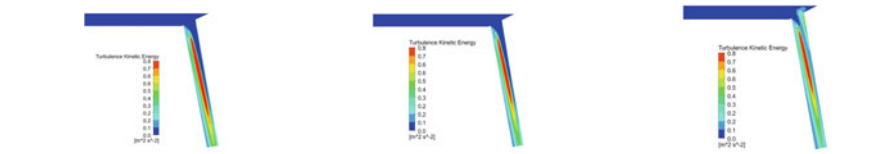

Fig. 7 Turbulent kinetic energy distribution: 180–160-10

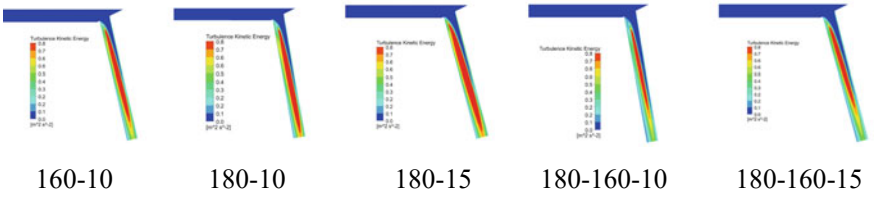

Fig. 8 Early stage of converter tapping: turbulent kinetic energy distribution

Figure 9 shows the statistical results of turbulent kinetic energy: When the process parameters of the tapping hole are 180–10, 180–15, 160–10, 180–160-10, and 180–160-15, the average turbulent kinetic energy of the central section of the tapping pipe is 2.62 m^2/s^2, 2.75 m^2/s^2, 2.49 m^2/s^2, 1.91 m^2/s^2, and 1.95 m^2/s^2, respectively. When the shape of the tapping hole is a segmented variable diameter type, the turbulent kinetic energy of the tapping pipe is reduced by at most 27.1% (comparison of 180–10 and 180–160-10). The diameter of the tapping hole is increased by 20 mm, and the turbulent kinetic energy of the tapping pipe is reduced by 5% (comparison of 180–10 and 160–10). The angle of the tapping hole and the horizontal direction is

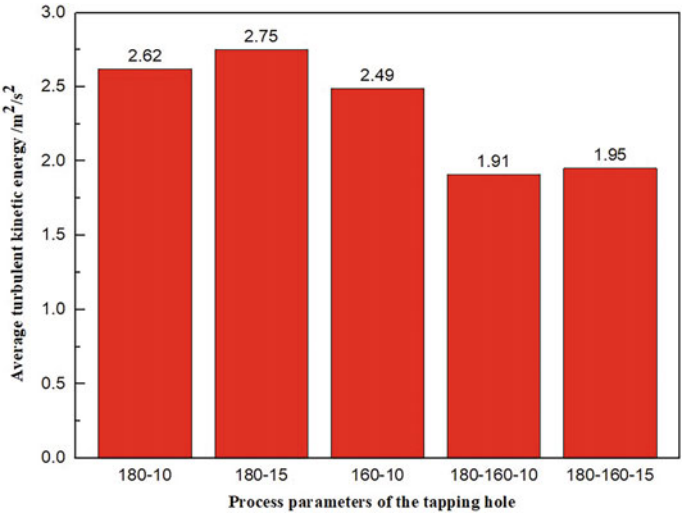

Fig. 9 The average turbulent kinetic energy

reduced by 5°, and the turbulent kinetic energy of the tapping pipe is reduced by 4.7% (comparison of 180–10 and 180–15).

Erosion Law of Ladle Bottom in the Converter Tapping Process

From Fig. 10, it can be concluded the magnitude and range of the impact force of the molten steel on the bottom of the ladle.

Figure 11 shows the statistical results of the impact force of molten steel on the bottom of the ladle: When the process parameters of the tapping hole are 180–10, 180–15, 160–10, 180–160-10, and 180–160-15, the average wall shear of the ladle bottom is 1345.58 Pa, 1418.92 Pa, 1258.61 Pa, 1108.38 Pa, 1110.67 Pa, respectively. When the shape of the tap hole is a segmented variable diameter type, the diameter

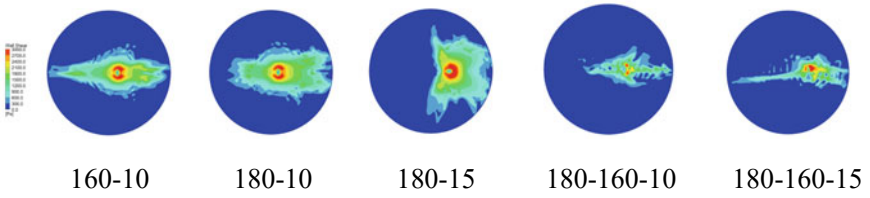

Fig. 10 Early stage of converter tapping: distribution of wall shear at the bottom of the ladle

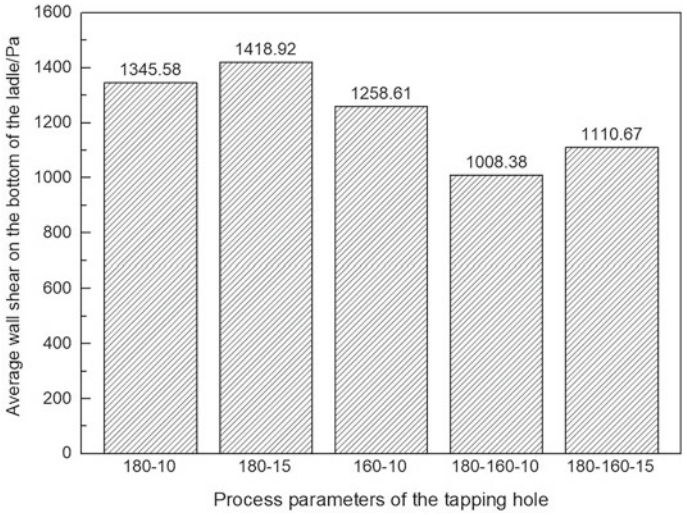

Fig. 11 The early stage of converter tapping: average wall shear on the bottom of the ladle

is 180–160, and the tap hole and the horizontal direction are 10°, the impact wall shear of the molten steel on the bottom of the ladle can be reduced by up to 21.9%.

The Mixing Characteristics of the Ladle During the Converter Tapping Process

During the tapping process of the converter, the molten steel in the converter is injected into the ladle through the tapping pipe under the action of gravity. Continuous injection of molten steel promotes agitation of the molten ladle. The area in the molten pool where the velocity is less than 0.1 m/s is defined as the dead zone, which is shown in red. The dead zone distribution of the ladle is different in Fig. 12.

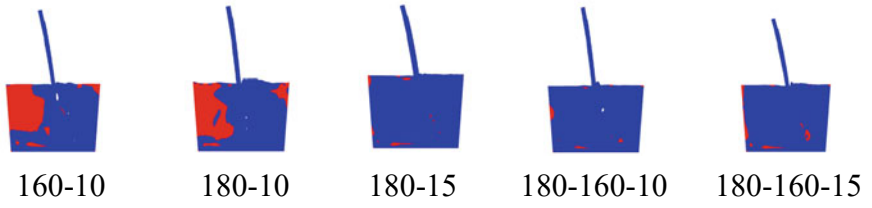

Fig. 12 Late stage of converter tapping: distribution of dead zone

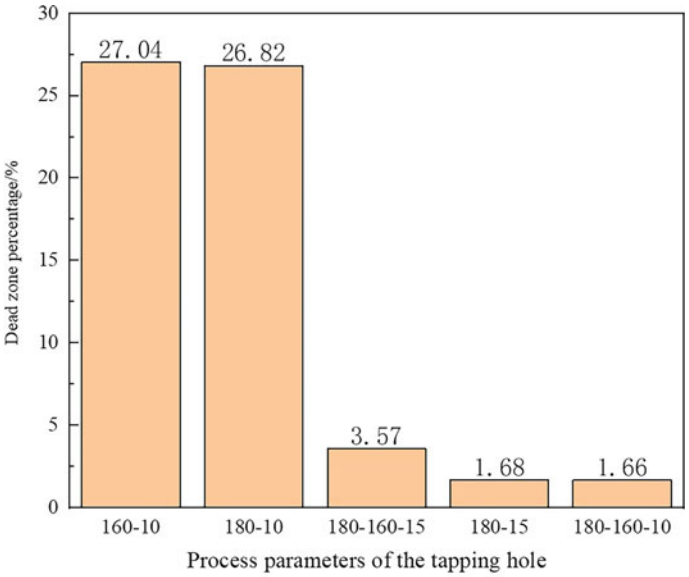

Fig. 13 The later stage of converter tapping: Percentage of the dead zone

Figure 13 shows the statistical results of the dead zone percentage of the central section of the ladle: When the process parameters of the tapping hole are 180–10, 180–15, 160–10, 180–160-10, and 180–160-15, The dead zone percentages of the central section of the ladle are 26.82%, 1.68%, 27.04%, 1.65%, and 3.57%, respectively, which shows that when the process parameters of the tapping hole are 180–160-10, the molten steel has the best stirring effect on the molten pool of the ladle.

Conclusion

(1) During the tapping process of the converter, the flow characteristics of the molten steel at the tapping hole with different process parameters are different. When the shape of the tapping hole is a segmented variable diameter type, the diameter is 180–160 mm, and the angle with the horizontal direction is 10°, the molten steel flow rate is more uniform and stable, and the turbulence is significantly reduced. At this time, the impact force of the molten steel on the bottom of the ladle is the smallest and the stirring effect of the molten steel in the ladle is the best.

(2) When the diameter of the converter tapping hole is 160 mm, the error between the numerical simulation and the actual tapping time is within 5%, which verifies the accuracy of the model.

(3) Ranking of the effects of tapping process parameters on the flow characteristics of molten steel: Shape > Diameter > Angle.

Acknowledgements This work is supported by the Scientific and Technological Innovation 2030—New Generation Artificial Intelligence Major Project (2022ZD0119201)

Conflict of Interest No potential conflict of interest was reported by the authors.

References

1. Lee S, Kim S, Lee H (2016) New idea of suppressing free surface vortex during tapping liquid steel from converter. Metals Mater Int 22(1):136–142
2. Choh T, Iwata K, Inouye M (1983) Estimation of oxygen and nitrogen absorption of liquid steel during tapping from converter. Trans Iron Steel Inst Jpn 23(8):680–689
3. Wu M (2016) Production practice of improving the use effect of the converter tapping hole. Steelmaking 32(01):20–22
4. Gu MQ, Xu AJ, Liu X et al (2022) A data-driven dynamic prediction model for molten steel temperature in the second blowing stage of a converter. J Eng Sci 44(09):1595–1606
5. Feng K, Yang L, Su B et al (2022) An integration model for converter molten steel end temperature prediction based on Bayesian formula. Steel Res Int 93(2):2100433
6. Dignani ML, Camelli S, Vazquez A et al (2012) Main properties for the selection of converter tap-hole materials. Proc Mater Sci 1:382–388
7. Liu X, Xu A, Yuan F et al (2023) Optimisation of the bottom blowing process for a 200 t converter. Ironmaking Steelmaking 50(1):1–12
8. Cao L, Wang Y, Liu Q et al (2018) Physical and mathematical modeling of multiphase flows in a converter. ISIJ Int 58(4):573–584
9. Olivares O, Elias A, Sánchez R et al (2002) Physical and mathematical models of gas-liquid fluid dynamics in LD converters. Steel Research 73(2):44–51
10. Zhang YL, Xie ZH (2015) The influence of the composition and shape of the lining brick of the tapping hole on its durability and tapping time. Refractory and Lime 40(02):36–37
11. Li CJ (2020) The practice of process technology optimization of 120 t converter tapping process. Modern Metall 48(01):45–47
12. Yang W, Wang L, Liu S et al (2023) Physical simulation of powder spraying at the bottom of a converter. Steel Res Int 94(1):2200364
13. Li W, Zhu R, Dong K et al (2020) Physical simulation and industrial testing of bottom-blown O2-CaO converter for steelmaking process. Metall Mater Trans B 51(3):1060–1069
14. Zhang J, Lou W, Zhu M (2022) Physical modelling of particle transport phenomenon and vibration behavior of converter with bottom powder injection. J Iron Steel Res Int 29(11):1771–1788
15. Lu T, Xiao Y, Zhou Y et al (2021) Numerical simulation of nozzle height on the effect of fluid flow in a Peirce-Smith converter. JOM 73(10):2938–2945
16. Zhang J, Lou W, Zhu M (2023) Numerical simulation of particle motion and wall scouring behavior in steelmaking converter with bottom powder injection. Metall Mater Trans B
17. Zhang J, Lou W, Zhu M (2023) Numerical simulation of particle transport phenomenon in steelmaking converter with bottom powder injection based on eulerian-multifluid VOF-granular flow model. Metall Mater Trans B 54(3):1449–1467
18. Dubois D, Swickard D, Jandl C, et al (2011) i-TAP: performance improvement of the BOF tapping system at Arcelormittal USA, Burns Harbor, IN[M]

19. Li KH (1983) Improvement on the design of the tapping hole of the oxygen top-bottom double blowing converter and the tapping operation method. Iron Steel Res Inf 04:26–37
20. Li SE, Zhao YP, Zhang JZ et al (2017) Simulation study on the gas injected into the fluid during the tapping process. J Guizhou Univ Technol (Natl Sci Edn) 02:33–36

Interaction Between MgO-Bearing Lining Refractory Rods and a High-Carbon SiMn-Killed Steel

Yujie Cheng and Lifeng Zhang

Abstract In the current study, the interaction between refractory rods and a high-carbon SiMn-killed steel was investigated via laboratory experiments and thermodynamic calculations. The carbon-bonded magnesia (MgO-C) refractory and the magnesite (MgO) refractory were compared. After 90 min of contact, the penetration of the molten steel into the MgO refractory was little and the interfacial reaction layer was little observed so the inclusions in the steel varied little. After 90 min of contact, the molten steel penetrated the MgO-C refractory for 1 mm through grain boundaries and C-phase channels in the lining refractory. A 80 μm thick CaO-CaS-MgO-MgS layer between the steel and the MgO-C refractory formed and inclusions in the steel were transformed from original SiO_2-MnO-Al_2O_3 ones with a spherical morphology to MgO and MgO-Al_2O_3 ones with an irregular shape, indicating the occurrence of the desulfurization of the steel by the CaO-phase in the grain boundary of the lining refractory.

Keywords MgO refractory · MgO-C refractory · High-carbon SiMn-killed · Inclusion

Introduction

Aluminum metal and Si-Mn alloy are usually used as deoxidizers in the steelmaking process. Al or Si-Mn alloy is chosen based on the requirement of steel grades due to the different properties of inclusions after deoxidation. In the case of SiMn-killed steel grades, liquid inclusions are the main type of deoxidation products at steelmaking temperature. Si-Mn alloy is widely employed as the deoxidizer of tire cord steel grades, which require deformable inclusions with low melting points. Tire cord steel

Y. Cheng
School of Mechanical Engineering, Yanshan University, Qinhuangdao 066004, Hebei, China

L. Zhang (✉)
School of Mechanical and Materials Engineering, North China University of Technology, Beijing 100144, China
e-mail: zhanglifeng@ncut.edu.cn

S. Wagstaff et al. (eds.), *Materials Processing Fundamentals 2024*, The Minerals, Metals & Materials Series, https://doi.org/10.1007/978-3-031-50184-5_13

grades have long been used as a reinforcement of rubber products because they can add excellent elasticity and strength to the rubber [1]. The diameter of steel cords can be less than 0.2 mm after hot rolling and cold drawing from billets [2]. The breakage of the steel during cold drawing and fabrication is mainly caused by nonmetallic inclusions and is a crucial issue. The effects of inclusions on steel properties are different owing to their different plasticities. Nondeformable inclusions are extremely detrimental to the drawing performance of tire cord steel grades and can cause fractures [3–6]. Especially, the Al_2O_3-rich inclusions should be avoided due to their high hardness and high melting point [7–9]. However, wire breakage caused by Al_2O_3 inclusions still occurred frequently during the production practice even though [Al]s concentration in steel was limited to a trace level by employing some technologies [10]. To clarify the source of Al_2O_3-rich inclusions, the effect of refractory should also be taken into consideration for its long contact with molten steel. The corrosion of the refractory could also result in the inclusion in the steel and it has been confirmed that MgO inclusions and calcium aluminate inclusions with MgO islands in Al-killed steel grades originate from the corrosion of refractory [11, 12]. These exogenous inclusions from refractories are an important source of nondeformable inclusions in SiMn-killed steel as well.

Magnesia (MgO) and carbon-bonded magnesia (MgO-C) refractories are widely used in the ladle refining process, however, with the introduction of new techniques in modern processes, the degradation rate of these refractories has accelerated substantially along with shorter service life [13–15]. Additionally, accelerated refractory wear has reduced the product quality while increasing the proportion of nonmetallic inclusions in the metal. Many studies have claimed that adding graphite to the MgO matrix could greatly improve thermal shock resistance and slag corrosion resistance of MgO-C refractories due to its low coefficient of thermal expansion and non-wettability with molten slag [16, 17]. Nonetheless, graphite is susceptible to oxidative damage and can react with reducible components in molten slag and the refractory [18, 19]. These redox reactions can consume graphite and form porous structures in the MgO-C refractory and can be susceptible to thermal shock [20]. To overcome this, the antioxidants are added to the refractory. Typical antioxidants are Al and Si powder, but also SiC, B_4C, TiO_2, ZrO_2, and other compounds have been applied [14, 21, 22].

Many publications implied that MgO-based refractory can influence the formation and evolution of inclusions in the steel. These mechanisms mainly focused on the reactions that MgO in the refractory reduced by [Al] and [C] in the steel and C in the refractory independently [23, 24]. The independent effect of the refractory on SiMn-killed steel is rarely reported. Chen et al. [25] explored the source of Al_2O_3-rich inclusions in high-carbon steel for saw wire reacted with Al-containing MgO-C refractory. They claimed that the pores at the boundary of MgO and C are generated by the reaction between MgO and C within the refractory and then molten steel penetrated the refractory through the pores, which caused the dissolution of C particles together with Al particles surrounded by C particles and resulted in the presence of Al_2O_3-rich inclusions. Deng et al. [26] found that the purity of MgO refractory is crucial for tire cord steel and even 0.3% of Al_2O_3 in MgO refractory

causes an evident increase of Al_2O_3 content in the inclusions. MgO and Al_2O_3 inclusions transform into $MgO{\cdot}Al_2O_3$ spinel and it is stable in SiMn-killed steel due to the effect of MgO refractory. Li et al. [27] studied the reaction between MgO refractory and ultra-low Al high C steel. It was found that pure MgO inclusion is formed due to the MgO in the MgO refractory can be reduced by [C] to generate [Mg] and CO gas. However, when the [Al] content in steel increased to larger than 0.0015%, inclusions were changed to spinel some of which were rich in MgO. Therefore, high purity and high quality MgO-based refractory is crucial during the steelmaking and casting processes of high-carbon SiMn-killed steel grades.

In the current study, interactions of high-carbon SiMn-killed steel and two kinds of industrial refractories containing MgO refractory and MgO-C refractory were investigated via laboratory experiments and thermodynamic calculations. The MgO-C is refractory on the steel cleanliness and corrosion degree of the refractory in comparison with MgO refractory were analyzed. The morphology and composition of the refractory/steel interface layer and inclusions in the molten steel were performed. The current research result will guide the selection of refractories in the steel industry.

Experimental Procedure and Sample Analysis

The experimental steel grade is a high-carbon SiMn-killed steel from an industrial slab, of which the chemical composition is listed in Table 1. The steel was cut into small pieces and the surface was polished to remove the oxide scale. The refractory rods employed in the current experiment were cut from commercial MgO brick and MgO-C brick respectively, of which the composition is listed in Table 2. It was analyzed in detail next that no oxygen element is found in the area that the Al element distributed in the MgO-C refractory. This implies that only metal Al particles existed in the MgO-C refractory instead of Al_2O_3 particles. The rod samples had a diameter of 10 mm and a height of 110 mm.

The experimental setup and condition are illustrated in Fig. 1 and Table 3 respectively. Approximately 800 g of the steel was melted in a dense alumina crucible with

Table 1 Chemical composition of the steel employed in the current study (wt.%)

Element	T.O	T.Al	T.Mg	T.Ca	S	C	Si	Mn
Content	0.0015	0.0013	0.0004	0.0003	0.004	0.71	0.20	0.56

Table 2 Chemical composition of the refractory employed in the current study (wt.%)

Composition	MgO	C	CaO	SiO_2	Fe_2O_3	Al_2O_3	Al
MgO refractory	95.94	0.101	1.626	1.027	0.908	0.398	–
MgO-C refractory	68.185	20.53	2.188	3.165	1.05	–	4.882

a 56 mm outer diameter and a 120 mm height using a silicon–molybdenum resistance tube furnace that was flushed with the argon gas at a rate of 2 L/min to create an inert atmosphere. Around the alumina crucible, a graphite crucible was set to suppress the induction stirring of the metal phase and as a reducing atmosphere role. The first sample was taken using a quartz sampler and then the refractory rod was immersed into the molten steel when the steel was heated to 1873 K and melted. The time to dip the rod was set as the start time of the experiment. Next, the steel samples were taken at 5, 10, 20, 30, 60, and 90 min to study the evolution of inclusions with time. It was approximately 30 g for each steel sample. For each sampling process, the inlet of the sampler was kept at the same direction and depth from the bottom of the molten steel to ensure the same sampling position. To keep the original composition and morphology of inclusions in the steel and prevent new precipitates during cooling and solidification, the molten steel samples were quenched quickly into water once they were taken out from the molten steel. After the reaction time, the resistance furnace was turned off. The alumina crucible with the steel and the refractory rod was taken out of the furnace as quickly as possible and rapidly quenched in the water when the temperature in the furnace dropped to about 773 K to study the interface between the refractory and the steel.

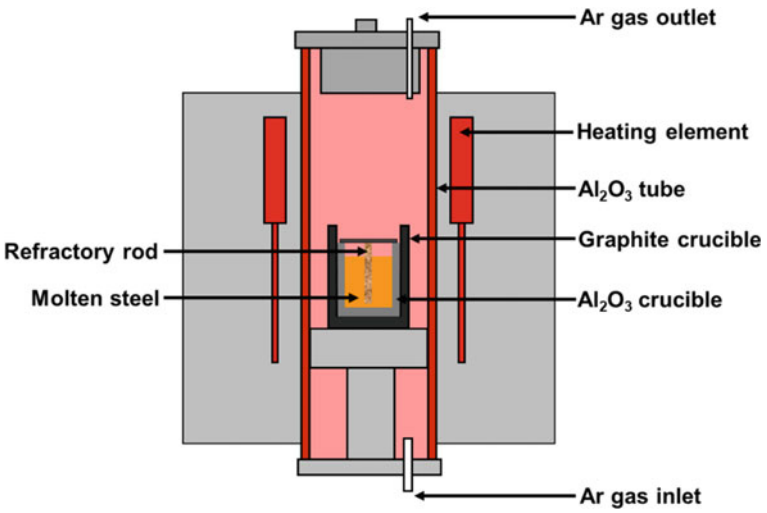

Fig. 1 Schematic of experimental setup

Table 3 Experimental conditions

Steel	Refractory	Temperature (K)	Immersion time (min)
High-carbon SiMn-killed	MgO, MgO-C	1873	0, 5, 10, 20, 30, 60, 90

The steel samples and the refractory rod were prepared for analysis. The morphology and composition of the cross-sectional interface between the refractory and the steel were detected by an optical microscope and a field-emission scanning electron microscope (SEM) equipped with energy dispersive spectrometer (EDS). The morphology and composition of inclusions in the steel were analyzed through an automated scanning electron microscope with OTS (one bond inclusion analysis system) and the minimum size of inclusions detected was set as 1 μm.

Chemical Composition of Original Lining Refractories

It is of great interest to observe the microstructure of raw refractories to investigate the mechanism of the interaction between the refractory and the steel. The morphology and elemental mapping of the initial MgO and MgO-C refractory are shown in Fig. 2(a) and (b) respectively. The employed two refractories contained some impurities with a light gray color [28, 29]. The main composition of the impurity in the MgO refractory and the MgO-C refractory was CaO-SiO_2-MgO [28, 30]. The initial MgO refractory consisted of large-size magnesite particles with a dark gray color as the main crystal phase and a large quantity of reticular CaO-SiO_2-MgO as the intergranular phases and the boundary of magnesite was straight and filled with CaO-SiO_2-MgO as depicted in Fig. 2a. The initial MgO-C refractory consisted mainly of magnesite with a dark gray color, graphite with a black color, CaO-SiO_2-MgO with a light gray color, and Al antioxidant existed in the graphite with a bright white color as depicted in Fig. 2b.

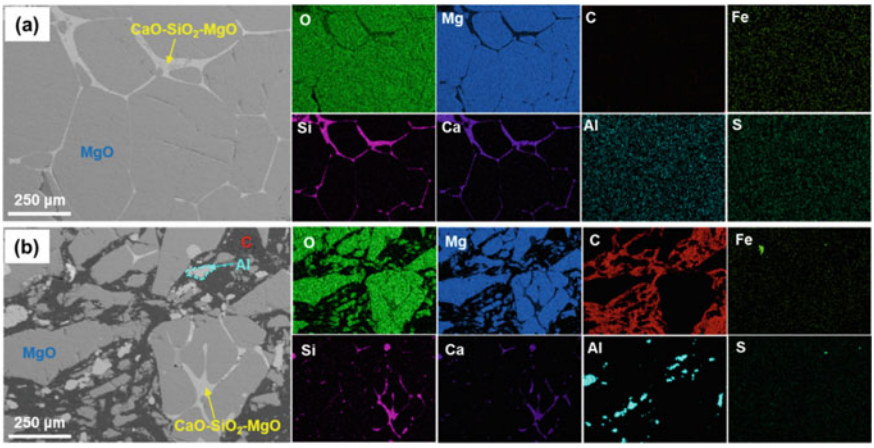

Fig. 2 Elemental mapping of raw refractory: **a** MgO refractory; **b** MgO-C refractory

Interface Between the Lining Refractory and the Steel

The macro morphology of the interface between the refractory and the high-carbon SiMn-killed steel after interaction at the end of the experiment is shown in Fig. 3. Figure 3a shows that no interfacial layer at the interface between the MgO refractory and the steel. Figure 3b shows that molten steel penetrated MgO-C refractory for 1 mm when MgO-C refractory reacted with the molten steel for 90 min. It was deemed of interest to examine the cross-section area of the refractory and infiltrated steel after each experiment. The area of the refractory and the infiltrated steel for each sample was measured by Image-Pro Plus 6.0 using this cross-section photograph as an object. The result shows that the ratio of the area of the molten steel infiltrated into the refractory to the refractory. The ratio of the area of the molten steel infiltrated into the refractory to the MgO refractory and the MgO-C refractory are 0 and 6.114 respectively. The reason that molten steel penetrated the MgO-C refractory was that molten steel initially penetrated the MgO-C refractory along the MgO grain boundaries and it caused the dissolution of C particles. Meanwhile, the MgO grains were reduced by C within the MgO-C refractory to produce Mg(g) and CO(g) and created pores and gaps. Based on the two reasons above, the enlarged pores were inevitable to promote the molten steel's penetration of the MgO-C refractory. [25, 31–34] The molten steel penetrated the MgO-C refractory through grain boundaries, and the channels were formed by the consumption of graphite.

The elemental mapping analysis of the interface between high-carbon SiMn-killed steel and the refractory is shown in Fig. 4. Figure 4a shows the mapping analysis at the interface between the steel and MgO refractory after 90 min reaction. This shows that no evident elemental enrichment and a continuous gap layer can be found at the interface between the MgO refractory and the steel. Figure 4b shows the morphology

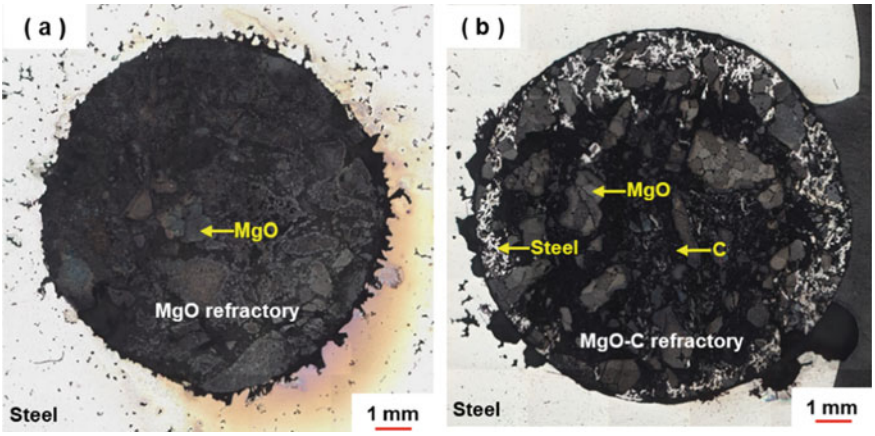

Fig. 3 Macro-interface between the refractory and the steel after reaction for 90 min: **a** MgO refractory; **b** MgO-C refractory

of the interface between the molten steel and MgO-C refractory after 90 min reaction. The composition of the interface layer was 31.38wt.%O, 1.59wt.%Mg, 1.5wt.%S, and 0.75wt.%Ca, so a new oxysulfide interface layer containing CaO-MgO-CaS-MgS was generated. Meanwhile, there were some dispersed MgO particles on the side of the steel. The new layer formed at the interface contains some oxides and sulfides due to volatilization and oxidation reactions. The main reaction taking place within the MgO-C refractory can be obtained as Eqs. (1 and 2). [35] CaO and MgO are reduced by C within the MgO-C refractory accompanied by the generation of Ca(g), Mg(g), and CO(g). The Ca(g) and Mg(g) diffused to the interface where they reacted with [O] and [S] in molten steel and CO(g) to form CaO, MgO, CaS, and MgS, indicating the occurrence of the desulfurization of the steel by the CaO-phase in the grain boundary of the lining refractory. The formation of the oxysulfide interface layer inhibits further reaction between the refractory and molten steel. The consumption of carbon in MgO-C refractory causes the detaching of MgO particles from the large MgO grains through the loosening of such particles from the MgO grains and their consequent floating on the side of the steel.

$$\mathrm{MgO(s)} + \mathrm{C(s)} = \mathrm{Mg(g)} + \mathrm{CO(g)} \tag{1}$$

$$\mathrm{CaO(s)} + \mathrm{C(s)} = \mathrm{Ca(g)} + \mathrm{CO(g)} \tag{2}$$

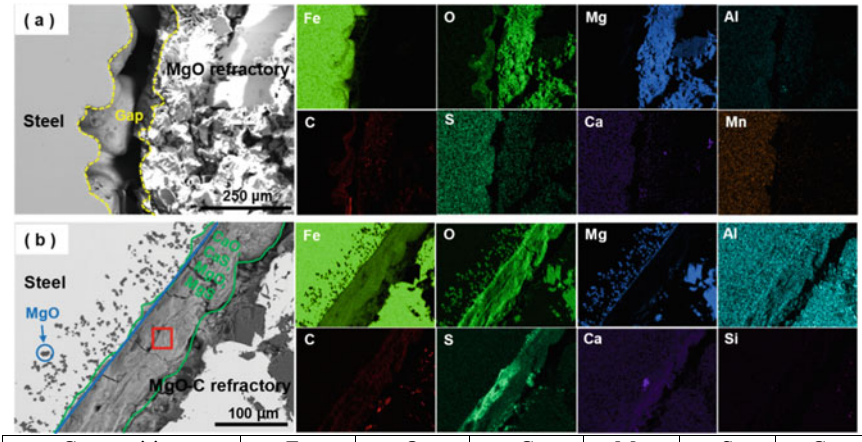

Composition	Fe	O	C	Mg	S	Ca
Content (wt.%)	43.30	31.38	21.48	1.59	1.50	0.75

Fig. 4 Elemental mapping of the interface between high-carbon Al-killed steel and the refractory rod: **a** MgO rod; **b** MgO-C rod

Evolution of Nonmetallic Inclusions in the Steel with Time

Figure 5 shows the evaluation of inclusion composition in the steel reacted with MgO refractory after different reaction times. In the case of the Al_2O_3-MgO-SiO_2 system inclusions, the primary inclusions in the steel had a low content of Al_2O_3 at 13.41wt.% and a high content of SiO_2 at 85.78wt.% with a melting point lower than 1873 K. With the reaction time increase to 90 min, the average content of SiO_2 decreases to 53.01wt.% and the average content of Al_2O_3 increases to 45.35wt.%. A small amount of inclusions become solid from 5 to 90 min due to the increase of Al_2O_3 content. Figure 6 shows the morphology and elemental mapping: SiO_2-MnO-Al_2O_3-CaO-MgO inclusion with globular shape.

Figure 7 shows the evaluation of inclusion composition in the steel reacted with MgO-C refractory after different reaction times. The original inclusions having a low content of Al_2O_3 and a high content of SiO_2 in the steel existed in the 1873 K

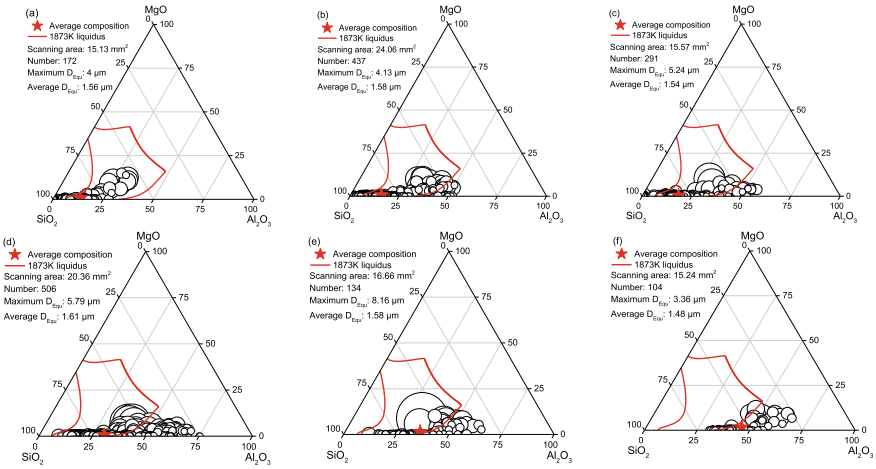

Fig. 5 Evolution of inclusions in the steel reacted with MgO refractory *versus* time: **a** 0 min; **b** 5 min; **c** 10 min; **d** 30 min; **e** 60 min; **f** 90 min

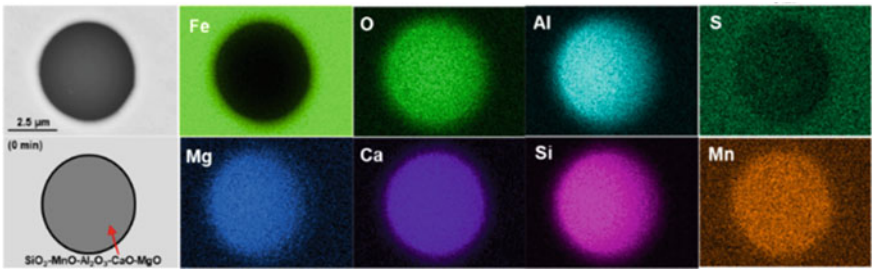

Fig. 6 Typical inclusion in the steel reacted with MgO refractory at a certain reaction time

liquid region when reacted for 0 min. The liquid inclusions become solid inclusions from 5 to 90 min. Increasing the reacting time to 5 min, a lot of MgO-Al_2O_3 spinel inclusions were generated. Increasing the reacting time to 10 min, the average content of MgO in inclusions was further increased to 46.79wt.%, and a small amount of pure MgO inclusions were generated. With the reaction time increase to 30 min, the average content of SiO_2 decreased to 0.22wt.% and the average content of Al_2O_3 and MgO increased to 37.18wt.% and 62.59wt.% respectively. With the reaction time increased to 90 min, the average content of MgO in inclusions was reduced to 37.63wt.%. Figure 8 shows the morphology and elemental mapping of five types of inclusions in the steel: SiO_2-MnO-Al_2O_3-CaO-MgO inclusion with a globular shape (Fig. 8a), SiO_2-Al_2O_3-CaO-MgO inclusion that MgO-Al_2O_3 was surrounded by a SiO_2-Al_2O_3-CaO-MgO system out layer(Fig. 8b), MgO-Al_2O_3 inclusions with an irregular shape(Fig. 8c), MgO-Al_2O_3 inclusion that MgO was surrounded by a MgO-Al_2O_3 system out layer(Fig. 8d), MgO inclusions with a small amount of MgO-Al_2O_3(Fig. 8e).

Figure 9 shows the variation trend of the number density and the average diameter of inclusions in the molten steel reacted with MgO-C refractory with an increase in contact time. The average diameter of inclusions increased from 1.52 μm to 3.59 μm with the contact time. The number density of inclusions increased from 4.99 /mm^2 to 30.57 /mm^2 with the contact time increasing from 0 to 60 min and then decreased to 21.57 /mm^2 when the contact time was 90 min due to inclusions floating up.

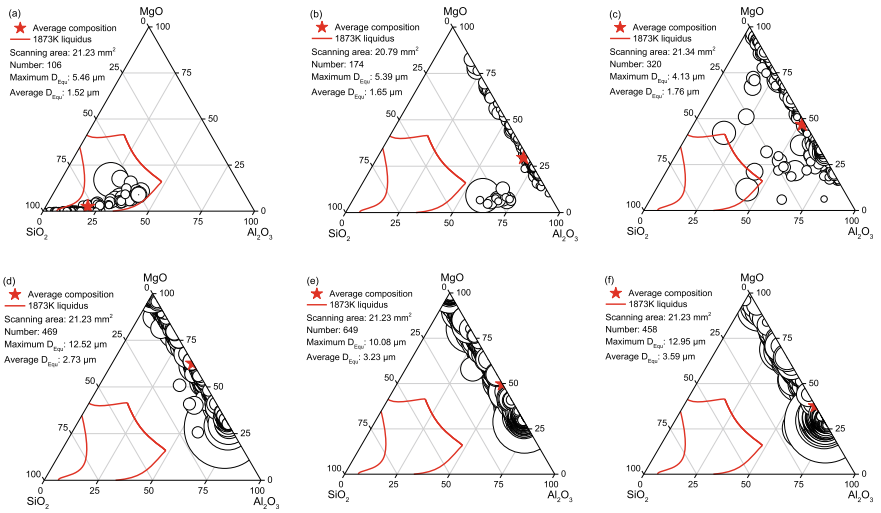

Fig. 7 Evolution of inclusions in the steel reacted with MgO-C refractory *versus* time: **a** 0 min; **b** 5 min; **c** 10 min; **d** 30 min; **e** 60 min; **f** 90 min

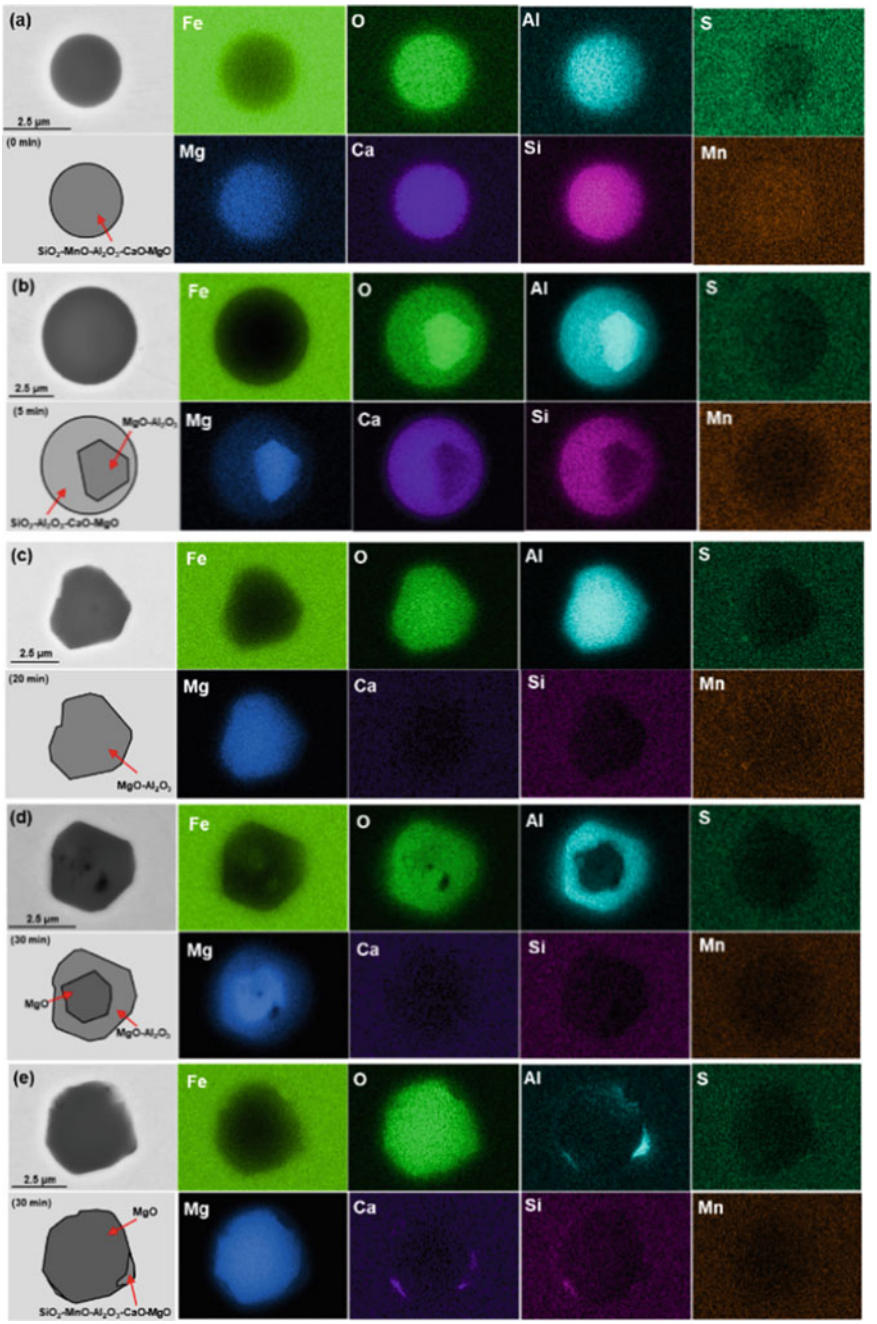

Fig. 8 Typical inclusion in the steel reacted with MgO-C refractory at a certain reaction time

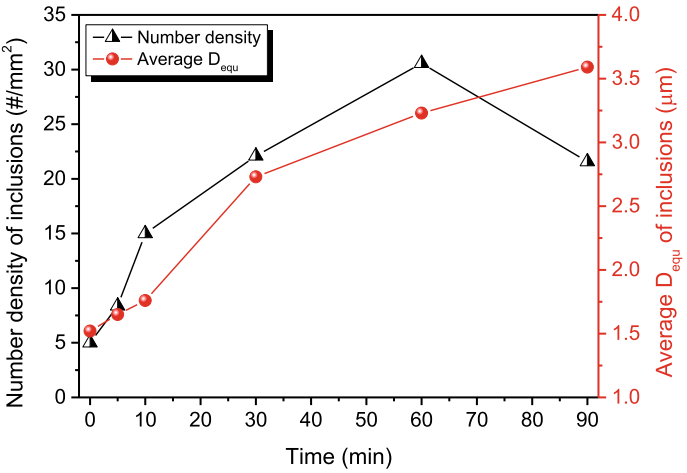

Fig. 9 Number density and average diameter of inclusions in the steel versus time

Thermodynamic Calculations

The equilibria between the steel and the refractory were thermodynamically calculated using FactSage7.1 using the equilibrium module. The thermodynamic databases FToxid, FTmisc, and FactPS were selected. The compositions of the steel and refractories are shown in Tables 1 and 2 respectively. The immersion depth of the refractory rod in the molten steel is 30 mm and a layer of 1 mm of the refractory would correspond to about 2.69 g of refractory as Fig. 3b. The interaction at 1600 °C and 1 atm between the 800 g steel and an increasing amount from 0 to 10 g of the refractory was calculated.

Refractory Composition

The evolution of the composition of the liquid slag phases and spinel in the refractory are shown in Figs. 10 and 11. Figures 10 and 11 show that the content of liquid oxides (CaO, MgO, Al_2O_3, SiO_2), sulfides (CaS, MgS, Al_2S_3, SiS_2) and spinels in case for MgO refractory was approximately constant and equal to the content in case for 0 g MgO refractory. Meanwhile, the content of sulfides and spinels was small. This indicates that no interface layer containing oxides, sulfides, and spinels was formed between the MgO refractory and high-carbon SiMn-killed steel. The calculated results were consistent with the experimental results as shown in Fig. 4a. Figure 11 shows that the amount of the spinel was high in MgO-C refractory due to having antioxidant Al compared with MgO refractory. The content of spinels in the refractory increased with the content of refractory from 0 g to 1.2 g and then

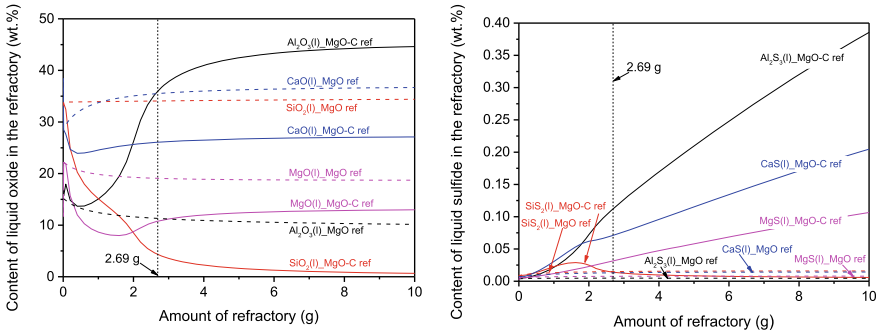

Fig. 10 Content of generated oxides and sulfides at the interface varied with the mass of the lining refractory reacted with 800 g molten steel

Fig. 11 Content of spinels at the interface varied with the mass of the lining refractory reacted with 800 g molten steel

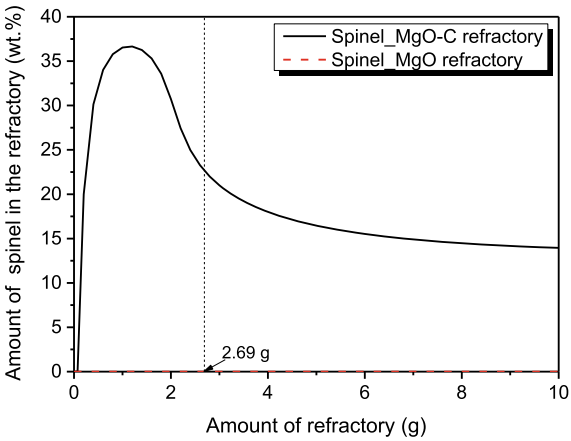

decreased, which caused the content of CaO, MgO, and Al_2O_3 to first decrease and then increase. The increase in SiO_2 content may be due to the reaction with [Al] in the steel to generate [Si]. The concentration of sulfides containing CaS and MgS increased increasingly in the MgO-C refractory due to oxides reduced by the C to gas phase within the refractory increasingly and then reacted with [S] in the interface. The calculated results were consistent with the experimental results as shown in Fig. 4b.

Steel Composition

The concentration of [Al], [Mg], [C], [Si], [O], and [S] in the molten steel at 1600 °C from the interaction between the steel and the refractory were shown in Fig. 12. The concentration of elements in the molten steel reacted with the MgO refractory

changed little compared with MgO-C refractory, which indicated that MgO refractory has little influence on the high-carbon SiMn-killed steel. The content of [Al], [Mg], [C], and [Si] in the molten steel increased with increasing MgO-C refractory amount. The content of [Al] and [C] increased due to the dissolution of C and Al from MgO-C refractory. The content of [Mg] and [Si] increased due to the MgO and SiO_2 in the refractory being reduced by carbon to gas and then dissolved in the molten steel. The content of [S] in the molten steel decreased with increasing MgO-C refractory amount due to the formation of a sulfide layer at the interface. This indicated that the occurrence of the desulfurization of the steel when reacted with MgO-C refractory. The dissolution of C from the refractory in the steel shifts the concentration of [O] in the steel to lower values. The measured values of T.Mg, T.Si, and T.C of the steel were compared to the thermodynamically calculated values of [Mg], [Si], and [C] in the molten steel as shown in Fig. 13. The measured values of T.Si and T.C were consistent with the thermodynamically calculated values of [Si] and [C]. The measured values of T.Mg are greater than the thermodynamically calculated values of [Mg], which may be caused by the fall-off of the MgO-C refractory.

Inclusion Composition

To analyze the source of inclusions in the molten steel after reacting with the refractory, thermodynamic calculations were conducted and results are depicted in Fig. 14. Results showed that endogenous inclusions were inexistence in the steel after reacted with MgO and MgO-C refractory in 1600 °C. However, SiO_2-MnO-Al_2O_3-CaO-MgO inclusions were observed in the molten steel reacted with the MgO refractory, and some complex inclusions containing MgO and MgO-Al_2O_3 were observed in the molten steel reacted with the MgO-C refractory as shown Figs. 5 and 7 respectively. According to experimental results and calculation results, it can be inferred that SiO_2-MnO-Al_2O_3-CaO-MgO inclusions are initial inclusions in the molten steel, and complex inclusions containing MgO and MgO-Al_2O_3 are mainly derived from the fall-off of the MgO-C refractory. For the MgO-Al_2O_3 inclusion, two possible reactions are proposed as shown in Eqs. (4 and 5). The MgO particles from the fall-off of MgO-C refractory, as Fig. 4b, interacted with the Al_2O_3 inclusions or the dissolved [Al] and [O] in the molten steel to generate MgO-Al_2O_3.

$$\mathrm{MgO(s)} + 2[\mathrm{Al}] + 3[\mathrm{O}] = \mathrm{MgO} \cdot \mathrm{Al_2O_3(s)} \tag{3}$$

$$\mathrm{MgO(s)} + \mathrm{Al_2O_3(s)} = \mathrm{MgO} \cdot \mathrm{Al_2O_3(s)} \tag{4}$$

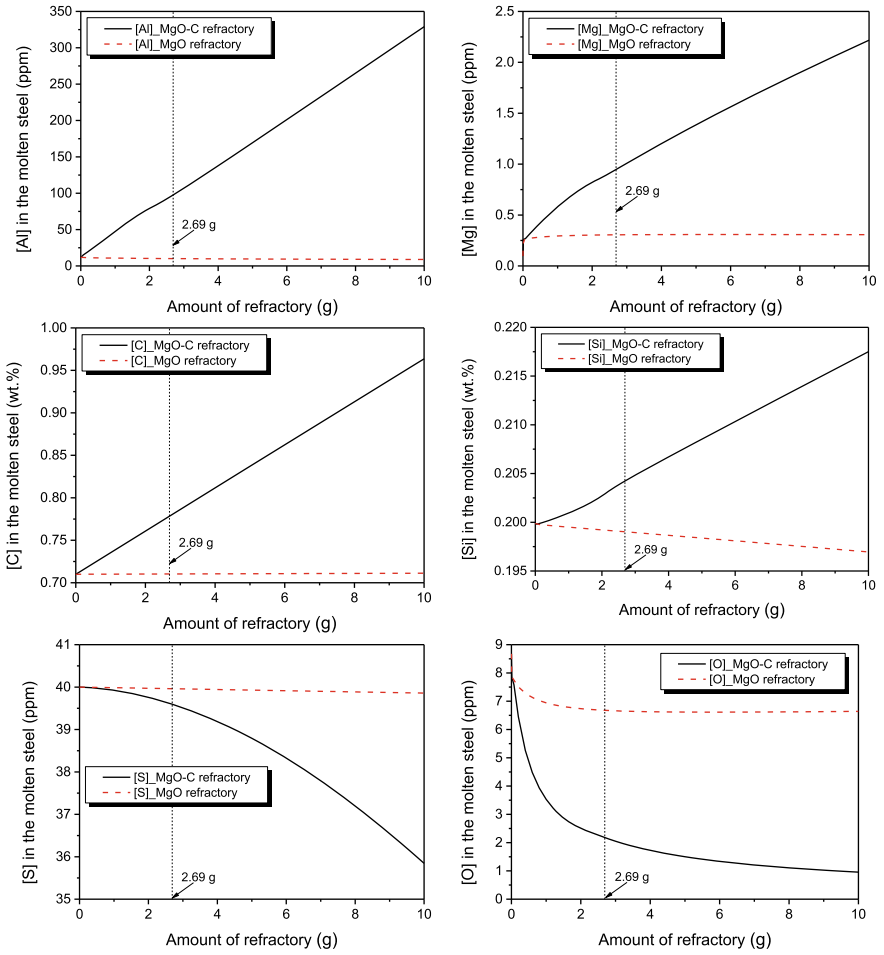

Fig. 12 Concentration of [O], [S], [Al], [Mg], [C], and [Ca] in the 800 g molten steel at 1600 °C reacting with lining refractory

Conclusions

In the current study, interactions of a high-carbon SiMn-killed steel and two kinds of industrial refractories containing MgO refractory and MgO-C refractory were investigated via laboratory experiments and thermodynamic calculations. The MgO-C refractory on the steel cleanliness and corrosion degree of the refractory in comparison with MgO refractory were analyzed. The morphology and composition of the refractory/steel interface layer and inclusions in the molten steel were performed. The following results were obtained.

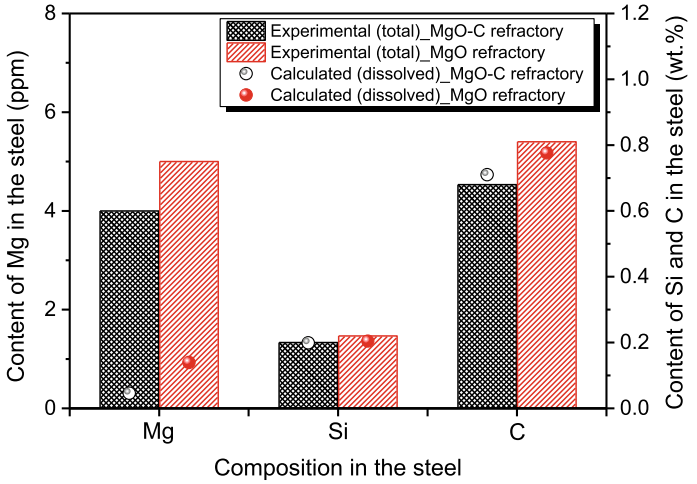

Fig. 13 Comparison between the measured and the calculated composition of the steel

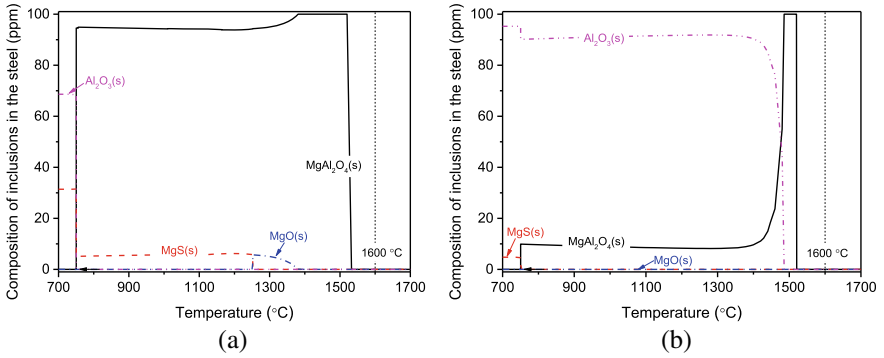

Fig. 14 Composition of inclusions in the steel reacting with lining refractory: **a** MgO refractory; **b** MgO-C refractory

(1) After 90-min contact, the penetration of the molten steel into the MgO refractory was little and abundant molten steel penetrated MgO-C refractory for 1 mm through grain boundaries, and the channels were formed by the consumption of graphite when reacted with high-carbon SiMn-killed steel.

(2) After 90-min contact, the interfacial reaction layer was little observed near the surface of the MgO refractory. A new 80 μm thick interface layer containing CaO-CaS-MgO-MgS was generated between the MgO-C refractory and high-carbon SiMn-killed steel. The consumption of carbon in the MgO-C refractory causes the detaching of MgO particles from the large MgO grains through the loosening of such particles and their consequent floating on the side of the steel.

(3) After 90-min contact, the effect of MgO refractory on inclusions in high-carbon SiMn-killed steel was little, and the primary inclusions in the steel were SiO_2-MnO-Al_2O_3-CaO-MgO inclusions. The effect of MgO-C refractory on inclusions in high-carbon SiMn-killed steel was great. Primary inclusions in the steel were complex inclusions containing MgO and MgO-Al_2O_3 and were mainly derived from the fall-off of MgO-C refractory.

Acknowledgements The authors are grateful for support from the Natural Science Foundation China (Grant No. U22A20171), and the High Steel Center (HSC) at North China University of Technology, Yanshan University and University of Science and Technology Beijing.

References

1. Zhang L, Thomas BG (2006) State of the art in the control of inclusions during steel ingot casting. Metall Mater Trans B 37(5):733–761
2. Zhang L, Guo C, Yang W, Ren Y, Ling H (2017) Deformability of oxide inclusions in tire cord steels. Metall Mater Trans B 49(2):803–811
3. Yilmaz M, Ertunc HM (2007) The prediction of mechanical behavior for steel wires and cord materials using neural networks. Mater Des 28(2):599–608
4. Yilmaz M (2006) Failures during the production and usage of steel wires. J Mater Process Technol 171(2):232–239
5. Guo C, Ling H, Zhang L, Yang W, Ren Y, Zhou H (2017) Effect of slag basicity adjusting on inclusions in tire cord steels during ladle furnace refining process. Metall Res Technol 114(6):602
6. Wang K, Jiang M, Wang X, Wang Y, Zhao H, Cao Z (2016) Formation mechanism of CaO-SiO_2-Al_2O_3-(MgO) inclusions in Si-Mn-killed steel with limited aluminum content during the low basicity slag refining. Metall Mater Trans B 47(1):282–290
7. Shinsho Y, Nozaki T, Sorimachi K (1988) Influence of secondary steelmaking on occurrence of non-metallic inclusions in high-carbon steel for tire cord. Wire J Int 21(9):145
8. Lombaerts J, Lefever I (1992) Non-metallic Inclusions in steel for tire cord. Clean Steel 4:26–42
9. Chen S, Jiang M, He X, Wang X (2012) Top slag refining for inclusion composition transform control in tire cord steel. Int J Minerals Metall Mater 19(6):490–498
10. Iemura K, Ichihashi H, Kawami A, Mizutani M (1986) Steelmaking process for high-carbon tyre cord steel. Clean Steel 3:160–167
11. Imashuku S (2021) Identification of MgO·Al_2O_3 spinel on MgO refractory for aluminum deoxidation process of stainless steel using cathodoluminescence and X-ray excited optical luminescence imaging. Metall Mater Trans B 53(1):190–197
12. Alhussein A, Yang W, Zhang L (2019) Effect of interactions between Fe-Al alloy and MgO-based refractory on the generation of MgO·Al_2O_3 spinel. Ironmaking Steelmaking 47(4):424–431
13. Nightingale SA, Monaghan BJ, Brooks GA (2005) Degradation of MgO refractory in CaO-SiO_2-MgO-FeO_x and CaO-SiO_2-Al_2O_3-MgO-FeO_x slags under forced convection. Metall Mater Trans B 36(4):453–461
14. Zhang S, Marriott NJ, Lee WE (2001) Thermochemistry and microstructures of MgO-C refractories containing various antioxidants. J Eur Ceram Soc 21(8):1037–1047
15. Luz A, Leite F, Brito M, Pandolfelli V (2013) Slag conditioning effects on MgO-C refractory corrosion performance. Ceram Int 39(7):7507–7515
16. Kahrizsangi SG, Dehsheikh HG, Karamian E (2017) Impact of Titania nanoparticles addition on the microstructure and properties of MgO-C refractories. Ceramics Intt 43(17):15472–15477

17. Yu C, Ding J, Deng CJ, Zhu HX, Peng N (2018) The effects of sintering temperature on the morphology and physical properties of In Situ Si_3N_4 bonded MgO-C refractory. Ceram Int 44(1):1104–1109
18. Zhang S, Lee WE (2001) Influence of additives on corrosion resistance and corroded microstructures of MgO-C refractories. J Eur Ceram Soc 21(13):2393–2405
19. Mukai K (1992) Wetting and Marangoni effect in iron and steelmaking processes. ISIJ Int 32(1):19–25
20. Jansson S, Brabie V, Jonsson P (2005) Corrosion mechanism and kinetic behaviour of MgO-C refractory material in contact with CaO-Al_2O_3-SiO_2-MgO slag. Scand J Metall 34(5):283–292
21. Malfliet A, Mazzon A, Otegbeye OO, Qiu Z, Butin G, Eliazord N, Willoughby C, Touzo B, Guo M (2023) Impact of antioxidants in MgO-C refractory on steel cleanliness and refractory degradation. Open Ceramics 14:100352
22. Atzenhofer C, Harmuth H (2021) Phase formation in MgO-C refractories with different antioxidants. J Eur Ceram Soc 41(14):7330–7338
23. Liu C, Gao X, Kim SJ, Ueda S, Kitamura SY (2018) Dissolution behavior of Mg from MgO-C refractory in Al-killed molten steel. ISIJ Int 58(3):488–495
24. Liu C, Huang F, Suo J, Wang X (2016) Effect of magnesia-carbon refractory on the kinetics of MgO·Al_2O_3 spinel inclusion generation in extra-low oxygen steels. Metall Mater Trans B 47(2):989–998
25. Chen L, Chen W, Hu Y, Chen Z, Xu Y, Yan W (2016) Effect of Al antioxidant in MgO-C refractory on the formation of Al_2O_3-rich inclusions in high-carbon steel for saw wire under vacuum conditions. Ironmaking Steelmaking 45(3):272–279
26. Deng Z, Cheng L, Chen L, Zhu M (2019) Effect of refractory on nonmetallic inclusions in Si-Mn-killed steel. Steel Res Int 90(12):190026801–190026820
27. Li Y, Yang W, Zhang L (2020) Formation mechanism of MgO containing inclusions in the molten steel refined in MgO refractory crucibles. Metals 10(4):4441–4449
28. Wang L, Zhu H, Zhao J, Song M, Xue Z (2022) Steel/refractory/slag interfacial reaction and its effect on inclusions in High-Mn High-Al steel. Ceram Int 48(1):1090–1097
29. Liu C, Huang F, Suo J, Wang X (2016) Effect of magnesia-carbon refractory on the kinetics of MgO·Al_2O_3 spinel inclusion eneration in extra-low oxygen steels. Metall Mater Trans B 47(2):989–998
30. Yuan C, Liu Y, Li G, Zou Y, Huang A (2022) Adsorption mechanism of oxide inclusions by microporous magnesia aggregates in Tundish. Ceram Int 48(1):427–435
31. Robinson P (1966) Some observations on unused and used refractories from oxygen steelmaking vessels. Refr. J. 42(6):218–222
32. Watanabe A, Takahashi H, Nakatani F (1986) Mechanism of dense magnesia layer formation near the surface of magnesia-carbon Brick. J Am Ceram Soc 69(9):213–214
33. Kim SM, Lu WK (1978) Kinetics and mechanism of the formation of dense MgO layer in pitch-bearing magnesite brick during service. Metall Trans B 9(3):353–364
34. Brezny B, Healy G, Simkovich G (1973) Equilibrium partial pressures of Mg, SiO, and CO in carbon-containing magnesite refractories. J Am Ceram Soc 56(11):611–612
35. Brabie V (1997) A study on the mechanism of reaction between refractory materials and aluminium deoxidised molten steel. Steel Res 68(2):54–60

Effect of Stirring and Lanthanum in the Steel on the Interfacial Reaction Between the Steel and the MgO-C Refractory

Mingzhe Zhao and Lifeng Zhang

Abstract In the current study, laboratory experiments were performed to investigate the interfacial reaction between the molten steel and the MgO-C refractory, and the effect of lanthanum in the steel was studied. A dense MgO reaction layer with a 50 μm thickness at the interface between the quiescent steel without lanthanum and the refractory was observed. Under stirring condition, the thickness of the MgO reaction layer was only 25 μm and the layer was non-continuous and broken at some places. For the interfacial interaction between the lanthanum-bearing steel and the MgO-C refractory, under quiescent condition, a double-layer structure was generated, with a MgO layer close to the refractory side and a La_2O_3 layer close to the steel side. Under stirring condition, a La_2O_3-La_2O_2S layer was generated and a few $LaAlO_3$ particles were embedded inside the MgO reaction layer. The stirring induced the dislodgement of MgO particles from the lining refractory into the molten steel.

Keywords Interfacial reaction · Lanthanum-bearing steel · MgO-C refractory

Introduction

During the steelmaking process, the refractory material is in direct contact with molten steel. The chemical corrosion and physical scouring of molten steel on the refractory material are inevitable, which significantly reduces the service life of the ladle lining. This limitation affects the steel quality and smelting safety [1]. It is well known that the addition of rare earth elements can modify the inclusions in steel and improve its mechanical properties [2–5]. However, due to their strong

M. Zhao
School of Materials Science and Engineering, Yanshan University, Qinhuangdao 066004, China

L. Zhang (✉)
School of Mechanical and Material Engineering, North China University of Technology, Beijing 100144, China
e-mail: zhanglifeng@ncut.edu.cn

S. Wagstaff et al. (eds.), *Materials Processing Fundamentals 2024*, The Minerals, Metals & Materials Series, https://doi.org/10.1007/978-3-031-50184-5_14

chemical activity, rare earth elements readily react with refractory materials during the steelmaking process. Yu et al. [6] investigated the interfacial reaction between rare earth steel and different kinds of refractory materials. It was found that there are great differences in the reaction mechanisms between various refractory materials and rare earth steel. SiO_2 refractory can react with rare earth steel to form a glass phase with a low melting point, which can accelerate the corrosion of refractory materials. For the reaction between Al_2O_3 refractory and rare earth steel, a silicate phase with a high melting point was observed. This phase exhibits a weak adsorption force for the inclusions. However, the low melting point glass phase formed by the reaction between silica-aluminum refractory and molten steel exhibits stronger adsorption forces compared to the inclusion. Wang et al. [7, 8] reported that the rare earth element lanthanum in the steel first reacts with Si-Mn-Al-O inclusions and then reacts with the refractory material. Sun et al. [9] investigated the effect of cerium content on the interaction between stainless steel and Al_2O_3 refractory. The results indicate that during the initial reaction, the Al_2O_3 inclusion in the steel was reduced by dissolved cerium, forming Ce-Al-O composite inclusion. However, due to the reaction between the refractory materials and steel, the cerium content in the steel continuously decreases, and the Ce-Al-O composite inclusions are modified to aluminum-rich silicate inclusions. Zhang et al. [10] observed a rare earth oxide layer at the interface between cerium-bearing steel and Al_2O_3-MgO refractory. This reaction layer inhibits the diffusion of molten steel into the refractory and increases the contact angle. However, previous studies on the reaction between rare earth-bearing steel and refractory materials have mostly focused on quiescent conditions, with few studies conducted under dynamic conditions. In the current study, author investigate the interfacial reaction between molten steel and the MgO-C refractory under rotational conditions.

Laboratory Experiment and Analysis

Commercial stainless steel with the composition shown in Table 1 was used as the base material in the experiment. MgO-C refractory rods (Ø 50 × H 150 mm) were cut from commercial MgO-C refractory bricks. The chemical compositions are shown in Table 2. The experimental conditions are shown in Table 3. For the dynamic experiment, the rotational speed was 120 rpm. For the lanthanum-bearing steel, the addition of lanthanum was 1000 ppm.

The experimental setup and procedure are depicted in Figs. 1 and 2. A silicon molybdenum resistance furnace was used to investigate the dynamic interaction

Table 1 Chemical composition of steel (wt.%)

Elemental	C	Mn	Si	Cr	S	T.Al	Ti	N	Ca, Mg
wt.%	0.021	1.08	0.547	11.66	0.0009	0.026	0.117	0.017	< 0.0005

Table 2 Chemical composition of refractory (wt.%)

Composition	MgO	C	Al	SiO_2	CaO	Fe_2O_3	Others
wt.%	77.6	10	4.91	4.41	2.09	0.6	$\leq$ 0.39

Table 3 Experimental condition

Sample	Lanthanum addition (ppm)	Rotational speed (rpm)
M0-0	0	0
M0-120	0	120
M1000-0	1000	0
M1000-120	1000	120

between MgO-C refractory and molten steel. The experimental devices are shown in Fig. 1. 700 g of steel were placed into a crucible made of alumina castable. Argon was then pumped into the resistance furnace, heating the crucible containing steel to 1600 °C. After the steel melted, it was kept at a temperature of 1600 °C for 5 min to ensure uniform composition. Lanthanum alloy was added to the liquid steel, and after 5 min, the MgO-C refractory rod was inserted into the liquid steel. The rod was rotated using an electrical machinery device, as shown in Figs. 1 and 2.

The compositions of the refractory were determined using X-ray fluorescence (XRF) analysis. The steel-refractory boundary was cut to obtain a horizontal cross-section and then polished. The boundary layer was investigated to analyze its morphology, composition, and thickness using scanning electron microscopy (SEM) with energy-dispersive X-ray spectrometry (EDS).

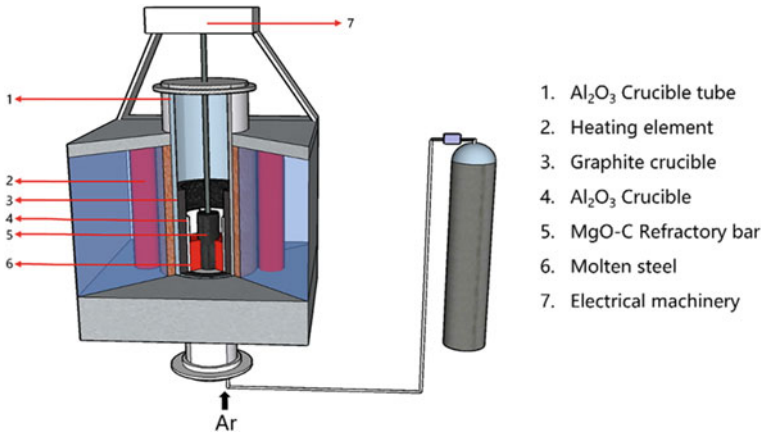

Fig. 1 Schematic of experimental setup

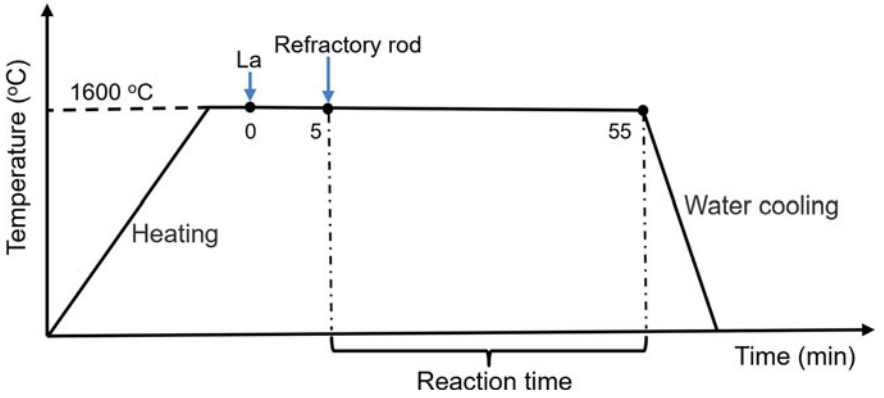

Fig. 2 Schematic of procedure in the present study

Interfacial Reaction Between the Steel and the MgO-C Refractory

Figure 3 displays the typical morphology and elemental diagrams of MgO-C refractories before and after the reaction of refractories with molten steel under quiescent conditions. A significant amount of CaO(-SiO_2) impurities were observed at the boundary of MgO particles, as shown in Fig. 3a. However, after the reaction between the refractory and molten steel, the CaO(-SiO_2) impurity disappears and creates voids, as shown in Fig. 3b. According to the report of Brabie's [11], the reaction equation is presented as follows:

$$\mathrm{CaO(s) + C(s) = Ca(g) + CO(g)} \tag{1}$$

$$\mathrm{SiO_2(s) + C(s) = SiO(g) + CO(g)} \tag{2}$$

At high temperatures, the Ca vapor and SiO vapor generated by reaction Eqs. (1) and (2), diffuse through the pores of MgO particles to reach the interface between the refractory materials and steel.

The morphology and elemental mapping of the typical interface between the quiescent steel without lanthanum and the refractory are shown in Fig. 4. Figure 4b is an enlarged view of Square 1 in Fig. 4a. A dense MgO reaction layer with a thickness of 50 μm was observed at the interface between the steel and refractory. Some molten steel penetrated the refractory, and a dense layer was formed, separating the refractory from the molten steel. The penetration of molten steel into the MgO-C refractory was inhibited, as shown in Fig. 4a. The formation mechanism of the MgO layer has been widely recognized. It has been widely reported that the primary reaction occurring at high temperatures is the reduction of MgO by C within the refractory. The reaction equation is shown in Eq. (3). [12–14] Brabie and Liu et al. [11, 15–17] reported

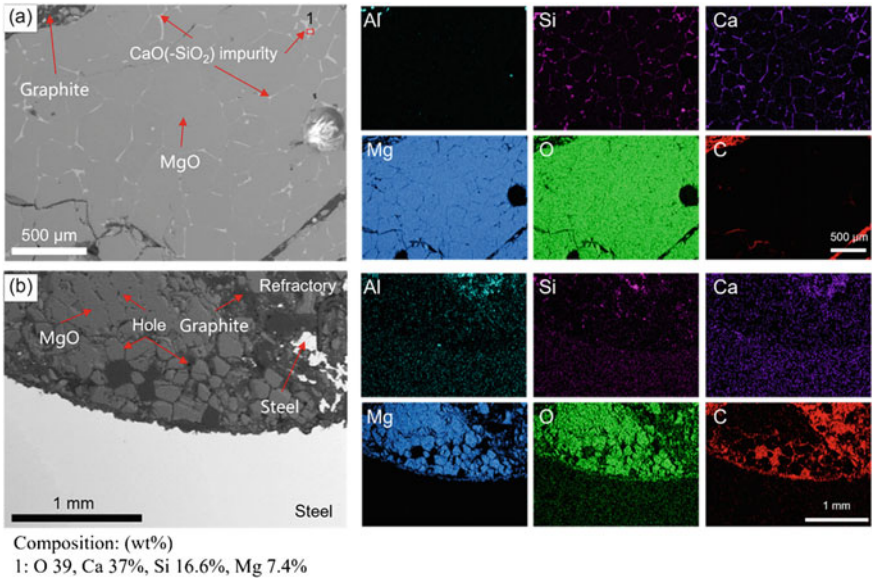

Fig. 3 Morphology and element mapping of the MgO-C refractory under quiescent conditions. **a** Before reaction; **b** after reaction

that at high temperatures, the magnesia-carbon refractory undergoes a reaction to produce magnesium vapor and CO, as shown in Eq. (3). The magnesium vapor can then diffuse towards the interface of the molten steel through the pores of the MgO-C refractory, driven by the concentration gradient. At the interface, the magnesium vapor is oxidized to form MgO, which then condenses and creates a layer of MgO.

$$\mathrm{MgO(s)} + \mathrm{C(s)} = \mathrm{Mg(g)} + \mathrm{CO(g)} \tag{3}$$

Figure 5 shows the morphology and elemental mapping of the interface between the lanthanum-free steel and the refractory under stirring conditions. Figure. 5b, c were the enlarged views of Square 1 and Square 2, respectively, in Fig. 5a. A dense MgO reaction layer with a thickness of 25 μm was observed at the interface between the steel and refractory. However, the layer was found to be non-continuous and broken at certain locations, as shown in Fig. 5a, b. It can be seen that the molten steel penetrated into the refractory through the crack in the MgO layer, as shown in Fig. 5b, c. Under stirring conditions, the impact force of molten steel on the MgO reaction layer was greater than that under quiescent conditions, thereby causing cracks in the reaction layer. In addition, the stirring induced the MgO particles to become dislodged from the MgO-C refractory and enter the molten steel, as shown in Fig. 6. Figure. 6b is an enlarged view of Square 1 in Fig. 6a.

Figure 7 shows the morphology and elemental mapping of the interface between the lanthanum-bearing steel and the MgO-C refractory under quiescent conditions.

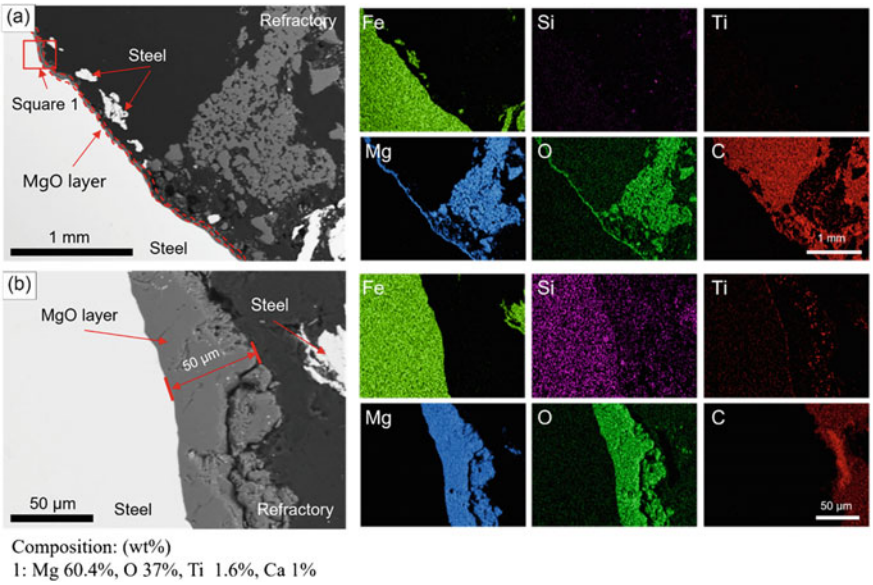

Fig. 4 Morphology and elemental mapping of the typical interface between the quiescent steel without lanthanum and the MgO-C refractory. **b** is an enlarged view of Square 1 in (**a**)

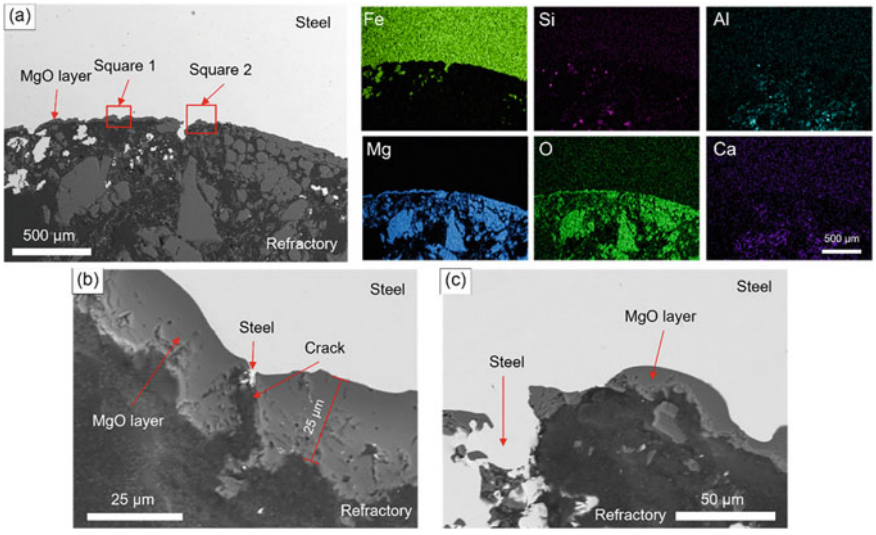

Fig. 5 Morphology and elemental mapping of the interface between the steel without lanthanum and the MgO-C refractory under stirring conditions. **b** is an enlarged view of Square 1 in (**a**); **c** is an enlarged view of Square 2 in (**a**)

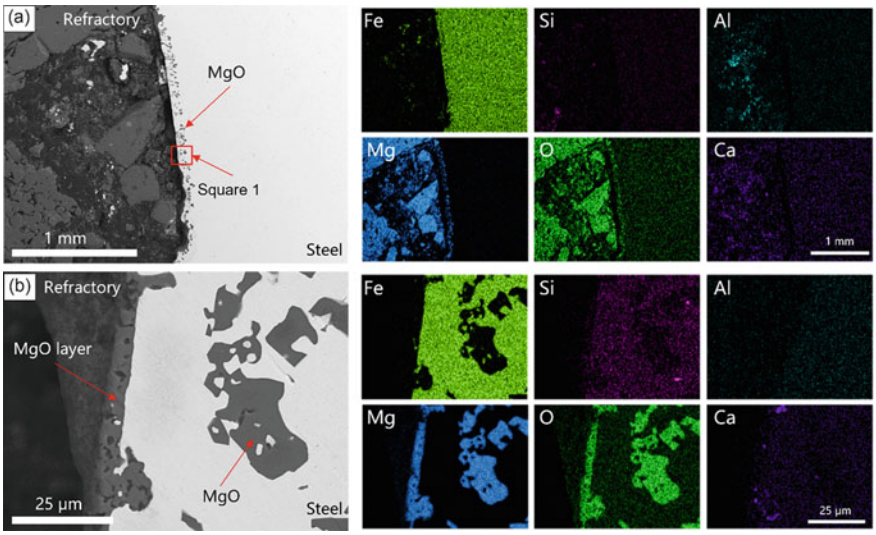

Fig. 6 Morphology and elemental mapping of the interface between the steel without lanthanum and the refractory under stirring conditions. **b** is an enlarged view of Square 1 in (**a**)

A double-layer structure was observed, with a MgO layer close to the refractory side and a La_2O_3 layer close to the steel side, as shown in Fig. 7a. The La_2O_3 layer was only 3–5 μm thick, but it was dense and continuous. The La_2O_3 layer forms as a result of the reaction between dissolved lanthanum in the steel and MgO at the interface between the molten steel and refractory. The reaction equation is presented as follows:

$$2[\mathrm{La}] + 3\mathrm{MgO(s)} = \mathrm{La_2O_3(s)} + 3\left[\mathrm{Mg}\right] \tag{4}$$

Figure 8 shows the morphology and elemental mapping of the interface between the lanthanum-bearing steel and the MgO-C refractory under stirring conditions. A MgO reaction layer was formed at the interface between the steel and refractory, as shown in Fig. 8a. Additionally, a layer containing La was detected outside of the MgO reaction layer. The La-containing reaction layer was primarily composed of La_2O_3 and La_2O_2S, as shown in Fig. 8b. The La_2O_2S layer forms as a result of the reaction between dissolved lanthanum and sulfur in the steel, as well as MgO at the interface between the molten steel and refractory. The reaction equation is presented as follows:

$$[\mathrm{S}] + 2[\mathrm{La}] + 2\mathrm{MgO(s)} = \mathrm{La_2O_2S(s)} + 2\left[\mathrm{Mg}\right] \tag{5}$$

In addition, a few $LaAlO_3$ particles were embedded within the MgO reaction layer, as shown in Fig. 9. Under stirring conditions, the MgO particles formed were drawn into the steel, as shown in Fig. 6a. Subsequently, the MgO particles in the

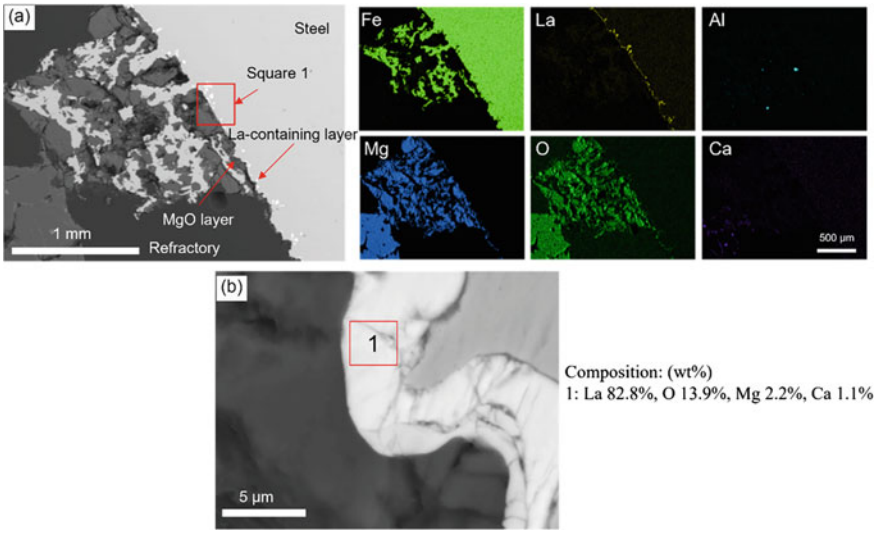

Fig. 7 Morphology and elemental mapping of the interface between the lanthanum-bearing steel and the MgO-C refractory under quiescent conditions. **b** is an enlarged view of Square 1 in (**a**)

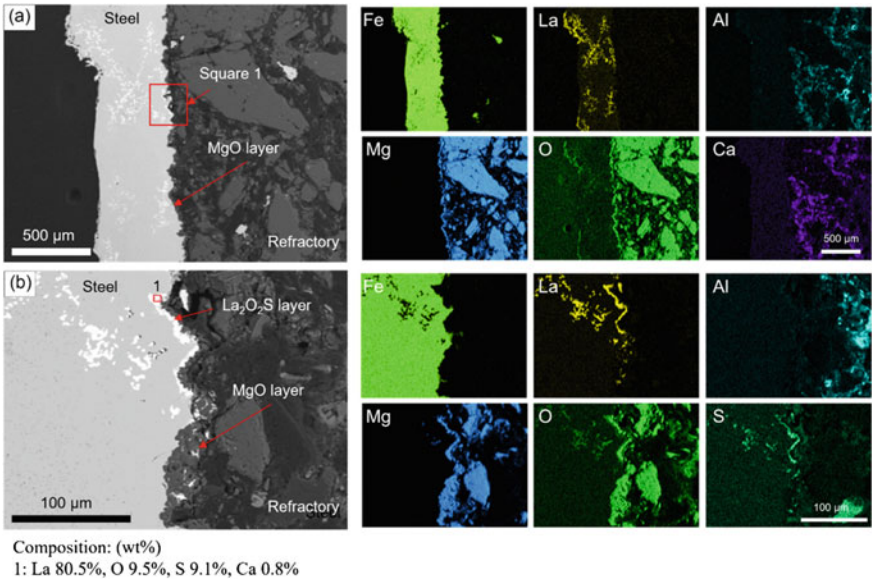

Fig. 8 Morphology and elemental mapping of the interface between the lanthanum-bearing steel and the MgO-C refractory under stirring conditions. **b** is an enlarged view of Square 1 in (**a**)

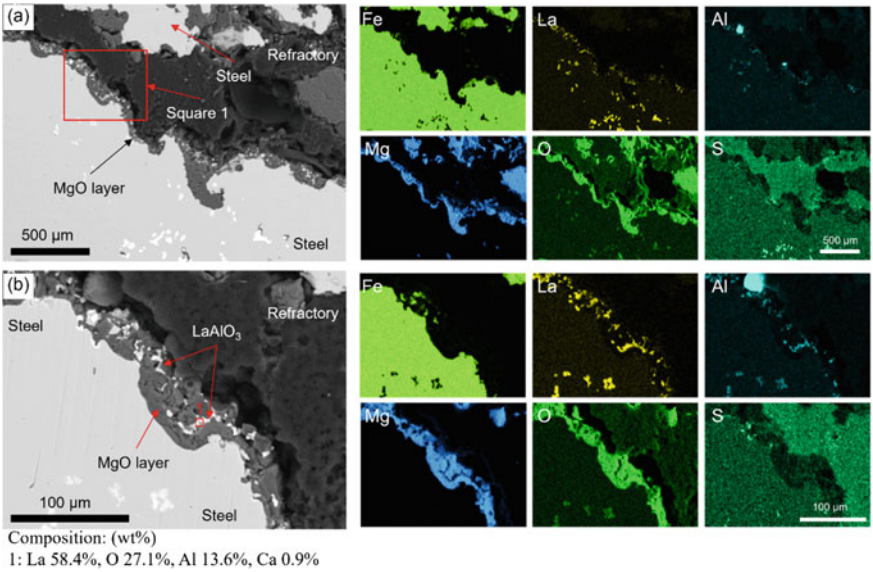

Fig. 9 Morphology and elemental mapping of the reaction layer at the interface between the lanthanum-bearing steel and the MgO-C refractory under stirring conditions. **b** is an enlarged view of Square 1 in (**a**)

steel precipitate to form a reaction layer. At the same time, the lanthanum oxides were formed at the MgO reaction layer, as shown in Fig. 9b. The lanthanum oxides embedded in the MgO layer react with aluminum in the MgO-C refractory to form $LaAlO_3$, as shown in Fig. 9b.

For the interfacial reaction between lanthanum-bearing steel and refractory under stirring conditions, numerous foreign inclusions from the refractory fall off into the steel, as shown in Fig. 10. The MgO particles in the steel initially react with dissolved lanthanum and sulfur to form La_2O_2S and La_2O_3 inclusions, as shown in Eqs. (4) and (5). Then, the lanthanum-containing inclusions react with dissolved titanium and aluminum in the steel to form La-Ti–Al-O inclusions, as shown in Fig. 10. The transformation of inclusion is as follows: MgO → La_2O_2S → La-Ti–Al-O.

Interaction Mechanism

The schematic diagram of the interface reactions between the MgO-C refractory and the molten steel is shown in Fig. 11. Under quiescent conditions, a MgO reaction layer forms at the interface between molten steel and MgO-C refractory. After adding lanthanum to the steel, the dissolved lanthanum diffuses to the interface and reacts with MgO, resulting in the formation of a reaction layer that contains lanthanum. Under stirring conditions, the reaction layer was non-continuous and fragmented.

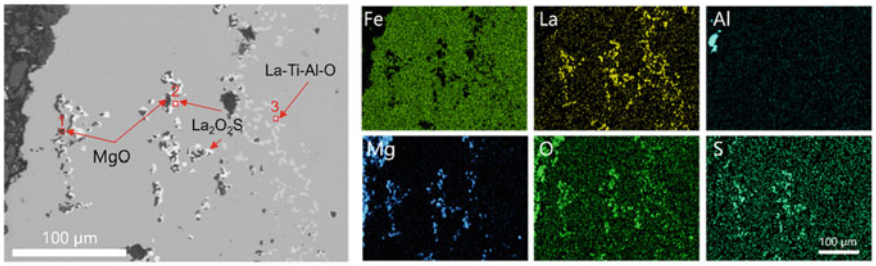

Fig. 10 Morphology and elemental mapping of the interface between the lanthanum-bearing steel and the MgO-C refractory under stirring conditions

The stirring induced the dislodgement of MgO particles from the MgO-C refractory into the molten steel. For the lanthanum-bearing steel, the MgO particles from the refractory are transformed into La_2O_2S and La-Al-Ti–O inclusions.

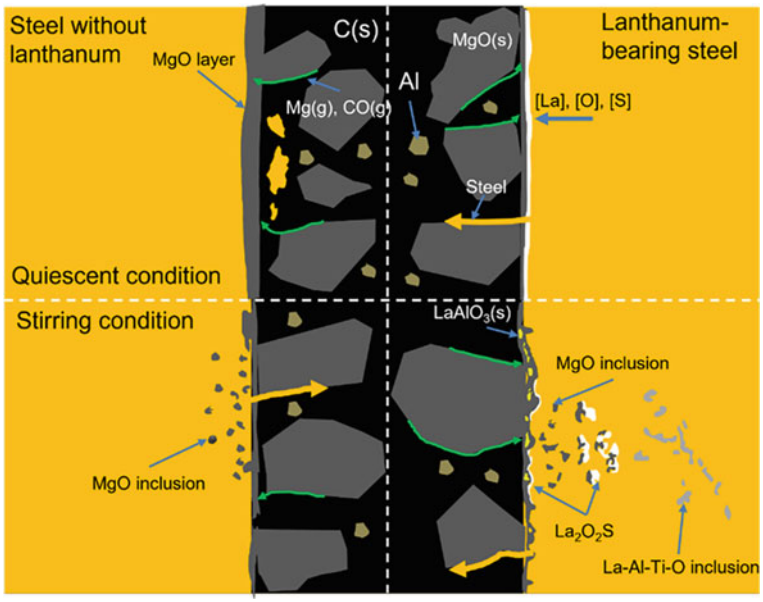

Fig. 11 Schematic of the interaction between steel and refractory

Conclusions

(1) For the reaction between steel without lanthanum and MgO-C refractory, a dense 50 μm thick MgO reaction layer was observed under quiescent conditions. However, under stirring conditions, the thickness of the MgO reaction layer was only 25 μm. Additionally, the layer was non-continuous and broken at certain locations. In addition, the molten steel will penetrate the refractory through the crack in the MgO reaction layer.
(2) After the reaction between lanthanum-bearing steel and MgO-C refractory under quiescent conditions, a double-layer structure is formed. The structure consists of a MgO layer close to the refractory side and a La_2O_3 layer close to the steel side. The La_2O_3 layer can inhibit the penetration of molten steel into refractory materials. Under stirring conditions, a layer of La_2O_3-La_2O_2S was formed, with a few $LaAlO_3$ particles embedded within the MgO reaction layer.
(3) Under stirring conditions, the stirring induced the MgO particles to detach from the refractory lining and enter the molten steel. For the lanthanum-bearing steel, the MgO particles from the refractory will react with dissolved lanthanum, aluminum, and titanium in the steel, resulting in the transformation of inclusions as follows: MgO → La_2O_2S → La-Ti–Al-O.

Acknowledgements The authors are grateful for support from the National Natural Science Foundation of China (Grant No. U22A20171, No. 52104343), the Natural Science Foundation of Hebei Province (Grant No. E2021203222), and the High Steel Center (HSC) at Yanshan University and the High Steel Center (HSC) at North China University of Technology, China.

References

1. Huang A, Wang Y, Gu H, Zou Y (2018) Dynamic interaction of refractory and molten steel: effect of alumina-magnesia castables on alloy steel cleanness. Ceram Int 44(18):22146–22153
2. Wang L (2004) Application prospects and behavior of RE in new generation high strength steels with superior toughness. J Chinese Rare Earths 22(1):48–54
3. Yin N, Jing CL, Li HB, Chu RS, Chen B (2019) Effect of rare earth elements on the inclusion behavior in low alloy structural steel. Mater Sci Forum 944(1):364–372
4. Zhang J, Zhang L (2020) Application and research progress of rare earth elements in stainless steels. J Yanshan Univ 44(3):268–273
5. Liang Y, Shi Z, Li G, Zhang R, Li M (2019) Effects of rare earth modification on microstructure refinement and mechanical properties of Al-2 wt%Fe alloys. Mater Res Express 6(10):106504
6. Yu Z, Zhao W, Xie Y, Yu Q (1983) Investigation on the reaction of refractories with rare earht metals bearing steels and nozzle blockage. Iron and Steel 19(19):3
7. Wang H, Xiong L, Zhang L, Wang Y, Shu Y, Zhou Y (2017) Investigation of RE-O-S-As inclusions in high carbon steels. Metall Mater Trans B 48(6):2849–2858
8. Wang H, Jiang S, Yu P, Sun L, Wang Y (2020) Effect of steel-refractory reactions on removal of arsenic from molten steel with lanthanum additions. ISIJ Int 60(11):2316–2324
9. Kwon SK, Park JS, Park JH (2015) Influence of refractory-steel interfacial reaction on the formation behavior of inclusions in ce-containing stainless steel. ISIJ Int 55(12):2589–2596

10. Zhang L, Cheng L, Ren Y, Zhang J (2020) Effect of cerium on the wettability between 304 stainless steel and MgO–Al_2O_3-based lining refractory. Ceram Int 46(10):15674–15685
11. Voicu B (1997) A study on the mechanism of reaction between refractory materials and aluminium deoxidised molten steel. Steel Res 68(2):54–60
12. Li X, Rigaud M, Palco S (1995) Oxidation kinetics of graphite phase in magnesia-carbon refractories. J Am Ceram Soc 78(4):965–971
13. Volkova O, Scheller PR, Lychatz B (2014) Kinetics and thermodynamics of carbon isothermal and non-isothermal oxidation in MgO-C refractory with different air flow. Metall and Mater Trans B 45(5):1782–1792
14. Wang L, Zhu H, Zhao J, Song M, Xue Z (2022) Steel/refractory/slag interfacial reaction and its effect on inclusions in high-Mn high-Al steel. Ceram Int 48(1):1090–1097
15. Chen L, Chen W, Hu Y, Chen Z, Xu Y, Yan W (2016) Effect of Al antioxidant in MgO–C refractory on the formation of Al_2O_3-rich inclusions in high-carbon steel for saw wire under vacuum conditions. Ironmaking Steelmaking 45(3):272–279
16. Jansson S, Brabie V, Jönsson P (2006) Magnesia–carbon refractory dissolution in Al killed low carbon steel. Ironmaking Steelmaking 33(5):389–397
17. Watanabe A, Takahashi H, Nakatani F (2010) Mechanism of dense magnesia layer formation near the surface of magnesia-carbon brick. J Am Ceram Soc 69(9):213–214

Study on the Key Technology of Preparing Vanadium Base Alloy for Nuclear Power

Heli Wan, Lanjie Li, Wenxiang Tian, Suxin Zhang, and Jiujiang Li

Abstract This paper reports about the key technology of preparing vanadium base alloy (vanadium nitrogen alloy) for nuclear power. The large particle ammonium metavanadate and the control of low-temperature carbonization and high-temperature nitriding reaction process were studied; ultimately, the high nitrogen type vanad-based alloy was obtained. The results show that ammonium metavanadate particles with an average particle size of more than 100 μm can be obtained by metastable control. After physical densification, the maximum compressive strength of the material particles is 120 N/cm^2, and high-density V_2O_3 raw materials are obtained. When the double nitriding method was used in bidirectional nitriding reaction, the nitrogen content in the product was significantly increased, N/V reached 0.22, and the nitriding rate was increased by more than 4.5%. This method breaks through the technical bottleneck of low N/V in traditional vanadium alloys and has a good industrial application prospect.

Keywords Metastable control · Physical densification · Bidirectional nitriding · High N/V ratio · Vanadium alloy

Introduction

Vanadium-containing special steel has excellent characteristics such as high strength and strong corrosion resistance, and it is used in the construction of key structures such as nuclear island foundations and nuclear reactors in nuclear power plants, and the proportion of its use reaches more than 80% [1–5]. With the development goals of "carbon peak" and "carbon neutrality" put forward, the position of nuclear energy in the clean energy low-carbon system will be more important. Therefore, the demand

H. Wan · W. Tian · S. Zhang · J. Li
Chengde Vanadium Titanium New Material Co. Ltd, Chengde 067102, Hebei, China

L. Li (✉)
HBIS Material Technology Research Institute, Shijiazhuang 050023, Hebei, China
e-mail: lilanjie20040014@163.com

S. Wagstaff et al. (eds.), *Materials Processing Fundamentals 2024*, The Minerals, Metals & Materials Series, https://doi.org/10.1007/978-3-031-50184-5_15

for special steel containing vanadium will be more urgent in the future. Vanadium nitrogen alloy is the key intermediate alloy in the production of vanadium-containing special steels, and its N/V ratio (N/V) is a key index that directly affects the properties of vanadium-containing special steels [6–9]. At present, The N/V of the alloy is difficult to be effectively improved in the traditional production process of vanadium nitrogen alloy, which seriously restricts the grain refinement of vanadium in special steel. Furthermore, the properties of strength, corrosion resistance, and creep resistance of vanadium-containing special steel are affected [10–12]. Therefore, breaking through the technical bottleneck of the preparation of high nitrogen vanadium-based multi-element alloys with low N/V and high impurity content in existing vanadium alloys is an important research to support the development of vanadium-containing nuclear steel materials.

In this paper, the preparation of vanadium nitrogen alloy raw materials, the control of the preparation process, and the effect of the application of the alloy were studied. The crystallization regulation of ammonium metavanadate in complex system was studied, and the strengthening mechanism of active nitrogen on carbonization reduction was analyzed. Finally, the key technologies of microalloying of multi-phase regulation-dry granulation secondary reinforcement of raw materials, multi-stage temperature control, and high efficiency micro-positive pressure nitriding fine control products were developed, and the key equipment was optimized. The preparation method of high N/V vanadium nitrogen alloy was obtained by optimizing the conditions. The product has a remarkable application effect in the production of special steel and is helpful to the Industrial application and promotion of high nitrogen vanadium alloy.

Experimental Method

Raw materials used in this study included sodium vanadate solution (>30 g/L provided by CHENGDE VANADIUM TITANIUM NEW MATERIAL Co. LTD), high pure graphite powder (>99% purity), and nitrogen (>95% purity). The main equipment is nitriding push-plate kiln. Adding a certain proportion of ammonium sulfate into sodium vanadate solution, large particles of ammonium vanadate were obtained by adjusting the crystallization temperature (60–80 °C). High-purity V_2O_3 was obtained by calcination of large particles of ammonium vanadate. A high N/V alloy product is obtained when a mixture of vanadium trioxide and graphite is heated to 1200–1447 °C after a reduction nitriding reaction.

Results and Discussion

Study on the Mechanism of Crystallization Process

The quality of ammonium metavanadate directly affects the purity and density of V_2O_3. The traditional preparation method is to obtain ammonium vanadate by precipitation of vanadium with acidic ammonium salt. In the process of vanadium precipitation, there are problems of nucleation of ammonium vanadate, fine grain, and high impurity content. These phenomena have seriously affected its application as raw material for the production of high nitrogen vanadium alloy.

The changes of supersaturation (S) and induction period (ind) of ammonium metavanadate at 60–80 °C were studied. According to classical nucleation theory, $\ln t_{ind}$ and $\ln^{-2}S$ have linear correlation, and the linear equation obtained by fitting the two is shown in Table 1 [13, 14]. The parameters of the induction period change curve of the saturated solution with ammonium metavanadate at different temperatures are shown in Table 1, which indicates that the induction period is gradually shortened with the increase of supersaturation. When the supersaturation is large, the difference of induction period corresponding to different S is small, indicating that the solution crystallizes quickly when the supersaturation is large.

Linear analysis was performed on $\ln t_{ind}$ and $\ln^{-2}S$ under different supersaturations, and the trend diagram was shown in Fig. 1. It can be seen from the figure that when the supersaturation is low, the fitting curve is flatter and the slope is lower. When the supersaturation is greater than a certain value, which is the lower slope of the line (black line), the fitting curve is steeper and the slope increases. According to the state presented by the fitting curve, it can be inferred that the nucleation mechanism in the solution is different under different supersaturation conditions.

When the supersaturation is low, which is the lower slope of the line (red line), the formation of new phase in the solution is mainly heterogeneous nucleation. With the increase of supersaturation, when the value exceeds a certain value, homogeneous nucleation is dominant in the solution. The reason for this phenomenon may be that the increase of supersaturation changes the surface energy between the new phase microcrystals and the solution, which leads to the change of nucleation mechanism in the solution. Therefore, the fitting curves of $\ln t_{ind}$ and $\ln^{-2}S$ appear segmented in different supersaturation ranges.

Table 1 Fitting equations of $\ln t_{ind}$ -$\ln^{-2}S$ at different temperatures

Temperature/K	Hyper-supersaturation	R^2	Low supersaturation	R^2
353	$y = -46.57774 + 3.38705x$	0.95705	$y = 162.69704 + 0.16376x$	0.99581
343	$y = -174.68625 + 36.6493x$	0.99691	$y = 139.32183 + 3.07592x$	0.99896
333	$y = -479.20296 + 30.96329x$	0.9957	$y = 116.65012 + 2.0101x$	0.99998

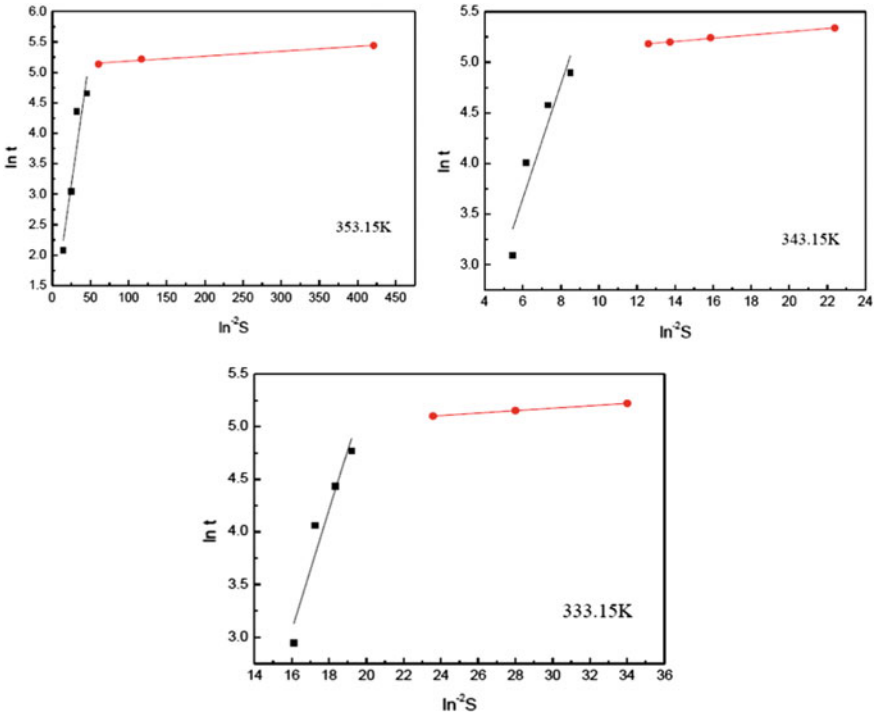

Fig. 1 Crystallization equation of ammonium metavanadate $\ln t_{ind}$-$\ln^{-2}S$ fits the curve

If the two fitted curves with different slopes are lengthened separately, the intersection point is the dividing point of the two nucleation modes, that is, homogeneous and heterogeneous nucleation, and the corresponding horizontal coordinate is the dividing point of oversaturation when the nucleation mechanism changes. At lower oversaturation, heterogeneous nuclei occur in the solution, which are susceptible to interference from impurity ions or external environmental particles during crystallization, which act as the core of crystal growth. However, when the oversaturation is high, the nucleation mode is homogeneous nucleation, there are no other impurity particles in the solution, and the solute molecules rely on each other to nucleate.

Study on Mechanism of Low-Temperature Carbonization and High-Temperature Nitriding

As we all know, the strength and corrosion resistance of special steel can be significantly improved after the addition of vanadium nitrogen to special steel, among which N/V is a key parameter affecting the use of vanadium nitrogen alloy [15, 16]. In the traditional production process of vanadium nitrogen alloy, the vanadium

nitrogen alloy produced has small N/V ratio, poor performance and unstable product quality, making it difficult to meet the demand of vanadium special steel for nuclear power. This paper is to obtain the best reduction and nitriding process route. The high-density V_2O_3 is used as raw material, and the carbonization reduction reaction path of raw material and the synthesis mechanism of nitriding are systematically studied.

Firstly, thermodynamic analysis of the reduction and nitriding reactions of vanadium oxides was carried out. The possible reaction equations in the whole reduction process were shown in (1–4) [17, 18].

$$V_2O_3(s) + C(s) = 2VO(s) + CO(g) \tag{1}$$

$$VO(s) + C(s) = V(s) + CO(g) \tag{2}$$

$$VO(s) + 2C(s) = VC(s) + CO(g) \tag{3}$$

$$V(s) + C(s) = VC(s) \tag{4}$$

Since the carbothermal reduction process of V_2O_3 is carried out step by step, the reaction products may be VO, V, VC. Therefore, the reaction equations that may exist during its nitriding reaction are shown in (5–7).

$$V(s) + 1/2N_2(g) = VN(s) \tag{5}$$

$$V_2O_3 + 3C + N_2(g) = 2VN + 3CO(g) \tag{6}$$

$$VO + 1/2N_2(g) + C = VN + CO(g) \tag{7}$$

$$VC + N_2(g) + VO = 2VN + CO(g) \tag{8}$$

The relationship between the standard Gibbs free energy and the reaction equilibrium constant for all of the above reactions is calculated by thermodynamic software (HSC), as shown in Fig. 2. It can be seen from Fig. 2 that in the range of 0 ~ 1600 °C, the reduction products of V_2O_3 are successively VO, VC, and V in the process of carbothermal reduction. At 1200 °C, the carbon thermal reduction of $_{\triangle}G < 0$. It indicates that in the carbonization reaction stage of V_2O_3, its initial temperature should be selected above 1200°C. In the process of nitriding, according to the calculation results of reactions (6) ~ (8), it can be seen that carbothermal reduction and nitriding are carried out at the same time, but the efficiency of nitriding reaction at this stage is low. As can be seen from the figure: when $\Delta G = 0$, T = 1226.6 °C. Therefore, in order to obtain a higher nitriding reaction efficiency, the nitriding reaction temperature should be selected higher than 1266.6 °C.

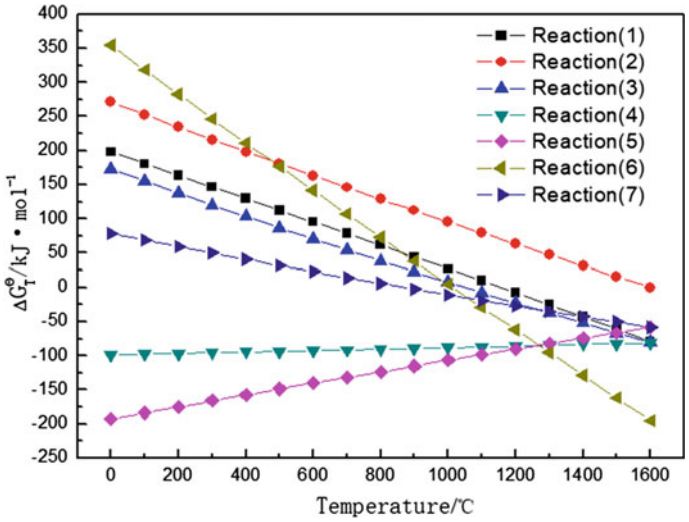

Fig. 2 Gibbs free energy variation in reduction nitriding process

In addition, in the process of low-temperature carbothermal reduction and high-temperature nitriding, due to the presence of a large number of gases in the reaction process and participate in the reaction. The main components of these gases are the generated carbon and oxygen byproducts and nitrogen participating in the sample nitriding process. These gases are mainly nitrogen and participate in the nitriding process of the sample. Therefore, gas pressure changes throughout the reaction process are another key factor affecting reduction and nitriding. The main gas–solid reaction equations involved in the whole reaction process are as follows:

$$V_2O_3 + 3C + N_2(g) = 2VN + 3CO(g) \tag{9}$$

$$\Delta G_R = 418{,}458–316.33\ T + RT \ln (P_{co}/\sqrt{P_{N2}})\ J \cdot mol^{-1}$$

$$K^0 = \frac{\left(\frac{P_{CO}}{P^0}\right)^2}{\frac{P_{O_2}}{P^0}}$$

$$\lg\left(\frac{P_{O_2}}{P^0}\right) = -\ln + 2\lg\left(\frac{P_{CO}}{P^0}\right)$$

From the above equation, we find that $\lg\left(\frac{P_{O_2}}{P^0}\right)$ and $\lg\left(\frac{P_{CO}}{P^0}\right)$ are proportional. Therefore, in the optimal thermal region of V-C-O-N system, the advantages of reduction and nitriding under different temperatures and pressures are studied. $\lg\left(\frac{P_{O_2}}{P^0}\right)$ and $\lg\left(\frac{P_{CO}}{P^0}\right)$ are taken as the plane coordinate system, and FactSage thermodynamic

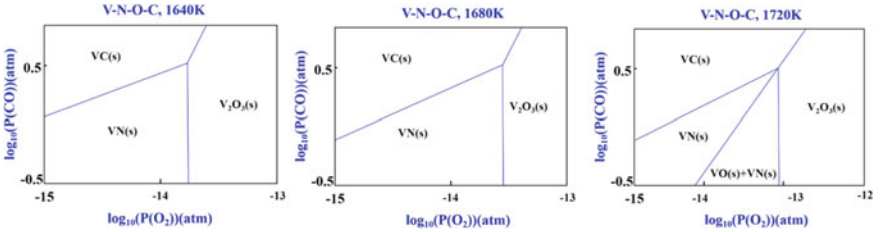

Fig. 3 Hot zone diagram of V–O-C-N system at different temperatures

software is used to analyze the advantageous region diagram of reduction nitriding of V_2O_3 under different temperature conditions, and the results are shown in Fig. 3.

As can be seen from Fig. 3, VC is more easily converted to VN than at 1680 K when the temperature is controlled at 1640 K, in the V-C-O-N main region. It shows that under high-temperature conditions, more stringent CO partial pressure conditions are needed to achieve the conversion of VC to VN. At the high temperature of 1720 K, the dominant region of VN is further reduced, so it can be seen that simply increasing the reaction temperature is not conducive to the reduction of nitriding reaction. Therefore, based on the above analysis results, the optimal temperature of the reduction nitriding reaction should be controlled between 1640 and 1720 K.

Optimization of Reaction Equipment and Application of Products

In this paper, through studying the mechanism of crystallization and nitriding, the mould and nitriding equipment are innovatively optimized and the nitrogen pressure in the kiln is precisely controlled at 5–10 Pa, and the crystallization effect and nitriding efficiency are effectively improved. Large particles of ammonium metavanadate can be continuously and stably prepared, the pass rate is increased to more than 95%, and the average particle size of high-purity ammonium metavanadate after crystallization reaches more than 100 μm, which is used for the production of high-purity and high-density V_2O_3. Finally, the N/V of the vanadium nitrogen alloy produced by this method is 0.22, the impurity content is low and the quality is stable. It can be added to the steel to refine the grain and improve the performance of the special steel material, as shown in Fig. 4.

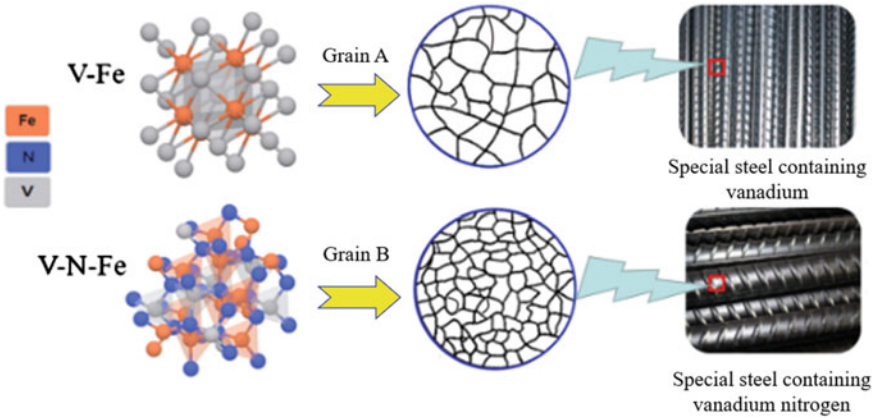

Fig. 4 Application effect of high nitrogen vanadium alloy

Conclusions

In the paper, we carried out the key technology of preparing vanadium base alloy for nuclear power. The results obtained in this study are as follows. The ammonium metavanadate particles with an average particle size of more than 100 μm can be obtained by metastable control. After physical densification, the maximum compressive strength of the material particles is 120 N/cm^2, and high-density V_2O_3 raw materials are obtained. The optimal temperature of the reduction nitriding reaction should be controlled between 1640 and 1720 K. When the double nitriding method was used in bidirectional nitriding reaction the nitrogen content in the product was significantly increased, N/V reached 0.22. In the future, we will continue to pay attention to the large-scale production and application of high nitrogen vanadium alloy.

References

1. Lan HF, Du LX, Misra RDK (2014) Effect of microstructural constituents on strength–toughness combination in a low carbon bainitic steel. Mater Sci Eng A 611:194–200
2. Xie H, Du LX, Hu J, Misra RDK (2014) Microstructure and mechanical properties of a novel 1000MPa grade TMCP low carbon microalloyed steel with combination of high strength and excellent toughness. Mater Sci Eng A 612:123–130
3. Siwecki T, Eliasson J, Lagneborg R, Hutchinson B (2010) Vanadium microalloyed bainitic hot strip steels. ISIJ Int 50(5):760–767
4. Xie ZJ, Fang YP, Han G, Guo H, Misra RDK, Shang CJ (2014) Structure–property relationship in a 960 MPa grade ultrahigh strength low carbon niobium–vanadium microalloyed steel: the signiffcance of high frequency induction tempering. Mater Sci Eng A 618:112–117

5. Sourmail T, Garcia-Mateo C, Caballero FG, Cazottes S, Epicier T, Danoix F, Milbourn D (2017) The inffuence of vanadium on ferrite and bainite formation in a medium carbon steel. Metall Mater Trans 48(9):3985–3996
6. Cao H, Liu Y, Zhao ZW, Ye JW, Tu MS (2007) Study on preparation of vanadium nitride alloy by carbothermic reduction and nitriding. Func Mater 38:3796–3798
7. Huang ZX, Chen WL, Wu HD, Xing JB (2008) Research progress of vanadium nitride. Ferroalloy 39(3):20
8. Li ZT, Wu CJ, Wan HL (2022) Microstructure evolution and work hardening behavior of HotRolled DP780 Ferrite/Bainite dual-phase steel. Adv Mater Sci Eng 2023:1–7
9. Wang YQ et al (2018) Investigating nano-precipitation in a V -containing HSLA steel using small angle neutron scattering. Acta Mater 145:84–96
10. Wang Z, Hui W, Chen Z, Zhang Y, Zhao X (2020) Effect of vanadium on microstructure and mechanical properties of bainitic forging steel. Mater Sci Eng A 771
11. Hu J, Li X, Meng Q, Wang L, Li Y, Xu W (2022) Tailoring retained austenite and mechanical property improvement in Al–Si–V containing medium Mn steel via direct intercritical rolling. Mater Sci Eng A 855
12. Funakawa Y, Shiozaki T, Tomita K, Yamamoto T, Maeda E (2004) Development of high strength hot-rolled sheet steel consisting of ferrite and nanometer-sized carbides. ISIJ Int 44(11):1945–1951
13. Leng YX, Tan Q, Huang CX, Wang J, Zhao H (2016) Determination of metastable zone and induction period of L-tartaric acid aqueous solution. J Chem Eng 067(006):7
14. Wang LG, Yu F, Pan GX, Ying YW, Gong Y, Ni ZM (2009) Influence of pH on crystallization metastable zone, induction period and crystallization rate of magnesium ammonium phosphate. J Chinese Ceramic Soc 37(1)
15. Wang BH, Wu CL, Lu YJ, Wang HL, Wang N (2009) Study on industrial production of high nitrogen vanadium nitride alloy. Non-ferrous Metals: Smelting Parts 7:4
16. Korchynsky M, Glodowski RJ (1998) The role of nitrogen in microalloyed forging steels[A]. In: International conference of forging Brazil[C]. Proto Alegre-RS: US Vanadium Corporation, pp 2–11
17. Dong ZH, Wu CL, Li JJ, Li LJ (2018) Preparation of vanadium ferric nitride alloy by carbothermal reduction. Min Metall 027:64–67
18. Li JJ, Huang CY, Wang N, Zhang ZQ, Wu CL, Sun SN, Li JG, Lu ML (2019) Ferrovanadium nitride (FeVxNy) alloy was prepared by carbothermic reduction and nitriding. Min Metall 12:64–67

Part IV
New Processes

Thermodynamic Analysis of Vacuum Carbothermal Reduction for Synthesis of Ferrosilicon Alloy from Pickling Sludge

Gangqiang Fan, Jianfen Tan, Qun Yang, and Xiaoqian Peng

Abstract In the process of silicon steel sheet production, the hydrochloric acid pickling process was employed to remove the oxides on the surface of the silicon steel sheet. In this process, a lot of pickling sludge was generated and suspended in the acid, which could seriously block the effect of the pickling process, so it must be removed from the acid. However, silicon is not used effectively, which results in a waste of resources. In this study, a new utilization method, synthesis of ferrosilicon alloy from pickling sludge by vacuum carbothermal reduction, has been proposed. The Gibbs free energies of reductions and the reduction sequence had been calculated. The results showed that it obeyed the step-by-step reduction process, and the formation temperature of ferrosilicon alloy decreased with the gas pressure drop. The appropriate reaction conditions were ascertained, which can be employed in the experiments.

Keywords Pickling sludge · Vacuum carbothermal reduction · Ferrosilicon alloys · Thermodynamic analysis

Introduction

In order to reduce greenhouse gas emissions and pollution, and reduce the use of fossil energy, the proportion of clean energy such as hydropower, wind power, nuclear power, and solar energy has gradually increased. Silicon steel sheet has been widely used in the core of electric machines, dynamos, and power transformers for its good magnetic properties, and the silicon steel sheet consumption increases with the increase of electric power generation [1–4]. In silicon steel, the silicon

G. Fan (✉) · J. Tan · Q. Yang · X. Peng
Chongqing Key Laboratory of High Performance Oriented Electrical Steel, Chongqing Wangbian Electric (Group) Corp., Ltd, Chongqing 401254, China
e-mail: fangangqiang@cqwbdq.com

G. Fan
College of Materials Science and Engineering, Chongqing University, Chongqing 400044, China

S. Wagstaff et al. (eds.), *Materials Processing Fundamentals 2024*, The Minerals, Metals & Materials Series, https://doi.org/10.1007/978-3-031-50184-5_16

content is within 7%, and the production process is as follows: iron making, steel making, continuous casting, hot rolling, normalizing and pickling, cold rolling, and high-temperature annealing [3–5].

In the process of hot rolling of silicon steel, due to the high-temperature environment and air atmosphere, the surface of hot rolled silicon steel plate will inevitably form an oxide sheet. The oxide sheet consists of FeO, Fe_3O_4, and Fe_2O_3 successively from inside to outside, and Fe_2SiO_4 phase is formed at the interface between the iron sheet and the matrix, and SiO_2 particles are dispersed on the surface of the matrix [6]. In the normalizing and pickling process, the iron-containing oxide in the oxide sheet reacts with hydrochloric acid and is completely dissolved into hydrochloric acid. SiO_2 particles cannot react with acid and are suspended in the acid liquid. Eventually, SiO_2 particles deposit on the bottom of the device, forming pickling sludge.

In the steel industry, there are abundant iron elements in pickling waste liquid, which can be used to prepare nano-Fe_3O_4 [7, 8] and magnetic materials [9]. The metal elements of pickling waste liquid can also be recovered to prepare alloy powder [10] or other utilizations [11]. The waste liquid of pickling silicon steel contains a lot of pickling sludge, which is treated as solid waste.

Silicon is an important component of silicon steel. The silicon of pickling sludge in industrial production has not been utilized, resulting in a great waste of resources. Therefore, a method of high-value utilization of silica sludge has been proposed in this paper, the preparation of ferrosilicon alloy by vacuum carbothermic reduction of pickling sludge.

Experimental

Materials and Process

The wet silica sludge was obtained from the pickling liquor by the Nutsche filter, washed with distilled water, and then dried at 120 °C for 12 h, to obtain the dry sludge powder. The red mud, as the raw material of ferrosilicon alloy, was prepared from the pickling waste liquor by adding the concentrated ammonium liquid and injecting the air, and then calcined at 800 °C for 1 h. The graphite powder was used as the reductant during the reduction process.

The dry silica sludge powder and dry red mud powder were thoroughly mixed with a predetermined quantity of graphite powder to prepare a cylindrical sample (20 mm in diameter and 30 mm in height). The graphite powder dosage was designed for a molar ratio of 1:1. The sample was heated at 1300 °C or 1400 °C in a vacuum furnace with a pressure of less than 100 Pa (~0.001 atm) for 2 h. The whole experimental process is shown in Fig. 1.

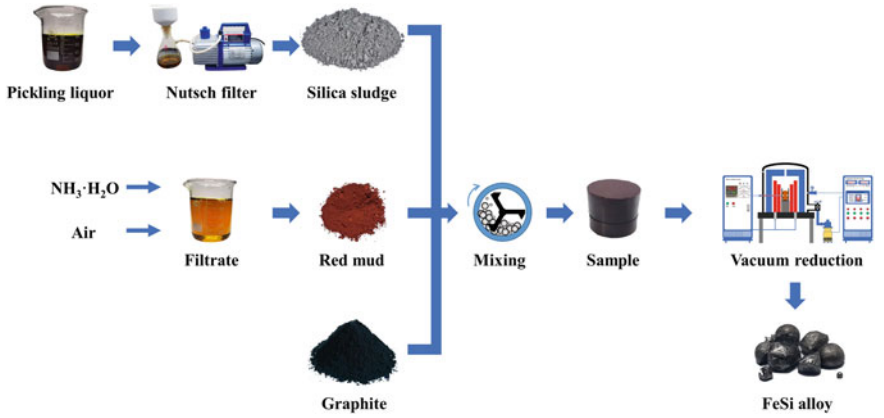

Fig. 1 Schematic diagram for the vacuum carbothermic reduction of pickling sludge

Thermodynamic Calculation Method

In order to predict the reduction process of pickling sludge by vacuum carbothermal reduction, thermodynamic analysis was performed by using FactSage ™ 8.1 with the pure substance database (FactPS) and oxide database (FToxid), based on the Gibbs free energy minimization. The Fe-Si phase diagram was calculated by the phase diagram module, the Gibbs free energies of reductions were calculated by the reaction module, and the reduction sequence was analyzed by the Equilibrium module.

Results and Discussion

Fe-Si Phase Diagram

The Fe-Si phase diagram was calculated by the phase diagram module, as shown in Fig. 2. It can be found that the lowest melting point of Fe-Si binary alloy was 1181 °C with a mass fraction of Si at 17.39%, and the next was 1202 °C with Si at 21.8%. When the silicon content is less than 17.39%, the melting temperature of Fe-Si alloy decreases with the increase of Si content. In the carbothermal reduction process, Fe_2O_3 was first completely reduced to Fe, and then SiO_2 was reduced to Si. The reduced Fe and Si formed the Fe-Si alloy. Taking the reduction temperature at 1400 °C as an example, with the progress of the reaction, metal iron was preferred to be reduced from the ferric oxide as BCC crystal structure, and then silicon is reduced from silicon dioxide. The iron and silicon formed the iron-silicon binary alloy. When the silicon content reaches 6.3 wt.%, the solid with BCC structure begins to transform

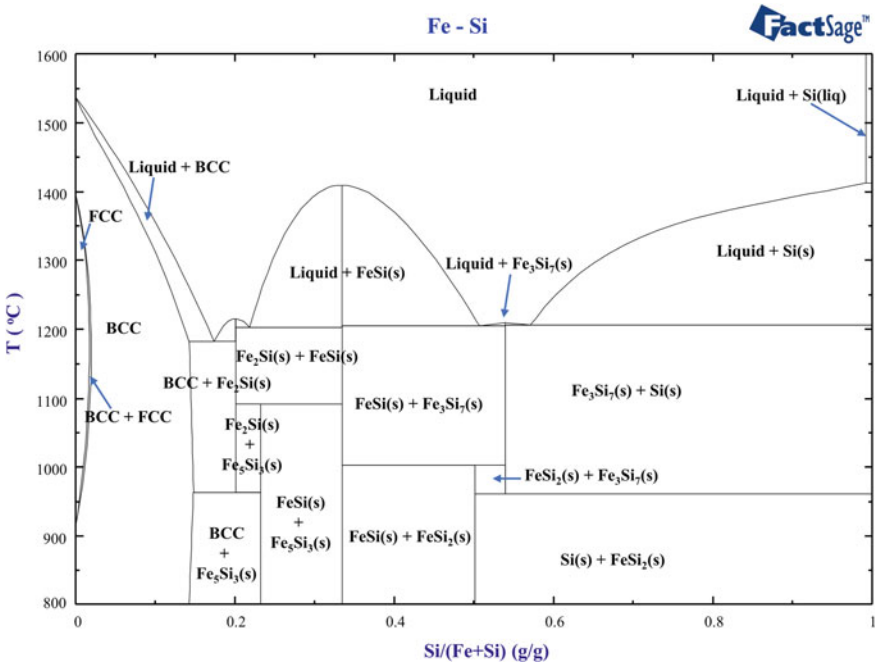

Fig. 2 Fe-Si phase diagram

into a liquid phase. When the silicon content reached 7.8 wt.%, the alloy completely transformed into a liquid phase. The specific reaction process will be discussed in detail later.

Gibbs Free Energies of Reductions

In the vacuum carbothermal reduction process of pickling sludge with ferric oxide, there may exist reactions as follows:

$$3Fe_2O_3 + C = 2Fe_3O_4 + CO \tag{1}$$

$$Fe_2O_3 + C = 2FeO + CO \tag{2}$$

$$1/3Fe_2O_3 + C = 2/3Fe + 3CO \tag{3}$$

$$SiO_2 + C = SiO + CO \tag{4}$$

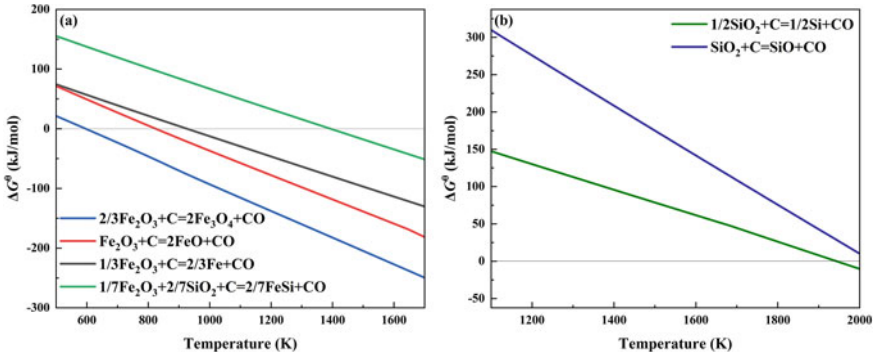

Fig. 3 Relationship of Gibbs free energy of reactions versus temperature

$$1/2\mathrm{SiO_2} + \mathrm{C} = 1/2\mathrm{Si} + \mathrm{CO} \tag{5}$$

$$1/7\mathrm{Fe_2O_3} + 2/7\mathrm{SiO_2} + \mathrm{C} = 2/7\mathrm{FeSi} + \mathrm{CO} \tag{6}$$

The reaction Gibbs free energy above reactions has been calculated, as shown in Fig. 3. It can be found that the ΔG^{θ} of Reaction (1) is always lower than the other reactions, meaning that Reaction (1) can take precedence. When the reaction temperature reaches 1943 K, the ΔG^{θ} of reaction (5) is 0.

Figure 4 shows the effect of the CO partial pressure on the reaction Gibbs free energy of Reaction (6). It can be found that the ΔG^{θ} decreases with the decline of CO partial pressure, indicating that a decline of system pressure is conducive to the formation of Fe-Si alloy by the carbothermal reduction process. When the partial pressure of CO drops to 0.001 atm, the formation temperature of Fe-Si alloy can decrease to 1038 K. The above results proved that the vacuum condition can dramatically promote the carbothermal reduction of SiO_2 with Fe_2O_3.

Reduction Sequence

The reduction sequence of SiO_2-0.5Fe_2O_3 with the additive of C has been calculated by equilibrium calculation as well. In the calculation, the system was set as an open system, with the partial pressure of gas set as 0.001 atm simulating the vacuum environment, and C was added as a reducing agent, with adding 0.005 mol per step for a total of 800 steps. Figure 5 shows the equilibrium results of the reaction at 1300 °C and 1400 °C.

It can be found that Fe_2O_3 is first reduced to Fe_3O_4, then reduced to FeO, which reacts with SiO_2 to form Fe_2SiO_4 (Fayalite), and then Fe_2SiO_4 is reduced to Fe. At 1300 °C, Fe first existed as an FCC structure and then changed to a BCC structure.

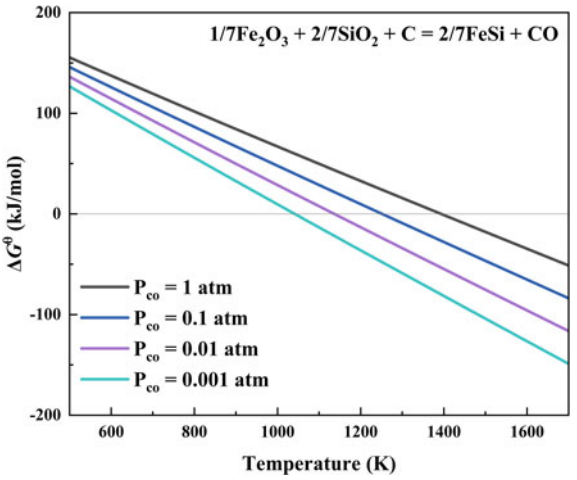

Fig. 4 Effect of the CO partial pressure on the reaction Gibbs free energy of reaction (6)

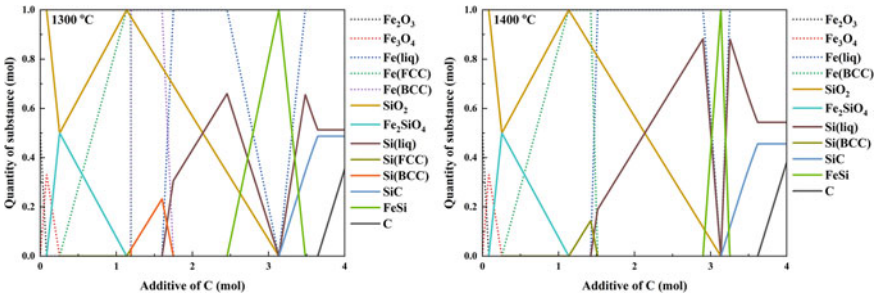

Fig. 5 Calculated equilibrium of SiO_2–$0.5Fe_2O_3$ with the additive of C at different temperatures

While at 1400 °C, Fe exists just as a BCC structure. The difference can be explained from the Fe-Si phase diagram as shown in Fig. 2. After Fe_2SiO_4 has been completely reduced to Fe and SiO_2, SiO_2 begins to be reduced to Si, existing as FCC structure (at 1300 °C) and BCC structure (at 1300 °C and 1400 °C) with Fe. With the increase of Si content, Fe-Si alloys change from solid phase to liquid phase. When the Si content is within a certain range, the Fe-Si solid phase precipitates from the liquid phase. With the increase of the additive of C, the Fe-Si phase transforms into the liquid phase, and at the same time SiC solid phase forms. When the additive of C reaches a certain amount, the SiC reaches the maximum, and then C exists as the residual C.

According to the above equilibrium calculation results, the reduction sequence could be inferred as the following: $Fe_2O_3 + SiO_2 \rightarrow Fe_3O_4 + SiO_2 \rightarrow Fe_2SiO_4 \rightarrow Fe + SiO_2 \rightarrow$ Fe-Si alloy $\rightarrow$ Fe-Si alloy + SiC. The Fe-Si alloy includes FCC structure, BCC structure, and liquid. It is worth noting that the required amount of C for completely reducing SiO_2 to Si is lower than the theoretical value of Eq. (6), because the gas in the equilibrium phase is mainly CO_2 at the early stage of the

reaction. It is one of the imperfections of calculation by an open system, but it can still provide a theoretical reference for the reduction process.

Conclusions

In the pickling process of silicon steel, a large amount of pickling sludge was produced, which was not effectively utilized. In this study, a new utilization method, synthesis of Fe-Si alloy from pickling sludge by vacuum carbothermal reduction, has been proposed. The Fe-Si phase diagram, the Gibbs free energy of reactions, and the reduction sequence were calculated by thermodynamics. The results proved the feasibility of vacuum carbothermal reduction and the phase transition paths at different temperatures can be obtained as the following: $Fe_2O_3 + SiO_2 \rightarrow Fe_3O_4 + SiO_2 \rightarrow Fe_2SiO_4 \rightarrow Fe + SiO_2 \rightarrow$ Fe-Si alloy $\rightarrow$ Fe-Si alloy + SiC.

However, the method described herein is just a technical prototype; more detailed work, such as the reaction mechanism and the optimum reaction condition, needs to be done in the future.

Acknowledgements This research was funded by the China Postdoctoral Science Foundation (Grant No. 2023M730426).

References

1. Zeng W et al (2023) Mechanism of silicon distribution and oxide morphology in the internal oxidation zone of grain-oriented silicon steel during decarburization. Corros Sci 221
2. Leuning N et al (2023) A new approach to measure fundamental microstructural influences on the magnetic properties of electrical steel using a miniaturized single sheet tester. J Magnetism Magnetic Mater 583
3. Moses AJ (2012) Energy efficient electrical steels: magnetic performance prediction and optimization. Scripta Mater 67(6):560–565
4. Yilmaz C et al (2023) Dislocation-assisted particle dissolution: a new hypothesis for abnormal growth of Goss grains in grain-oriented electrical steels. Acta Materialia 258
5. Ros-Yáñez T et al (2004) Advances in the production of high-silicon electrical steel by thermomechanical processing and by immersion and diffusion annealing. J Alloy Compd 369(1–2):125–130
6. Jégou S et al (2021) Influence of oxidizing and Nitriding parameters on nitrogen concentration of electrical steels. Mater Character 182
7. Huang R et al (2014) Ultrasonic Fenton-like catalytic degradation of bisphenol A by ferroferric oxide (Fe_3O_4) nanoparticles prepared from steel pickling waste liquor. J Colloid Interface Sci 436:258–266
8. Guo P et al (2023) Insights into the well-dispersed nano-Fe3O4 catalyst supported by N-doped biochar prepared from steel pickling waste liquor for activating peroxydisulfate to degrade tetracycline. Chem Eng J 464
9. Yi Y et al (2021) Magnetic biochar derived from rice straw and stainless steel pickling waste liquor for highly efficient adsorption of crystal violet. Bioresour Technol 341:125743

10. Wu M-T et al (2019) Harmless treatment and resource utilization of stainless steel pickling sludge via direct reduction and magnetic separation. J Clean Prod 240
11. Shi C et al (2023) Status of research on the resource utilization of stainless steel pickling sludge in China: a review. Environ Sci Pollut Res Int 30(39):90223–90242

Production of Soft Magnetic Composites Using Cold Sintering Technique for Metals

Linsea Foster, Ramakrishnan Rajagopalan, Noor-ul-huda Altaf, and Clive Randall

Abstract Soft magnetic composites are a necessary component to produce efficient electric vehicles. However, the relationship between structure and material properties results in a nearly inevitable trade-off between efficiency and strength. The work presented here investigates a means of directly addressing improvement in both strength and magnetic properties by use of cold sintering technique. The technique utilizes surface modification of individual particles which are warm compacted to improve strength and provide the necessary insulating properties to attain the characteristic soft magnetic properties required for use in electric motors. Materials are investigated using scanning electron microscopy, transmission electron microscopy, energy dispersive X-ray spectroscopy, electron energy loss spectroscopy, 3-point bending tests, 4-point probe tests, permeability measurement, and AC and DC magnetic testing. These characterization methods are used to qualitatively and quantitatively inspect the applicability of the material as a soft magnetic composite. Finally, this study contributes to understanding how to improve strength at relatively low temperature via cold sintering method.

Keywords Cold sintering · Soft magnetic composite · Core loss

Introduction

Powder metallurgy is a robust technique for forming net-shape or nearly net-shape products from powdered metals. This technique is utilized for producing a variety of products, most notably parts for motor vehicles. From sprockets to shock absorbers to pistons, powder metallurgy is essential for producing the cars we drive and will become more critical in the manufacturing of electric cars, specifically for stator and rotor cores. These stators and rotors use the relationship between electricity and magnetism to power electric motors; therefore, the magnetic properties are critical. Current technology uses 2D laminates to form these products, and their

L. Foster (✉) · R. Rajagopalan · N. Altaf · C. Randall
The Pennsylvania State University, State College, PA 16801, USA
e-mail: lhp5038@psu.edu

S. Wagstaff et al. (eds.), *Materials Processing Fundamentals 2024*, The Minerals, Metals & Materials Series, https://doi.org/10.1007/978-3-031-50184-5_17

efficiency is greatly determined from the spacing between neighboring laminates and the thickness of the laminates themselves. Decreasing spacing and thickness improves magnetic properties but becomes increasingly costly [1]. 3D soft magnetic composites made using coated powder metal offer an alternative to these laminates. Rather than restricting the material to two dimensions, 3D soft magnets increase the magnetic flux pathways, increasing efficiency.

The reason for using thin, finely spaced laminates or coated powder metal is to limit magnetic domain size. Reduced particle size increases electrical resistivity, which is imperative to form a soft magnet. Soft magnets are characterized by their low coercivity, allowing for efficient alternation of magnetic orientation. In other words, the material can easily magnetize and demagnetize with frequency, a material requirement for AC electric motors. In addition to low coercivity, SMCs should have high resistivity, high permeability, high magnetic induction, and low core losses, as well as adequate strength. The main issue with forming SMCs is the trade-off between good magnetic properties and good strength. The formation of an insulating coating over individual iron particles limits processing temperature, as many insulating coatings will break down at elevated temperatures.

There are two main categories of insulating coatings which are organics and inorganics. Many organic coatings like thermosets work well to form continuous, uniform layers over particles and are fairly easy to apply. Some of the more popular coatings investigated include epoxies, acrylics, polyesters, and polyurethanes [2–4]. Unfortunately, organic coatings tend to break down at much lower processing temperatures than inorganics. Inorganics tend to be more intricate in their application, but can handle higher processing temperatures, granting greater strength than most SMCs. Common coatings that have been investigated include iron oxides, ferrites, sulfates, and phosphates [2, 4]. Phosphates are favorable for their ease of application and can be used to improve green strength of PM compacts. In this group's previously published work, the use of cold sintering technique was used to apply phosphate coating to improve green strength of iron compacts [5].

The cold sintering technique used a two-step technique to substantially increase green strength. First, the surface is modified using direct addition of a phosphoric acid solution. This resulted in uniformly coated hydrated phosphate on iron particles. Second, the modified powders were warm compacted, which resulted in accelerated particle rearrangement of the hydrated phase, quickly densifying the material, and leaving behind a co-continuous, chemically bonded matrix of phosphate coated iron particles. Although the process here was efficient and easy to apply, phosphates do not have good insulating properties. In the current study here, the authors look to apply an insulating boundary using the same cold sintering process. Application of a copper oxalate-iron oxalate system was considered for improved electrical insulation through cold sintering conditions. Additionally, low-moderate processing temperatures are suspected to transform these oxalate systems to copper and iron oxides, which would improve strength and maintain insulating properties.

Methods

The cold sintering technique utilizes a two-step method, first with surface modification of particles, and then warm compaction. ATOMET-1001 powders were first prepared using surface modification. In this study, co-deposition of copper oxalate and iron oxalate was applied using aqueous chemistry. A solution of 0.0031 mol sodium citrate, 0.100 mol iron (III) nitrate, and 0.031 mol copper sulfate pentahydrate was prepared in 100 mL of water. 250 g of iron powder was added, and a separate 0.010 mol, 100 mL oxalic acid solution was added dropwise and mixed for 10 min. Powders were sufficiently air-dried then warm compacted at 100 °C and pressure of 620 MPa for 10 s, resulting in a cold sintered compact. Compacts further treated under annealing conditions were subjected to air atmosphere and maximum processing temperatures ranging from 300 °C to 800 °C, with a ramp rate of 2 °C/min, and a holding time of 4 h.

Results and Discussion

Cold sintered compacts were examined via scanning electron microscopy (SEM) and electron dispersive X-ray-spectroscopy (EDS). A JEOL JSM-7200F was used to examine the particle boundaries. Samples processed up to 300C displayed nicely defined oxygen and copper boundaries between neighboring particles. To further understand the structure, scanning transmission electron microscopy (TEM) with EDS capabilities and electron energy loss spectroscopy (EELS) was performed using a Talos F200X. This revealed particle boundaries sub-microns thick with distinctive Fe, Fe–O, and Cu regions. EELS confirmed the presence of copper metal rather than copper oxide. Future work aims to achieve copper oxidation through steam treatment, but the present work shows good magnetic results despite the presence of copper metal, which is discussed later in this section.

After examination of compacted samples, the strength of these samples was tested. Conventionally prepared transverse rupture strength (TRS) bars of ATOMET-1001 powder typically yield green strength of about 13 MPa. Some manufacturers and researchers will use warm compaction to improve strength, which here yielded strength of about 21 MPa. In a previous cold sintering study, use of both a hydrated phosphate coating and warm compaction yielded strength of 71 MPa [5]. With the replacement of a hydrated phosphate with copper and iron oxalates, strength was still significantly improved (58 MPa) versus both conventionally prepared and warm compacted samples. Additionally, low temperature annealing at 300°C yielded strength of 116 MPa, which is comparable to many soft magnetic composites both in the market and under study [1, 6–9]. This is despite lower processing temperatures and density not exceeding 7.02 g/cc.

18 g toroids with 1.5″ outer diameter and 1.25″ inner diameter were produced under cold sintering conditions to test the magnetic properties of the material. Some

of these samples were further processed up to 300 °C, 500 °C, or 700 °C. Both DC and AC magnetic testing were performed using a Magnetic Instrumentation SMT-700 magnetic measurement device. Under DC testing maximum permeability, coercivity, remnant magnetization, and magnetization at 20kA/m were collected (Table 1). With increasing maximum processing temperature, permeability also increased due to reduced porosity. Additionally, coercivity increased with increasing temperature up to 500 °C, but dropped by 700 °C, likely due to thermal stressing followed by relieving [10, 11]. Remnant magnetization also increased with rising temperature, which is typical. Magnetization at 20kA/m met or exceeded 1 T for samples subjected to further heat treatment.

Under AC testing, B-H diagrams were produced by testing samples at 100 Hz, 1 kHz, 10 kHz, and 100 kHz up to 42kA/m (Figs. 1, 2, 3 and 4). Samples tested at 100 Hz and 1 kHz exceeded 1 T. Additionally, with increased maximum processing temperature, magnetization increased more rapidly at low magnetic field. Peak magnetization was relatively the same for all samples, at about 1.2 T.

Core losses were also measured and showed that core losses increased with both frequency and maximum processing temperature, as expected (Table 2). At low frequency, the core loss values are mostly within one order of magnitude compared to state-of-the-art SMC industry reported values [8, 9]. Increases due to temperature occur from thinning of the coating, contributing to greater inter-particle losses. The total core losses may be separated into hysteresis loss contributions and eddy current loss contributions. K_h and K_e are the hysteresis and eddy current factors for the material constants, respectively. B and α are also material constants, and f is frequency. Here, the first set of terms represents the hysteresis loss contributions, and the second set of terms represents the eddy current loss contributions. The sum of these terms is the total core losses. Empirical analysis of the core loss data, where either B or alpha are fixed, the K_h and K_e values are determined. This was used to determine the total of the hysteresis and eddy current contributions and determine their respective contributions. When plotted, the estimated transition temperature where eddy current losses begin to dominate is ~ 655 °C for 100 Hz and 315 °C for 1000 Hz. This shift to lower transition temperature with increased frequency is due to eddy current loss contributions having a square frequency dependence according to the Bertotti Eq. (1).

$$P_t = K_h B^{\alpha} f + K_e B^2 f^2 \tag{1}$$

Table 1 Magnetic properties of samples processed up to 700 °C

Maximum processing temperature (°C)	Maximum permeability	H_c (A/m)	B_r (T)	B at 20 kA/m (T)
100	76	454	0.058	0.93
300	123	603	0.138	1.02
500	187	622	0.256	1.04
700	300	443	0.347	1.00

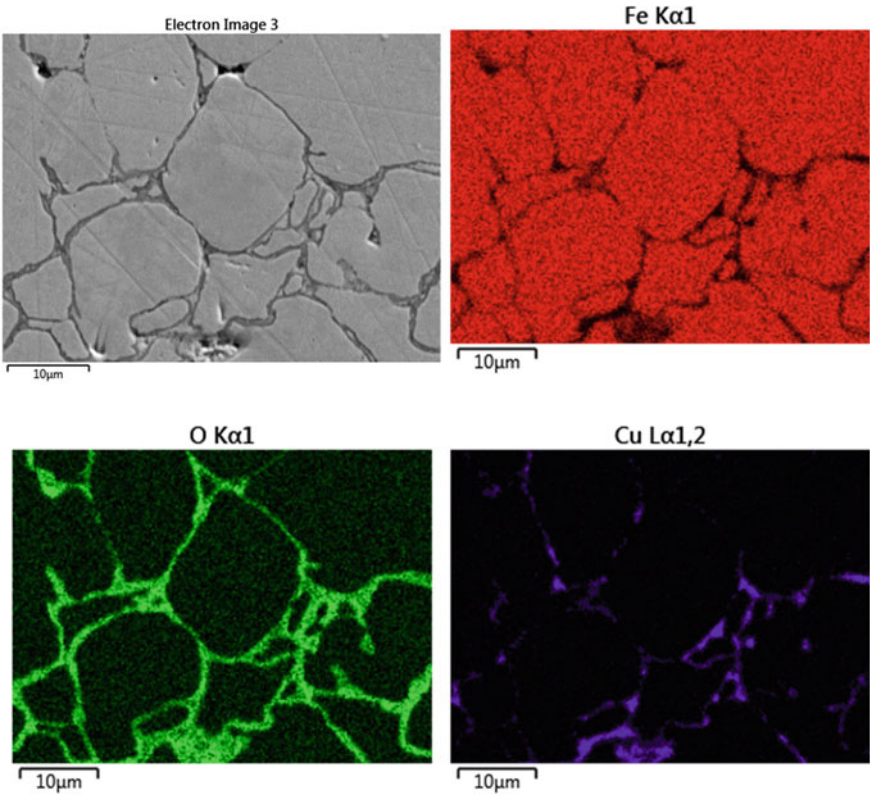

Fig. 1 SEM/EDS imaging of cold sintered plus heat treated at 300 °C sample

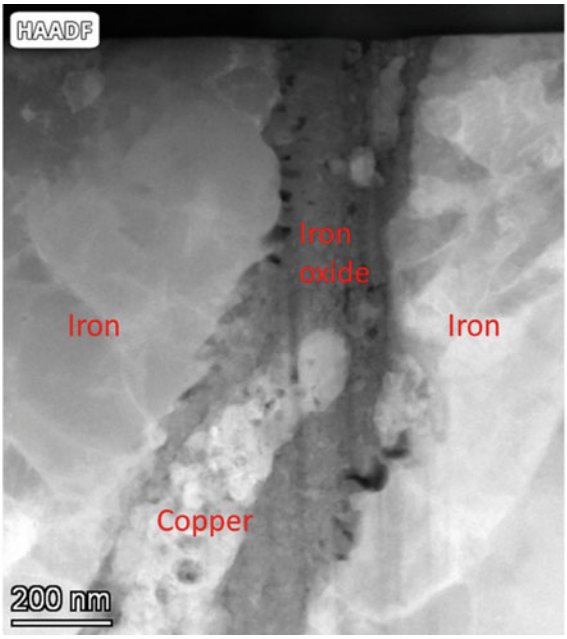

Fig. 2 TEM image of particle coating after cold sintering and annealing at 300 °C

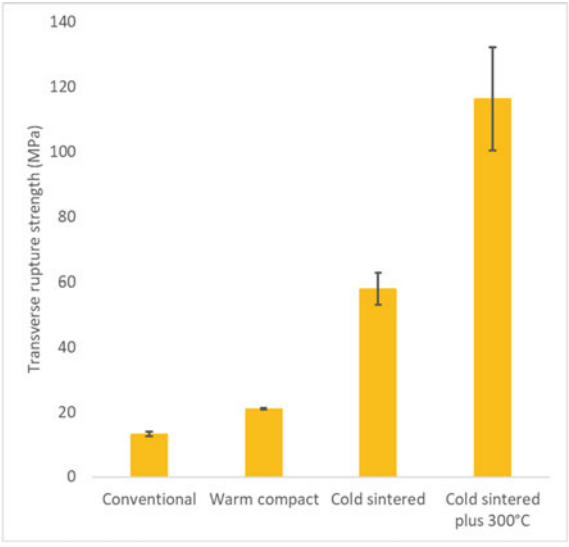

Fig. 3 Transverse rupture strength of cold sintered sample, cold sintered plus annealing sample, and controls

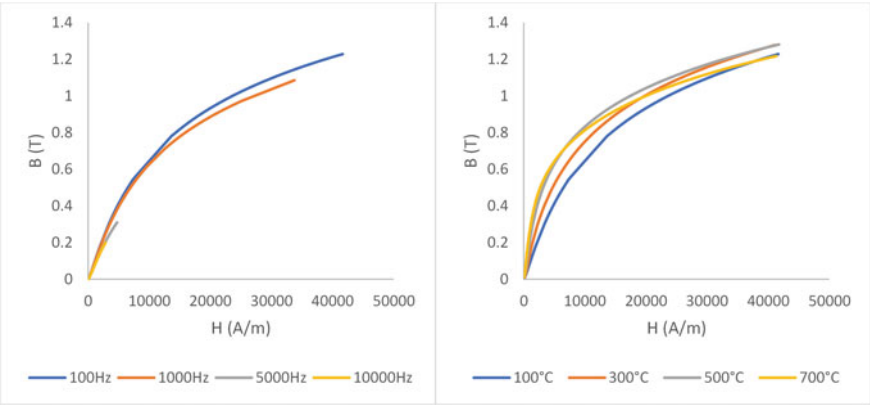

Fig. 4 Cold sintered samples at various frequency (left) and cold sintered samples processed up to 700 °C at 100 Hz (right)

Table 2 Core loss (W/kg) for various frequencies and maximum processing temperatures

	100 °C	300 °C	500 °C	700 °C
100 Hz	25.00	31.50	61.82	121.14
1000 Hz	277.43	524.09	2619.42	6807.52

Conclusions

The work presented has amply shown the viability of applying cold sintering technique of metals for use in producing soft magnetic composites. The study has shown that cold sintering itself improves strength fourfold, and subsequent heat treatment at 300 °C improves ninefold despite densities limited to less than 7.15 g/cc. The two-step (surface modification and warm compaction) method used for cold sintering has thus been demonstrated beyond the use of hydrated phosphate and supports the concept of accelerated particle rearrangement and chemical bonding to form a co-continuous interphase yielding improved strength and magnetic properties comparable to that found in literature. In terms of further improvement to magnetic properties, electrical resistivity and eddy current losses may be improved through application of steam in replacement of air during heat treatment, converting copper metal to copper oxide and potentially improving the magnetic properties.

Acknowledgements The authors would like to acknowledge Advantage Metal Powders for supply of the powder used in this study. Additionally, the authors would like to thank the PA Manufacturing Innovation Program PA Department of Community and Economic Development grants for financial support.

References

1. Sunday K (2017) Development of ferrite-coated soft magnetic composites: correlation of microstructure to magnetic properties. Drexel University, Doctor of Philosophy
2. Shokrollahi H, Janghorban K (2007) Soft magnetic composite materials (SMCs). J Mater Process Technol 189(1):1–12. https://doi.org/10.1016/j.jmatprotec.2007.02.034
3. Encyclopedia of Chemical Technology (1987), vol 9, Kirk-Othmer (ed), 4 edn
4. Sunday KJ, Taheri ML (2017) Soft magnetic composites: recent advancements in the technology. Met Powder Rep 72(6):425–429. https://doi.org/10.1016/j.mprp.2016.08.003
5. Paradis L et al (2022) Densification and strengthening of ferrous-based powder compacts through cold sintering aided warm compaction. Adv Eng Mater 24(12):2200714. https://doi.org/10.1002/adem.202200714
6. Sunday KJ, Taheri ML (2018) NiZnCu-ferrite coated iron powder for soft magnetic composite applications. J Magn Magn Mater 463:1–6. https://doi.org/10.1016/j.jmmm.2018.05.030
7. Dias MM, Mozetic HJ, Barboza JS, Martins RM, Pelegrini L, Schaeffer L (2013) Influence of resin type and content on electrical and magnetic properties of soft magnetic composites (SMCs). Powder Technol 237:213–220. https://doi.org/10.1016/j.powtec.2013.01.006
8. Somaloy, powders for electromagnetic applications. Höganäs. https://www.hoganas.com/en/powder-technologies/soft-magnetic-composites/products/coated-powders-for-electromagnetic-applications/
9. Marucci ML, Narasimhan KS, Advancements in insulated powder composites for soft magnetic applications. Hoeganaes Corporation
10. Hancock MH, Bay N (2007) Effect on deformation process of adding a copper core to multifilament MgB2 superconducting wire. Appl Superconductivity IEEE Trans 17:3054–3058. https://doi.org/10.1109/TASC.2007.899059
11. Kalpakjian S (1995) Manufacturing engineering and technology, 3rd edn. Addison-Wesley Publishing Co., Boston

Removing the Inclusions in Four-Strand Asymmetrical Tundish by Using a Crutch-Shaped Baffle

Weining Shi, Mingzai Ye, Hongxing Li, Jun Wang, Qing Fang, and Cheng Yao

Abstract The tundish structure is a very important factor to remove the inclusions and unify the molten steel. In the condition of four-strand asymmetrical tundish form, there are many problems in Al-deoxidized steel, such as a large number of inclusions and excessive inclusion size. In order to remove the inclusions and increase the cleanliness of molten steel, the crutch-shaped baffle was designed for the four-strand asymmetrical tundish. The numerical simulation results showed that by applying the proposed baffle, the average residence time of the molten steel in the tundish is increased by 43.1 s, the dead zone ratio is decreased by 3.4%, and the flow consistency among strands is apparently increased. Industrial experiments showed that the excessive-sized inclusions are eliminated and the inclusion number is decreased by 46.23% when adding the crutch-shaped baffle in four-strand asymmetrical tundish. Therefore, the inclusion removal rate and the cleanliness of molten steel are greatly improved.

Keywords Asymmetrical tundish · Crutch-shaped baffle · Numerical simulation · Industrial experiments · Inclusions

W. Shi (✉) · M. Ye
Xiangtan Iron and Steel Group Co., LTD. Steelmaking Plant, Xiangtan 411101, Hunan, China
e-mail: 1454696769@qq.com

H. Li · J. Wang
Xiangtan Iron and Steel Group Co., LTD. Steel Research Institute, Xiangtan 411101, Hunan, China

Q. Fang
School of Materials and Metallurgy, Wuhan University of Science and Technology, Wuhan 430081, Hubei, China

C. Yao
State Key Laboratory of Advanced Metallurgy, University of Science and Technology Beijing, Beijing 100083, China

S. Wagstaff et al. (eds.), *Materials Processing Fundamentals 2024*, The Minerals, Metals & Materials Series, https://doi.org/10.1007/978-3-031-50184-5_18

Introduction

The tundish metallurgical technology is widely used in the special steel manufacturing [1]. In the traditional steelmaking process, the first step is to oxidize and remove elements such as C, Si, and Mn. from the molten iron through a converter, and then perform deoxygenation and alloying. However, this process can form a large number of inclusions, which needs to undergo refining for removing inclusions further. And then, the molten steel from the refining station is injected into the tundish through the long nozzle at ladle bottom for split flow casting or single flow casting [2, 3]. The tundish metallurgy plays a crucial role in affecting the steel cleanliness.

The continuous casting tundish is a molten steel container with a steel shell and three layers of internal structure: insulation layer, permanent layer, and working layer. The refractory material contacting with molten steel directly is called the working layer. Furthermore, two main types of materials that contact with molten steel directly are shown below: the first type is the various flow control devices in the tundish, such as baffle, dam and flow stabilizer, which are also made of refractory materials; the another type is the covering agent on the molten steel in the tundish. When these refractory materials and auxiliary materials are used improperly, the metallurgical effect of the tundish cannot be guaranteed and even the molten steel can be polluted due to secondary oxidation and various physicochemical reactions [4–6]. Therefore, the manage of these materials should be reasonable. When the above issues are well controlled, the metallurgical effect of the tundish can be maximized.

The metallurgical effect of the tundish mainly relies on the effective volume of the tundish and the reasonable use of flow control devices [7]. Enlarging the effective volume of the tundish can increase the residence time of the molten steel and improve the floating removal of inclusions. Reasonable control devices in the tundish are beneficial for improving the flow consistency among strands and average residence time, reducing the dead zone ratio, so improving the cleanliness of the molten steel [8, 9]. A steel plant adopts a four-strand asymmetrical tundish without any flow control devices, resulting in a short average residence time of the molten steel and poor flow consistency among strands. Customer complaints about the inclusions exceeding the standard frequently when using the prototype tundish. To improve the inclusion removing in the molten steel, series of flow control devices are designed for the four-strand asymmetrical tundish, and the flow control device of crutch-shaped baffle is adopted due to its excellent tundish metallurgy. Furthermore, the molten steel cleanliness is illustrated by the numerical simulation and industrial experiments.

Experimental Methods

In order to study the flow field distribution of the prototype tundish and the tundish with crutch-shaped baffle, the Fluent platform was used to analyze the continuity equation, momentum equation, energy equation, and standard K-ε equation [10].

When calculating, the following assumptions were made for the model: (1) the fluid flow inside the tundish is a three-dimensional steady-state viscous incompressible flow; (2) the fluid inside the tundish is treated as a homogeneous medium; (3) neglecting the influence of covering agents and slag layers on flow; (4) the heat transfer process in the tundish is steady-state heat transfer.

The boundary conditions of the model were as follows:

(1) The flow speed of the molten steel is determined by the casting speed and billet size, and the turbulent kinetic energy and turbulent flow energy dissipation rate are calculated by the following formula.

$$k_{\text{inlet}} = 0.01 v_{\text{inlet}}^2 \tag{1}$$

$$\varepsilon_{\text{inlet}} = \frac{k_{\text{inlet}}^{1.5}}{D_{\text{inlet}}/2} \tag{2}$$

In the formula: k_{inlet} is the turbulent kinetic energy at the inlet; v_{inlet} is the inlet molten steel flow rate; $\varepsilon_{\text{inlet}}$ is the inlet turbulent energy dissipation rate; D_{inlet} is the inner diameter of long nozzle.

(2) The outlet boundary of the tundish is set to outflow.
(3) The solid wall of the tundish is a non-slip wall, and a standard wall function is used near the wall. The gradient in the normal direction is zero.

The relevant parameters involved in numerical simulation are given in Table 1.

Table 1 Calculation parameters of numerical modeling

Parameters	Value
Billet size/(mm × mm)	150 × 150
Casting speed/(m·min^{-1})	1.9
Inner diameter of long nozzle/(mm)	70
Inlet velocity/(m·s^{-1})	0.76
Density of molten steel/(kg·m^{-3})	$\rho = 8523–0.8358\ T$
Viscosity coefficient of molten steel/(Pa·s)	0.006 7
Thermal conductivity of molten steel/(W·m^{-1}·K^{-1})	42
Specific heat capacity/(J·kg^{-1}·K^{-1})	750
Free surface heat dissipation intensity/(W·m^{-2})	15,000
Heat dissipation intensity of tundish wall/(W·m^{-2})	3800
Heat dissipation intensity at the bottom of the tundish/(W·m^{-2})	1400
Tracer diffusion coefficient/(m^2·s^{-1})	1.1 × 10^{-8}
Turbulent Schmidt number	0.9
Inlet molten steel temperature/K	1785

40Cr steel as the experimental steel was used in the industrial experiments, and the inclusion removal effect of the prototype tundish and the tundish with crutch-shaped baffle was analyzed. The process path for 40Cr steel is "100 t converter → LF → CC". The inclusions in the molten steel were respectively taken from S1 to S4 billets to analysis the tundish metallurgy. All samples were ground and polished, and inclusions were counted using a 100 × metallographic microscope. Each sample had more than 30 metallographic images. Finally, the number and size of inclusions were calculated using Image J software.

Experimental Results

The flow process of molten steel in tundish is analyzed by numerical simulation, and the flow trace before and after tundish optimization is shown in Fig. 1. Figure 1a shows the flow trace of the molten steel in the prototype tundish, it can be seen that after the molten steel is injected into the tundish through the long nozzle, the molten steel flows directly to each flow of the molten steel outlet without the dynamic energy dissipation process, the short-circuit flow of the molten steel closest to the injection area is obvious, the flow trace of the molten steel far from the injection area is very few, and the flow consistency among strands is poor. Figure 1b shows the flow trace of the tundish with crutch-shaped baffle, it can be seen that after the molten steel is injected into the tundish, a part of the energy is dispersed, and the molten steel is dispersed to each molten steel outlet through the baffle diversion. The short-circuit flow of the molten steel closest to the injection area is relatively improved, the flow trace of the molten steel far from the injection area is increased, and the flow consistency among strands is improved.

The RTD curve calculated by numerical simulation is shown in Fig. 2a shows the curve of the prototype tundish and Fig. 2b shows the curve of the tundish with crutch-shaped baffle. It can be seen that the RTD curve of the prototype tundish has poor flow consistency among strands, and the curve is relatively steep, indicating that the average residence time of molten steel is short and the removal time of inclusions is small, which is not conducive to the realization of tundish metallurgical function. However, the RTD curve of the tundish with crutch-shaped baffle has good flow consistency among strands, the curve is smooth and the dimensionless concentration decreases flatly after the peak time of the curve, indicating that the dead zone ratio is reduced compared with the prototype tundish. The RTD curve parameters are given in Table 2. It shows that when the tundish is added to the crutch-shaped baffle, the response time and the peak time of each flow are changed, but the change law is not obvious. However, the average residence time and the dead zone ratio of molten steel are changed significantly, the average residence time and the dead zone ratio of molten steel in prototype tundish are 990.5 s and 23%, and the tundish with crutch-shaped baffle are 1033.6 s and 19.6%. In addition, the error of the average residence time decreases from 54.8 to 20.7, indicating a significant improvement in the flow consistency among strands.

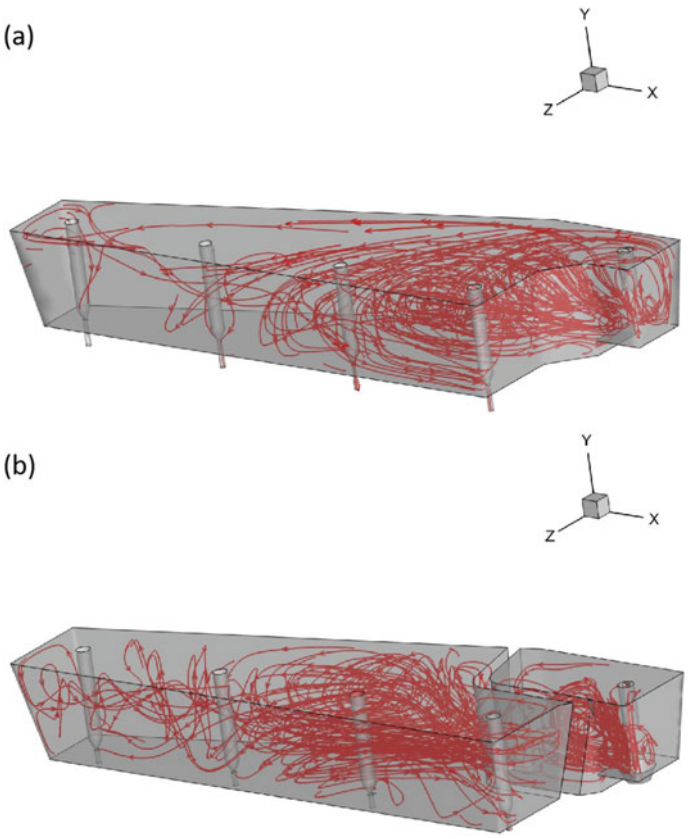

Fig. 1 Flow trace before and after tundish optimization, **a** before and **b** after

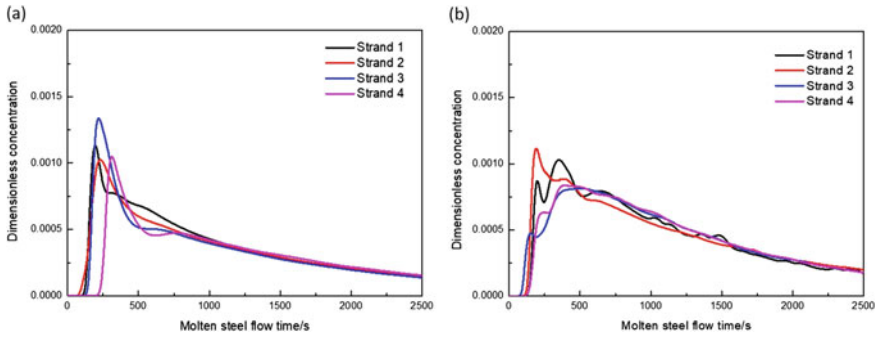

Fig. 2 RTD curve **a** the prototype tundish; **b** the tundish with crutch-shaped baffle

Table 2 RTD curve parameters

Case	Outlet	T_r/s	T_p/s	T_a/s	$\overline{T_a}/s$	V_d/%	Ω
The prototype tundish	Strand 1	111	191	958.1	990.5	23	54.8
	Strand 2	79	230	971.3			
	Strand 3	131	216	955			
	Strand 4	216	308	1087.2			
The tundish with crutch-shaped baffle	Strand 1	128	341	1012.7	1033.6	19.6	20.7
	Strand 2	90	185	1011.9			
	Strand 3	70	493	1047.8			
	Strand 4	107	383	1058.2			

Among them: T_r is the response time, indicating the time when the molten steel at the inlet first flows out of the outlet at each strand; T_p is the peak time, indicating the time when the molten steel at the inlet the most flows out of the outlet at each strand; T_a is the average residence time, indicating the inclusion float removal time at each strand; $\overline{T_a}$ is the average residence time of each strand, indicating the inclusion float removal time in a specific tundish; V_d is the average dead zone ratio of each strand, indicating the area proportion where the inclusions float remove inactively in a specific tundish; Ω is the average residence time error, indicating the flow consistency among strands.

The industrial experiment results are shown in Fig. 3, it shows that the inclusion number of the prototype tundish is significantly higher than that of the tundish with crutch-shaped baffle. The inclusion number counted in this method is based on the number of spherical inclusions, the total inclusion number in S1 to S4 is 76, 84, 72, 60, respectively, when using the prototype tundish, but that in S1 to S4 is 39, 41, 39, 38, respectively, when using the tundish with crutch-shaped baffle. Therefore, both the inclusion removal rate and the flow consistency among strands are significantly improved, and the inclusion removal rate increased by 46.23%. Furthermore, the inclusion exceeding the standard size is greatly reduced.

Conclusions

(1) According to the flow trace of the molten steel, adding the crutch-shaped baffle in four-strand asymmetrical tundish can improve the dynamic energy dissipation, increase the flow trace of the molten steel away from the injection area and improve the flow consistency among strands;
(2) When adding the crutch-shaped baffle in four-strand asymmetrical tundish, the average residence time of molten steel increases from 990.5 s to 1033.6 s, the dead zone ratio decreases from 23% to 19.6% and the average residence time

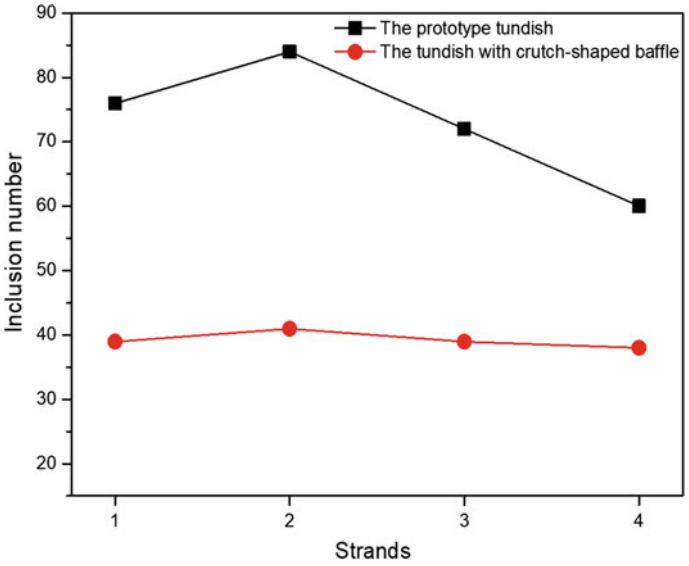

Fig. 3 Statistical results of billet inclusions in industrial experiments

error decreases from 54.8 to 20.7, indicating that the cleanliness of molten steel and the flow consistency among strands are significantly improved;

(3) Industrial experiment results show that the inclusion removal rate increased by 46.23% after the application of the crutch-shaped baffle, and the industrial experiment results are consistent with the numerical simulation results. Furthermore, the inclusion exceeding the standard size is greatly reduced. Therefore, applying the crutch-shaped baffle in the four-strand asymmetrical tundish improve the metallurgical effect of the tundish and the cleanliness of the molten steel.

References

1. Sahai Y (2016) Tundish technology for casting clean steel: a review. Metall Mater Trans B 47(4):2095–2106
2. Merder T, Warzecha M (2012) Optimization of a six-strand continuous casting tundish: industrial measurements and numerical investigation of the tundish modification. Metall Mater Trans B 43(4):856–868
3. Warzecha M, Merder T, Warzecha P, et al (2013) Experimental and numerical investigations on non-metallic inclusions distribution in billets casted at a multi-strand continuous casting tundish. ISIJ Int 53(11SI):1983–1992
4. Marochkin O, Vdovin K, Yachikov I et al (2016) Improving the designs of elements of refractory materials for the tundish of continuous section casters. Refract Ind Ceram 57(1):1–3
5. Wang Q, Qi F, Li B et al (2014) Behavior of non-metallic inclusions in a continuous casting tundish with channel type induction heating. ISIJ Int 54(12):2796–2805

6. Cui H, Liu Y, Li D (2015) Fluid flow characterization in asymmetric tundish. ISIJ Int 55(12):2604–2608
7. Chatterjee S, Chattopadhyay K (2017) Transient steel quality under non-isothermal conditions in a multi-strand billet caster tundish: part II. Effect of a flow-control device. Ironmaking Steelmaking 44(6):413–420
8. Xing F, Zheng S, Zhu M (2018) Motion and removal of inclusions in new induction heating tundish. Steel Res Int 89:1700542
9. Ai X, Han D, Li S et al (2020) Optimization of flow uniformity control device for six-stream continuous casting tundish. J Iron Steel Res Int 27(9):1035–1044
10. Xiao H, Xu H, He H et al (2021) Flow field optimization of five-stream induction heating tundish based on numerical simulation. China Metall 31(1):14–19

Study on Flow Characteristics of Extracted Titanium Tailings in a Fluidized Furnace with Liquid Addition

Yan Zhao, Liangying Wen, and Bo Liu

Abstract Extracted titanium tailings are produced by high-titanium blast furnace slag using "high-temperature carbonization–low-temperature chlorination" technology. In this paper, the flow characteristic of extracted titanium tailings is experimentally investigated on the base of the fluidized furnace over a range of superficial gas velocity and bed temperatures. The evaporation rate of liquid addition was studied at different temperatures. The influence of superficial gas velocity, temperatures, and height-to-diameter ratio on flow characteristics was analyzed. The particle microstructures of the tailings were characterized by scanning electron microscopy and energy dispersive spectroscopy (SEM–EDS). The results show that there exists a linear correlation between the actual amount of liquid before and after entering into the bed at different temperatures. The mean pressure drop and standard deviation show an overall enhancing trend with the increasing gas velocity and height-to-diameter ratio of bed. However, the bed temperature poses a significant effect on the bed pressure after liquid addition.

Keywords Extracted titanium tailings · Fluidized furnace · Flow characteristics · Liquid addition

Introduction

Fluidized furnace has been widely used in different industrial fields due to their high efficiency of heat and mass transfer and their ability to process many particles continuously [1–3]. The properties of particles are changed in diverse industrial

Y. Zhao · L. Wen (✉) · B. Liu
School of Materials Science and Engineering, Chongqing University, Chongqing 400044, China
e-mail: cquwen@cqu.edu.cn

Y. Zhao · L. Wen
Chongqing Key Laboratory of Vanadium-Titanium Metallurgy and Advanced Materials, Chongqing University, Chongqing 400044, China

S. Wagstaff et al. (eds.), *Materials Processing Fundamentals 2024*, The Minerals, Metals & Materials Series, https://doi.org/10.1007/978-3-031-50184-5_19

processes. The appearance of contact viscous forces between particles is represented by liquid and solid bridge forces. The presence of viscous forces reduces the mobility of particles, resulting in the fluidization behaviors different from that of conventional non-sticky particles. The reaction efficiency and the stable operation are affected in the fluidized furnace. Liquid addition into fluidized furnace has been widely used in various industrial production processes, such as combustion gasification [4], hydrogen production by catalytic cracking [5], biomass gasification [6], and low-temperature boiling chlorination in the metallurgical industry [7]. In the low-temperature selective chlorination process, the reaction speed of titanium carbide (TiC) is more significant than other components such as calcium oxide and magnesium oxide. The titanium carbide slag was chlorinated and turned to $TiCl_4$ in a chlorination furnace, leaving other impurities in the slag. During the direct chlorination process at 530 °C, only TiC and TiN can spontaneously react with chlorine, and the reaction tendency of TiC is prominent. Many tailings containing chloride are produced, which accounts for about 85% of the total amount of carbonized slag, and its chlorine content is as high as 3% or more. The generated tailings cannot be directly utilized and occupy a large amount of land, resulting in waste of land and pollution of water bodies. The extracted titanium tailings are fluidized by introducing air in the furnace and then dechlorinated by spraying water, so that the tailings can be utilized.

In particular, the gas–solid–liquid three-phase coexistence within the fluidized bed is formed after the liquid addition, which has an impact on the flow characteristics [8]. The state of fluidization is disrupted with the increase of liquid addition, resulting in the phenomenon of localized sticking and dead zones, which in turn affects the mass and heat transfer capacity of reactor. Therefore, the effect of liquid addition or generation on the fluidization stability in the furnace has been researched extensively [9]. Boyce et al. [10] found that a small amount of liquid addition (about 1% or less of the total amount of particles in the bed) can also form liquid bridging forces between solid-phase particles in the bed, causing solid-phase adhesion. Fan et al. [11] showed that the liquid droplets were rapidly vaporized in large quantities in the high-temperature fluidized bed reactors, causing a significant increase in the gas flow inside the reactor. The temperature distribution in the contact area and the gas–solid fluidization state were significantly influenced, thus affecting the process efficiency and product quality of the production. In order to more accurately study the theoretical laws of multiphase flow, the critical parameter of pressure that needs to be obtained when measuring the flow characteristics in the fluidized bed is pressure, which can be directly related to the continuous phase and the dispersed phase of the bed regions in the industrial application of fluidization or laboratory research [12–14]. In industrial production, pressure is a vital detection index. In recent years, the pressure fluctuations in fluidized bed have been mainly used to describe various fluidized bed hydrodynamic models. Loezos et al. [15] investigated the pressure drop of glass particles with sizes ranging from 63 μm to 210 μm in gas–solid micromini-fluidized beds with inner diameters of 12.7, 25.4, and 50.8 mm and concluded that the presence of wall effect leads to the generation of additional pressure drop, and the additional pressure drop is enhanced with the decreasing bed diameter. Felipe et al.

Table 1 Physical parameters of carbonized slag

Parameters	Values	Units
Bulk density	982	kg/m^3
Actual density	2565	kg/m^3
Compaction density	1358	kg/m^3
Minimum porosity	0.47	
Critical fluid porosity	0.61	

[16] calculated and analyzed the standard deviation of pressure fluctuation and found that the standard deviation at low gas velocities increases approximately linearly, and the standard deviation can be used to determine the minimum fluidization velocity. Guo et al. [17] studied the pressure drop of quartz sand particles and FCC particles in micro-fluidized beds with inner diameters of 4.3, 5.5, 10.5, 15.5, 20.5, and 25.5 mm. They found that the actual values of the bed pressure drop differed significantly and were attributed to the wall effect and bed void fraction.

In this paper, the extracted titanium tailings generated from the high-temperature carbonization-low-temperature chlorination process of high-titanium blast furnace slag are taken as the research object. A laboratory fluidized bed with liquid addition is set up to investigate the gas–solid flow characteristics of titanium tailing using the residual heat of the boiling chlorination tailing (around 500 °C). The evaporation rate of water at different temperatures was studied. The effect of superficial gas velocity, heating temperature, and height-to-diameter ratio on the pressure, standard deviation, and fluidization index was explored.

Experimental Setup

Raw Materials for Experiment

In this experiment, the titanium tailing slag provided by Pangang Group was used as the raw material (granular phase), and the relevant physical parameters were shown in Table 1. The actual density was 2565 kg/m^3, and oxygen was used as the fluidizing gas (gas phase). The scanning electron microscopy (SEM) microscopic morphology of titanium tailing slag is shown in Fig. 1a.

Experimental Equipment

As shown in Fig. 1b, the experimental setup mainly consists of 1-gas cylinder, 2-relief valve, 3-gas flowmeter, 4-quartz reactor, 5-constant temperature heating device, 6-computer, 7-pressure sensor, 8-mass sensor, 9-liquid atomizing nozzle, 10-flow

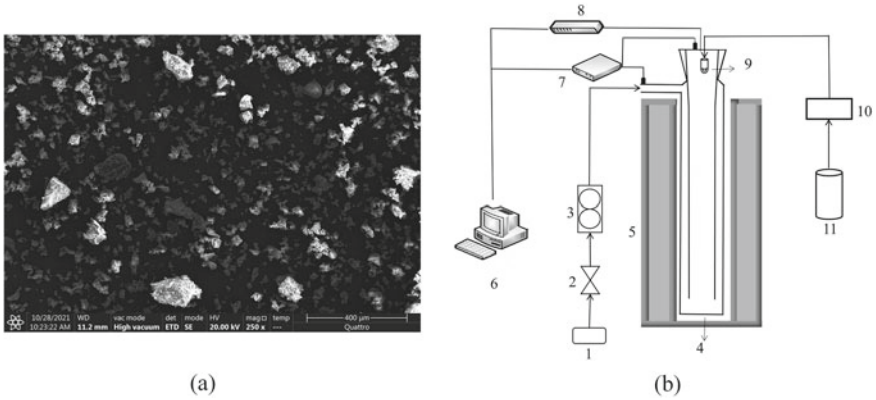

Fig. 1 **a** Scanning electron microscope images of tailings; **b** schematic of experiment apparatus

pump, and 11-liquid storage tank. The quartz reactor consists of an inner tube with an inner diameter of 35 mm and a length of 245 mm, and an outer tube with an inner diameter of 45 mm and a length of 275 mm. The inner and outer tubes are embedded in each other. The top of the quartz reactor is closed by a refractory fiber cotton. The gas supply system consisted of a gas cylinder, a relief valve and a rotameter, and the oxygen supplied from the gas cylinder was metered through the relief valve and the rotameter. The atomization spraying system concludes with an atomization nozzle and liquid storage tank. The nozzle is arranged in a position of 4 cm from the top of the reactor. The ends of nozzle are connected with a liquid pipeline and the liquid storage tank, respectively. The liquid storage tank is connected to the flow pump, and water is injected into the furnace from the atomization nozzle through the liquid pipeline. The reactor is heated by a constant temperature heating device, and the temperature is controlled by a thermocouple. A quartz sand sieve plate is placed at the bottom of the reactor to carry the particles and distribute the gas entering into the furnace. The pressure and mass data of the reactants during the experiment are monitored in real time by the sensors and transmitted to the computer for recording. The range of the mass sensor is 0~1.2 kg, and the range of the pressure sensor is 0~100 kPa.

Experimental Method

Before experiments, 15 g particles were weighed and placed into a quartz reactor. The furnace is purged with a small amount of nitrogen to evacuate the air. Afterwards, the furnace was heated, the temperature in the reaction tube was increased from room temperature to the required temperature (300 °C, 400 °C, 450 °C, 500 °C) and kept warm. The O_2 was passed into the furnace for nearly 60 s at a gas velocity of 0.15, 0.17, 0.20, 0.25 m/s. Then, 10 ml of pure water was injected into the quartz

reactor through the nozzle. The reactor naturally cooled to room temperature. Each experiment was repeated at least three times, and the test results were averaged for data analysis. The accuracy of temperature control was ± 2 °C, and the accuracy of the mass sensor was 0.01 g. The results were obtained by the average of the repeated results.

The pressure pulsation standard deviation is used to characterize the magnitude of pressure fluctuations and is calculated using the following formula:

$$\sigma_p = \sqrt{\frac{1}{N}\sum_{n=1}^{N}(p_n - \overline{p})^2} \tag{1}$$

where σ_p is the standard deviation of pressure pulsation; N is the number of sampling points; $\overline{p}$ is the mean value of pressure pulsation; p_n is the time series of pressure pulsation.

The fluidization index is used to evaluate the fluidization quality [18]: it is generally believed that the smaller the fluidization index R, i.e., the smaller the average value of pressure drop pulsation and the higher the frequency, the better the fluidization quality. The formula is as follows:

$$R = \frac{\Delta\overline{p}}{f\overline{p}} \times 10^4 \tag{2}$$

where $\Delta\overline{p}$ is the average value of the pressure drop pulsation between the pressure point and the atmosphere; f is the frequency of the pressure drop fluctuation, the value is 60; $\overline{p}$ is the average value of the pressure drop.

Results and Discussion

Evaporation Rate of Liquid Addition

In a high-temperature fluidized bed with liquid injection, part of the added water evaporates and part of it contacts with the bed. To ensure that the amount of liquid phase that enters the bed in the hot state experiment is the same as that in the cold state, it is necessary to add an excessive amount of liquid water, but to get the accurate amount of liquid added in the high temperatures, it is necessary to study the evaporation rate of water at different temperatures. Based on the weight sensor, the mass of the liquid phase in the bed was recorded at different temperatures. As shown in Fig. 2, the linear correlation between the amount of liquid added and the amount of liquid phase actually entering the bed at different temperatures was obtained based on linear fitting with the amount of liquid added (x) as the horizontal coordinate and the amount of liquid phase actually entering the bed (y) as the vertical coordinate, and the coefficients of determination R^2 were located in the range of 0.967–0.989,

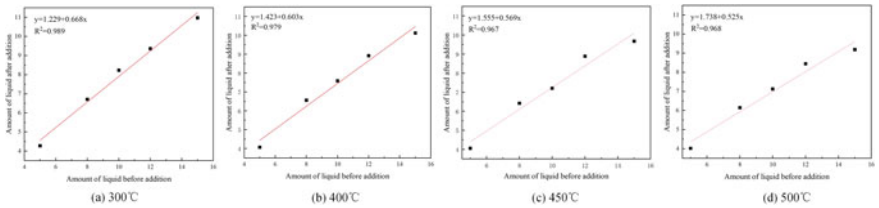

Fig. 2 Linear fitting of evaporation of liquid water at different temperatures

indicating a good fit. The fitted equations are as follows: $y = 0.668x + 1.229$ (300 °C); $y = 0.603x + 1.423$ (400 °C); $y = 0.569x + 1.555$ (450 °C); $y = 0.525x + 1.738$ (500 °C). It also can be seen that the ratio of liquid added to bed liquid phase increased with the temperature.

Effect of Superficial Gas Velocity on Bed Pressure Drop

As shown in Fig. 3a, the instantaneous curve of bed pressure with time pulsated up and down under different fluidized gas velocities. With the increase in gas velocity, the average bed pressure shows an upward trend without obvious fluctuations. The amount of gas entering the bed rises per unit time with the increased fluidization gas velocity, the gas–solid interaction is strengthened, and the interphase resistance increases, resulting in a gradual increase in the average pressure value. The average pressure after liquid addition under the same gas velocity is smaller than that before adding liquid, this is because the evaporation of water occurs instantly after the liquid enters into the bed at high temperatures, and plenty of vapors are produced rapidly. The vapor and fluidized gas acts jointly on the tailings particle, the liquid evaporation makes the liquid phase transform to gas phase, then increases the local gas flow rate and thus intensifies the fluidization stability. The liquid bridge action tends to increase interparticle forces, which promotes the formation of particle agglomerations and thus severely destroys fluidization stability; it therefore plays a negative role in the particle fluidization and the size growth and movement of the bubbles.

The differential pressure pulsation mainly reflects the growth and fragmentation behavior of gas bubbles (or particle agglomerates) in the fluid area. As shown in Fig. 3b, the standard deviation of pressure pulsation shows a rising trend with the increase of superficial gas velocity before and after liquid addition, and the standard deviation of pressure pulsation is higher than that after liquid addition at the same gas velocity. The bubbles are constantly generated, aggregated, and broken under the effect of turbulence in the aeration, and the strong interaction between the bubbles leads to sharp fluctuations in the bed pressure. The reaction between the interface of titanium tailings and water is enhanced after liquid addition. The bed layer becomes thinner due to the consumption of the tailings particles and the bubble diameter decreases, which contributes to the decrease of the standard deviation of pressure

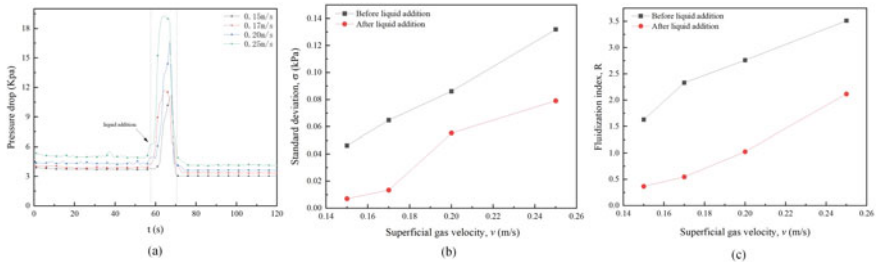

Fig. 3 Effect of gas velocity conditions **a**: pressure **b**: standard deviation; **c**: fluidization index

pulsation. With the increase in gas velocity, the interface reaction in the bed is more intense due to the amount of gas per unit time increasing. On the one hand, the decrease in particle amount also leads to a decrease in the standard deviation of pressure pulsation. On the other hand, the liquid addition brings the agglomeration of wet particles to influence the fluidization quality. The fluidization index changing with the superficial gas velocity before and after the liquid addition is shown in Fig. 3c. The fluidization index is gradually rising with increasing gas velocity. When the fluidization gas velocity is more than 0.17 m/s, the trend of fluidization index has a steep rise, and it means the fluidization quality beginning to deteriorate.

Effect of Temperatures on Bed Pressure Drop

The pressures against time at the different temperatures are shown in Fig. 4a. It can be seen that the average pressure increasing with the temperatures displays the opposite trend before and after the liquid addition. The average pressure rises with the increasing temperature before liquid addition, while the pressure shows a downward trend after liquid addition. When no liquid is involved in the fluidized furnace, the expansion of gas phase becomes more intense with the higher temperature. The gas–solid interaction stronger, the value of the resistance greater. As a result, the average value of the pressure has an upward trend before the liquid addition. The temperature has a direct effect on the evaporation rate of the liquid. The water vapour is produced instantly at the high temperatures. Meanwhile, the interface reaction gets more intense, the porosity of the bed layer increases and the resistance of gas–solid interaction is inhibited. The average pressure of the bed reduces with the increased temperature after the liquid addition.

The standard deviation of pressure pulsation at different temperatures is shown in Fig. 4b. The standard deviation of pressure pulsation before liquid addition has a rise trend. The particles content of bed is consistent at different temperatures with the absence of liquid phase, and the expansion of gas phase dominates over. The expansion of gas phase becomes more intense with the increasing temperatures. The bubble diameter increases and bubble behaviors rupture violently during gas–solid

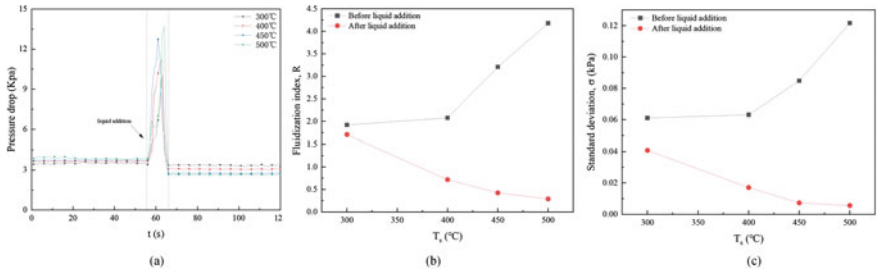

Fig. 4 Effect of temperatures **a**: pressure **b**: standard deviation; **c**: fluidization index

fluidization. As a result, the standard deviation of pressure pulsation rises. After adding liquid, the standard deviation of pressure pulsation shows a decreasing trend. The liquid begins to gradually occupy the space between the particles when the liquid phase enters into the bed, resulting in an increase in the resistance for the gas to pass through the space between the particles. As the temperature increases to more than 400 °C, the evaporation rate of liquid phase is greater. At the same time, the extracted titanium tailing particles have interface reaction with water. The bed porosity increases and the bubble diameter decreases, the resistance of gas phase through the particles is weakened, resulting in a decrease in the standard deviation of pressure pulsation.

The fluidization index changed with temperature as shown in Fig. 4c. The overall trend of fluidization index is gradually increasing with the increased temperatures. When the temperature exceeds 400 °C before liquid addition, the fluidization index rises rapidly, and the fluidization quality is gradually deteriorated. The gas phase expands at the high temperature, causing the amount of gas per unit bed area raised. The homogeneous state of the particles in the fluidized bed is destroyed, and the fluidization index decreases. The fluidization index has little difference at a temperature of 300–400 °C, and the state of the gas–solid fluidization is relatively close. The expansion of the gas phase is limited at this temperature range, and the amount of gas in the fluidized bed is similar. Hence, the gas–solid fluidization behaviors make no difference. While the fluidization index is gradually reduced after liquid addition. The fluidization index decreased significantly at the temperature range of 300–400 °C, and the fluidization index tends to stabilize over 450 °C. When the liquid phase is involved in the bed, the interface reaction between water and tailings particles becomes more intense with the higher temperature. The gas–solid pressure pulsation decreases, which promotes uniform distribution of particles and better fluidization quality.

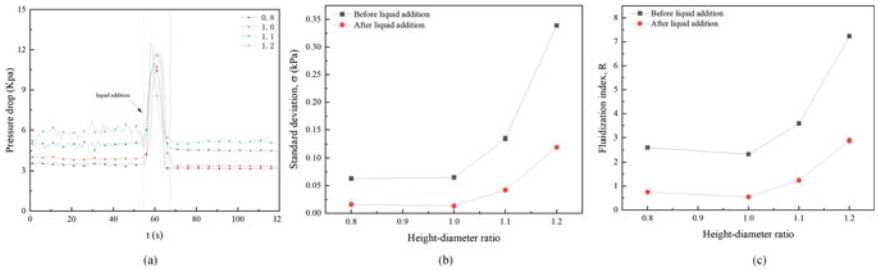

Fig. 5 Effect of temperatures **a**: pressure **b**: standard deviation; **c**: fluidization index

Effect of Height-to-Diameter Ratio on Bed Pressure Drop

The pressure pulsation curves under different aspect ratios are shown in Fig. 5a, and it can be clearly observed that the bed pulsation pressure shows an upward trend with increasing the height-to-diameter ratio. The increase in height-to-diameter ratio is related to the mass of particles raised. The resistance of the gas passing through the bed is enhanced, leading to the increase of the fluidized bed pressure.

Figure 5b shows that the standard deviation of bed pressure pulsation changes with the height-to-diameter ratio. The standard deviation of pressure pulsation before liquid addition is larger than that after adding liquid at the same height-to-diameter ratio. This is because the particles of the bed layer are reacted and consumed between water after liquid addition, the time for the gas passed through the bed is shorten. Moreover, the generation, rise, aggregation, and rupture of bubble are inhibited, the bubble diameter decreases. Therefore, the standard deviation of pressure pulsation after liquid addition is lower than that before liquid addition.

The variation trend of fluidization index with the increase of the height-to-diameter ratio is shown in Fig. 5c. The fluidization index tends to decline firstly and rise, and the fluidization index is the lowest in the aperture ratio of 1.00. The gas is easy to blow empty as the bed layer is too thin, the phenomenon of channeling fluidization occurs. The distribution of bed particles is uneven, destroying the fluidization quality. When the material layer is too thick, the stirring ability of the gas in the fluidized bed is weakened, and the particles in the local area are difficult to fluidize, contributing to the appearance of dead zones and the poor fluidization quality. In addition, when the height-to-diameter ratio exceeds 1.10, the fluidization index has an increasing tendency before or after the liquid addition. This is due to the fact that the mixing ability of the gas in the fluidized furnace is limited, and the inhomogeneity of the bed layer is prominent.

Conclusions

In this paper, the experiments of gas–liquid fluidization of the extracted titanium tailings with liquid addition were carried out. The evaporation rate of water in fluidized furnace under different temperatures was researched. The amount of liquid is set as the horizontal coordinate (x), and the actual amount of liquid entered into the bed is set as the vertical coordinate (y). The specific equations under different temperatures based on the linear fitting are as follows: $y = 0.668x + 1.229$ (300 °C); $y = 0.603x + 1.423$ (400 °C); $y = 0.569x + 1.555$ (450 °C); $y = 0.525x + 1.738$ (500 °C). The coefficient of determination of R^2 is located in the range of 0.967 ~ 0.989, indicating that the degree of fitting is good. The effects of factors on the flow characteristics of pressure were further investigated. The results show that the mean pressure and standard deviation of pressure pulsation showed an overall increasing trend with the increase in gas velocity. With the increase in temperature, the mean pressure and the standard deviation of pulsation showed an increased tendency before the liquid addition and then showed a decreasing tendency after the liquid addition. The fluidization index first decreased and then increased with the increase of the height-to-diameter ratios, and the lowest value was taken at the height-to-diameter ratio of 1.00.

Results shown in this article could have a significant effect on understanding the liquid phase mixing and gas–solid pressure characteristics in the fluidized furnace. It provides an effective method for flow characterization and is beneficial for the stable operation of industrial fluidized bed reactors.

Acknowledgements The work is supported by the National Natural Science Foundation Project of China (51974046).

References

1. Shabanian J, Chaouki J (2016) Influence of interparticle forces on solids motion in a bubbling gas-solid fluidized bed. Powder Technol 299:98–106
2. Ma JL, Liu DY, Chen XP (2016) Bubble behaviors of large cohesive particles in a 2D fluidized bed. Ind Eng Chem Res 55:624–634
3. Xu HB, Zhong WQ, Yu AB, Yuan ZL (2015) Spouting characteristics of wet particles in a conical-cylindrical spouted bed. Ind Eng Chem Res 54(40):549894–549902
4. Dong K, Zhou Y, Huang Z (2014) Gas bubble behaviors in a gas–solid fluidized bed with an arch agitator. Powder Technol 266:38–44
5. Basu P (2006) Combustion and gasification in fluidized Beds. CRC Press, Boca Raton, pp 1–496
6. Amin AM, Croiset E, Epling W (2011) Review of methane catalytic cracking for hydrogen production. Int J Hydrogen Energy 36(4):2904–2935
7. Zhao Y, Wen LY, Zhang YF, Liu B, Yang H, Deng QY (2022) Experimental and numerical study on dynamic characteristics of droplet impacting on a hot tailings surface. Processes 10:1766
8. Lim KS, Zhu JX, Grace JR (1995) Hydrodynamics of gas-solid fluidization. Int. J. Multiphase Flow 21:141–193
9. Wu MQ, Khinast JG, Radl S (2018) The effect of liquid bridge model details on the dynamics of wet fluidized beds. AICHE J 64:437–456

10. Boyce CM (2018) Gas-solid fluidization with liquid bridging: a review from a modeling perspective. Powder Technol 336:12–29
11. Fan LS, Lau R, Zhu C, Vuong K, Liu G (2001) Evaporative liquid jets in gas–liquid–solid flow system. Chem Eng Sci 56(21–22):5871–5891
12. Quan H, Fatah N, Hu C (2020) Diagnosis of hydrodynamic regimes from large to micro-fluidized beds. Chem Eng J 391:123615
13. Vanni F, Caussat B, Ablitzer C, Brothier M (2015) Effects of reducing the reactor diameter on the fluidization of a very dense powder. Powder Technol 277:268–274
14. Cheng NS (2011) Wall effect on pressure drop in packed beds. Powder Technol 210(3):261–266
15. Loezos PN, Costamagna P, Sundaresan S (2002) The role of contact stresses and wall friction on fluidization. Chem Eng Sci 57(24):5123–5141
16. Felipe CAS, Rocha SCS (2007) Prediction of minimum fluidization velocity of gas-solid fluidized beds by pressure fluctuation measurements-Analysis of the standard deviation methodology. Powder Technol 174(3):104–113
17. Guo QJ, Xu Y, Yue X (2009) Fluidization characteristics in micro-fluidized beds of various inner diameters. Chem Eng Technol 32(12):1992–1999
18. Zhao Y, Wen LY, Liu B, Wang JX, Wang CS, Zhang SF (2021) Effect of liquid addition on gas-solid fluidization. Chem Eng Technol 44(9):1596–1603

Part V
Poster Session

Density Functional Theory (DFT) Simulation of Microsurface Properties of FeO

Hao Wu and Haibin Zuo

Abstract Importance of DFT simulation of microsurface properties of FeO in ironmaking research is emphasized, as FeO serves as a limiting factor in the iron reduction process. The interface reaction mechanisms involved in CO reduction of FeO are revealed, adsorption properties are predicted, and crucial parameters such as surface energy and electronic structure are provided. Additionally, the formation modes of defects for various types of atoms are anticipated. These results offer powerful tools and a theoretical foundation for understanding and optimizing the ironmaking process, thereby contributing to increased production efficiency, reduced energy consumption, and the promotion of sustainable development within the iron and steel industry.

Keywords Density · Functional theory · Microsurface · Properties · CO · Reduction

Introduction

As global warming becomes an increasingly pressing concern worldwide, research on reducing carbon dioxide emissions is growing in importance [1, 2]. The steel industry, being a key economic pillar and one of the major sources of carbon emissions, needs to strike a balance between reducing pollution and enhancing production efficiency. Pelletizing iron ore, a primary raw material, may encounter expansion issues during the reduction process, especially with high-alkaline pellets [3–5]. These issues not only affect production stability and resource utilization efficiency but also pose challenges to environmentally friendly steel production.

Investigating the mechanisms and solutions for pellet expansion during the reduction of iron ore pellets is not only crucial for ensuring the sustainable development of the steel industry but also holds significant potential for driving the entire industrial sector towards a more environmentally friendly and efficient direction.

H. Wu · H. Zuo (✉)
University of Science and Technology Beijing, Beijing, China
e-mail: zuohaibin@ustb.edu.cn

S. Wagstaff et al. (eds.), *Materials Processing Fundamentals 2024*, The Minerals, Metals & Materials Series, https://doi.org/10.1007/978-3-031-50184-5_20

Most current research on reduction expansion primarily operates at the macroscopic level, lacking a thorough examination of the microscale mechanisms underlying reduction expansion [6–11]. There has been limited exploration into the microscale behaviors during the reduction process of pelletized iron ore and the influence of various elements on crystal structures. This paper, employing Density Functional Theory (DFT), conducts simulations to elucidate the formation mechanisms and formation energies of various types of doping defects on the FeO surface. Additionally, it utilizes ab initio molecular dynamics (AIMD) simulations to investigate certain microscale behaviors during the reduction process of the FeO surface. These efforts are aimed at microscopically unraveling the mechanisms responsible for the expansion observed during pelletized iron ore reduction. This research provides a fundamental understanding of the root causes of reduction swelling in pelletized iron ore, empowering scientists and researchers to address this issue at its core. By doing so, it becomes possible to enhance the pellet-to-blast furnace ratio, consequently reducing emissions from the sintering process and advancing pollution control measures.

Experimental and Computational Methods

In this study, pelletized samples were prepared by homogeneously mixing analytical-grade reagents (purity >99%) with basicity of 0.2, 0.4, 0.6, 0.8, 1.0, and 1.2.These samples were subsequently subjected to sintering at 1280 °C. Following sintering, the samples were placed in a reduction furnace under a protective N_2 atmosphere with a flow rate of 0.83 L/min. The pellets were heated to 900 °C in the presence of N_2. At 900 °C (with a gas mixture of CO:N_2 = 3:7, the purity of all the gases used is greater than 99%.), the gas flow rate was maintained at 15 L/min for a duration of 60 min. Upon completion of the reaction, the pellets were cooled to 100 °C under the protection of N_2 (flow rate, 15 L/min).

Considering that the FeO-Fe phase transition represents the limiting step in the entire pelletized iron ore reduction process, this study employed FeO as the basis for Density Functional Theory (DFT) and Ab Initio Molecular Dynamics (AIMD) simulations. Ionic cores were described using soft pseudopotentials. The exchange–correlation term was treated with the Perdew-Burke-Ernzerhof (PBE) functional. A Fermi smearing of 0.1 eV was applied to expedite convergence [12]. The convergence criteria were set as follows: energy cutoff (400 eV), convergence threshold energy (1.0×10^{-5} eV/atom), maximum force (0.03 eV/Å), and maximum displacement (0.01 Å). A time step of 1 fs was employed, and a total of 5000 steps were utilized during the annealing process to raise the temperature to 900 °C (1173 K). During the equilibration stage, an NVE ensemble was employed, and a simulation consisting of 20,000 steps was performed, with the use of a Nose–Hoover thermostat. The model used was referenced from the literature [13–15]. These parameters were derived from references [16–18]. Brillouin zone integration was performed using the Monkhorst–Pack scheme with a $4 \times 4 \times 1$ k-point set for adsorption studies [19].

Results and Discussion

Impact of Different Gangue Components and Reducing Gas Atmospheres on Reduction Expansion

Experiments were carried out involving the preparation of pelletized samples with varying basicity levels (0.2, 0.4, 0.6, 0.8, 1.0, 1.2) by mixing pure reagents in different proportions. These samples were subsequently sintered and transformed into pellets. The pellets were then subjected to reduction expansion experiments under different reducing gas atmospheres ($CO:N_2 = 3:7$, $H_2:N_2 = 3:7$) following the GB/T 13,240–91 standard, with the aim of investigating the impact of basicity and reducing gas atmospheres on reduction expansion. The results, as illustrated in Fig. 1, indicate that with increasing basicity, the reduction swelling rates are initially increased and then declined in both gas atmospheres. When the basicity reaches 0.8, the maximum reduction expansion rates are achieved in both H_2 and CO atmospheres, measuring 28% and 16.1%, respectively. Furthermore, under H_2 reduction gas atmosphere, the pellet's reduction expansion rate is lower than that under CO atmosphere, with the most significant reduction observed at a basicity level of 0.8.

SEM images of the surfaces of pelletized samples with basicity levels of 0.2, 0.8, and 1.2 after reduction under different atmospheres are shown in Fig. 2. Panels a-c depict pelletized samples with basicity levels of 0.2, 0.8, and 1.2 under a CO atmosphere, while panels d-f depict pelletized samples with the same basicity levels under an H_2 atmosphere.

Under the CO atmosphere, distinct slender iron whisker can be observed on the surfaces of the pellets. Additionally, with an increase in basicity, these whiskers are gradually lengthened and become more numerous. Further, increases in basicity lead to the whiskers thickening. In contrast, under the H_2 atmosphere, no iron whiskers are generated. Instead, granular structures dominate the surfaces of the pellets. Moreover, as basicity increases, the quantity of granular iron phases exhibits a trend of initially

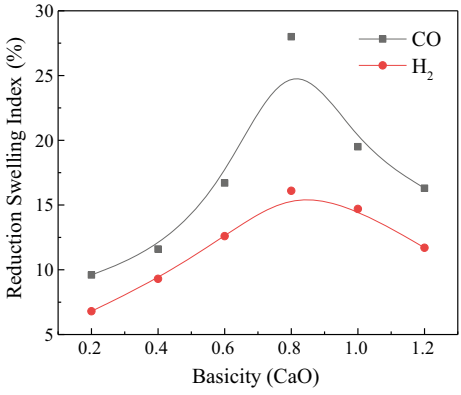

Fig. 1 Variation of reduction expansion rates with basicity under different atmospheres

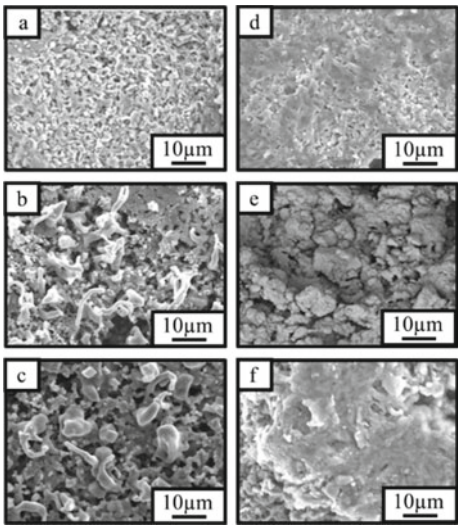

Fig. 2 SEM analysis of pelletized samples' surfaces after reduction under different atmospheres

increasing and then decreasing. The quantity and morphology of iron whiskers are closely related to the reduction swelling of pellets. Therefore, under hydrogen reduction conditions, the reduction swelling rate of pellet is lower than that under a CO atmosphere [20].

Formation Energy of Defects with Different Dopant Atoms

Dopant defects are primarily divided into two types: substitution defects and interstitial defects. In this study, different atomic substitutions of Fe atoms on the FeO{0 0 1} surface or interstitial defects between the first-layer FeO atoms were calculated to determine the formation energies of different types of defects. The results, as given in Table 1, reveal that the formation energy for creating Mg substitution defects is the lowest, at −1.99 eV, while the formation energy for Ca substitution defects is the highest, at 4.41 eV. Under the same atomic conditions, defects tend to form in a manner that yields lower formation energies. Once all structures with a specific atom have formed, the next type of atom's defects will form in the order of increasing formation energy, as listed in Table 1.

In Fig. 3, red spheres represent oxygen (O) atoms, and brown spheres represent iron (Fe) atoms. By measuring the atomic spacing after relaxation, it can be determined when no defects are formed, the Fe–O interatomic spacing on the FeO surface is 2.076 Å. After Mg and Si atomic doping, the average Fe–O interatomic spacing around Mg and Si atoms increases by approximately 0.001 Å, with minimal influence. However, with Al atomic doping, the nearby O atoms tend to approach the Al

Table 1 Defect formation energy of different defect types

Defect type	Al		Ca		Mg		Si	
	Interstitial	Substitution	Interstitial	Substitution	Interstitial	Substitution	Interstitial	Substitution
Formation energy/eV	1.38	−1.07	0.7	4.41	0.66	−1.99	2.84	1.59

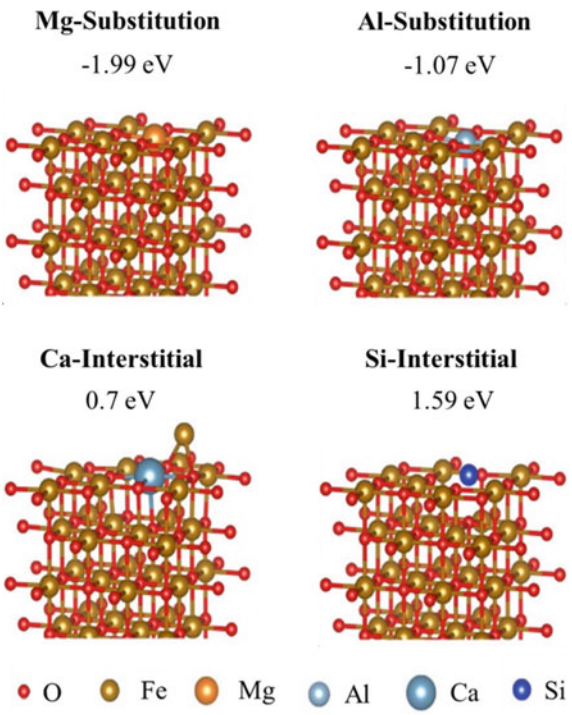

Fig. 3 Types and sequence of defect formation by different atoms

atom, resulting in an increased Fe–O interatomic spacing, with an average increase of around 0.02 Å.

Based on the simulation results from Fig. 3 and Table 1, it can be concluded that, when defects are formed on the surface of FeO with Ca, a surface Fe atom's position is initially occupied by it, the original Fe pushed to the surface of the lattice, resulting in the formation of point defects in the form of an interstitial solid solution. The measurement of atomic spacings in the lattice after relaxation reveals that, due to repulsive forces, the oxygen atoms surrounding the Ca atom are pushed away from the Ca atom, resulting in an increase of approximately 0.5 Å in the atomic spacing between Fe and O atoms perpendicular to the Ca-O direction. Conversely, the atomic spacing between Fe and O atoms parallel to the Ca-O direction has decreased by approximately 1 Å. Due to the displacement of some Fe atoms from the lattice, turning them into free Fe atoms, conditions are provided for the growth of iron whiskers. Consequently, as alkalinity increases, the number of iron whiskers in the spheroidal aggregates increases.

According to Fig. 3, it can be observed that, compared to Ca, surfaces doped with Mg, Al, or Si appear smoother, and the formation energy for Mg and Al doping is lower. This inhibits the formation of Ca interstitial solid solutions, thereby restraining the growth of iron whiskers.

Distribution of Differential Charge Density Under Different Defects

Differential charge density is obtained by subtracting the self-consistent charge density from the non-self-consistent charge density to represent the charge density distribution within the crystal. For a more intuitive representation, a plane located 3.6 Å above the Z-direction was selected to observe the electronic distribution, as shown in Fig. 4. When Mg, Al, or Si atoms form doped defects on the FeO surface, their weaker electron-binding capacity compared to oxygen atoms results in all their free electrons being taken away by surrounding oxygen atoms. As a result, in Fig. 4, the positions of these three atoms do not show any electrons, and due to the loss of electrons, they exhibit a positive charge. The O atoms, having taken in the excess electrons, display a negative charge. This results in mutual attraction between them, allowing Al, Mg, and Si to enter the lattice with minimal lattice distortion.

Due to Mg atoms exhibit the weakest positive charge, resulting in a circular distribution of electrons around Mg atoms. On the other hand, Si and Al atoms, being heavier, exhibit relatively stronger positive charges, causing some residual attraction around them, resulting in a water droplet-shaped distribution of electrons around them. The pointed end of these water droplets points towards the Si and Al atoms, leading to the convergence of nearby O atoms towards Al atoms. Ca atoms, due to their stronger electron-binding capabilities compared to O atoms, do not allow O atoms to capture electrons around them. Therefore, in Fig. 4, the positions of Ca atoms still exhibit electron distribution, causing Ca atoms to exert repulsive forces on surrounding atoms, leading to the separation of nearby O atoms.

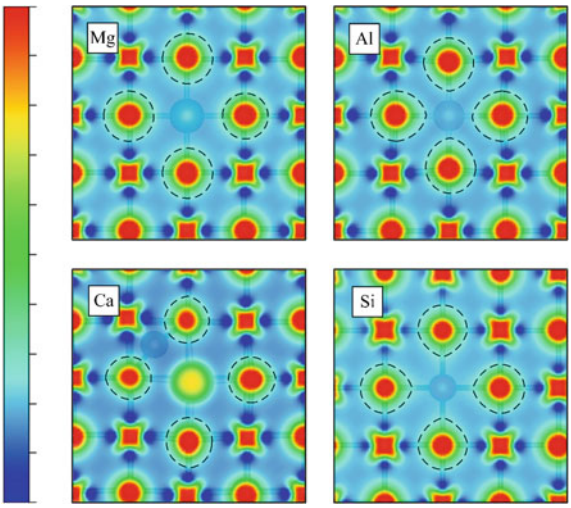

Fig. 4 Distribution of differential charge density after different atomic doping

Atomic Motion Behavior Under Different Defects at High Temperatures

To understand the growth mechanism of iron whiskers, the atomic motion under different defect conditions was simulated by reducing the first-layer oxygen atoms. Figure 5 displays the mean square displacement of atoms at 1173 K (900 °C) for different defects, with Fe representing the defect-free surface. The mean square displacement represents the average displacement of all particles in the system from their initial positions at a given moment. Due to the restricted diffusion of atoms within the crystal, the mean square displacement exhibits a sinusoidal trend.

After calculation, it is found that the surface without any atomic doping has a mean square displacement of approximately 0.05 Å. However, the vibration amplitude of surface atoms doped with Al atoms initially slightly increases and then gradually decreases over time. Doping with Mg atoms leads to a slight increase in vibration amplitude, with a mean square displacement of about 0.07 Å, and the amplitude decreases with time. The doping of Ca atoms significantly increases the amplitude, with a mean square displacement of approximately 0.13 Å, and the amplitude gradually increases over time. While Fe and Si can coexist in complex mixtures under certain conditions, they do not form direct covalent or ionic bonds, resulting in Si atoms being unable to be anchored within vacancies entirely surrounded by Fe atoms, thereby causing a significant distinction in the mean square displacement after Si doping compared to doping with other elements.

Furthermore, the presence of silicon results in a reduction of vibrational amplitudes of surface atoms, thereby stabilizing the FeO surface properties [21–23]. This also accounts for why an increase in silicon content in agglomerates leads to a reduction in their reactivity during reduction and a decrease in the formation of surface iron whiskers.

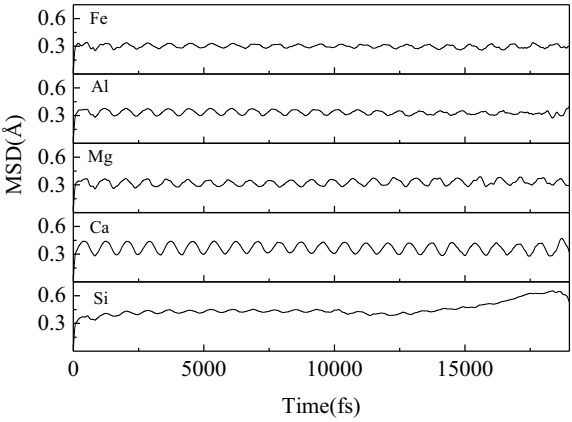

Fig. 5 MSD variation curves after different atomic dopings

AIMD Simulations of Crystal Surface After Adsorption of Different Molecules

The results of AIMD simulations are shown in Fig. 6. The grid in the figure represents the simplification of non-essential atoms and bonds. Each of the two red spheres below each diagram represents oxygen atoms positioned at different locations within the lattice, while the yellow sphere above represents free-state Fe atoms. From the figure, it can be clearly seen that, with the passage of time, CO causes Fe to migrate from position A of oxygen to position B. This process is accompanied by the formation of a new Fe–O bond and the rupture of the old Fe–O bond. While Fe atoms adsorbed with H2 can also generate new Fe–O bonds due to the thermal motion of the atoms themselves, the inability of two hydrogen atoms to move in the same direction, along with their low mass, prevents them from assisting Fe in overcoming migration barriers. This results in the rapid rupture of the newly formed Fe–O bonds, preventing the free Fe atoms from migrating.

Crystal growth is characterized by directionality. However, when FeO is reduced by H_2, the growth of crystals relies solely on the migration of Fe atoms within the crystal lattice, and this migration is restricted in distance. Therefore, the directionality of the metallic iron crystals formed after reduction is not significant, and no iron whiskers are generated. In a CO atmosphere, free Fe atoms can be induced to migrate by CO, increasing the mobility of Fe atoms and promoting the directed growth of crystals. Consequently, this macroscopically manifests as the growth of iron whiskers.

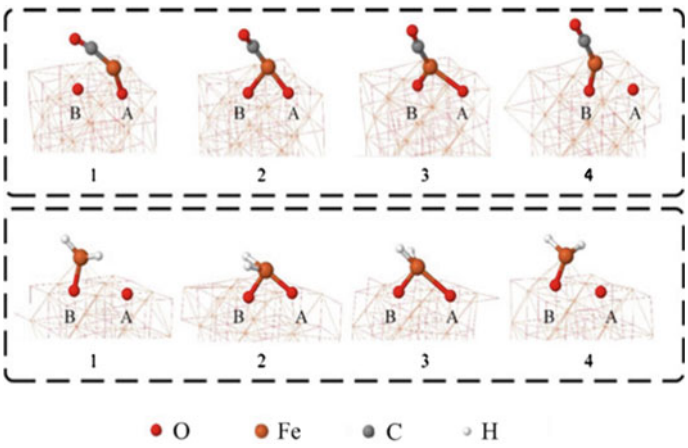

Fig. 6 AIMD simulations of surface-adsorbed different molecules on free Fe atoms

Conclusions

(1) In the study, it was observed that with an increase in basicity, the reduction swelling rate exhibited an initial rise followed by a subsequent decline, reaching its peak at the basicity level of 0.8, and the occurrence of this phenomenon is related to the growth of iron whiskers. Under a H_2 atmosphere, the reduction swelling rate of pellet is significantly lower than it is under a CO atmosphere, and no iron whiskers are formed on the surface of the pellet.
(2) Al, Si, or Mg primarily form defects by substituting Fe atoms, and the surface remains flat after formation. However, in the case of Ca, defects are primarily formed through interstitial solid solutions, pushing an Fe atom toward the lattice surface after defect formation, thereby promoting the growth of iron whiskers. This is due to Ca's strong electron-binding capability, which prevents oxygen atoms from stripping its electrons. As a result, Ca atoms have a larger atomic radius, leading to their maximum impact on the lattice. On the other hand, Al, Si, and Mg possess weaker electron-binding capabilities, allowing them to easily enter the lattice.
(3) The formation energy of defects for Mg and Al is significantly lower than that of Ca, resulting in the preferential formation of defects by Mg and Al over Ca. This effectively suppresses lattice distortion caused by Ca and prevents Ca from displacing Fe atoms from the lattice, thereby inhibiting the growth of iron whiskers.
(4) CO can induce the movement of free Fe atoms, enhancing the directionality of Fe crystal growth, which is macroscopically manifested as the promotion of iron whisker growth, leading to an increase in reduction expansion. On the other hand, H_2 cannot facilitate the migration of Fe atoms, so there is no iron whisker formation in the pure H_2 reduction process.

References

1. Liu Z, Lee SS, Nellikkattil AB, et al (2023) The East Asian summer monsoon response to global warming in a high resolution coupled model: mean and extremes. Asia-Pacific J Atmos Sci
2. Koven CD, Ringeval B, Friedlingstein P, et al (2011) Permafrost carbon-climate feedbacks accelerate global warming. Proc Natl Acad Sci
3. Wang T (2015) Analysis of the advantages, disadvantages, and development trends of major ironmaking processes. Shandong Indus Technol 17:2
4. Zhou Y, Qian H, Zhang Y et al (2009) Development direction and strategy of non blast furnace ironmaking technology. World Steel 9(1):8
5. Liu QC, Zhang YB, Lan YP, Chen QX (2013) Effect of lightly fired dolomite on metallic properties of singer. Iron Steel 48(03):15–18
6. Srinivas D, Banerjee PK (2014) Effect of fluxing agents on the swelling behavior of hematite pellets. Int J Mineral Process 126:76–89

7. Srinivas D, Ghosh TK, Shankar A, Tathavadkar V, Bhattacharjee D, Venugopal R (2011) Effect of pellet basicity and MgO content on the quality and microstructure of hematite pellets. Int J Mineral Process 99(1):43–45
8. Sesen MK (2001) The influence of CaO on the precipitation behavior of iron in the reduction of iron oxide. Scandinavian J Metall 30:1–7
9. Wang HT, Sohn HY, Chaudhary P et al (2014) Effect of fluxing agents on the swelling behavior of hematite pellets. Int J Mineral Process 126:76–89
10. Sesen MK (2001) The influence of CaO on the precipitation behavior of iron in the reduction of iron oxide. Scandinavian J Metall 30:1–7
11. Panigrahy SC, Jena BC, Rigaud M (1990) Characterization of bonding and crystalline phases in fluxed pellets using peat moss and bentonite as binders. Metall Trans B 21:463–474
12. Hammer B, Hansen LB, NoRskov JK (1999) Improved adsorption energetics within density-functional theory using revised Perdew-Burke-Ernzerhof functionals. Phys Rev B 59(11):7413–7421
13. Zhang S, Li K, Ma Y et al (2023) The adsorption mechanism of hydrogen on FeO crystal surfaces: a density functional theory study. Nanomaterials 13(14):2051
14. Lu F, Liangying et al (2023) The competitive adsorption behavior of CO and H_2 molecules on FeO surface in the reduction process—ScienceDirect. Int J Hydrogen Energy 44(13):6427–6436
15. Zhong H, Wen L, Li J et al (2016) The adsorption behaviors of CO and H2 on FeO surface: a density functional theory study. Powder Technol
16. Zhou C, Qingfan, et al (2010) Density functional theory study of water dissociative chemisorption on the Fe3O4(111) surface. J Phys Chem C
17. Freund HJ, Bauer E, et al (2015) Weak thermal reduction of biphase Fe2O3(0001) films grown on Pt(111): sub-surface Fe2+ formation. Surf Sci J Devoted Phys Chem Interfaces
18. Yu X, Li Y, Li YW, et al (2013) DFT+U study of molecular and dissociative water adsorptions on the Fe3O4(110) Surface. J Phys Chem C
19. Huang DM, Cao DB, Li YW et al (2006) Density function theory study of CO adsorption on Fe3O4(111) surface. J Phys Chem B 110(28):13920–13925
20. Zhong S, Guo L, Ding Z et al (2018) Observation on the growth of iron whiskers during the gas based direct reduction process of iron ore powder. Non Ferrous Metals Sci Eng 9(1):7
21. Jiang T, He G, Li G et al (2007) Effect of gangue composition on reduction expansion performance of iron ore pellets. Iron Steel 42(5):5
22. Fujuying W, Tang S et al (2001) Effect of different SiO_2 sources on the structure and properties of acid pellets. Iron Steel Res 1(3):1–5
23. Qinggele, W, Liuwenwang, et al (2011) Study on pelletizing technology with Peruvian magnetite powder. Sintered Pellets 36(6):6

Effect of Super-Gravity Field on the Purification and Solidification Structure of Oxygen-Free Copper (OFC)

Lu Wang, Xi Lan, Zhe Wang, and Zhancheng Guo

Abstract With the rapid development of the electrical and electronic industries, the quality requirements for oxygen-free copper (OFC) materials have become increasingly stringent, and the difficulty of oxygen removal content in OFC has increased accordingly. In this paper, the effect of super-gravity field on the purification of high-purity metals was investigated using oxygen-free copper. Microanalysis revealed that the oxygen elements in the samples primarily existed in the form of cuprous oxide. The effects of different gravity coefficients (G) and centrifugal time (t) on the distribution of oxygen in samples at 1200 °C were studied. The results showed that oxygen elements move in the opposite direction of the super-gravity. Moreover, the oxygen content in the sample could be significantly reduced from 31.37 ppm to 2.47 ppm at G = 1000 and t = 60 s, while the electrical conductivity improved from 103.23% IACS to 105.95% IACS. It is concluded that solidification under super-gravity conditions promotes grain refinement in the sample, with an increase in the gravity coefficient being advantageous.

Keywords Oxygen-free copper · Super-gravity · Oxygen content · Electrical conductivity

Introduction

Oxygen-free copper (OFC) has been widely applied in many technical fields such as electrical engineering and electronics because of its higher electrical conductivity, thermal conductivity, and better welding performance compared with traditional pure copper [1]. Oxygen content is one of the most important performance indicators of oxygen-free copper, requiring an oxygen content of less than 0.003%. OFE (C10100) and OF (C10200) are two typical grades of OFC recognized worldwide with purity of 99.99% and 99.95%, respectively. The former is used for vacuum electronics,

L. Wang · X. Lan · Z. Wang · Z. Guo (✉)
State Key Laboratory of Advanced Metallurgy, University of Science and Technology Beijing, Beijing 100083, China
e-mail: zcguo@ustb.edu.cn

S. Wagstaff et al. (eds.), *Materials Processing Fundamentals 2024*, The Minerals, Metals & Materials Series, https://doi.org/10.1007/978-3-031-50184-5_21

the latter is mainly used for electrical conductivity. The purity grade of the most used OFC is 99.95% in China, also called the National Standard No. 2 oxygen-free copper (TU2). Oxygen in copper is almost not a solid solution, which precipitates in the form of ($Cu–Cu_2O$) eutectic distributed on the grain boundaries of copper at the oxygen-containing copper melt solidifies. When heated in a reducing atmosphere, hydrogen (H_2) and carbon monoxide (CO) can rain cuprous oxide (Cu_2O) at high temperatures by reacting ($Cu_2O + 2[H] = 2Cu + H_2O$, $Cu_2O + CO = 2Cu + CO_2$). Water vapor and carbon dioxide are insoluble in copper. The pressure generated in order to precipitate, when the pressure is greater than the metal strength is, will cause the material along the grain boundary cracking, in serious cases, the surface bubbles visible to the naked eye. Therefore, it is crucial to reduce the oxygen content in oxygen-free copper [2, 3].

The production of OFC is mainly used in the following two methods, one is the vacuum furnace melting technology and the other is the power frequency induction furnace melting technology. The OFC produced by the former method can have an oxygen content of 0.0005% or less. However, the vacuum system is complicated and troublesome to maintain, the production cost is high and the output is low, so it is generally used to produce very demanding electric vacuum oxygen-free copper. The latter method has the advantage of stable and reliable product quality, but due to the complexity of the process, high cost, the capacity is not yet available.

In recent years, super-gravity technology has been applied in the preparation of gradient functional materials, removal of inclusions in metals, and enrichment of valuable components in metallurgical slag, all of which have achieved good results [4−6]. In the process of preparation and purification of metal melt, the super-gravity does not directly contact the metal melt, so it will not pollute the melt, which is an efficient melt purification technology. At the same time, from the microscopic point of view, the super-gravity field also has a favorable effect on the solidification structure of metal. Therefore, the feasibility of purifying and strengthening the grades of TU2 by super-gravity was studied in this paper.

Materials and Methods

The National Standard No. 2 oxygen-free copper (TU2) was purchased as raw material for this experiment, which was machined into a rod of 30 mm in length and 20 mm in diameter. The initial oxygen content was 32 ppm. Figure 1 shows a SEM image and element distribution maps from a typical region of an original OFC sample. It is evident from the SEM image that it mainly contains three colors. The dark gray hexagon particles are distributed within the continuous copper matrix (light gray). Point analysis by SEM revealed that the hexagon particles consisted of 67.9 at% Cu and 32.1% at % O, with a chemical formula of Cu_2O, which was a typical inclusion particle in oxygen-free copper. Additionally, the element mapping indicates that the inclusion particles were rich in Cu and O, as shown in Fig. 1c and d. Furthermore, a

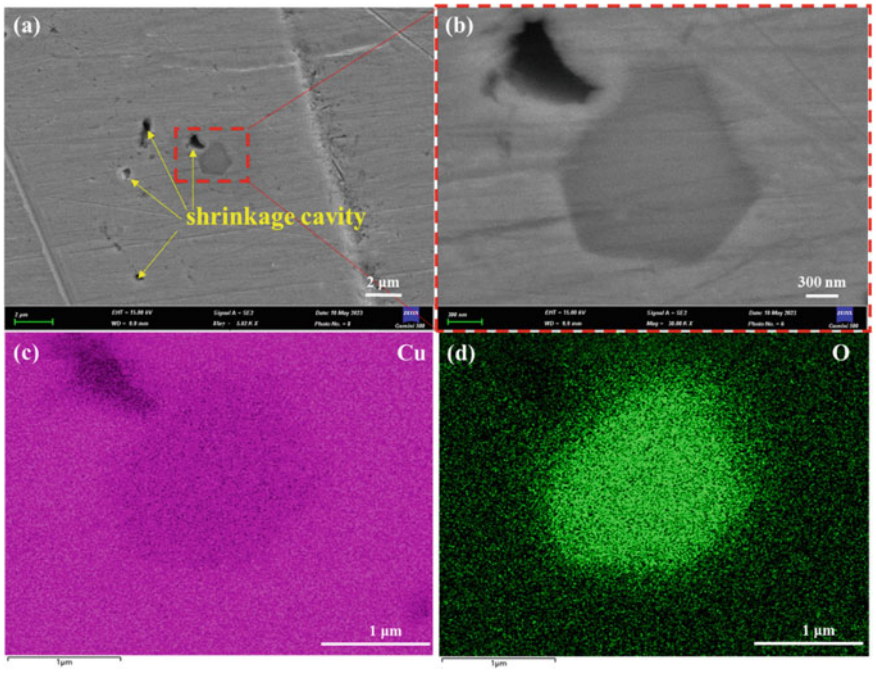

Fig. 1 Micro-morphology of the original OFC sample. **a** SEM image of the low power, **b** enlarged view of the region presented in image **a**, **c** SEM mapping analysis of the Cu element, **d** SEM mapping analysis of the O element

small amount of black region was also found in the copper matrix, which was defect in raw materials.

The super-gravity field was generated using a centrifugal apparatus consisting of two furnaces: the heating furnace and the counterweight furnace, which revolve around a rotation axis. A programmable controller and a B-type thermocouple are used to control the heating furnace temperature (within ±3 °C). Moreover, a slip ring attached to the centrifugal axis enables power transfer and electrical signaling during rotation. Reference [5, 7]. Approximately 120 g of OFC and 10 g of charcoal powder were placed into a quartz crucible and then put it into a graphite crucible with a lid to prevent the sample oxidation in the super-gravity purification experiments. Subsequently, heat preservation at 1200 °C for 30 min and then initiated and adjusted the super-gravity apparatus to achieve the desired rotating speed for a time. Finally, the sample was cooled at a constant rate until it was completely solidified. Reference samples were prepared using the same method under normal gravity (acceleration 1 g) conditions.

The gravity coefficient (G) is defined as the ratio of centrifugal acceleration to normal gravity acceleration. The purification efficiency is evaluated using the removal ratios of oxygen (γ) as shown in Eq. (1) and Eq. (2), respectively.

$$G = \frac{\omega^2 r}{g} = \frac{N^2 \pi^2 r}{900\ \mathrm{g}} \tag{1}$$

$$\gamma = \frac{\omega_{\mathrm{raw}} - \omega_G}{\omega_{\mathrm{raw}}} \times 100\% \tag{2}$$

where ω is the angular velocity (in rad·s^{-1}), N is the rotating speed of the centrifuge (in r·min^{-1}), r is the distance from the axis to the sample center (equal to 0.25 m in this work), ω_{raw} and ω_{G} are the oxygen content of the copper sample of original and after experimental, respectively.

Results and Discussion

Theoretical Analysis

Based on the Stokes formula theory, the feasibility of removal Cu_2O inclusions from OFC metal using super-gravity centrifugal forces was conducted. Meanwhile, a theoretical analysis was performed to investigate the impact of experimental factors on the motion behavior of these inclusions. The solid-phase inclusion particles within the melt were subjected to centrifugal forces in the horizontal direction and gravitational forces in the vertical direction. Compared to the horizontal centrifugal forces, the influence of ordinary gravity on inclusion particles in the vertical direction can be considered negligible. Moreover, the inclusion particles encountered not only centrifugal forces but also buoyant forces and viscous resistance in the horizontal direction. In this paper, the density of the inclusion particles (Cu_2O) was determined to be 6.0×10^3 kg/m^3, which was lower than the density of the OFC melt. Consequently, the inclusions within the melt exhibit reverse motion against the super-gravity field. Therefore, the force analysis of the inclusion particles in the horizontal direction was illustrated in Fig. 2 as follows.

A metal sample is placed into a controllable rotating centrifugation device, where the inclusion particles in the molten material (assuming them to be spherical) experience a centrifugal force (F_G) of

$$F_G = V \rho_{\mathrm{P}} \omega^2 r \tag{3}$$

According to Archimedes' principle, solid inclusions in a high-temperature molten substance experience buoyancy (F_B), the magnitude of which is

$$F_B = V \rho_L \omega^2 r \tag{4}$$

$$\rho_L = 8.75 \times 10^3 - 0.66T \tag{5}$$

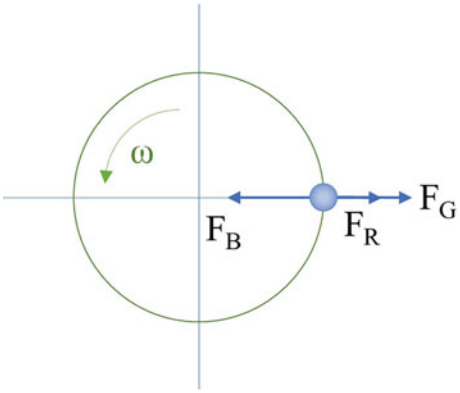

Fig. 2 Force analysis of inclusion particles in the horizontal direction

During the super-gravity purification of inclusions, due to the inclusion particles being relatively small, the relative motion between solid-phase inclusions and the molten liquid can be considered as a laminar flow state. Therefore, the viscous resistance (F_R) exerted on solid-phase inclusions during the molten material purification process can be expressed as

$$F_R = 3\mathrm{A}\pi\eta d v_r \tag{6}$$

$$\eta = 0.53\ \exp\left(\frac{23.9}{\mathrm{RT}}\right) \tag{7}$$

where $\rho_P = 6.0 \times 10^3$ kg/m^3 is the density of Cu_2O, ρ_L is the density of the high-temperature copper melt, T is the melt temperature, d is the diameter of Cu_2O, v_r is the relative velocity between the solid inclusion particles and the liquid-phase fluid medium, and η is the dynamic viscosity of the melt. A is the particle shape correction factor [8, 9]. When the inclusion particle shape exhibits a spherical or cubed, the value of A approaches 1. In addition, the shape cultivation coefficient of other inclusions ranged from 1.5 to 2.8.

Therefore, according to Newton's second law, the resultant force experienced by inclusion particles in the horizontal direction under a super-gravity field is

$$F = F_B - F_G - F_R = ma \tag{8}$$

Furthermore,

$$F = V\rho_L\omega^2 r - V\rho_P\omega^2 r - 3\mathrm{A}\pi\eta d v_r = V\rho_P\frac{\mathrm{d}^2 x}{\mathrm{d}t^2} \tag{9}$$

According to reference [8, 10], particles in high-temperature molten materials subjected to centrifugal forces may potentially reach their equilibrium velocity

instantly. Ultimately, these particles transition into uniform motion, experiencing a net external force of zero. Therefore, we can derive the equilibrium equation for particle motion as follows:

$$V\rho_L\omega^2 r - V\rho_P\omega^2 r - 3\mathrm{A}\pi\eta d v_r = 0 \tag{10}$$

The equilibrium velocity of particle motion is,

$$v_r = \frac{V(\rho_L - \rho_P)}{3\mathrm{A}\pi\eta d}\omega^2 r \tag{11}$$

Put Eq. (1) into Eq. (11), the ultimate settling velocity of inclusions within the molten metal is

$$v_r = \frac{V(\rho_L - \rho_P)}{3A\pi\eta d}Gg \tag{12}$$

It is evident that the final settling velocity (v_r) of inclusions is directly proportional to the gravity coefficient (G) and the square of the inclusion size. When the initial condition of centrifugation time (t) is $t = 0$ and $\mathrm{d}x/\mathrm{d}t = 0$, the velocity equations for inclusions in a super-gravity field at different time intervals as follows:

$$v_r = \frac{\mathrm{d}r}{\mathrm{d}t} = \frac{(\rho_L - \rho_P)VGg}{3\mathrm{A}\pi\eta d}\left[1 - e^{\left(-\frac{3\mathrm{A}\pi\eta d}{\rho_P V}t\right)}\right] \tag{13}$$

In this study, the inclusion particles are characterized as diminutive polyhedral bodies and ellipsoids. To facilitate calculations, it is assumed that the inclusion particles approximate spheres ($\mathrm{A} = 1$, $V = \pi\mathrm{d}^3/6$). Consequently, the equilibrium velocity of particle motion can be determined as follows:

$$v_r = \frac{\mathrm{d}r}{\mathrm{d}t} = \frac{(\rho_L - \rho_P)d^2Gg}{18\eta}\left[1 - e^{\left(-\frac{18\eta}{\rho_P d^2}t\right)}\right] \tag{14}$$

When $T = 1200$ °C (1473.15 K) is applied to Eq. (5) and Eq. (7), it can be concluded that the melt density is 7.78×10^3 kg/m^3, and the viscosity is 0.0028 Pa·s. According to Eq. (14), the motion behavior of Cu_2O ($\mathrm{d} = 2$ μm) inclusions in OFC melt under different gravity coefficients is illustrated in Fig. 3. Figure 3a shows the gravity coefficient significantly impacts the motion velocity of inclusion particles. It is evident that inclusion particles can reach equilibrium in a very short time at the super-gravity field. Additionally, with an increase in the gravity coefficient, the motion velocity of inclusion particles sharply increases. Figure 3b shows the relationship between the motion distance and time of inclusion particles in OFC at different gravity coefficients is depicted. It can be observed that higher gravity coefficients result in greater motion distances of inclusion particles at the same time interval. This implies more effective inclusion removal in the sample.

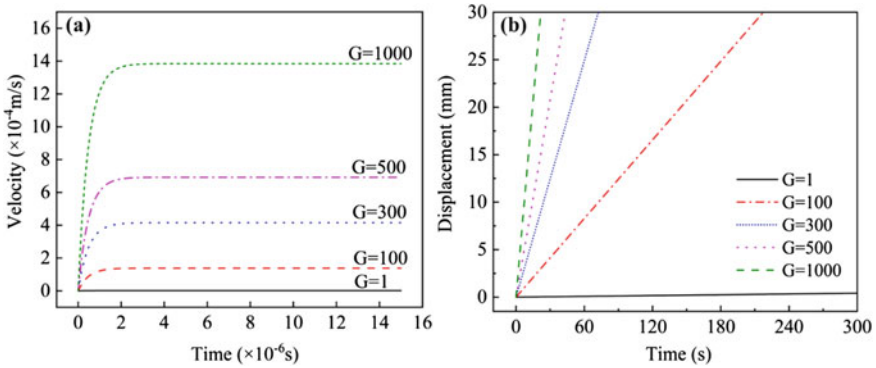

Fig. 3 Motion behavior of Cu_2O inclusions in OFC melts at different gravity coefficients. **a** relationship between the motion velocity of inclusion particles and time, **b** influence of gravity coefficient on the motion positions of Cu_2O inclusions

Super-gravity Purification of Oxygen-Free Copper

Based on the above findings, a super-gravity experiment was designed to investigate the purification effectiveness of OFC under different gravity coefficients and centrifugation time.

Effect of Gravity Coefficient

Figure 4 presents line graph depicting the effect of different gravity coefficients on oxygen content and oxygen removal rate in OFC. It can be observed that the oxygen content of the sample significantly decreases in the early stages of introducing super-gravity field. When $G = 100$, the oxygen content was reduced to 13.28 ppm, achieved a removal rate of 57.7%. As the gravity coefficient increased, the oxygen content continued to decrease, corresponding to an increase in the removal rate of oxygen. At $G = 1000$, the oxygen content in OFC sample decreased from 31.37 ppm to 2.47 ppm, and the oxygen removal rate was up to 92.1%. Detailed experimental parameters and results are listed in Table 1.

Effect of Centrifugal Time

Figure 5 illustrates the impact of different centrifugation time on oxygen content and oxygen removal rate in OFC at $G = 1000$. In Fig. 5, the values 5 mm, 15 mm, and 25 mm represented the average oxygen content at positions 5 mm, 15 mm, and 25 mm distance from the sample bottom, respectively. It can be seen that when the centrifugation time was 10 s, the oxygen content of the sample increased from bottom to top, with values of 9.31 ppm, 11.77 ppm, and 13.36 ppm, respectively. The results

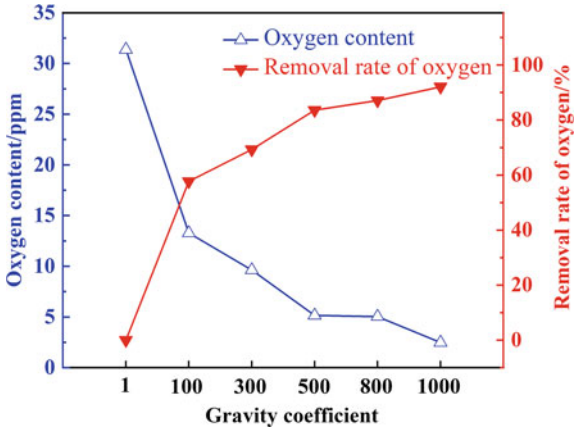

Fig. 4 Line graph depicting the purification effectiveness of OFC at different gravity coefficients

Table 1 Experimental parameters and purification results of OFC under different gravity coefficients

Gravity coefficient/*G*	Centrifugation time during insulation/s	Oxygen content/ppm	The removal rate of oxygen/%
1	0	31.37	0
100	60	13.28	57.7
300	60	9.63	69.3
500	60	5.15	83.6
800	60	5.04	87.1
1000	60	2.47	92.1

indicate that oxygen elements within the melt continued to move upward against super-gravity direction, but the centrifugation time was insufficient to completely remove the oxygen. As the centrifugation time was extended to $t = 30$ s, the oxygen content in the sample decreased from bottom to top, with values of 3.52 ppm, 6.1 ppm, and 7.06 ppm, respectively. Although the distribution of oxygen content still exhibited an upward trend contrary to the super-gravity direction, the overall oxygen content in the sample decreased. When the constant centrifugation time was further extended to $t = 60$ s, the oxygen content in the sample significantly decreased and stabilized, reaching a minimum of 2.47 ppm. Additionally, as the constant centrifugation time extended from 10 to 60 s, the oxygen removal rate increased from 63.4% to 92.1%. Detailed experimental parameters and results were listed in Table 2.

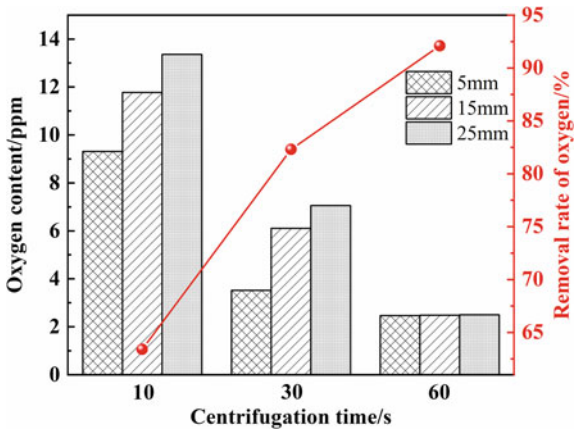

Fig. 5 Effect of oxygen content and oxygen removal rate in OFC at different centrifugation time

Table 2 Experimental parameters and purification results of OFC under different centrifugation time

Gravity coefficient/G	Centrifugation time/s	Distance from the sample bottom			γ/%
		5 mm	15 mm	25 mm	
1000	10	9.31	11.77	13.36	63.4
1000	30	3.52	6.11	7.06	82.3
1000	60	2.47	2.48	2.50	92.1

Effect of Solidification Structure Under Different Gravity Coefficient

Figure 6 shows macroscopic cross-sectional views of samples under different gravity coefficients after the purification experiment at $G = 1000$ and $t = 60$ s. It is evident that the grain size of the samples significantly decreased with an increase in the gravity coefficient. Meanwhile, a conductivity test was conducted on a sample taken from the red region in Fig. 6f, revealing that the conductivity of OFC increased from the original 103.23% IACS to 105.95% IACS.

Figure 7 displays SEM images of samples at different super-gravity coefficients. It can be seen that the microstructure matrix of the sample exhibits significantly increased purity after super-gravity purification, accompanied by a reduction in pore defects.

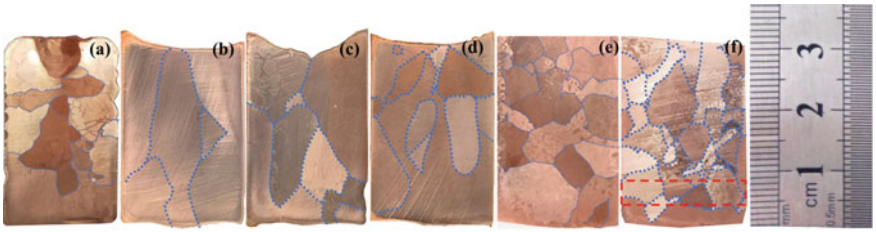

Fig. 6 Macroscopic cross-sectional views of OFC at different gravity coefficients. **a** $G = 1$, **b** $G = 100$, **c** $G = 300$, **d** $G = 500$, **e** $G = 800$, **f** $G = 1000$

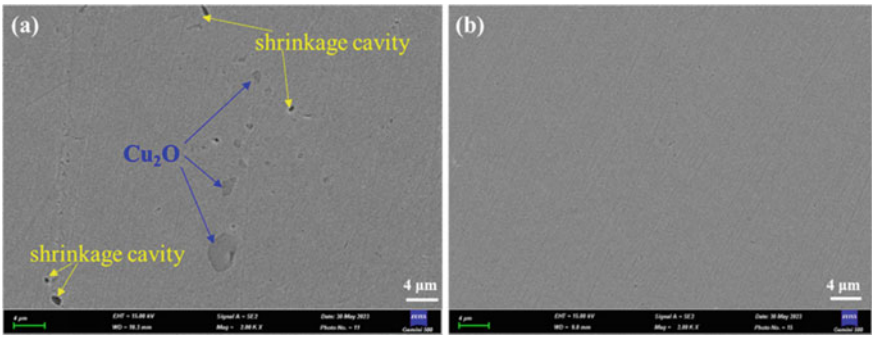

Fig. 7 SEM image of the sample at different super-gravity coefficients **a** $G = 1$, **b** G = 1000

Conclusions

The purification and solidification process of high-purity OFC is feasible and efficient through the super-gravity method. The purification effectiveness of oxygen in OFC under different gravity coefficients and centrifugation time were investigated. The main conclusions are summarized as follows:

(1) According to Stokes' law of motion, it has been determined that inclusion particles in a super-gravity field can quickly reach equilibrium settling velocity, with the velocity of inclusion particles directly proportional to the gravity coefficient.
(2) Super-gravity effectively removes Cu_2O inclusion particles from oxygen-free copper, migrating them in the opposite direction of super-gravity to the top of the sample. The average oxygen content decreased from an initial 31.37 ppm to 2.47 ppm, with an oxygen removal rate of up to 92.1%. Furthermore, the electrical conductivity of OFC increased from the original 103.23% IACS to 105.95% IACS.
(3) Super-gravity solidification of OFC benefits the grain refinement of the sample, with a more pronounced enhancement of grain refinement observed as the gravity coefficient increases.

Acknowledgements This work was supported by the National Natural Science Foundation of China [grant number 52174275].

References

1. Prasad YVRK, Rao KP (2006) Effect of oxygen content on the processing maps for hot deformation of OFHC copper. J Eng Mater Technol 128(2):158–162
2. Moller PJ, Hojlund Nielsen PE (1976) A study of copper(I) oxide in equilibrium with gold+copper alloys of low copper content. J Chem Thermodyn (8):141–150
3. Lancaster JF (1999) 10- non-ferrous metals. In: Lancaster JF (ed) Metallurgy of welding, 6th edn. Woodhead Publishing, pp 353–398
4. Wen XC, Dai PQ, Wang JL, Guo L, Guo ZC (2022) An environmentally-friendly method to recover silver, copper and lead from copper anode slime by carbothermal reduction and super-gravity. Miner Eng 180
5. Sun N, Wang Z, Sun B, Li Y, Guo Z (2022) Purification of primary aluminum liquid through supergravity-induced filtration. Chem Eng Process 182
6. Shi A, Li R, Zhang Y, Wang Z, Guo Z (2020) Effect of enhanced gravity on the microstructure and mechanical properties of Al(0.9)CoCrFeNi high-entropy alloy. Entropy (Basel) 22(11)
7. Meng L, Liu Y, Qu J, Guo Z (2023) Enrichment and separation behaviors of impurities from stripped copper wire with super-gravity fields. Chem Eng Process 191:109483
8. Li C, Gao J, Wang Z, Guo Z (2017) Separation of fine Al_2O_3 inclusion from liquid steel with super gravity. Metall Mater Trans B 48(2):900–907
9. Song GY, Song B, Yang YH, Yang ZB, Xin WB (2015) Separating behavior of nonmetallic inclusions in molten aluminum under super-gravity field. Metall Mater Trans B 46(5):2190–2197
10. Yang Y, Song B, Song G, Yang Z, Xin W (2016) Enriching and separating primary copper impurity from Pb-3 mass Pct Cu melt by super-gravity technology. Metall Mater Trans B 47(5):2714–2724

Modeling of Temperature Drop Prediction of Hot Metal Based on Heat-Transfer Mechanism and Machine Learning

Jianping Yang, Pan Gao, Liujie Yao, Haibo Li, Xiaodong Zhao, and Hanwen Jing

Abstract Predicting the temperature drop of hot metal is greatly significant for the decision-making of scrap steel amount in basic oxygen furnace (BOF). In addition, accurate prediction of temperature drop can guide the scheduling of hot metal, keeping the steelmaking process stable. In this paper, a prediction model of temperature drop was developed by integrating heat-transfer mechanisms and machine learning models. Extreme learning machine (ELM) was applied to establish the machine learning model (MLM). Further, the performance of MLM was optimized by introducing regularization and particle swarm optimization (PSO). Based on actual data from a steelmaking plant in China, the above models were trained and verified. The results show that the hit ratio of the integration model is 88.53% when the prediction error is within 10 °C, which is higher than those of the heat-transfer mechanism and the optimized machine learning models. Meanwhile, the robustness of the integration model is also optimal.

Keywords Temperature drop prediction · Hot metal · Heat-transfer mechanism · Machine learning · Extreme learning machine

Introduction

The temperature drop of hot metal at the ironmaking-steelmaking interface is one of the important indicators for evaluating the energy efficiency of the steel manufacturing system. Excessive temperature drop of hot metal not only causes energy loss but also affects subsequent iron pretreatment and steelmaking processes [1]. Therefore, real-time and accurate prediction of the temperature drop and its changing trend

J. Yang (✉) · P. Gao · L. Yao · H. Li
Shougang Research Institute of Technology, Beijing 100043, China
e-mail: pinggegeyjp@163.com

X. Zhao · H. Jing
Beijing Shougang Co., Ltd., Beijing 100041, China

S. Wagstaff et al. (eds.), *Materials Processing Fundamentals 2024*, The Minerals, Metals & Materials Series, https://doi.org/10.1007/978-3-031-50184-5_22

at the ironmaking-steelmaking interface is of great significance for efficient operation of hot metal, optimization of the production scheduling system, improvement of hot metal quality, and efficient thermal linkage.

At present, the issue of temperature drop at the ironmaking-steelmaking interface has attracted widespread attention, and certain research has been conducted [2–4]. The current research methods of temperature drop of hot metal mainly focus on two aspects: (1) Establish a mathematical model for the temperature drop of hot metal based on the heat dissipation phenomenon during transportation at the ironmaking-steelmaking interface [5, 6], but due to the actual transportation of hot metal is very complex, the thermal state and turnover time of torpedo ladles (TPC) are not the same, which makes the mechanism model has low computational accuracy, high time-consuming cost, and low real-time performance. (2) Establish a mathematical model for the temperature drop of hot metal based on supply–demand balance of hot metal and queuing theory [7, 8]. This type of model can effectively shorten the operating cycle and improve the turnover rate, but there is a lack of detailed research on the relationship between turnover rate and temperature drop of hot metal [9], making it difficult for this model to predict actual temperature drop.

To sum up, assumptions must be made to ensure the availability of the mechanism model, so its prediction accuracy may not be desirable. Machine learning methods solve the prediction problems just in dependence on data, in which assumptions should not be made, and underlying relationships between inputs and outputs also can be revealed. Therefore, the machine learning method is used to predict the temperature drop of hot metal in this paper. Since extreme learning machine is a high-efficient machine learning method, the machine learning model is established by using it, which is optimized by introducing regularization and PSO. Then the machine learning model is integrated with the mechanism model established based on the analysis of heat-transfer mechanism, in order to further improve the prediction accuracy of temperature drop of hot metal. This paper can provide effective guidance for relevant production operators to reasonably control the temperature of hot metal.

Establishment of the Machine Learning Model

Basic ELM Model

ELM is a new single hidden layer feedforward neural network [10]. A typical single hidden layer feedforward neural network structure is shown in Fig. 1.

For a single hidden layer neural network, there are n different data samples $(X_j, Y_j) \in R_n \times R_m$. The hidden layer nodes and activation function are respectively set L and $G(x)$ in this neural network, and the values of connection weight and deviation of neurons in hidden layer network are respectively set ω and b. Then, the mathematical expression of ELM model is shown in Eq. (1).

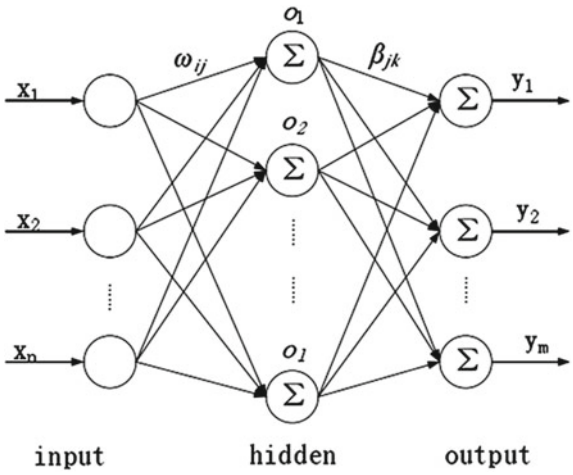

Fig. 1 Typical single hidden layer feedforward neural network model

$$Y_m = \sum_{i=1}^{L} \beta_i G\left(\omega_i, b_i, x_j\right) \quad (j = 1, 2, \ldots, n) \tag{1}$$

where Y_m is the output of the neuron in the m-th output layer of the network, $G\left(\omega_i, b_i, x_j\right)$ is the output of the i-th hidden layer neuron.

It is only necessary to determine the appropriate number of hidden layer nodes and activation function since input layer weight ω and hidden layer deviation b are randomly generated in the model before training samples. Then the connection weight β between the hidden and output layers can be calculated.

The first step for establishing the ELM model is to determine the input variables. Based on the analysis on the turnover process of hot metal in the studied steel mill, the following influencing factors of temperature drop are selected as input variables of the ELM model and shown in Table 1. In the studied steel mill, cold bond pellets from the treatment of steelmaking slag are charged into TPC to realize the reuse of Fe-containing solid waste, and meanwhile, its addition will increase the temperature drop of hot metal. Thus, the addition of cold bond pellets should be considered as one input variable.

After the input variables being determined, the network structure can be built, and the temperature drop of hot metal is the output variable. The temperature drop of hot

Table 1 Input variables in the ELM model

Input variables	Tapping temperature/°C	Transportation time of empty TPC/min	Transportation time of full TPC/min	Turnover times of TPC	Amount of cold bond pellets/t
Value range	1470 ~ 1530	60 ~ 180	15 ~ 60	≤1000	0 ~ 9

metal is the difference between tapping temperature and temperature after hot metal being poured from TPC to ladle.

Regularization of the ELM Model

ELM is only based on the principle of empirical risk minimization. It takes the minimum training error as the measurement criterion and does not take the structural risk into account. Therefore, there may be over-fitting problems, when the number of hidden layer nodes is too large.

The problem of over-fitting can avoid in the process of training the ELM model by introducing structural risk and regularization coefficient λ to adjust the ratio between structural and empirical risks, and enhance the prediction accuracy [11]. The ELM model corrected by regularization is named as RELM and expressed as:

$$\min E = \min_{\beta}\left(\lambda\left\|\beta^2\right\| + \left\|\varepsilon^2\right\|\right) \tag{2}$$

$$s.t.\sum_{i=1}^{N}\beta_i f\left(w_i x_j + b_i\right) - t_j = \varepsilon_j (j = 1, 2, \ldots, N) \tag{3}$$

where $\lambda\left\|\beta^2\right\|$ indicates structural risk, $\left\|\varepsilon^2\right\|$ means experience risk, λ is the regularization coefficient, ε_j represents the sum of errors generated during training.

The Lagrange equation is thus constructed:

$$L(\beta, \varepsilon, \alpha) = \lambda\left\|\beta^2\right\| + \left\|\varepsilon^2\right\| - \alpha(H\beta - T - \varepsilon) \tag{4}$$

Where $\alpha = [\alpha_1, \alpha_2, \ldots, \alpha_N]$, $\alpha_i \in R(i = 1, 2, \ldots, N)$ is a Lagrangian operator. Calculate the partial derivative of each variable in Eq. (5):

$$\begin{cases} \frac{\partial L}{\partial \beta} \rightarrow 2\lambda\beta^T = \alpha H \\ \frac{\partial L}{\partial \varepsilon} \rightarrow 2\varepsilon^T + \alpha = 0 \\ \frac{\partial L}{\partial \alpha} \rightarrow H\beta - T - \varepsilon = 0 \end{cases} \tag{5}$$

When $\lambda I + H^T H$ is a nonsingular matrix, the solution of Eq. (6) is:

$$\hat{\beta} = \lambda I + H^T H^{-1} H^T T \tag{6}$$

where I is the identity matrix. Then the output of the network is:

$$Y = H\hat{\beta} = H\lambda I + H^T H^{-1} H^T T \tag{7}$$

It can be seen from the above formula that this paper has successfully introduced the structural risk minimization theory and regularization coefficient into the ELM model and constructed the RELM model.

Optimization of PSO

Although the RELM model improves the generalization ability by introducing the structural risk minimization theory, it cannot ensure that the trained RELM model is optimal when solving the gradient descent problem, since the input layer weights and hidden layer deviations are randomly generated. Therefore, the RELM model needs more hidden layer nodes to achieve the desired accuracy, which leads to problems such as slow convergence speed, low prediction efficiency, and poor stability. Aiming at the above problem, the RELM model is improved by PSO algorithm which has the advantages of easy implementation, high accuracy, and fast convergence speed.

The theory of PSO algorithm will not be stated, since it can be known in any articles or books which introduce the machine learning [12]. In this paper, an improved PSO algorithm is adopted by genetic algorithm (GA) [13], due to the standard PSO easy to fall into local extremum in the process of iterative optimization.

(1) Use a nonlinear weighting method to improve the shortcomings of standard PSO algorithm [14], which can be described as:

$$\omega = \omega_{\max} - (\omega_{\max} - \omega_{\min}) * \tan\left(\frac{k}{N} \times \frac{\pi}{4}\right) \tag{8}$$

where $\omega_{\max}$, $\omega_{\min}$ represent the initial value and the minimum value at the end of the iteration, k is the current iteration number, and N is the maximum iteration number.

(2) Use the mutation idea of GA for reference, the "mutation" factor is added to the PSO algorithm; that is, the particle has a certain mutation rate. After each update of the particle, the particle is initialized with a certain probability, so that it can jump out and continue to search when it falls into a local extreme value.

The weights of the input layer and the deviations of the hidden layer in the RELM model are used as the particles of the PSO algorithm, and the improved PSO algorithm is used to optimize them. The mean square error (MSE) of the predicted and measured values of the training set is used as the fitness function, so as to improve the prediction accuracy and efficiency of the RELM model.

Figure 2 shows the training flowchart of RELM model optimized by improved PSO algorithm (IPSO-RELM). The specific training process is summarized as follows:

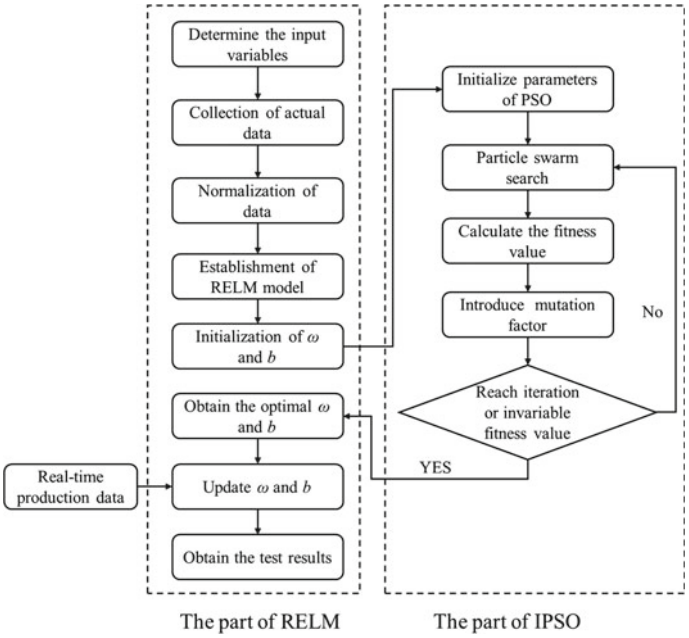

Fig. 2 Training flowchart of IPSO-RELM

Establishment of the Mechanism Model

The occurrence of temperature drop of hot metal should include the process of hot metal flowing through the groove, the process of hot metal falling into the TPC, the process of TPC transporting through the railway, and the process of hot metal falling into the ladle from TPC. Li has established the mechanism model by considering the above processes except for the process of hot metal flowing through the groove [15]. Therefore, the temperature drop prediction for the process of hot metal flowing through the groove is considered in the paper. The temperature drop prediction for other processes refer to Li's study, and the relevant formulas will not be shown in this paper.

The process of hot metal flowing through groove mainly includes convective heat dissipation to the groove, radiative heat dissipation, and convective heat dissipation to the external environment. Based on this, an energy balance equation is established, as shown in Eqs. (9) to (11):

$$\begin{aligned} Q_{\mathrm{grv}} = &\left(\varepsilon_{\mathrm{Fe}} \cdot \sigma \cdot \left(T_0^4 - T_{\mathrm{air}}^4\right) \cdot S_{\mathrm{Fe}} + \alpha_{\mathrm{Fe\,-\,air}} \cdot (T_0 - T_{\mathrm{air}}) \cdot S_{\mathrm{Fe}}\right) \cdot \tau_{\mathrm{gry}} \\ &+ \alpha_{\mathrm{Fe\,-\,gry}} \cdot \left(T_0 - T_{\mathrm{gry}}\right) \cdot S_{\mathrm{gry}} \cdot \tau_{\mathrm{gry}} \end{aligned} \tag{9}$$

$$\alpha_{\mathrm{Fe\,-\,air}} = 0.664 \cdot \frac{\lambda_{\mathrm{air}}}{L_{\mathrm{gry}}} \cdot \mathrm{Re}^{\frac{1}{2}} \cdot \mathrm{P}_r^{\frac{1}{3}}$$

$$= 0.664 \cdot \frac{\lambda_{\text{air}}}{L_{\text{gry}}} \cdot \left(\frac{L_{\text{gry}} \cdot v_{\text{air}} \cdot \rho_{\text{air}}}{\mu_{\text{air}}} \right)^{\frac{1}{2}} \cdot \left(\frac{c_{\text{air}} \cdot \mu_{\text{air}}}{\lambda_{\text{air}}} \right)^{\frac{1}{3}} \tag{10}$$

$$Q_{\text{gry}} = c_{\text{Fe}} \cdot M_{\text{gry}} \cdot (T_0 - T_1) \tag{11}$$

In the formula, Q_{gry} is the total heat dissipation through the groove, J; ε_{Fe} is the blackness coefficient of hot metal; σ is the Stefan–Boltzmann constant; T_0 and T_1 are hot metal temperature at the start and end points of the groove, K; T_{air} and T_{gry} are the ambient and groove temperature, K; S_{Fe} is the contact area between hot metal and the environment, m^2; $\alpha_{\text{Fe - air}}$ is the convective coefficient between hot metal and the environment, W/(m^2 K); τ_{gry} is the time for hot metal through the groove, s; $\alpha_{\text{Fe - gry}}$ is the convective coefficient between hot metal and the groove, W/(m^2 K); S_{gry} is the contact area between hot metal and iron trench, m^2; λ_{Fe} is the thermal conductivity of hot metal, W/(m·K); D_{gry} is the equivalent diameter of the groove, m; c_{Fe} is the heat capacity of hot metal, J kg^{-1} K^{-1}; λ_{air}, v_{air}, ρ_{air}, μ_{air}, and c_{air} are the air thermal conductivity, wind speed, density, dynamic viscosity, and heat capacity, W/(m K), m/s, kg/m^3, kg/(m s), and J kg^{-1} K^{-1}; L_{gry} is the length of the groove, m; M_{gry} is the amount of hot metal stored in the groove, t.

Establishment of the Integrated Model

Both machine learning and mechanism models have advantages and disadvantages, and the prediction accuracy may be further improved by integrating them through some methods. The weight coefficient method is applied widely for models integration [16]. The basic expression is shown in Eq. (12):

$$R_{\text{inte}} = a \cdot R_{\text{data}} + b \cdot R_{\text{mech}} \tag{12}$$

where R_{inte}, R_{mech}, and R_{data} represent the prediction results of the integrated model, mechanism model, and machine learning model, respectively; a and b represent the weight coefficients of the machine learning and mechanism models, respectively, satisfying $a + b = 1$.

By adjusting the values of a and b, the prediction accuracy of the integrated model may be changed, and the optimal a and b can be determined corresponding to the highest prediction accuracy of the integrated model.

Model Testing

After preprocessing the production data collected from a steelmaking plant in China (removing discrete, abnormal, and duplicate data, smoothing noise data, and filling in missing data), 3031 sets of production data were obtained. The ISPO-ELM model takes 3031 sets of production data as samples, in which 2500 sets of sample data are randomly selected to train the prediction model, and the remaining data are used to test the trained model. The simulation of the model is implemented in the Python environment. After extensive experiments adjusting model parameters, it was found that the IPSO-ELM model had the best prediction performance when the network structure parameters shown in Table 2 were selected.

The test result of the integrated model is shown in Fig. 3 with the changing of a from 0 to 1. The robustness can represent the model stability in complex working conditions. In this study, root mean square error (RMSE) is used to evaluate the robustness of the integrated model, and the result is shown in Fig. 4. With a increasing, the prediction accuracy and robustness of the integrated model show an increasing trend. When a is 0.8, the integrated model has the highest prediction accuracy within the error range of ± 10 °C, reaching 88.53%, and the minimum root mean square error is 6.3. Indeed, the larger value of a means the machine learning model has a larger contribution on prediction accuracy, which indicates its high availability.

In Fig. 5, the prediction accuracy of the integrated model is compared with the mechanism model, the machine learning model, and the industry practices by manual statistics. Obviously, the prediction accuracy of the integrated model is higher than others, in which both the mechanism and machine learning models can exploit their advantages to the full. Indeed, the performance of ELM model shows an improvement by the consideration of regularization and the optimization of PSO. In addition, the performance of the mechanism model is better than the RELM model, but worse than the IPSO-RELM model. In fact, the prediction accuracy within ± 10 °C is more concerned by operators in-site, and the performance of the integrated model, namely 88.53%, is better than 84.75% shown in Ref. 14.

For actual use, the integrated model is continuously updated with ongoing processing data to keep a stable performance with process variations. The expected size of the training dataset is chosen in the range from 2000 to 3000, being a good trade-off between generalization performance and update rate.

Table 2 Basic parameters of IPSO-RELM model

Parameter	Value	Parameter	Value
Number of input layer nodes	5	Population size, P	40
Number of hidden layers	1	Iterations, N	80
Number of hidden layer nodes	20	Maximum weight coefficient, $\omega_{\max}$	1.2
Number of output layer node	1	Minimum weight coefficient, $\omega_{\min}$	0.4

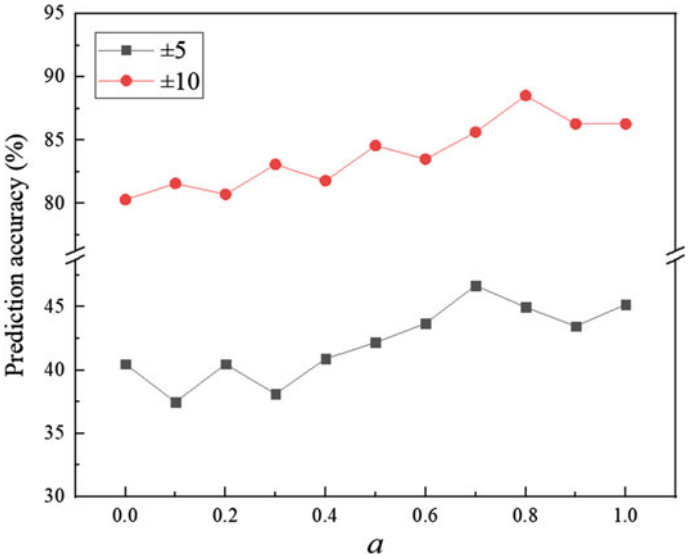

Fig. 3 Prediction accuracy test of the integrated model

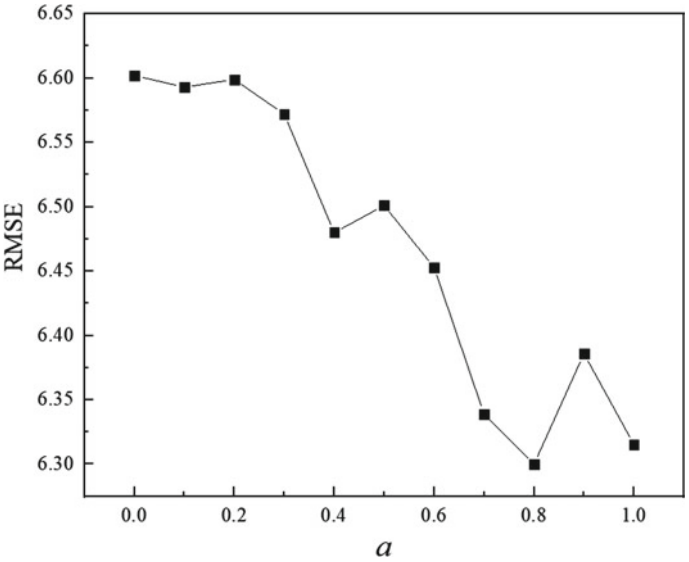

Fig. 4 Robustness test of the integrated model

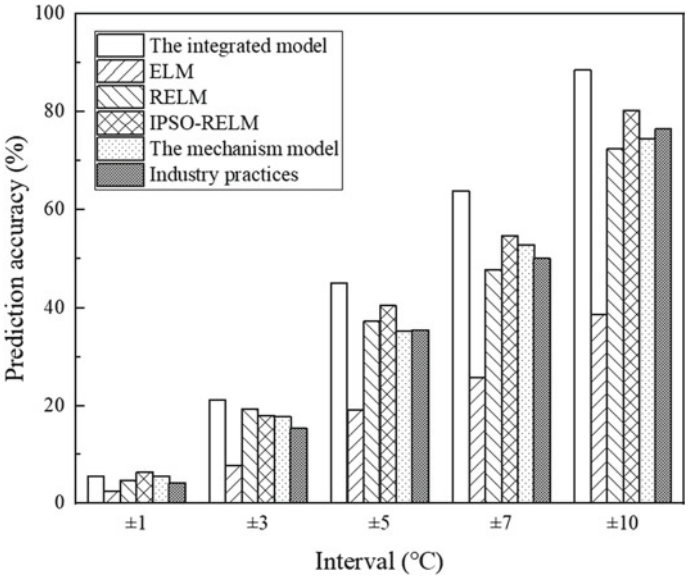

Fig. 5 Comparison of prediction accuracy of different models

Conclusions

(1) An integrated model for predicting the temperature drop of hot metal was developed by combining heat-transfer mechanism and machine learning models through weight coefficient method.
(2) The prediction accuracy of the machine learning model based on ELM has an obvious improvement by regularization and optimization of PSO algorithm.
(3) The highest hit ratio of temperature drop is 88.53% within 10 °C, when the weight coefficients of the machine learning and mechanism models are 0.8 and 0.2 in the integrated model, which is better than those of the mechanism and machine learning models.

References

1. Xu DY, Liu CP, Yang DZ et al (2007) Analysis and evaluation of temperature value about hot metal. Energy Metall Ind 26(3):7–9+42
2. Qiu J, Tian NY, Li XP et al (2005) Research on BF/BOF interface route with one open ladle from BF to BOF. Iron Steel 40(8):18–21+47
3. Li XP, Zhang CX, Zhang XX et al (2006) Evolvement of techo-interface mode of blast furnace and basic oxygen furnace region. Chin J Process Eng 6(S1):118–122
4. Yang G, Xu AJ, He DF (2018) Review on temperature drop of hot metal from BF to BOF. China Metall 28(4):1–6+12

5. Wu ML, Zhang YH, Yang SF et al (2002) Analysis of hot metal temperature drop in torpedo car. Iron Steel 37(4):12–15
6. Wang J, Tang E, Fan XG et al (2015) Brief analysis of heat loss calculation in the hot metal transportation. China Metall 25(4):12–17
7. Huang BF, Tian NY, She Z et al (2014) Material flow control technology of ironmaking and steelmaking interface. J Central South Univ 21(9):3559–3567
8. Gu ZX, Xu AJ, He DF et al (2017) A calculation model for determining number of hot metal ladle based on queuing theory with constraints of system capacity. J Chongqing Univ 40(8):70–77
9. Wan W, Zhao ZY, Zhao J (2013) Temperature control of torpedo ladle car. Metall Collections 5:24–26
10. Chen HZ, Yang JP, Lu XC et al (2018) Quality prediction of the continuous casting bloom based on the extreme learning machine. Chin J Eng 40(7):815–821
11. Na WB, Su ZW, Ji YF (2013) Research of single well production prediction based on improved extreme learning machine. Appl Mech Mater 333–335(3):1296–1300
12. Chen CY (2011) PSO-based evolutionary learning[M]. LAP Lambert Academic Publishing
13. Zhang Z (2018) Research on models of end-point manganese content prediction and calculation of silicon-manganese alloy addition for HRB400 steel in converter steelmaking process[D]. University of Science and Technology Beijing, Beijing
14. Tao HL (2012) Research on railway traffic volume prediction based on hybrid intelligent algorithms[D]. Lanzhou, Lanzhou Jiaotong University
15. Li YJ (2008) Study on hot metal temperature drop on BF/BOF region in iron & steel factory[D]. Northeastern University, Shenyang
16. Gu MQ, Xu AJ, Yuan F et al (2021) An improved CBR model using time-series data for predicting the end-point of a converter. ISIJ Int 61(10):2564–2570

Modification and Evaluation of Desulfurization and Denitrification of 360 m^2 Sintering Machine in Shougang Qian'an Company

Yapeng Zhang, Shuhai Ou, Wen Pan, Chunlai Wang, Huaiying Ma, and Sida Ren

Abstract Technical transformation and modification have been carried out on the dense flow absorber for desulfurization of 360 m^2 sintering machine in Shougang Qian'an Iron and Steel Company. Also, selective catalytic reduction (SCR) denitrification system was added at the same time. Desulfurization efficiency of sintering flue gas was improved by changing the desulfurization agent and expanding the capacity of desulfurization system. The desulfurization efficiency increased to over 95%. By applying selective catalytic reduction (SCR) denitrification technology, the nitrogen oxide emission at the outlet is reduced to about 30 mg/m^3. Through the above technical transformation measures, the sintering process has achieved ultra-low emissions of pollutants. The outlet dust is lower than 10 mg/m^3, the outlet concentration of SO_2 is lower than 35 mg/m^3, and NOx is lower than 50 mg/m^3.

Keywords Dense flow absorber · Desulfurization · SCR · Denitrification

Introduction

As an important pillar industry of the national economy, the iron and steel industry is also a major energy consumer and polluter. The iron ore sintering process is the largest source of SO_2 and NOx emissions in the iron and steel industry [1–3]. About 51–62% of SO_2 and 48% of NOx in the iron and steel production process come from the sintering process, which is the largest source of SO_2 and NOx [4, 5]. Therefore,

Y. Zhang (✉) · W. Pan · C. Wang · H. Ma · S. Ren
Beijing Key Laboratory of Green Recyclable Process for Iron and Steel Production Technology, Beijing 100043, China
e-mail: zyp1989zyp@163.com

Research Institute of Iron and Steel, Shougang Group Co., LTD Research Institute of Technology, Beijing 100043, China

S. Ou
Ironmaking Department, Shougang Qian'an Iron and Steel Company, Tangshan 063200, China

S. Wagstaff et al. (eds.), *Materials Processing Fundamentals 2024*, The Minerals, Metals & Materials Series, https://doi.org/10.1007/978-3-031-50184-5_23

desulfurization and denitrification of sintering flue gas has become an important measure for clean production and pollutant emission reduction in iron and steel company.

The 360 m^2 sintering machine of Shougang Qian'an Iron and Steel Company was put into construction in 2007 and operation in 2008. In 2009–2010, a dense flow tower semi-dry desulfurization device was added. In order to achieve ultra-low emissions, it was determined to expand the existing dense flow tower semi-dry desulfurization system and add a new SCR denitrification process. It has great advantages in terms of investment, technical reliability, and follow-up operation.

In response to the government's request for ultra-low emissions in iron and steel enterprises, the 360 m^2 sintering machine at Shougang Qian'an Iron and Steel Company remodeled the original desulfurization and added an SCR denitrification device. After the project was completed and put in operation, the particle matter (PM), SO_2, NOx concentration of outlet were lower than 10 mg/m^3, 35 mg/m^3, 50 mg/m^3. It became the first batch of sintering machines in Tangshan area to pass the acceptance inspection of ultra-low emission standard.

Transformation of Dense Flow Semi-Dry Desulfurization Device

Dense flow tower desulfurization technology, as a kind of humidification and activation calcium-based semi-dry desulfurization technology, is widely used in steel plant pelletizing and sintering system flue gas desulfurization and has been valued by more and more domestic scholars and institutions. Pellet and sintering flue gas volume is large, SO_2 content fluctuates greatly, and the flue gas composition is complex. The dense flow tower desulfurization and PM removal treatment system is developed on the basis of the dense flow tower. It is an integrated technology with low cost and high integration.

Dense Flow Tower Desulfurization Device

The desulfurization process adopts the dense flow tower semi-dry desulfurization method, and the specific process is shown in Fig. 1. The sintering flue gas enters from the upper part of the dense flow tower, and flows downward from the top of the desulfurization tower together with the humidified desulfurizer (lime bag dust collector). During the movement, the lime undergoes a series of reactions with water and SO_2 to produce desulfurization by-products, the main components are $CaSO_4$ and $CaSO_3$. A large amount of flue gas containing particles is discharged from the lower outlet of the dense flow tower and enters the dust collector to separate gas and PM. After purification, the flue gas is discharged from the chimney through the dust

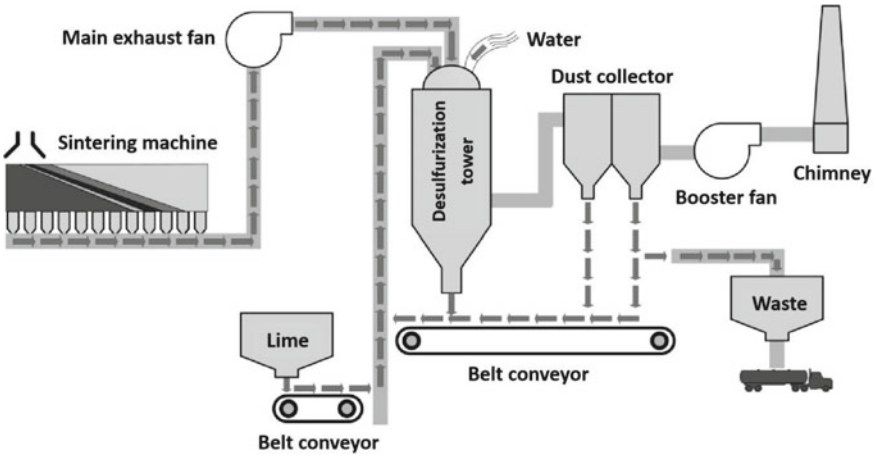

Fig. 1 Dense flow tower semi-dry desulfurization device

collector. The solid particles at the bottom enter the dense flow tower again to continue participating in the reaction, while a small amount of the reacted desulfurizer enters the waste bin, thus forming a complete system cycle.

The operating cost of the system is about 5.7 yuan/ton of ore. The designed SO_2 inlet concentration is lower than 800 mg/m^3, and the outlet is lower than 100 mg/m^3. The actual desulfurization efficiency is about 85%. The actual outlet emission can be controlled at about 120 mg/m^3 and achieving ultra-low emissions requires the desulfurization efficiency to be increased to more than 95%. The plant has carried out two efficiency improvement measures: one is to change the desulfurization agent to improve the desulfurization efficiency; the other is to expand the desulfurization system to increase the circulation amount of the desulfurization agent in the system.

Improvement and Transformation of Desulfurizer

Desulfurizer tests were carried out, using slaked lime instead of lime. The test was divided into three stages. The first stage of the test lasted for 7 days, and the main content was to replace the original desulfurizer in the system; the second stage of the test lasted for 6 days. Under the condition that the discharge standard remains unchanged, the change of the system operation data is analyzed; the third stage lasts for 6 days, and the main content is to analyze the system operation data on the basis of controlling SO_2 concentration below 50 mg/m^3. The experimental results are as follows:

In the first stage, the daily average SO_2 concentration at the inlet was about 800 mg/m^3, and SO_2 emission concentration was all above 110 mg/m^3, and the amount of water added to the humidifier was close to the upper limit, indicating that under

the condition of the SO_2 concentration at the inlet, it was difficult to decrease SO_2 concentration of outlet with quicklime. In the second stage, the amount of water added to the humidifier drops from 3.5 t/h to 2.2 t/h, which shows that the effect of using slaked lime was more obvious; In the third stage, the actual inlet SO_2 reaches about 900 mg/m_3. Under normal water addition, the outlet SO_2 concentration is controlled at about 50 mg/m^3.

Experiments have proved that the effect of using slaked lime for flue gas desulfurization is significantly better than that of quick lime, and the desulfurization efficiency is increased by 8%, reaching about 93%.

Capacity Expansion and Transformation of Dense Flow Tower Desulfurization Device

Using slaked lime as the desulfurizer, the desulfurization efficiency reaches about 93%. It is also necessary to expand and transform the desulfurization system to increase the circulation of the desulfurizer to further increase the desulfurization efficiency to over 95%. The operation process of the dense flow tower material is a scraper—bucket elevator—humidifier—desulfurization tower—transition warehouse—dust bag—scraper, among which scraper machine, bucket elevator and humidifier are the key links that affect the material circulation, and need to be expanded and modified.

(1) Renovation of scraper machine. The original scraper machine was removed, and a new scraper machine was installed on the original basis. The conveying capacity of the original scraper machine was 280 m^3/h, and the transport capacity of the new scraper machine was increased to 400 m^3/h.
(2) Bucket elevator modification. The box body of the bucket elevator was retained, and the original bucket elevator belt was removed. The conveying capacity of the original bucket elevator belt was 320 m^3/h, and the new bucket elevator belt had a conveying capacity of 470 m^3/h.
(3) Humidifier modification. The humidifier was dismantled, and a double-shaft horizontal humidifier was used on the original basis, and the processing capacity was increased from 200 t/h to 250 t/h.
(4) Other modifications. a chain-type agitator was installed (the rotation diameter: $\varphi = 1600$ mm), and the mixing effect of flue gas and desulfurization agent was improved; a waste ash bin was built near the desulfurization facilities, shortening the distance of the system to discharge waste ash. The waste ash discharge capacity by airflow is increased from 8 t/h to 15 t/h.

After completing the desulfurization expansion transformation and putting into operation, the desulfurization efficiency reached over 95%. On the premise that the inlet SO_2 concentration does not exceed 800 mg/m^3, the outlet SO_2 concentration is controlled at about 20 mg/m^3, which can meet the requirements of ultra-low emissions standard.

Transformation of SCR Denitrification Device

SCR Denitrification Process Flow and Design Parameters

The schematic diagram of the SCR denitration process of the 360 m^2 sintering machine is shown in Fig. 2. After desulfurization, the sintering flue gas exchanges heat with the denitrified hot flue gas through the air heat exchanger (GGH), then passes through the supplementary burner to increase the flue gas temperature to 280 °C, and then enters the SCR reactor. The SCR reactor contains a catalyst layer. Under the action of the catalyst, NH_3 reacts with NOx to remove NOx. The catalyst promotes the reaction of NH_3 and NOx. There is a rectification grid on the top of the SCR reactor to distribute the flowing flue gas evenly. The catalyst is housed in modular components for easy handling, installation, and replacement. An acoustic soot blower is installed between the catalyst layers of the SCR reactor to blow away dust and SCR reaction by-products deposited on the catalyst to reduce the pressure drop in the reactor. The denitrified flue gas exchanges heat with the desulfurized flue gas through an air heat exchanger and then is sent to the sintering main chimney for discharge [6, 7]. The design parameters of the SCR denitrification device of the 360 m^2 sintering machine are shown in Table 1.

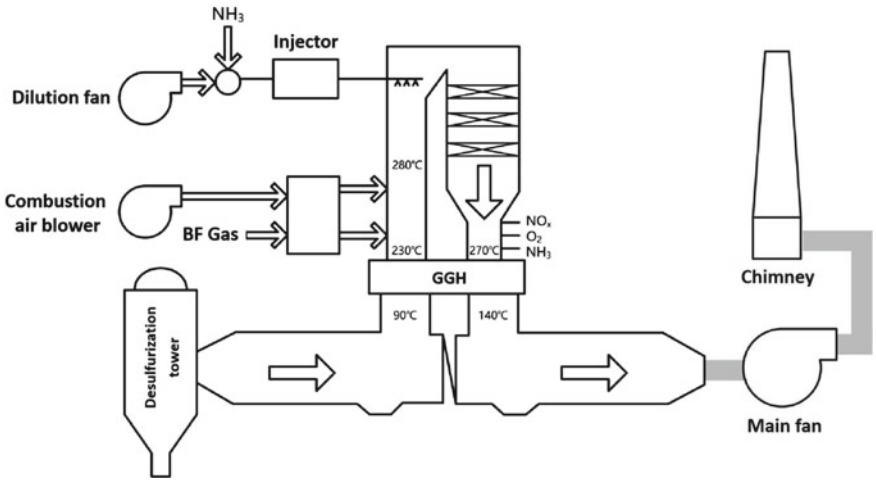

Fig. 2 Schematic diagram of SCR denitrification process

Table 1 Design parameters of SCR denitrification device for 360m2 sintering machine

No	Parameter	Unit	Value
1	Sintering machine specification	m^2	360
2	Flue gas volume in working condition	m^3/h	$2 \times 108 \times 10^4$
3	Flue gas temperature (after desulfurization)	°C	80 ~ 130
4	Dust content in flue gas (after desulfurization)	mg/Nm^3	≤40
5	SO_2 concentration (after desulfurization)	mg/Nm^3	≤160
6	NOx concentration of the inlet	mg/Nm^3	≤350
7	NOx concentration of the outlet	mg/Nm^3	≤50
8	Device sync rate	%	100

Ammonia Injection System

The ammonia storage and supply system includes ammonia storage tanks, ammonia absorption tanks, ammonia transfer pumps, wastewater pools and wastewater pumps, valves, and pipelines. Considering the safe use of ammonia, the ammonia tank is set up outside the working site, with a storage tank volume of $140m^3$. It can fully meet the needs of 7 days of production. The delivery pump is used for both purposes. The ammonia water is transported to the ammonia water evaporator. The clean flue gas from the reactor is drawn through the dilution fan to vaporize the ammonia water. With the help of compressed air, it is sprayed into the reactor.

Heating Furnace System

The double flue of the 360 m^2 sintering machine uses two heating furnaces. The coke oven gas is ignited, and the blast furnace (BF) gas is used for normal production. The hot flue gas after combustion enters the reactor under the action of system negative pressure, which increases the flue gas temperature of the reactor to above 280 °C, the actual production process controls the flue gas temperature to be 280–305 °C, and the blast furnace gas consumption is about 20,000 m^3/h.

GGH Heat Exchanger

SCR denitrification is very commonly used in the domestic power industry and is a very mature denitrification technology. The biggest difference between sintering companies using this process and the power industry is the need to use GGH heat exchangers. GGH heat exchangers make the original and clean flue gas realize heat exchange to achieve the purpose of reducing blast furnace gas consumption. Judging

from the actual parameters on site, the cold section flue gas temperature is about 90 °C. After passing through the GGH, it rises to about 230 °C. The hot section entrance flue gas is about 270 °C, and the outlet flue gas is about 140 °C. The application of GGH exchanger greatly reduces gas consumption.

Reactor System

The reactor is equipped with three layers of catalysts, with one layer left vacant for backup. The flue gas temperature reaches above 280 °C. Under the action of the catalyst, the following reactions occur between nitrogen oxides and ammonia:

$$4NO + 4NH_3 + O_2 \rightarrow 4N_2 + 6H_2O$$
$$6NO_2 + 8NH_3 \rightarrow 7N_2 + 12H_2O$$
$$NO + NO_2 + 2NH_3 \rightarrow 2N_2 + 3H_2O$$

Sintering flue gas is mainly NO. Based on the actual flue gas volume of 1,400,000 m^3/h, the nitrogen oxide concentration of 170 mg/m^3, and the discharge of nitrogen oxides reduced to less than 50 mg/m^3, the nitrogen oxides that need to be processed per hour are 204 kg, and 370 kg ammonia water with 20% ammonia is required. It is basically consistent with the actual consumption of ammonia water, and the concentration of nitrogen oxides discharged is about 30 mg/m^3.

The SCR denitrification device was put into operation quickly. After a short period of debugging, it reached ultra-low emission requirements and can stably control the nitrogen oxide concentration below 50 mg/m^3, the current actual control is about 30 mg/m^3. Furthermore, increasing the injection of ammonia water can further reduce the concentration of nitrogen oxides.

Effects of Desulfurization and Denitrification Transformation

The 360m^2 sintering machine has achieved ultra-low emission requirements through desulfurization and denitrification modifications. The statistics of flue gas emission effects are shown in Fig. 3.

It can be seen from the figure that the SO_2 emission is mainly distributed at 15–20 mg/m^3, the NOx emission is 20–30 mg/m^3, and the outlet dust is about 3 mg/m^3, achieving the goal of ultra-low emission.

From the analysis of sintering components: the original desulfurization cost is 5.7 yuan/ton of sintered ore, desulfurization uses slaked lime as a desulfurizer and capacity expansion transformation, the desulfurization cost increases by 0.68 yuan/ton; gas and ammonia consumption is 0.12 yuan/ton, and electricity consumption is

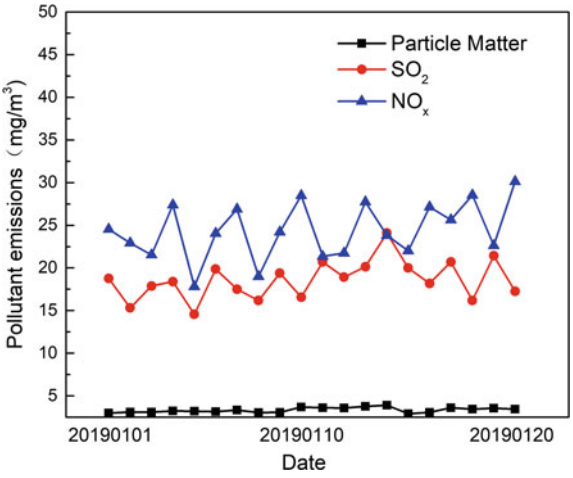

Fig. 3 Effect of desulfurization and destocking technology transformation on 360 m^2 sintering machine

increased by 3.71 yuan/ton, other consumables and labor are expected to be 0.8 yuan/ton, the overall cost of sintered ore increased by 4.62 yuan/ton, and the total cost of desulfurization and denitrification reached 10.32 yuan /ton of sintered ore.

Conclusion

Shougang Qian'an Iron and Steel Company carried out technical transformation of the 360 m^2 sintering confidential coherent tower semi-dry desulfurization equipment and added an SCR denitrification device. The total cost of desulfurization and denitrification was 10.32 yuan/ton of ore, thereby achieving ultra-low emissions of SO_2 and NOx. The outlet dust is less than 10 mg/m^3, the SO_2 outlet concentration is less than 35 mg/m^3, and the NOx outlet concentration is less than 50 mg/m^3. It has become the first sintering enterprise in Tangshan area to pass ultra-low emission standard.

Acknowledgements The authors are grateful for the financial support of the National Key R&D Program of China (2017YFB0304300 & 2017YFB0304302).

References

1. Kun Z (2016) Process design for environmental protection and energy-saving treatment of sintering flue gas. Metall Energy 35(3):16
2. Yuhua D, Yuanhong Q, Haifeng W (2010) Sintering flue gas desulfurization technology. J Iron Steel Res 22(5):1

3. Qingwei Z, Liyuan W (2015) Design and application practice of flue gas desulfurization of Tonghua No. 4 sintering machine. Metall Energy 34(2):9
4. Zhengqiu Q, Jianming L, Jianshan W et al (2014) Application status and development of Panzhihua iron and steel sintering flue gas desulfurization technology. Iron Steel 49(2):74
5. Hongliang Z, Qi S, Hongming L et al (2017) Analysis of nitrogen oxide removal process in sintering flue gas. Iron Steel 52(5):100
6. Yongqiang G (2014) Analysis of SCR denitrification technology for sintering flue gas. Environ Eng 32(S1):493
7. Lirong Z, Chunbo G, Shibo Y (2014) Discussion on the application of SCR denitrification technology for sintering flue gas in iron and steel plants. China Environ Prot Ind 06:33

New Strategy for the Optimization of Mold Flux During Continuous Casting of High-Ti Steel

Hebin Jin, Shuyao Yang, Shengping He, Qiangqiang Wang, and Xubin Zhang

Abstract Severe reactions occur at the steel-slag interface during continuous casting of high-Ti steel, leading to the interruption of smooth operation and strand defects. To settle the issue, this study proposed a new slag system with high basicity (the ratio of CaO/SiO_2: 1.5–1.9), aiming to maintain the stability of slag properties by providing sufficient O^{2-} ions from CaO. The main results indicate that as the basicity ranged from 0.8 to 1.5, the viscosity and melting temperature decreased first and then increased with the increase of TiO_2/SiO_2 ratio, and the precipitation transformed from glassy to high-melting temperature perovskite. In the range of 1.5 to 1.9, the melting and flow also deteriorated as the rise of TiO_2/SiO_2, but the extent of deterioration was greatly suppressed compared with that with low basicity, and no perovskite precipitated. This study could provide a new strategy to optimize the mold slag for high-Ti steel continuous casting.

Keywords Mold flux · High-Ti steel · Viscosity · Break temperature

Introduction

Steel-slag reaction occurs often in the continuous casting process of high-Ti steels (Ti > 0.2 wt%), causing a series of subsequent problems, such as pit, slag inclusion, crack defects, and even breakout [1, 2]. High-Ti steel contains the alloying elements [Ti] and [Al], which complicates the reaction between inclusions and steel slag [3]. SiO_2 in the traditional $CaO–SiO_2$ system slag is easily reacted with the [Ti] and [Al] elements in steel, as well as the [TiN] inclusion floating at the steel-slag interface, and the generated TiO_2 and the floating TiO_x are dissolved in the mold flux [4–9]. The content of SiO_2 in the slag decreases, the content of amphoteric oxides TiO_2 and Al_2O_3 increases, the slag basicity increases, and the mold flux is transformed from

H. Jin · S. Yang · S. He (✉) · Q. Wang · X. Zhang
College of Materials Science and Engineering, and Chongqing Key Laboratory of Vanadium–Titanium Metallurgy and Advanced Materials, Chongqing University, Chongqing 400044, China
e-mail: heshp@cqu.edu.cn

S. Wagstaff et al. (eds.), *Materials Processing Fundamentals 2024*, The Minerals, Metals & Materials Series, https://doi.org/10.1007/978-3-031-50184-5_24

the initial CaO–SiO_2–based slag to CaO–SiO_2–TiO_2(Al_2O_3)-based system slag with the continuous casting process.

Nowadays, the design strategy of high-Ti steel mold slag is based on high basicity and high glassy mold slag and non-reactive mold slag. The CaO–SiO_2–Al_2O_3 system high basicity mold flux is designed to absorb TiO_2 and Al_2O_3 inclusions in steel by the principle of 'multi-component and equal content of each component' slag formulation [10]. However, it is difficult to eliminate the floater of the high-Ti steel with those methods. In addition, some researchers have used BaO, Na_2O, and B_2O_3 to adjust the crystallization and melting properties of CaO–Al_2O_3-based and CaO–Al_2O_3–TiO_2-based mold flux, thereby inhibiting the precipitation of perovskite and cuspidine, and coordinating the lubrication and heat transfer characteristics [11, 12]. Due to the active components (Na_2O and B_2O_3) in the mold flux, the steel-slag reaction still occurs. Chen et al. [2] studied the design of CaO–SiO_2–Al_2O_3 system slag with the addition of oxidizing components such as Fe_2O_3, Cu_2O, and Mn_2O_3 to react with TiN and reducing group elements in steel to maintain the slag basic properties. However, in high titanium content steel grades, low-reaction mold flux will not fulfill the demand any further, and the problem of steel-slag reaction is the most significant issue. At the same time, high titanium content will change the solidification phase transformation of the steel and enter the peritectic steel region which is difficult to cast. Therefore, to smoothly continuous casting of high-Ti steel, it is necessary to start with the coordinated control of mold slag to control heat transfer and lubrication properties of mold flux.

To effectively utilize the steel-slag reaction and coordinate the properties of the slag before and after the reaction. In this study, CaO–SiO_2-based reactive slag system will be used. It means that the slag still has suitable properties after a certain amount of SiO_2 is consumed during the steel-slag reaction. Therefore, the effects of TiO_2/SiO_2 ratio in different basicity mold flux on the viscosity, melting properties, and phase of slag were studied, which laid a foundation for the design and selection of high-Ti steel mold flux.

Method

The steel-slag reaction was simulated by the variation of TiO_2/SiO_2 ratio to understand its effect rule on the slag properties. To obtain a mold slag suitable for continuous casting of high-Ti steel, a type of mold slag was designed with different binary basicity (R, from 0.8 to 1.9) and rate of TiO_2/SiO_2 (SiO_2 was replaced by TiO_2, TiO_2 content from 0 wt% to 20 wt% with a step of 2 wt%) under a constant content of Li_2O, Na_2O, F^-, Al_2O_3, MgO, and Fe_2O_3, as listed in Table 1. This study will focus on describing the effect of the basic properties of mold slag with basicity of 0.85 and 1.75, as listed in Table 2.

Viscosity properties were measured by a rotary viscometer, according to Chinese industrial standards (YB/T 185–2017). Viscosity, viscosity-temperature curve, and break temperature were obtained through this method. The slag temperature was

Table 1 Compositions of mold slag (wt%)

	R	TiO_2	F	Li_2O	Na_2O	Al_2O_3	$MgO + Fe_2O_3$	Sum
Range	0.8–1.9	0–20	8.1	4.5	10.8	4	2.5	100
Step	–	4	8.1	–	–	–		–

Table 2 Specifications of original Slag 1 and Slag 2

Slag	R	F	Li_2O	Na_2O	Al_2O_3	$MgO + Fe_2O_3$	Viscosity (Pa·s)	T_m (°C)
1	0.85	8.1	4.5	10.8	4	2.5	0.16	917
2	1.75	8.1	4.5	10.8	4	2.5	0.08	988

stabilized to 1300 °C and poured into the room temperature iron crucible. After cooling, the crystal ratio (%) of the slag sample fracture was observed. The melting temperature (T_m) of the mold slag was measured through the hemispherical method. The crystal phase of mold flux was determined by X-ray diffraction (XRD). The detailed experiment methods refer to previous studies in our group [13–15].

Results and Discussion

Effect of Viscosity and Melting Temperature Properties

The viscosity of mold slag fluctuates in a certain range of 0.05–0.20 Pa s. The fluctuation trend of the viscosity-temperature curve is to migrate first to the left and then to the right. And the T_{br} shows first decreasing and then increasing. However, with the steel-slag reaction, the lubrication and control heat transfer properties of the mold slag with a basicity of 0.85 are insufficient of high-Ti steel continuous casting processes with 14 wt% TiO_2 content. Compared with the mold slag with a high basicity of $R = 1.75$, which still has suitable lubrication characteristics and control of the heat transfer properties.

Figure 1 shows the variation of viscosity and melting temperature of two typical mold slags with the increase of TiO_2/SiO_2 ratio. Figure 2a shows that with increased TiO_2 content, viscosity first decreased and subsequently increased, the viscosity reached lowest point with 12 wt% TiO_2 content, and melting temperature decreased continuously. Figure 2b shows that viscosity first stabilizes and then increases sharply with TiO_2 addition; T_m increases slowly in the range of 0 ~ 16 wt% TiO_2 content and then increases sharply within the range of 16 ~ 20 wt% TiO_2 content. Compared with the basicity of 1.75 slag, when the 14 wt% TiO_2 content, T_m and viscosity of 1081 °C and 0.085 Pa s, respectively. The mold slag properties still have good lubrication ability and ensure smooth continuous casting of high-Ti steels.

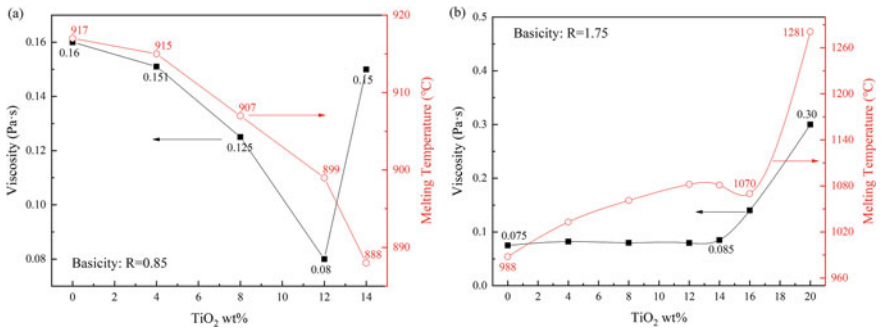

Fig. 1 Viscosity and melting temperature of mold slags with different TiO_2 content and basicity of **a** 0.85 and **b** 1.75

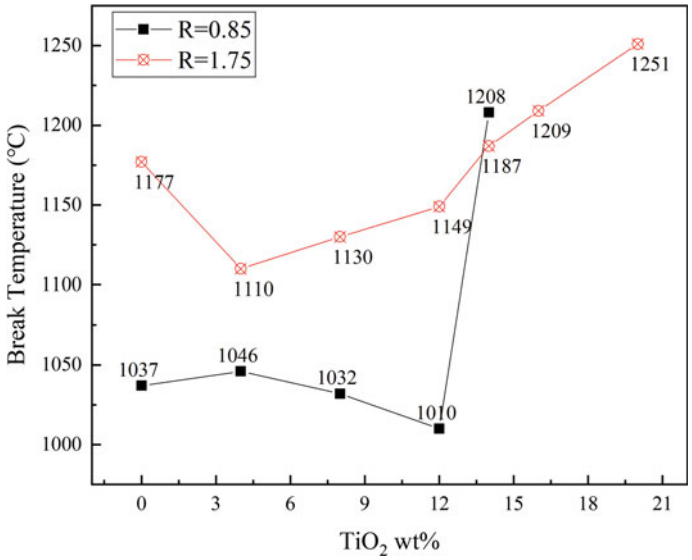

Fig. 2 Comparison of T_{br} of mold slags with different basicity

Figure 2 illustrates the break temperature (T_{br}) with different TiO_2 content and basicity. The break temperature with the different basicity slag shows various trends with the increase of TiO_2 content. When the basicity of 0.85 and 12 wt% TiO_2, the break temperature reached a minimum value of 1010 °C and then suddenly increased to 1208 °C. The variation of the break temperature of the mold slags with $R = 1.75$ was stable; T_{br} was in the range of 1110–1251 °C. The break temperature is related to the continuous crystal precipitation during the cooling process of the liquid slag. When the mold slag $R = 0.85$ and the TiO_2 content is in the range of 12–14 wt%, the T_{br} is suddenly increased, and the lubrication capacity of the slag will be deteriorated, resulting in surface quality problems of the casting such as cracks and pits.

XRD and Crystal Ratio

XRD analysis of the crystal phase of the mold slag after viscosity measurement is shown in Fig. 3. The liquid slag was poured into the iron crucible at a temperature of 1300 °C. The fracture morphology and crystal ratio (%) of the cooled mold slag are shown in Fig. 4. Mold slag with a basicity of 0.85 changes from a glassy phase to a crystalline phase with the TiO_2/SiO_2 ratio increases. And the perovskite was also gradually precipitated from the glassy phase to perovskite with the steel-slag reaction. The increase in basicity promotes slag crystallization [13]. CaO content addition provides low-melting temperature phase, and releases of significant large of O^{2-} ions to simplify the slag structure, the slag polymerization is decreased, and the conditions for crystallization kinetics are increased [16, 17]. When the basicity was 1.75, the precipitation phase shifted from $Ca_2NaF(SiO_4)$ phase to high-melting temperature perovskite ($CaTiO_3$) phase with the TiO_2/SiO_2 ratio increasing. Meanwhile, the increasing basicity releases sufficient O^{2-} ions, which makes the slag lubrication and control of heat transfer properties more effective.

With the amphoteric oxide TiO_2 addition [18] of the slag at a basicity of 0.85, the formation of basic oxides in the acidic slag reduces the viscosity and melting temperature with the TiO_2 content range from 0 to 12 wt%. As the TiO_2 content increases in the range from 0 to 14 wt% in the high basicity $R = 1.75$ mold slag, the slag becomes a basicity slag, and TiO_2 acts as an acidic slag, but the polymerization capacity of TiO_2 is lower than the depolymerization capacity of O^{2-} ions due to sufficient O^{2-} ions in the mold flux.

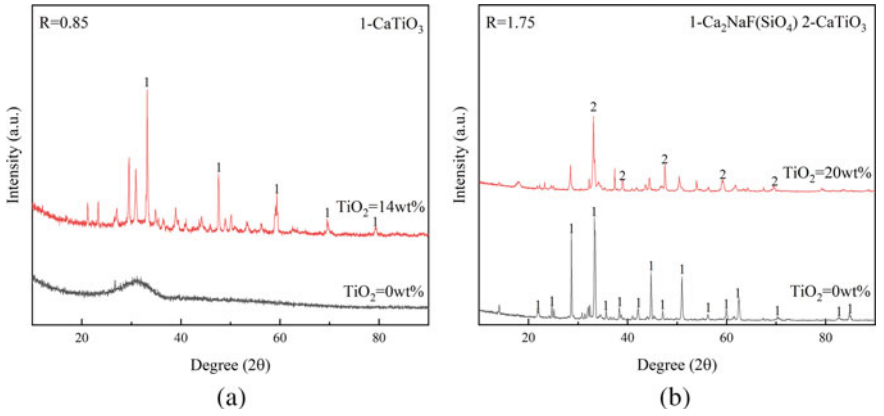

Fig. 3 XRD patterns of mold slags at different TiO_2 content of **a** $R = 0.85$ and **b** $R = 1.75$

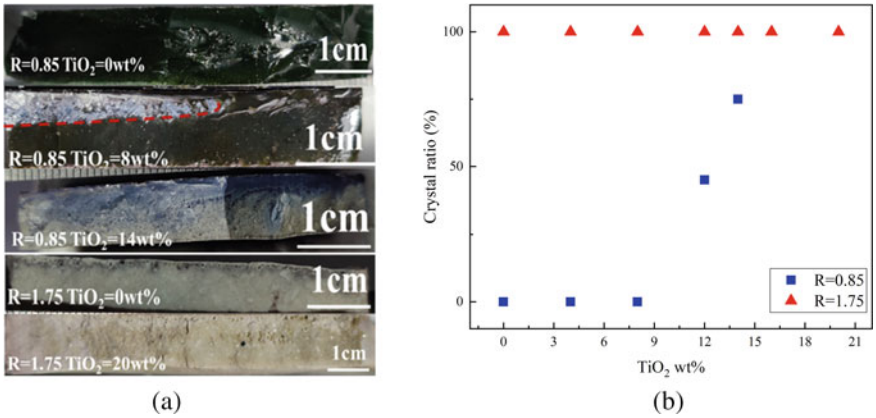

Fig. 4 Partially mold slag fracture morphology and fracture crystal ratio (%) of **a** fracture morphology and **b** crystal ratio

Conclusions

The influence of different TiO_2/SiO_2 ratios on the viscosity, melting temperature, and break temperature of CaO–SiO_2-based mold flux is investigated. A slag with high basicity and sufficient lubrication is proposed, and the following conclusions can be drawn:

(1) For the mold flux with a basicity of 0.85, the viscosity and break temperature of mold flux decreased and then subsequently increased with the increase of TiO_2 content. The turning point was at 12 wt% TiO_2, where the melting temperature decreased. Compared with 0.85 basicity slag, when the basicity of 1.75 slag ranged from 12 wt% to 14 wt%, the viscosity and melting temperature of slag are still stable. Break temperature was exceeded at 1200 °C for the 16 wt% TiO_2 content. With the addition of the amphoteric oxide TiO_2, the basicity oxide was formed in the acidic slag to reduce the viscosity and melting temperature, and the acidic oxide was formed in the basicity slag owing to the sufficient supply of O^{2-} ions, the slag polymerization degree was low, and the viscosity fluctuation was slight.

(2) The precipitation transformed from glassy to high-melting temperature perovskite when the basicity ranged from 0.8 to 1.5 with the increase of TiO_2/SiO_2 ratio. In the range of slag basicity from 1.5 to 1.9, the deterioration of slag properties was greatly inhibited with the increase of TiO_2/SiO_2 ratio. The precipitation of low-melting point $Ca_2NaF(SiO_4)$ in the slag with $R = 1.75$ makes the slag properties still stable at high TiO_2 content (excess of 14 wt%). The designed mold flux effectively promotes the lubrication and heat transfer properties, which lays a foundation for the selection of mold flux for high-Ti steel continuous casting process.

Acknowledgements The authors are grateful for support from the National Science Foundation China (Grant No. 52074054, 52374325).

References

1. Mizui N, Takayama T, Sekine K (2008) Effect of Mn on solubility of Ti-sulfide and Ti-carbosulfide in ultra-low C steels. ISIJ Int 48(6):845–850
2. Chen Z (2019) Theoretical research and application of continuous casting mold fluxes for high Ti-bearing alloy steel[D]. Chongqing University. https://doi.org/10.27670/d.cnki.gcqdu.2019.003261
3. Mukongo T, Pistorius PC, Garbers-Craig AM (2004) Viscosity effect of titanium pickup by mould fluxes for stainless steel. Ironmaking Steelmaking 31(2):135–143
4. Chen Z, Li M, Wang X et al (2019) Mechanism of floater formation in the mold during continuous casting of Ti-stabilized austenitic stainless steels. Metals 9(6)
5. Michelic SK, Loder D, Reip T et al (2015) Characterization of TiN, TiC and Ti(C, N) in titanium-alloyed ferritic chromium steels focusing on the significance of different particle morphologies. Mater Charact 100:61–67
6. Zhao K, Cai K, Liu X (1989) Titanium nitride behavior of mold fluxes for casting Ti-bearing stainless steel. J Iron Steel Res 1(3):21–28
7. Wang W, Cai D, Zhang L, Sohn I (2020) Effect of TiO_2 and TiN on the viscosity, fluidity, and crystallization of fluorine-free mold fluxes for casting Ti-bearing steels. Steel Res Int 92(2):2000314
8. He S, Wang Q, Zeng J et al (2009) Properties control of mold fluxes for high aluminum steel. J Iron Steel Res 21(12):59–62
9. Roy D, Pistorius PC, Fruehan RJ (2013) Effect of silicon on the desulfurization of Al-killed steels: part I. Mathematical model. Metall Mater Trans B 44:1086–1094
10. Ji J, Cui Y, Wang S et al (2022) Effect of TiO_2 substituting SiO_2 on the rheological and crystallization behavior of mold slags for casting Ti-containing steel. Ceram Int 48(1):256–265
11. Xiao D, Wang W, Lu B (2015) Effects of B_2O_3 and BaO on the crystallization behavior of CaO–Al_2O_3-based mold flux for casting high-Al steels. Metall Mater Trans B 46(2):873–881
12. Piao Z, Zhu L, Wang X, Liu Z, Wang B, Xiao P, Yuan Z (2020) Effects of BaO on the viscosity and structure of a new fluorine-free CaO–Al_2O_3–TiO_2-based mold flux for high titanium steel. Metall Mater Trans B
13. Long X, He S, Xu J et al (2012) Properties of high basicity mold fluxes for peritectic steel slab casting. J Iron Steel Res Int 19(7):39–45
14. Yan X, Yuan H, Zhang S et al (2020) Effect of interfacial reaction between CaO–BaO–Al_2O_3-based mold fluxes and high-Mn–high-Al steels on fundamental properties and lubrication of mold flux. Steel Res Int 91(6):1900581
15. Zhang S, Li M, Zhu L et al (2019) Effect of substituting Na_2O for SiO_2 on the non-isothermal crystallization behavior of CaO–BaO–Al_2O_3 based mold fluxes for casting high Al steels. Ceram Int 45(9):11296–11303
16. Gu K, Wang W, Zhou L et al (2012) The effect of basicity on the radiative heat transfer and interfacial thermal resistance in continuous casting. Metall and Mater Trans B 43(4):937–945
17. Jin H, Tu L, Zhang X et al (2023) Optimization of mold slag for continuous casting of peritectic steel. Steel Res 94:2200868
18. Bi Z, Li K, Jiang C et al (2022) New insights into the traditional charge compensation theory: amphoteric behavior of TiO_2 under the guidance of supply−demand relationship. ACS Omega 7:21225–21232

Optimization of Deflector Hole on Porous Baffle Wall in Six-Strand Tundish for Bloom Continuous Casting

Xianyang Wang, Hao Hu, Peng Shi, Xin Xie, Chenhui Wu, Dengfu Chen, and Mujun Long

Abstract Porous baffle wall is a common flow control device in tundish. The flow field in the tundish can be improved by adjusting the elevation angle and position of the deflector hole on porous baffle wall, so the residence time of liquid steel is prolonged, inclusions easily to be removed. In this paper, the method of orthogonal experimental design is used to simulate and optimize the deflector hole on the porous baffle wall. The results showed that the flow field of the casting region in tundish can be improved significantly with proper elevation angle and location of the deflector hole. The volume of dead zone decreased from 23.1% to 18.4%, the average residence time of each outlet changed from 572.6 s, 594.6 s, and 794.4 s to 663.5 s, 633.6 s, and 663.2, the standard deviation decreased from 99.8 to 14.0, and consistency of outlet was greatly improved.

Keywords Tundish · Porous baffle wall · Deflector hole · Numerical simulation · Orthogonal experiment

Introduction

High-speed rail and heavy rail have been widely used in many countries. The fatigue of rail steel is caused by the alternating frictional contact between the wheel and the rail, which will lead to the cracks in the holes of the rail and the shedding of the blocks, thus seriously affecting road safety [1, 2]. Tundish plays an important role in improving the quality of billet. During continuous steel casting, in addition

X. Wang · H. Hu · D. Chen (✉) · M. Long (✉)
College of Materials Science and Engineering, Chongqing University, Chongqing 400044, China
e-mail: chendfu@cqu.edu.cn

M. Long
e-mail: longmujun@cqu.edu.cn

P. Shi · X. Xie · C. Wu
State Key Laboratory of Vanadium and Titanium Resources Comprehensive Utilization, Sichuan, Panzhihua 617000, China

S. Wagstaff et al. (eds.), *Materials Processing Fundamentals 2024*, The Minerals, Metals & Materials Series, https://doi.org/10.1007/978-3-031-50184-5_25

to the basic functions of storage, pressure stabilization, and diversion to ensure the continuous pouring of molten steel, the tundish can also effectively prevent the steel slag from entering the mold, remove the non-metallic inclusions in the molten steel, homogenize the temperature and composition of molten steel, and ensure that the molten steel entering the mold meets the requirements. The effect of tundish is closely related to the flow characteristics of molten steel in tundish. An appropriate tundish flow field is very important to the uniformity of temperature and composition of molten steel in tundish, floating of inclusions, prevention of secondary oxidation, quality of molten steel, and the consistency of each flow [3–5].

At present, flow control devices such as weir, dam, turbulence inhibitor, filter, and gas curtain are mainly added in the tundish to improve the quality of molten steel by improving the flow of molten steel in the tundish, homogenizing the temperature of molten steel in the tundish and promoting the floating of inclusions [6–9]. The weir and dam can change the flow characteristic of the liquid steel, eliminate the short flow, promote the flow of the liquid steel towards the surface, extend the flow path in the tundish, increase the residence time of the liquid steel, so that the inclusions can float more time [10, 11]. The turbulence inhibitor has a good buffer on the liquid steel flow, so it can reduce the maximum speed and weaken the impact of the injection flow from ladle, thus reducing the erosion of refractory materials, reducing the emulsification of slag, extending the minimum residence time and average residence time, which is conducive to the floating of inclusions [12, 13]. The gas curtain is composed of tiny bubble clouds. By changing the flow direction of the liquid steel passing through the gas curtain, the residence time of the liquid steel can be prolonged. At the same time, the argon bubble can capture small particles of inclusions during the rising process, which is conducive to make the inclusions removed [14–17].

In the 1980s, a perforated baffle was introduced, called porous baffle wall, which is generally used for heavy rail tundish. The porous baffle wall refers to the establishment of a number of diversion holes on the adiabatic plate, which can be installed in the tundish to separate the upstream and downstream regions. The porous baffle wall has better metallurgical effect than the weir and dam, so it can be used to replace them. Dipak Mazumsar et al. [18] studied different flow control devices from the perspective of the influence of flow control devices on the flow condition of liquid steel in tundish and concluded that porous baffle wall has advantages in improving the metallurgical performance of tundish. Chen et al. [19] suggested the use of baffles with asymmetric pore distribution in multi-strand tundish to improve the flow of liquid steel. They found that the baffles with asymmetric pore distribution produced cross-flow, which was the most effective for removing inclusions from liquid steel. There were several studies [20–22] on the effect of the size, position, angle, and arrangement of the holes of the porous baffle wall on the flow of liquid steel in the multi-flow tundish. In these studies, it was found that reasonable arrangement of deflector hole arrangement can effectively enhance the metallurgical properties of the tundish.

In order to determine the best porous baffle wall parameter of a tundish, it is necessary to do a lot of complicated numerical simulations. In this paper, the porous baffle wall of a heavy rail tundish is optimized through orthogonal analysis, and the

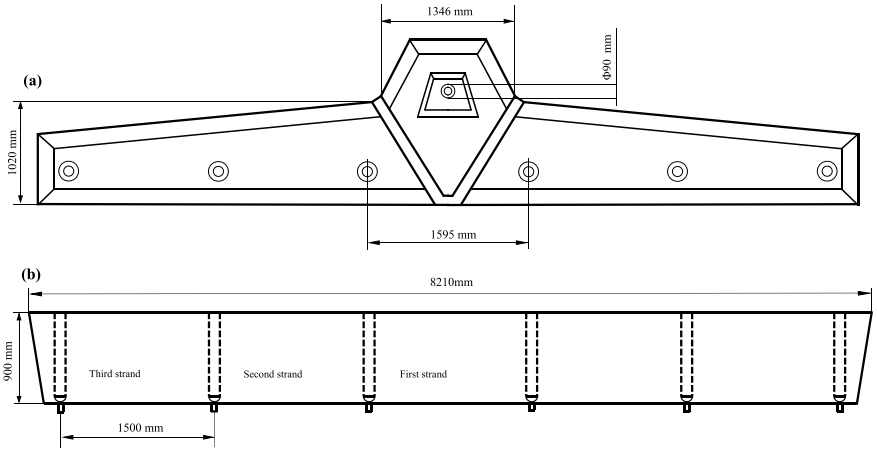

Fig. 1 Diagram of tundish structure: vertical view **a**; front view **b**

best porous baffle wall is obtained. It provides the basis for selecting the parameters of the porous baffle wall of heavy rail steel tundish.

Model Description

Geometric Models and Meshing

In this paper, 40 t bloom six-strand tundish is taken as the research object. The inner diameter of its ladle shroud is 90 mm, the insertion depth is 200 mm, and the inner diameter of the submerged nozzle is 40 mm. The specific size is shown in Fig. 1. In the software ANYSY-Meshing, tetrahedral structure is used to divide the mesh. After the local mesh is encrypted, the generated tetrahedral mesh is 2 488,823, as shown in Fig. 2.

Assumptions

In general, in order to enable the tundish to maximize the removal of inclusions in the liquid steel and achieve a certain optimization effect, attention should be paid to the following optimization principles:

(1) Extend the stagnation time $t_{\min}$ of the outlet;
(2) Extend the peak time t_{peak} of the outlet;
(3) Extend the average residence time of $\bar{t}$ the outlet;

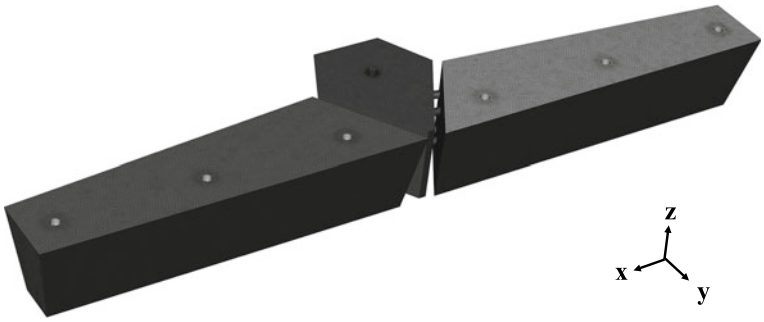

Fig. 2 Mesh of numerical model of tundish

(4) Increase the volume fraction of piston flow and total mixed flow zone as much as possible, reduce the proportion of dead zone, and improve the volume fraction ratio of plug zone to dead zone V_p/V_d;
(5) Reduce the peak concentration of the outlet;
(6) RTD curve is smooth.

Orthogonal Experimental of Deflector Hole

Orthogonal Experimental Design

Orthogonal experimental design is a method that uses orthogonal tables to arrange and analyze multi-factor experiments. In all the horizontal combinations of test factors, the method selects some representative horizontal combinations to carry out the test. Through the analysis of the test results, the situation of the comprehensive test will be understood and the optimal combination will be found.

Orthogonal analysis can shorten the test and reduce the workload greatly. It is an efficient, fast, and economical method for experimental analysis. Orthogonal analysis uses the corresponding orthogonal table to arrange the experiments and perform the analysis. In this simulation experiment, there are three factors affecting the flow control effect of the weir. According to the corresponding value range, three different levels are taken for each factor, thus forming an orthonormal table, as shown in Table 1.

The above table shows all the cases of this numerical simulation. If the test is required in accordance with the ordinary comprehensive test protocol, this will obviously greatly increase the workload of the simulation. According to the idea of orthogonal design, the orthogonal data set composed of representative test points among all test points only needs nine simulation tests, and the calculation and analysis process of orthogonal table is more simplified. Generally, the significance of the influence of various factors on the test results can be directly analyzed by calculating

Table 1 Porous baffle wall deflector hole structure orthogonal design table

Scheme	Bottom deflector elevation angle/°	Middle deflector elevation angle/°	Upward movement distance of the deflector hole/mm
1#	5	0	0
2#	5	5	50
3#	5	10	100
4#	10	0	50
5#	10	5	100
6#	10	10	0
7#	15	0	100
8#	15	5	0
9#	15	10	50

the range and variance of the corresponding test results. It can be seen that the fast and high efficiency brought by orthogonal test is no doubt.

Orthogonal Experiment Results and Analysis

The nine schemes listed in the orthogonal table are simulated, and the optimal scheme is determined by orthogonal analysis of the simulation results. It is necessary to select some representative indexes for orthogonal analysis in evaluating the flow control effect of the deflector hole structure. In this study, the average residence time, initial response time, the overall average residence time of the liquid steel in the tundish, and the consistency of outlet each flow were taken as the orthogonal analysis indexes. The simulation results are shown in Table 2.

Table 2 Simulation results of deflector hole orthogonal scheme of porous baffle wall

Scheme	t_1/s	t_2/s	t_3/s	$\bar{t}/s$	$t_{\min}/s$	S
1#	589.5	553.7	721.7	621.6	21.0	72.3
2#	626.1	600.2	712.7	646.3	27.0	48.1
3#	663.2	633.6	663.5	653.4	40.1	14.0
4#	610.1	607.5	675.4	631.0	16.2	31.4
5#	580.4	599.6	795.3	658.4	32.7	97.1
6#	610.5	599.1	740.4	650.0	60.0	64.1
7#	672.0	653.6	586.6	637.4	46.3	36.7
8#	606.9	622.1	716.3	648.4	55.4	48.4
9#	670.7	675.6	607.7	651.3	75.4	30.9

In Table 2, t_1 is average residence time of outlet 1, t_2 is average residence time of outlet 2, t_3 is average residence time of outlet 3, $\bar{t}$ is total average residence time of liquid steel, t_{min} is stagnation time of liquid steel, S is standard deviation of the residence time of liquid steel.

It can be seen from Table 3 that the elevation angle of deflector hole located in the middle has a significant effect on the total average residence time of the liquid steel in the tundish. The jet angle of the middle deflector hole plays a major role in the overall process of liquid steel flow in the tundish. Because it is in the middle of the porous baffle wall, the jet angle mainly determines the characteristics of liquid steel floating up to remove inclusions and the flow of liquid steel to the outlet 3 at the far end. When the velocity of liquid steel is constant, the average residence time of liquid steel basically extends with the increase of the middle elevation angle, and the flow of liquid steel in tundish is optimized.

It can be seen from Table 4 that the middle elevation angle has a significant influence on the stagnation time of the liquid steel in the tundish, and the bottom elevation angle takes second place. The position of the deflector hole determines the movement of the liquid steel through the surface of the steel to make inclusions removed and then outflow to the outlet. According to the parabolic trajectory of the jet from the deflector hole, the bottom elevation angle controls the time when the liquid steel first arrives at the outlets 1 and 2. The liquid steel flowing out of the deflector hole flows directly from the liquid steel to the outlets 1 and 2, and it can be considered that the stagnation time of outlets 1 and 2 represents the stagnation time of the whole tundish. When the velocity of liquid steel is constant, the total distance of fluid steel motion is extended with the increase of the middle elevation angle, and the stagnation time is prolonged; The increase of the bottom elevation angle delays the time for the liquid steel to reach the water outlets 1 and 2, the stagnation time is prolonged and the flow of liquid steel is improved.

It can be seen from Table 5 that the bottom elevation angle, the middle elevation angle, and the upward movement distance of the deflector hole have similar effects on the consistency of each flow in the multi-strand tundish. Under the condition of constant liquid steel injection velocity, the bottom elevation angle increases, the standard deviation of average residence time first increases and then decreases, and the intermediate level is poor in the given range. With the increase of the middle elevation angle, the comprehensive standard deviation of mean residence time decreases, and the larger the middle elevation angle is, the better it is. As the position of deflector hole

Table 3 Orthogonal analysis of total average residence time

Factor	Bottom deflector elevation angle	Middle deflector elevation angle	Position of deflector hole
Level 1	640.5	630.0	640.0
Level 2	646.5	651.1	642.9
Level 3	645.7	651.6	649.8
Range (R)	6.0	21.6	9.7

Table 4 Orthogonal analysis of stagnation time

Factor	Bottom deflector elevation angle	Middle deflector elevation angle	Position of deflector hole
Level 1	29.4	27.8	45.5
Level 2	36.3	38.4	39.5
Level 3	59.0	58.5	39.7
Range (R)	29.7	30.7	5.9

Table 5 Mean residence time synthetic standard deviation orthogonal analysis

Factor	Bottom deflector elevation angle	Middle deflector elevation angle	Position of deflector hole
Level 1	44.8	46.8	61.6
Level 2	64.2	64.5	36.8
Level 3	38.7	36.3	49.3
Range (R)	25.5	28.2	24.8

lifts, the comprehensive standard deviation of mean residence time first increases and then decreases, which indicates that the intermediate level of the position of deflector hole is poor in the given range.

Based on the above data, it can be concluded that in the indicators evaluating the flow control effect of the deflector hole, under the influence of various factors and levels, the average residence time and the comprehensive standard deviation of the average residence time of each flow vary greatly, while the total average residence time and stagnation time fluctuate, but the amplitude is relatively gentle. Therefore, when considering the optimal level of each factor, the consistency of each outlet is taken as the main reference, combined with the changes of stagnation time and total average residence time, it is finally decided to adopt the structural combination of the bottom deflector hole elevation angle of 5°, the middle elevation angle of 10°, and the deflector hole upward distance of 100 mm for optimization.

Flow Field Analysis of Optimal Porous Baffle Wall

Figures 3 and 4 show the simulation results of liquid steel flow in the optimal scheme.

It can be concluded from the above-related tundish optimization flow field results that the distribution of the overall velocity has no significant change. It can be seen from the distribution of liquid steel velocity flow lines that the flow streams are no longer concentrated in outlets 1 and 2, but are more uniform in the three outlets. After optimization, most of the flow streams closed to the liquid surface of the steel and the surface velocity did not rise sharply, which is conducive to the floating removal

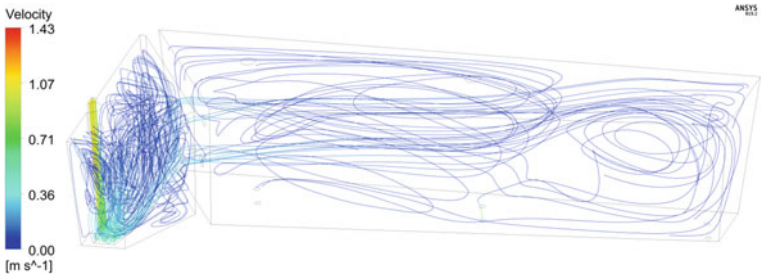

Fig. 3 Liquid steel streams in the tundish

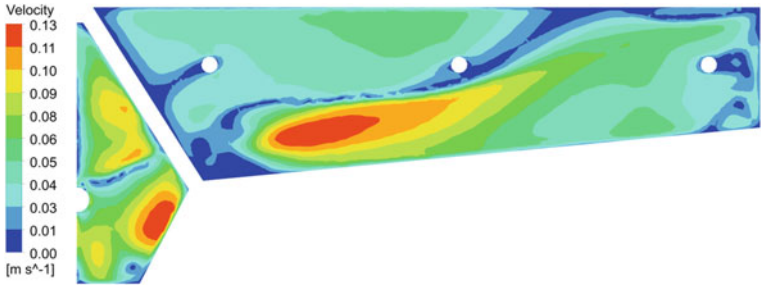

Fig. 4 Image of surface velocity in the tundish

of inclusions and did not increase the risk of slag entrapment on the surface of the tundish.

RTD Curve Analysis of Optimal Porous Baffle Wall

Figure 5 shows the RTD curves of each strand in tundish with the optimal porous baffle wall.

According to the RTD curve, the average residence time of liquid steel at outlets 1, 2, and 3 is 663.5 s, 633.6 s, and 663.2 s, respectively, and the comprehensive standard deviation of the average residence time of liquid steel is 14.0. The flow consistency of each outlet is good. This is consistent with the velocity distribution obtained from the velocity cloud map, and the liquid steel flow at the farthest end of the outlet 3 has been significantly improved, and the theoretical average residence time has not exceeded 801.2 s. According to the RTD curve, the average residence time is 653.4 s, and the volume fractions of dead zone, plug zone, and well-mixed zone are 18.4%, 17.0%, and 64.6%, respectively. Compared with the original tundish, the stagnation time of outlet 1 is extended, the total average residence time is almost unchanged, and the proportion of dead zone is slightly increased. The residence time of liquid steel at outlets 2 and 3 is also greatly improved, especially for outlet 3. The outlet 1

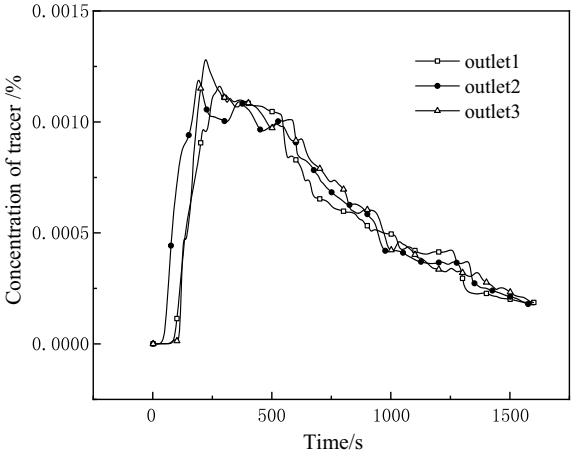

Fig. 5 RTD curve of tundish per strands

in the original tundish is the closest to the pound region, and most of the liquid steel flows directly to outlet 1 after flowing into it from the ladle shroud, resulting in a short average residence time, which is not conducive to the consistency of inclusion removal and flow. After adjusting the structure of the deflector hole of the porous baffle wall, the liquid steel in the casting region is redistributed and directed, which greatly prolongs the average residence time of liquid steel at outlet 3 and reduces the generation of short flow.

Conclusion

In this paper, the porous baffle wall of a heavy rail tundish is optimized through orthogonal analysis, and the best porous baffle wall is obtained. The conclusion is as follows:

1. In the indicators evaluating the flow control effect of the deflector hole, the average residence time and the comprehensive standard deviation of the average residence time of each flow vary greatly, while the total average residence time and stagnation time fluctuate, but the amplitude is relatively gentle. Therefore, when considering the optimal level of each factor, the consistency of each outlet is taken as the main reference.
2. Combined with the changes of stagnation time and total average residence time, it is finally decided to adopt the structural combination of the bottom deflector hole elevation angle of 5°, the middle elevation angle of 10°, and the deflector hole upward distance of 100 mm for optimization.
3. When the best solution is compared to the original solution, the volume of dead zone decreased from 23.1% to 18.4%, the average residence time of each outlet changed from 572.6 s, 594.6 s, and 794.4 s to 663.5 s, 633.6 s, and 663.2, the

standard deviation decreased from 99.8 to 14.0, and consistency of outlet was greatly improved.

Acknowledgements This work is financially supported by the National Natural Science Foundation of China (NSFC), Project Nos. 52074053 and 52274320.

References

1. Ren Q, Zhang Y, Zhang L et al (2020) Prediction on the spatial distribution of the composition of inclusions in a heavy rail steel continuous casting bloom. J Mater Res Technol 9(3). https://doi.org/10.1016/j.jmrt.2020.03.090
2. Zhang L (2016) Several important scientific research points of non-metallic inclusions in steel (in Chinese). Steelmaking 32(4):1–16
3. Chang S, Zou Z, Li B et al (2022) Modeling inclusion removal when using micro-bubble swarm in a full-scale tundish with an impact pad. Metall Mater Trans B 53. https://doi.org/10.1007/s11663-021-02388-z
4. Raghavendra K, Sarkar S, Ajmani SK et al (2013) Mathematical modelling of single and multi-strand tundish for inclusion analysis. Appl Math Model 37(9):6284–6300. https://doi.org/10.1016/j.apm.2013.01.013
5. CFD investigation of effect of multi-hole ceramic filter on inclusion removal in a two-strand tundish. Metall Mater Trans B 51(1):276–292 (2020). https://doi.org/10.1007/s11663-019-01736-4
6. KoriaS C, Singh S (1994) Physical modeling of the effects of the flow modifier on the dynamics of molten steel flowing in a tundish. ISIJ Int 34(10):784
7. Singh S, Koda SC (1993) Physical modeling of steel flow in continuous casting tundish. Ironmaking Steelmaking 20(3):221
8. Li DH, Li BK, He JC (2000) The removal of inclusion in tundish by gas blowing. Acta Metall Sin 36(4):411
9. Fan JL, Guo D, Ma HH et al (2013) Gas curtain dam technology in continuous casting tundish. Res Iron Steel 41(5):60
10. Sheng DY, Chen D (2021) Comparison of fluid flow and temperature distribution in a single-strand tundish with different flow control devices. Metals https://doi.org/10.3390/met11050796
11. de Sousa Rocha JR, d Souza EEB, Marcondes F et al (2019) Modeling and computational simulation of fluid flow, heat transfer and inclusions trajectories in a tundish of a steel continuous casting machine. J Mater Res Technol 8(5):4209–4220. https://doi.org/10.1016/j.jmrt.2019.07.029
12. Yang B, Lei H, Zhao Y et al (2019) Quasi-symmetric transfer behavior in an asymmetric two-strand tundish with different turbulence inhibitor. Metals—Open Access Metall J 9(8):855. https://doi.org/10.3390/met9080855
13. Chen YE, Yan J, Zhengsheng C et al (2017) Effect of turbulence inhibitor blades in tundish on removal rate of inclusion. Foundry Technol
14. Zhou L, Yu, Y (2015) Experimental study on gas-curtain generation characteristics by multicombustion-gas jets in the cylindrical liquid chamber. Ocean Eng Pergamon-Elsevier Sci Ltd 109(Nov.15):410–417
15. Hu Y, Yu Y, Zhang X (2022) Groove structure on the drainage characteristics of the gas curtain. Ocean Eng Pergamon-Elsevier Sci Ltd 243
16. Zhou L, Yu Y (2017) Study on the gas-curtain generation characteristics by the multiple gas jets in a liquid-filled tube. Appl Ocean Res Elsevier Sci Ltd 64:249–257

17. Chen D, Xie X, Long M (2014) Hydraulics and mathematics simulation on the weir and gas curtain in tundish of ultrathick slab continuous casting. Metall Mater Trans A 45(2):392–398
18. Sahay SK, De TK, Basu DS, Mazundar S (2001) Strand performance improvement through use of asymmetric baffles in tundish of six strand billet caster at DSP. Iron Steelmaker 28(7):71–74
19. Chen D, Hu R, Wang Q, Jin X, Yan X, Li J, Zhou K (2008) Physical and mathematical study on weir setting in continuous casting tundish. Chin J Process Eng 8(S1):49–53
20. Chen W, Ren Y, Wei X, Ji Y, Wu W (2007) Water model experiments on tundish of 5 strand asymmetrical round billet continuous caster. Steelmaking 23(3):41–44
21. Shi Z, Zhou L (2009) Water model experiment on the dam design of 6-strand tundish. Anhui Metall 2:13–15
22. Shuai Y, Cheng Z, Zhou L, Yu T (2009) Water model experiment on optimization of internal shape of 8-strand billet tundish. J Anhui Univ Technol 26(3):212–216

Optimization of Submerged Nozzle and Chamfer Design in the Mold of Bloom Continuous Casting Process Using Numerical Simulation

Jingzhou Lu, Weiming Pan, Kun Dou, Wanlin Wang, and Lejun Zhou

Abstract Bloom continuous casting is widely used in steel production. The flow state and liquid level fluctuation of molten steel inside the bloom continuous casting mold directly affect the quality of the bloom. In this study, numerical simulations are conducted with different immersion depths and side hole inclination angles of the submerged nozzle during the bloom continuous casting process, and the F index is used to judge the liquid level fluctuation during the casting process. The results show that the optimal nozzle combinations are 100 mm submerged depth with 15° port angle and 110 mm submerged depth with 15° port angle, when the continuous casting speed is 0.55 m/min. The flow field of the molten steel in the mold is appropriate, and the narrow surfaces are less impacted. Also, the fluctuation of the liquid level is appropriate. This method can be emulated to optimize the mold parameters in most steel production processes. In addition, as the chamfer decreases, the heat flux density at the corners continues to increase.

Keywords Numerical simulation · Bloom continuous casting · Submerged nozzle · Liquid level fluctuation · Mold

Introduction

Bloom continuous casting is mainly used for casting medium carbon steel, high carbon steel, and alloy steel. It is also widely used in steel production. The flow state and liquid level fluctuation of the molten steel inside the bloom continuous casting mold directly affect the quality of the bloom. Specifically, the flow behavior of molten steel in the mold is related to the growth of the billet shell, melting of slag, removal

J. Lu · W. Pan · K. Dou (✉) · W. Wang · L. Zhou
School of Metallurgy and Environment, Central South University, Changsha, Hunan 410083, China
e-mail: kun.dou@csu.edu.cn

J. Lu · K. Dou
Xiangjiang Laboratory, Changsha, Hunan 410083, China

S. Wagstaff et al. (eds.), *Materials Processing Fundamentals 2024*, The Minerals, Metals & Materials Series, https://doi.org/10.1007/978-3-031-50184-5_26

of inclusions, slag entrapment, and billet quality. At the same time, the flow and temperature fields of the mold are closely related to the structure, process parameters, and usage technology of the submerged nozzle [1, 2]. Therefore, reasonable nozzle parameters are of great significance for controlling the mold flow field, removing inclusions, and improving the quality of the final casting billet. In addition, the heat transfer of the bloom also has a significant impact on the quality of the billet. So, selecting different mold chamfers has some impact on interface heat transfer.

The chemical reaction rate, fluid flow and mass transfer in reactors, and other phenomena studied in the dynamics of steel metallurgical processes can all be accurately described using mathematical models, which makes it possible to simulate steel metallurgical processes using computational methods. In addition, the rapid development of computer technology provides powerful means for solving mathematical equations. Therefore, numerical simulation has been widely applied in the field of steel metallurgical engineering. Because the flow and heat transfer of molten steel in the mold are difficult to observe and measure, numerical simulation methods can be used to calculate the distribution of molten steel flow and temperature field [3, 4].

This article evaluates liquid level configurations through numerical simulations by also considering the fluctuation index F index for different parameter combinations of different immersion depths and side hole inclination angles of the submerged nozzle in the bloom continuous casting process and selects the optimal mold nozzle parameters. At the same time, by calculating the heat flux values of different mold chamfers, the heat transfer situation was compared, and the most suitable chamfer size was determined to provide research support to industry through computer simulation to ensure a smooth production and quality of bloom [5].

Model Description and Parameter Selection

Two models have been established: one is a 1/4 three-dimensional model of the mold, and the other is a 1/4 two-dimensional thin plate model of the mold, which are used for calculating the flow field and two-dimensional heat transfer inside the mold, respectively. To explore the influence of different chamfers on heat transfer, a total of four thin plate models with different chamfers were established. Figure 1 is 3D model of mold and local schematic diagram after grid division, and Fig. 2 is 2D slice model of casting billet pulling direction.

The parameters used in model 1 mainly include: The size of the casting billet is 400 × 325 mm; there is one water outlet on both sides, with a size of 30 × 40 mm; the inner diameter of the hole in the submerged nozzle is 50 mm; and casting speed is 0.55 m/min. The parameters used in Model 2 mainly include a copper mold thickness of 30 mm and a mold water flow rate of 3200L/min. The heat transfer q of cooling water is calculated by the formula in Fig. 2, where C is the specific heat capacity of water, L is the cooling water flow rate of the mold, ρ is the water density, Δt is the difference in inlet and outlet water temperature, and S is the contact area between the

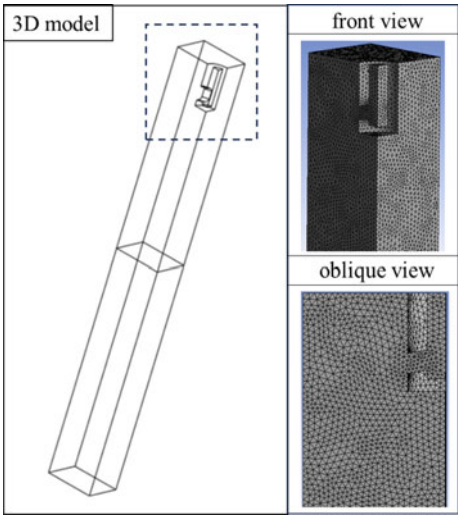

Fig. 1 3D model of mold and local schematic diagram after grid division

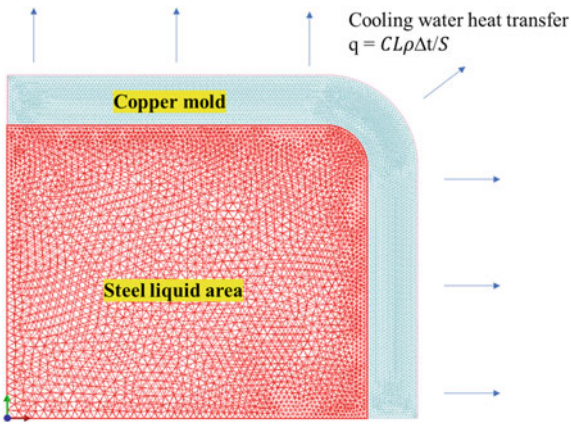

Fig. 2 2D slice model of casting billet pulling direction

steel liquid/billet shell and the copper mold. The interfacial heat transfer coefficient between the copper mold and the molten steel in Model 2 has increased from 2250 W/(m^2 K) to 3000 W/(m^2 K) from the center of the shell to the corner [6, 7].

Results and Discussion

Figures 3 and 4 show the velocity color maps of the flow field inside the mold under different conditions. The numerical simulation results indicate that under the same conditions, as the immersion depth of the nozzle increases, the impact depth of the molten steel increases, and the position of the impact on the narrow surface moves

downwards. However, the speed difference when it reaches the narrow surface is not significant. When the downward inclination angle of the nozzle increases, the speed at which the steel liquid reaches the narrow surface decreases, resulting in a smaller impact force on the narrow surface.

Let us consider two data lines from the top view/cross-section, one near the narrow surface (its direction is from top to bottom), and one line in the core area of the submerged nozzle (its direction is from the submerged nozzle to the narrow surface). We consider 20 points on each line to calculate the corresponding flow velocity and obtain two velocity comparison charts under three conditions. Compared to the narrow surface velocity, overall, the velocity of 100 mm 10° is the highest, while the velocity of 100 mm 15° is the lowest. The speed comparison results in the core area of the nozzle are also the same. The results are all in Fig. 5.

Previous studies have provided many expressions for the outlet velocity of the nozzle when the free surface fluctuation is stable. Among them, NKK Company in Japan defined the F index of the surface fluctuation of molten steel in the reaction mold and can control the slag entrapment in the mold by controlling the range of F index values [8]. To better evaluate the fluctuation of liquid level and obtain the best bloom production efficiency, the F index was introduced to compare different parameter combinations. If the F index is excessive, it can cause severe fluctuation of liquid level and serious slag entrapment. If the F index is too small, the liquid temperature is low, which is not conducive to slag melting and the floating of inclusions. Based on a large amount of production data and simulation calculations, it is determined that the F index should be maintained around 4 in production. The results of different parameter combinations are listed in Table 1. When the casting speed is 0.55 m/

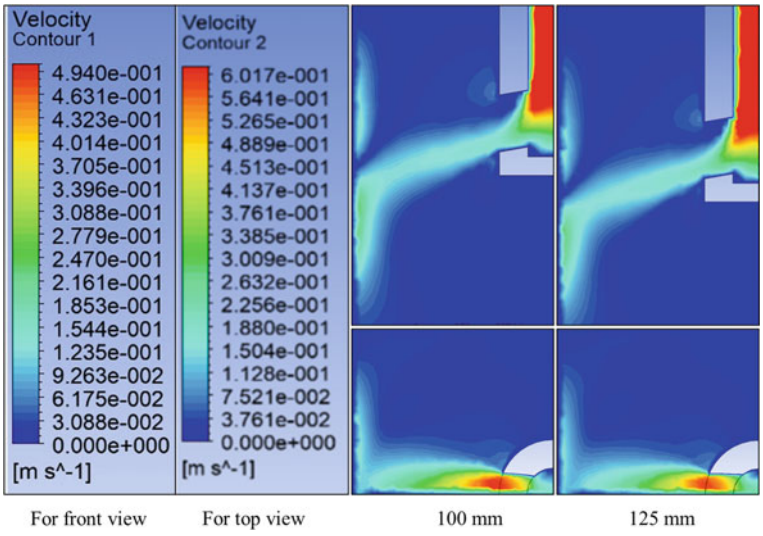

Fig. 3 Front and top views of the flow field inside the mold (insertion depth of submerged nozzle: 100 mm versus 125 mm)

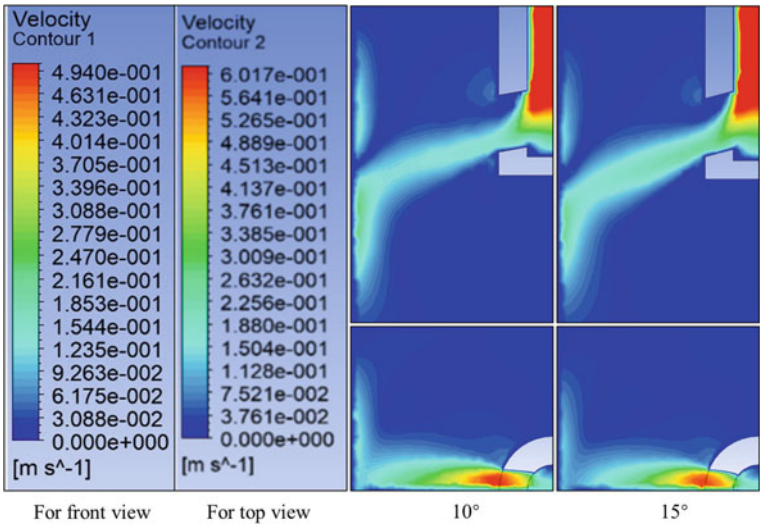

Fig. 4 Front and top views of the flow field inside the mold (dip angle of two side immersed nozzle: 10° versus 15°)

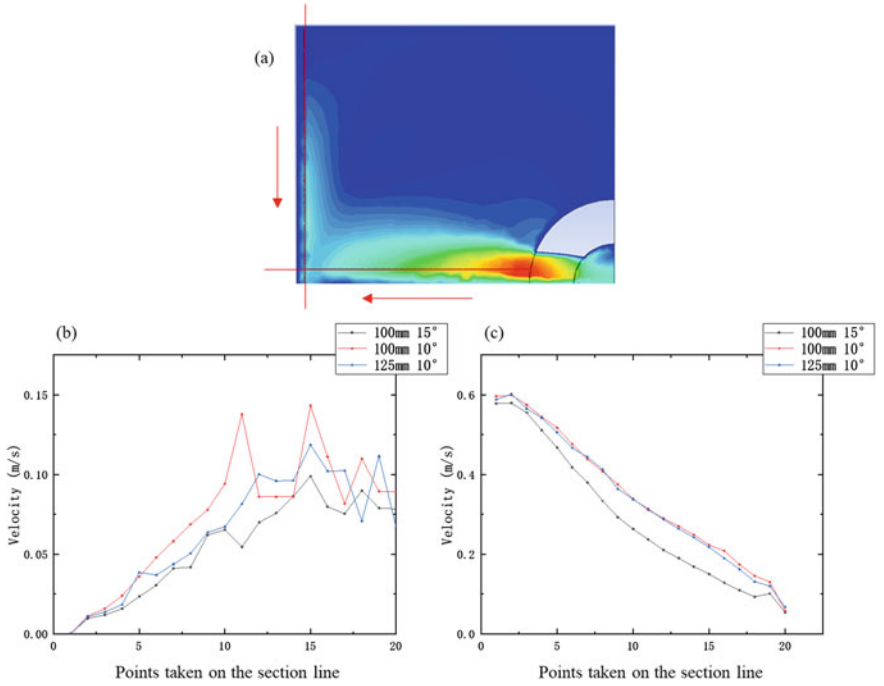

Fig. 5 **a** Taking points on the line in the top view of the flow field **b** Comparison of flow rates of molten steel at the narrow surface under different conditions. **c** Comparison of flow rates of molten steel at the core of the nozzle under different conditions

Table 1 F index under different conditions at a casting speed of 0.55 m/s

Velocity (m/s)	Nozzle immersion depth (mm)	Side hole inclination angles	F index
0.55	100	10°	5.13
0.55	**100**	**15°**	**4.17**
0.55	110	10°	4.76
0.55	**110**	**15°**	**3.90**
0.55	125	10°	4.30
0.55	125	15°	3.55

min, the optimal condition for the F index is that the insertion depth of the nozzle is 100 mm, and the inclination angle of the nozzle is 15° (the F index is 4.17); the insertion depth of the nozzle is 110 mm, and the inclination angle of the nozzle is 15° (the F index is 3.90). Under both parameters, the F index is close to 4.

The temperature field distribution and heat flux distribution under different chamfers are shown in Fig. 6. The temperature and heat transfer conditions are calculated for four different chamfers (25°, 22°, 20°, 12°). As the chamfer of the mold decreases, the temperature value at the corners also decreases (from 1268 °C to 1245 °C). The closer to the corner, the better the heat transfer efficiency and therefore the higher the heat flux. As the chamfer decreases, the heat flux at the corners continues to increase. The chamfer size continuously decreased from R25 to R12, and the peak heat flux at the corner increased from 2.02 MW/m^2 to 2.72 MW/m^2, an increase of 34.6%.

Conclusions

The narrow side of the bloom continuous casting mold is more impacted by molten steel than the wide side. When the insertion depth of the nozzle changes, the speed difference of the steel liquid impacting the wide surface is not significant. When the inclination angle of the water inlet decreases, the speed at which the steel liquid reaches the narrow surface increases, and the impact force on the narrow surface increases.

When the casting speed is 0.55 m/min, the optimal condition for the F index is that the insertion depth of the nozzle is 100 mm, and the inclination angle of the nozzle is 15° (the F index is 4.17); the insertion depth of the nozzle is 110 mm, and the inclination angle of the nozzle is 15° (the F index is 3.90). Under both parameters, the F index is close to 4.

As the chamfer decreases, the heat flux at the corners continues to increase. The chamfer size continuously decreased from R25 to R12, and the peak heat flux at the corner increased from 2.02 MW/m^2 to 2.72 MW/m^2, an increase of 34.6%.

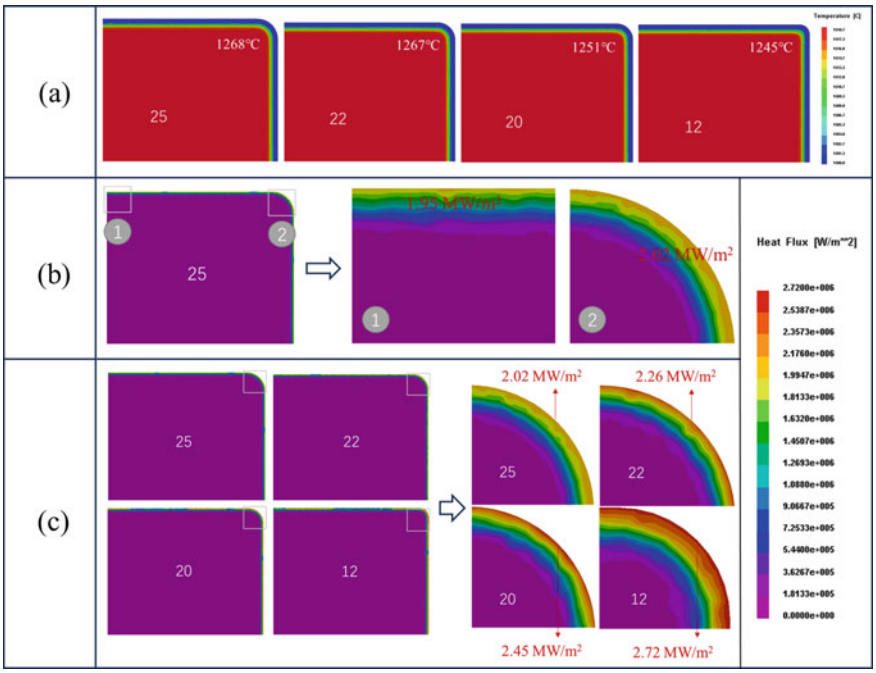

Fig. 6 Temperature field distribution and heat flux distribution under different chamfers, as well as corresponding peak heat flux. **a** Temperature field under different chamfering conditions. (the temperature value at the corner is in the upper right corner). **b** Comparison of heat flux at edges and corners (using R25 chamfer as an example). **c** Local heat flow color map under different chamfering conditions (corner area)

Acknowledgments The financial supports from the National Key Research and Development Program of China (No.2021YFB3702401), the National Science Foundation of China (52304360), the Open foundation of the State Key Laboratory of Advanced Metallurgy, University of Science and Technology Beijing, China (K22-07) and the Key Research and Development Program of Xiangjiang Laboratory (22XJ01002) are greatly acknowledged.

References

1. Chen W, Zhang L, Wang Y et al (2021) Mathematical simulation of two-phase flow and slag entrainment during steel bloom continuous casting. Powder Technol
2. Wang P, Tie Z, Xiao H et al (2022) Optimizing of submerged entry nozzle for bloom continuous casting based on physical and numerical simulation. Steel Res Int
3. Zhong L, Li B, Zhu Y et al (2007) Fluid flow in a four-strand bloom continuous casting tundish with different flow modifiers. ISIJ Int 47(1):88–94
4. Li S, Lan P, Tang H et al (2018) Study on the electromagnetic field, fluid flow, and solidification in a bloom continuous casting mold by numerical simulation. Steel Res Int 89(12)

5. Ji C, Li G, Wu C et al (2019) Design and application of CSC-roll for heavy reduction of the bloom continuous casting process. Metall Mater Trans B
6. Yong C, Zhu M, Cai K et al (2008) Numerical simulation of mold electromagnetic stirring in 280 mm × 380 mm bloom continuous casting. Iron Steel Vanadium Titanium
7. Gu W, Tang P, Wen G et al (2008) Study on submerged entry nozzle with four outlets for bloom continuous casting. Iron Steel
8. Lu Q, Wang X (2007) Calculation of F value and relationship between F value and slag entrapment in a slab continuous casting mold. J Univ Sci Technol Beijing 8(29):811

Research and Practice on the Technology of Ultra-Thick Bed Sintering of Iron Ore in Shougang Jingtang Sintering Plant

Yapeng Zhang, Wen Pan, Shaoguo Chen, Jingjun Zhao, Dongqing Wang, Huaiying Ma, Suochao Qiu, Yongjun Liu, and Huayang Liu

Abstract This paper analyzes the formation law of liquid phase in the process of ultra-thick bed sintering and emphatically expounds the key technology and production practice effect of two 500 m^2 sintering machines of Shougang Jingtang. Through the implementation of ultra-thick bed sintering, Jingtang sintering machine has achieved good results in terms of sintered ore quality, process energy consumption and pollutant discharge. The comprehensive solid fuel consumption of sintering has dropped from 53.95 kg/t in the base period to 48.86 kg/t, ignition gas consumption decreased from 2.391 m^3/t to 1.553 m^3/t; sintering utilization coefficient increased from 1.27 t/(m^2 h) to a relatively high level of 1.40 t/(m^2 h), sintering return fines rate decreased, quality indicators such as drum strength and screening index of sinter remained stable; flue gas volume decreased from 2280 Nm^3/t to 1779 Nm^3/t, a decrease of 21.0%; and NOx emission decreased from 0.58 kg/t to 0.46 kg/t, 20.3% reduction.

Keywords Ultra-thick bed sintering · Self-heat storage · Energy saving and emission reduction · Process energy consumption

Introduction

Thick bed sintering technology can improve the quality of sinter ore, increase the strength of sintered ore, increase the yield of products, and reduce fuel consumption. It has been widely used and developed rapidly in recent years [1–3]. Thick bed sintering

Y. Zhang (✉) · W. Pan · S. Chen · D. Wang · H. Ma
Beijing Key Laboratory of Green Recyclable Process for Iron and Steel Production Technology, Beijing 100043, China
e-mail: zyp1989zyp@163.com

Research Institute of Iron and Steel, Shougang Group Co., LTD Research Institute of Technology, Beijing 100043, China

J. Zhao · S. Qiu · Y. Liu · H. Liu
Ironmaking Department, Shougang Jingtang United Iron and Steel Co., Ltd., Tangshan 063200, China

S. Wagstaff et al. (eds.), *Materials Processing Fundamentals 2024*, The Minerals, Metals & Materials Series, https://doi.org/10.1007/978-3-031-50184-5_27

has an impact on the air permeability of the sintering layer, pollutant emissions and sinter quality. On the one hand, as the thickness of the raw sintering bed increases, the path of air passing through the sintering bed is extended, and the pressure loss increases. At the same time, as the thickness of the sintering bed increases, the lower sintering bed is compressed under the action of gravity of the sintering bed, so the resistance increases. Also, the thickness of the high-temperature molten layer is relatively increased, which will cause the resistance to increase, thereby causing the vertical sintering speed to decrease [4, 5]. On the other hand, the increase of the thickness of the sintering bed helps to strengthen the heat storage of itself, the residence time of the combustion zone is longer, the formation conditions of the sinter are improved, and the assimilation of the liquid phase and the crystallization of the melt are more sufficient making the grains well developed. Moreover, as the thickness of sintering bed increases, the amount of sinter in the surface layer decreases relatively. Therefore, thick bed sintering can improve the strength of sinter and increase the yield without increasing the amount of fuel. In recent years, thick bed sintering has been successfully applied in many steel companies and achieved good results [6–8]. At the same time, many metallurgical workers have also carried out research on technologies related to thick bed sintering [9, 10].

In 2010, two 500 m^2 sintering machines in Shougang Jingtang company were the first to reach the 800 mm level thick bed sintering in China, which reduced fuel consumption by 1.1 kg/t compared with that of the 750 mm sintering bed. In order to reduce solid fuel consumption and reduce pollutant emissions, it is necessary to further increase the thickness of the sintering bed. For this reason, technical research has been carried out, thus realizing the sintering of a large-scale sintering machine with an ultra-thick sintering bed of over 900 mm.

Basic Theoretical Analysis of Ultra-Thick Bed Sintering

Using Factsage7.1 thermodynamic software, the influence of different sintering temperature and atmosphere on the forming of sintering liquid phase was calculated under the condition of Shougang Jingtang sintering raw materials. The specific calculation and analysis include the formation ratio of sinter liquid phase, liquid phase viscosity and apparent viscosity of sinter under high temperature, as well as the equilibrium mineral composition of sinter cooling process.

Figures 1 and 2 show the amount of sintering liquid phase produced and the viscosity of the produced liquid phase at different combustion zone temperatures under the conditions of oxygen partial pressure 1e-2, 1e-3, and 1e-4 atm, respectively. It can be seen from Fig. 1 that under a certain oxygen partial pressure, a higher = temperature, the more liquid phase will be produced. The effect of different oxygen partial pressures on the amount of sintering liquid phase formation is opposite in different temperature ranges.

When the temperature of the combustion zone is below 1400 °C, the lower the oxygen partial pressure, the less the amount of sintering liquid phase produced. That

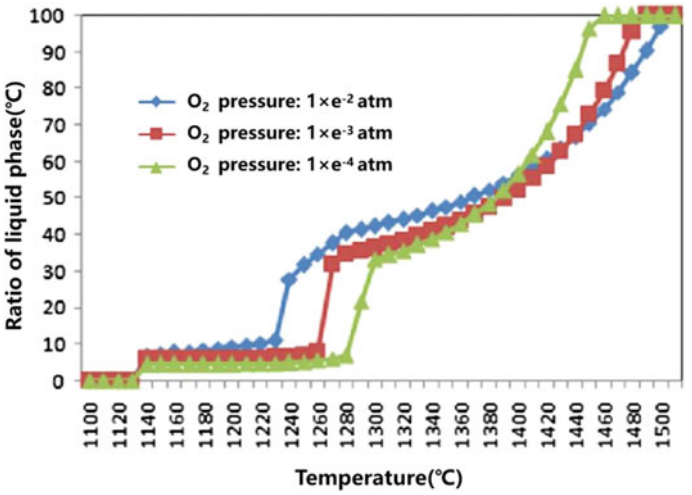

Fig. 1 High-temperature liquid phase formation under different oxygen partial pressures

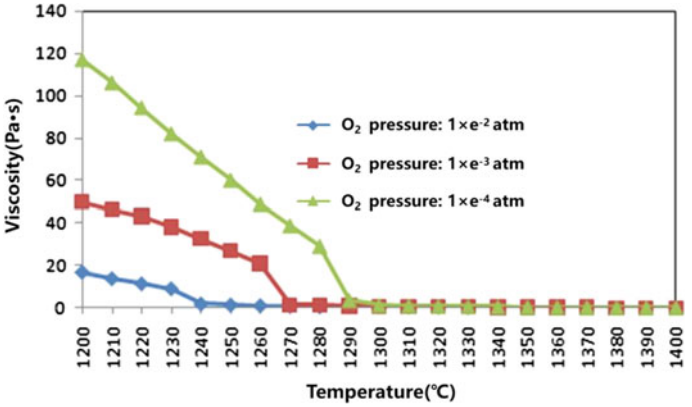

Fig. 2 Comparison of apparent viscosity values under different oxygen partial pressures

is to say, appropriately reducing the carbon distribution and increasing the oxidizing atmosphere of the sintering bed is beneficial to the formation of the liquid phase. Taking the formation of 40% liquid phase as an example, under low oxygen partial pressure (1e-3 atm), the combustion zone temperature needs to reach 1340 °C, and under high oxygen partial pressure (1e-2 atm), the combustion zone temperature is 1280 °C.

When the temperature of the combustion zone is over 1400 °C, more sintering liquid phase will be generated at lower oxygen partial pressure. That is to say, by increasing the fuel ratio and increasing the reduction atmosphere of the sintering bed, the generation of liquid phase can be promoted.

As shown in Fig. 2, the higher the oxygen partial pressure at the same combustion zone temperature, the lower the liquid phase viscosity. In the actual sintering process, as the temperature increases, the liquid phase appears earlier, and the viscosity is lower when the oxygen partial pressure is high. Therefore, the sintering temperature is controlled within 1400 °C, and the oxygen partial pressure in the sintering process is appropriately increased.

Combined with super-thick bed sintering, the self-heat storage capacity of the sintering bed is improved after the thickness of the sintering bed is increased, resulting in the reduction of solid fuel consumption.

As shown in Fig. 3, the temperature curves of the upper, middle, and lower layers of the sintering bed were tested when the thickness of sintering bed was 800 mm. The highest temperature exceeded 1400 °C. According to the above thermodynamic calculations and theoretical analysis, the combustion zone temperature should be controlled below 1400 °C. Reasonably adjust the solid fuel ratio and make full use of the advantages of high oxygen partial pressure in the combustion zone to achieve low-temperature ultra-thick bed sintering in Shougang Jingtang sintering machines.

Based on the above basic theory, it is proposed that the ultra-thick bed sintering needs to solve the following key technical problems: (1) Problem of insufficient heat in upper layer after increasing the sintering bed thickness. It requires the use of enhanced segregation technology of raw material distribution to increase the carbon segregation of the upper layer. (2) Problems of deteriorating air permeability of sintering bed and affecting sintering productivity when applying ultra-thick bed sintering. It is necessary to strengthen the control of air leakage and develop a material distribution device to improve the air permeability of the sintering bed. To this end, Shougang Jingtang company has successfully developed a set of key technologies for ultra-thick bed sintering suitable for Jingtang sintering machines through a series of technical research.

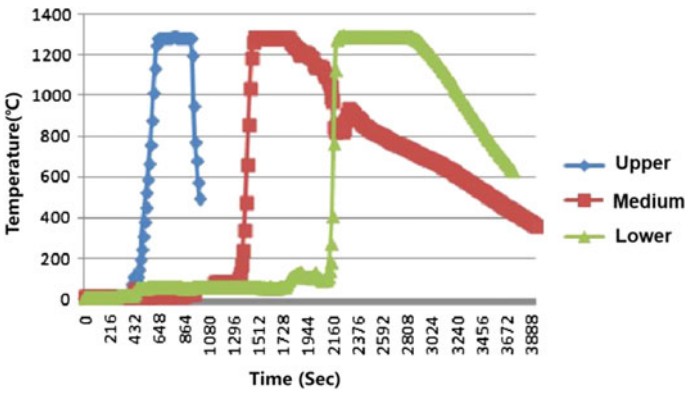

Fig. 3 Temperature curve of Jingtang sintered 800 mm sintering bed

Development of Key Technologies for Ultra-Thick Bed Sintering

Segregation Distribution Technology for Ultra-Thick Bed Sintering

The sintering trolley was lifted out several times to carry out blending particle size screening tests on the 500 m^2 sintering machine. The vertical distribution of blending showed a linear pattern. Figure 4 shows the comparison of vertical segregation of raw blending on the trolley. In order to facilitate the analysis of particle size segregation, the concept of segregation intensity *Yi* is introduced. According to the following formula, the relative size of the particle in each zone is calculated. If $Yi > 1$, it means that the particle size of the mixture in this area is big. If $Yi < 1$, it means that the particle size of the mixture in this area is small. Calculating the number of occurrences of $Yi > 1$ in each region indicates that the granularity of this region is relatively large.

$$Yi = D\_i/D,$$

in which, *D_i* is the average particle size of mixture i; *D* is the average value of the mean particle size of many mixture samples.

For charging raw blending on the sintering trolley, the raw blending particles are required to be evenly distributed in horizontal direction and well segregated in vertical direction. Then, the mixture with large particle and low carbon content can be distributed to the lower part of the sintering bed and the mixture with small particle and high carbon content can be distributed to the upper part. From the analysis results in Fig. 4, it can be seen that the particle size distribution in vertical direction is small at the top and large at the bottom, and the segregation effect is good, which has the basis for carbon reduction in ultra-thick sintering bed.

After the thickness of the sintering bed is increased, higher requirements are put forward for the vertical segregation. In order to further improve the current vertical

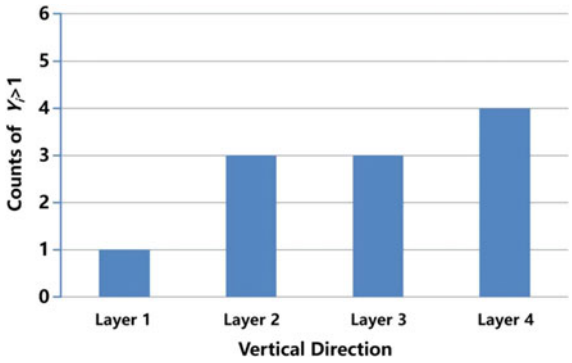

Fig. 4 Vertical particle size segregation of raw blending on the sintering trolley before transformation

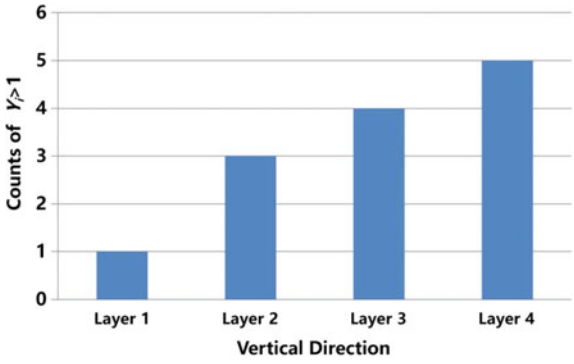

Fig. 5 Vertical particle size segregation of raw blending on sintering trolley after modification

segregation distribution effect, a simulation was carried out for the speed of the nine-roller distributor. The speeds were designed to be 9 rpm, 18 rpm, and 36 rpm. When the speed of nine-roller distributor is 36 rpm, the vertical segregation effect is relatively the best. The average particle size of the upper part is the lowest, and the lower part is the highest. Based on the above research results, the nine-roller distributor speed is adjusted from 18 to 30 rpm. After the adjustment, sampling was carried out by lifting out the trolley of raw blending to examine the effect of the transformation. The results are shown in Fig. 5. Compared with the segregation before modification, the vertical segregation increases, which not only improves the air permeability of the sintering bed but also helps to gradually reduce the carbon content of the raw blending from top to bottom, which is conducive to giving full play to the "automatic heat storage" effect of the thick sintering bed.

Development and Application of Device for Loosening Sintering Bed

In order to improve the air permeability of sintering bed, a device was developed to loosen sintering bed based on the process, equipment status, and raw material conditions of 500 m^2 sintering machine. First, a numerical simulation by ANSYS Fluent was performed for the device, and five different layouts of the device were designed. A rectangular cube with size of 1000 mm (length) × 500 mm (width) × 950 mm (height) was designed as the distribution space. The size of loosening device is 268 mm (length) × 20 mm (width) × 100 mm (height). A total of spherical particles of three sizes are arranged, with particle sizes of 6 mm, 4.5 mm, and 3 mm, respectively. The simulation results show that: (1) After adding a loosening device, the average void ratio is significantly increased, and the distribution of void ratio in the length direction is more dispersed; (2) after adding a loosening device, the void ratio on both sides is significantly increased in the length direction, and the void

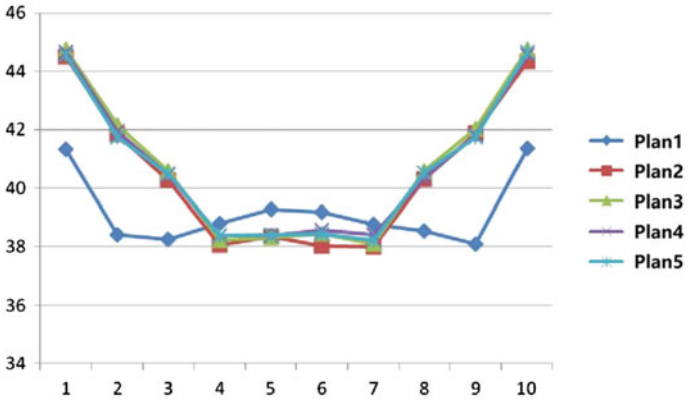

Fig. 6 Distribution trend of porosity along the length direction

Fig. 7 Comparison of the negative pressure of the main flue before and after the modification

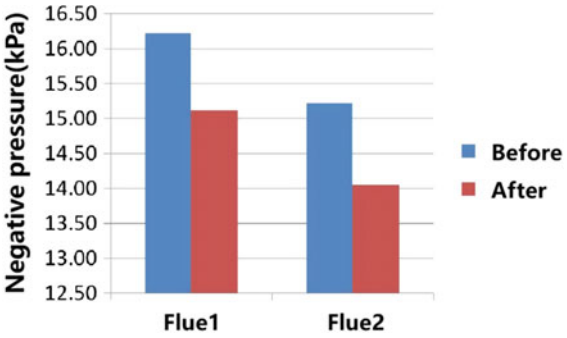

ratio in the center decreases slightly. Figure 6 shows the difference in void ratio in different length directions of each scheme.

Based on the simulation results, the size and layout of device for loosening sintering bed were determined for Jingtang 500 m^2 sintering machine. After transformation, the air permeability of the sintering bed is obviously improved, which is manifested by the decrease of the negative pressure of the main flue, as shown in Fig. 7. This transformation creates good conditions for the ultra-thick bed sintering.

New Method of Iron Ore Matching for Good Permeability of Sintering Bed

Combined with the sintering and mixing granulation process, a process method for effectively evaluating the granulation properties of iron ore fines has been developed, namely: a new process for iron ore fines granulation and bonding properties,

using a rheometer to measure the prepared mixture slurry. The performance of iron ore fines in sintering, mixing, and granulation can be judged by the measurement results. Compared with the mixing and granulating equipment, the process parameter adjustment is more flexible and active, and it has stronger guiding significance for the actual sintering production.

For the iron ores used by Shougang Jingtang company, the order of the bonding properties from large to small is: hematite > mix of hematite and limonite > limonite. According to the granulation bonding characteristic values of 14 iron ores, combined with the mineral types of iron ore, the iron ore can be divided into high bonding ores, medium-high bonding ores, medium-low bonding ores, and low bonding ores.

According to the experimental research results, the granulation bonding property index was applied to the structure adjustment and matching of iron ores in Shougang Jingtang sintering process and proposed an ore matching idea that takes into account the air permeability of the sintering bed, i.e., increasing the proportion of high bonding iron ores, reducing the ratio of low bonding iron ores. After the adjustment, the granulation of raw blending is improved, and the air permeability of the sintering bed is improved. While ensuring that other indicators are basically maintained stable, the sintering utilization coefficient is much improved.

Application Effect of Ultra-Thick Bed Sintering

On the basis of the development of key technologies for ultra-thick bed sintering, the sintering machine of Shougang Jingtang gradually increased the sintering bed thickness to 930 mm. According to the above results of thermodynamic calculations on sintering temperature and atmosphere on the forming of sintering liquid phase, the combustion zone temperature is controlled below 1400 °C in the sintering machine of Shougang Jingtang. The speed of nine-roller distributor is adjusted to 36 rpm. A device for loosening sintering bed was applied for the sintering machine. Also, the iron ore matching structure was adjusted according to the granulation bonding property index of iron ores.

As shown in Table 1, after the implementation of ultra-thick sintering bed sintering production, the sintering solid fuel consumption has shown a significant downward trend, and the sintering comprehensive solid fuel consumption has dropped from 53.95 kg/t in the base period to 48.86 kg/t. Ignition gas consumption dropped from 2.391 m^3/t to 1.553 m^3/t.

Table 1 Changes in related indicators of energy consumption in the sintering process

Stage	Solid fuel consumption (kg/t)	Ignition gas consumption (m^3/t)
Before implementation	53.95	2.391
After implementation	48.86	1.553

Table 2 Comparison of sintering technical and economic indicators and quality

Stage	Sintering utilization coefficient ($t/m^2.h$)	Return fines rate (%)	TI (%)	Screening index (−5 mm) (%)
Before implementation	1.265	21.43	82.66	2.37
After implementation	1.399	18.53	82.58	3.35

Table 3 Comparison of the amount of flue gas and NOx per ton of sintered ore

Stage	NOx concentration (mg/Nm^3)	Flue gas volume per ton of sinter (%)	NOx volume per ton of sinter (%)
Before implementation	1.265	21.43	2.37
After implementation	1.399	18.53	3.35

As shown in Table 2, after the implementation of ultra-thick layer sintering production, the sintering utilization coefficient increased from 1.27 t/(m^2 h) to a high level of 1.40 t/(m^2 h), the sintering return rate decreased, and the sinter drum strength and screening indexes and other quality indicators remained stable.

As shown in Table 3, after the implementation of ultra-thick bed sintering, the amount of flue gas per ton of sintered ore dropped from 2280 Nm^3/t to 1779 Nm^3/t, a decrease of 21.0%; the amount of NOx per ton of sintered ore dropped from 0.58 kg/t to 0.46 kg/t, a decrease of 20.3%.

Conclusions

(1) Through the analysis of the influence of different sintering temperatures and sintering atmospheres on the production process of sintering liquid phase, it is found that the influence of different oxygen partial pressures on the production of sintering liquid phase is opposite in different temperature ranges: when the combustion zone temperature is below 1400 °C, the lower the oxygen partial pressure is, the less the sintering liquid phase is generated; when the combustion zone temperature is above 1400 °C, the lower the oxygen partial pressure is, the more liquid phase generated.

(2) The use of ultra-thick bed sintering to strengthen segregation technology can increase the vertical segregation of raw blending, which not only improves the air permeability of the sintering bed but also helps to gradually reduce the carbon content of the mixture from top to bottom.

(3) The air permeability of the sintering bed is significantly improved after using the loosening device, which is manifested by a decrease in the negative pressure of the large flue; New method of iron ore matching taking into account the air permeability of the sintering bed can improve the air permeability of the sintering bed.
(4) Through the implementation of ultra-thick sintering bed sintering, Jingtang's sintering machine has achieved good results in terms of sintered mineral quality, process energy consumption and pollutant discharge, and the comprehensive solid fuel consumption of sintering has dropped from 53.95 kg/t in the base period to 48.86 kg/t, which is reduced to 42.16 kgce when converted into standard coal. Ignition gas consumption decreased from 2.391 m^3/t to 1.553 m^3/t; sintering utilization coefficient increased from 1.27 t/(m^2 h) to a relatively high level of 1.40 t/(m^2 h); flue gas volume per ton of sintered ore decreased from 2280 Nm^3/t to 1779 Nm^3/t, a decrease of 21.0%; NOx per ton of sintered ore decreased from 0.58 kg/t to 0.46 kg/t, a decrease of 20.3%.

Acknowledgements The authors are grateful for the financial support of the National Key R&D Program of China (2017YFB0304300 & 2017YFB0304302).

References

1. Xu M (2014) Experimental research and production practice of ultra-thick layer sinter [A]. Chinese metal society. 2014 national ironmaking production technology conference and ironmaking academic annual conference proceedings (Part 1) [C]. Chinese metal society, p 3
2. Jiangnan Z (2017) Overview and practice of thick layer sintering optimization technology. Sintered Pellets 42(02):1–9
3. Wang Y-Z, Zhang J-L, Liu Z-J et al (2017) Recent advances and research status in energy conservation of iron ore sintering in China. JOM 69(11)
4. Wang H, Angang, Wang Q et al (2010) Production practice of 800 mm thick layer sintering of Shougang Jingtang No. 1 sintering machine. Sintered Pellets 35(03):47–51
5. Zhengming C, Wenxin N, Wen P et al (2019) Research and application of ultra-thick sintering bed homogeneous sintering technology. Sintered Pellets 44(04):7–12
6. Wang Yuefei W, Shengli ZY et al (2014) Review and discussion of Baosteel's sintering energy-saving and emission reduction technology. Sintered Pellets 39(06):54–57
7. Fanqiu Z, Reform Z, Gaoming L, Shuigan W, Binbin C (2019) Production practice of 920 mm thick layer sintering of Xiangtan Iron and Steel 360 m^2 sintering machine. Sintered Pellets 44(03):6–9
8. Yonghai K (2020) Tiangang united special steel's 1000 mm ultra-thick sintering bed sintering production practice. Shandong Metall 42(03):9–11
9. Jianliang Z, Yonghai K, Shijun Z et al (2020) Application of fully active lime enhanced sintering technology in ultra-thick sintering bed. Steel 55(08):56–61
10. Jun L, Shijun Z, Jian K et al (2019) Optimization practice of flux structure under ultra-thick sintering bed sintering conditions. Tianjin Metall 06:11–13

Study on Resource Utilization of Sintering Semi-Dry Desulphurization Ash

Zhang Yang and Jiao Lina

Abstract The desulfurization ash contains high content of $CaSO_3$, which makes it difficult for its resource utilization. In the present study, the physical–chemical performance of the sintering flue gas desulfurization ash from a typical steel corporation was analyzed. On this basis, the H_2O_2 oxidation modification, $MnSO_4$ catalytic modification and air oxidation test with different process conditions of it were studied, and the best process conditions of desulfurization ash modification were analyzed. Considering the test results and the industrial practice, the optimal process conditions were thought as: hydrogen peroxide was oxidant, pH value was 5.5, the molar ratio of H_2O_2 and $CaSO_3$ was 1:1, the slurry solid content was 10%, and the reaction time was 1.5 h, and under these conditions, the $CaSO_3$ conversion rate reached 98%. However, $MnSO_4$ was not suggested to be added for oxidation of sintering semi-dry desulphurization ash.

Keywords Desulfurization ash · Modification · Oxidation · Comprehensive utilization

Introduction

The traditional long-term process in the steel industry consumes fuel and ore, while generating a large amount of pollutants such as SO_2, NO_x and dioxins. The SO_2 and NO_x pollutants emitted by the sintering process account for over 70% and 50% of the total emissions of steel enterprises, respectively [1, 2]. The emission of SO_2 and NO_x gas is harmful to the environment and human health; therefore, it is necessary to effectively remove pollutants from the flue gas.

At present, scholars have conducted extensive research on sintering flue gas desulfurization technology, with nearly 200 methods of desulfurization [3–5]. According to the differences of desulfurization products during the sintering flue gas treatment

Z. Yang · J. Lina (✉)
School of Metallurgy and Materials Engineering, Jiangsu University of Science and Technology, Zhangjiagang 215600, Jiangsu, China
e-mail: Linda2018@shu.edu.cn

S. Wagstaff et al. (eds.), *Materials Processing Fundamentals 2024*, The Minerals, Metals & Materials Series, https://doi.org/10.1007/978-3-031-50184-5_28

process, desulfurization technologies are divided into three categories: wet, dry, and semi-dry [6, 7]. The semi-dry flue gas desulfurization technology has the characteristics of both wet and dry flue gas desulfurization processes, with low energy consumption, simple process, and other advantages. At the same time, it can also remove pollutants such as NO_X and dioxins. It is an important process for flue gas desulfurization in the sintering process of the steel industry [8–10].

However, the semi-dry flue gas desulfurization process generates a large amount of sintered flue gas desulfurization ash during the pulping process, which contains about 35% $CaSO_3$. The reason is that a large amount of lime is added during the desulfurization process, resulting in a slow reaction rate at the gas–solid interface and a shorter residence time for SO_2 in the absorption process [11–13]. $CaSO_3$ is prone to slow oxidation by air to generate $CaSO_4$, which disrupts the stability of desulfurization ash and cannot be directly utilized [14–16]. In addition, $CaSO_3$ is extremely unstable and easily decomposes into SO_2 in the presence of heat or acid, causing secondary pollution [17]. Therefore, how to economically convert $CaSO_3$ into $CaSO_4$ is the key to solving the resource utilization of desulfurization ash [18–20]. Traditional oxidation methods include high-temperature oxidation method and low-temperature catalysis method. Currently, research on the oxidation of $CaSO_3$ in desulfurization ash to prepare $CaSO_4$ has achieved good results [21, 22]. The high-temperature oxidation method places desulfurization ash into equipment such as fluidized bed furnaces for heating and oxidation, but it is difficult to be industrialized. The low-temperature catalytic method involves adding a catalyst to oxidize $CaSO_3$ at room temperature, resulting in discontinuous production and low efficiency [23]. This oxidation method converts $CaSO_3$ into soluble $CaHSO_3$ under acidic conditions and then oxidizes it into $CaSO_4$. This method has low cost and high efficiency and is suitable for industrial production.

In this paper, the semi-dry desulfurization ash produced by a domestic steel plant was used as raw material. The physical and chemical properties of desulfurization ash were analyzed, the feasibility of adding different oxidants H_2O_2, $MnSO_4$ catalyst and air oxidation modification of $CaSO_3$ and the experimental conditions of the optimal conversion rate were discussed. The different influencing factors of the oxidation process were investigated, which provided experimental basis and technical support for the resource utilization of desulfurization ash.

Experimental

Experimental Materials and Testing Methods

The semi-dry sintering flue gas desulfurization ash used in the experiment was taken from the flue gas semi-dry desulfurization system of the 180 m^2 sintering machine of a domestic steel company and sampled according to the GB/T 2007.1–1987 [24].

The microstructural analyses of semi-dry desulfurization ash were observed using an emission scanning electron microscope (Quanta 450FEG, United States). The phase analysis was conducted by XRD using the Cu Kα radiation and tested in the range of 10°–90° (D8 Discover, German). Qualitative and quantitative analysis of desulfurization ash elements was investigated by the fluorescence spectrometer (Axios Max, Dutch). Thermal stability analysis was measured by high-temperature thermogravimetric analyzer (RZ-8-17, Chinese). The particle size of desulfurization ash was analyzed by the laser particle size analyzer (Malvern 3000, UK), and the slag samples were screened according to industry standards [25]. The moisture content of desulfurization ash is measured by drying under normal pressure, the density is measured by differential pressure transmitter, and the angle of repose is measured by injection angle. The content of $CaSO_3$ and $CaSO_4$ in desulfurization ash is tested and analyzed according to the GB/T 5484-2012 [26], and the content of $CaCO_3$ is tested according to the GB/T 19281–2014 [27].

Physical and Chemical Properties of Desulfurization Ash

The microstructure of the raw material is shown in Fig. 1. It can be seen from Fig. 1 that the semi-dry sintering flue gas desulfurization ash has irregular block shaped particles, rough surface, and loose structure. The formation of the microstructure was mainly due to the fact that the semi-dry sintering flue gas desulfurization ash was difficult in generating a liquid phase under high-temperature conditions. Although there was a significant solid phase diffusion effect during the formation of desulfurization ash, the new substances formed by solid phase diffusion were not yet sufficient to make the structure of desulfurization ash dense, resulting in a relatively loose surface structure of desulfurization ash [28].

The particle size distribution characteristics can generally be used as an indicator to characterize the thickness of the powder particles. The desulfurization ash is a

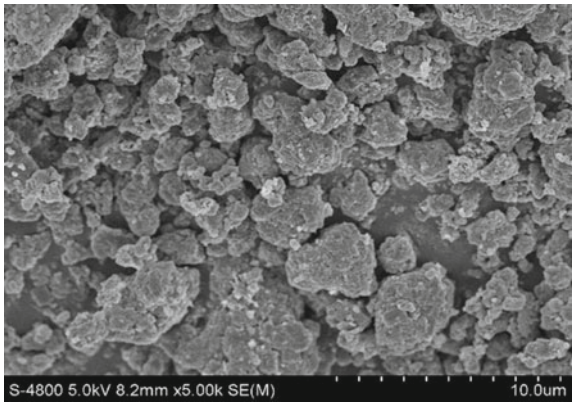

Fig. 1 Microstructures of semi-dry desulfurization ash

Table 1 Other physical properties of semi-dry desulfurization ash

Properties	Desulfurization ash
Percentage of moisture (%)	2.20
Bulk density (t/m^3)	0.900
Rest angle (°)	52

dry and very fine particle. According to the particle size analysis results, the median particle size of the desulfurization ash used in this study is about 15 μm.

The moisture content, density, and angle of repose of desulfurized ash were tested in batches for 5 times, and the measured results were taken as the average, as shown in Table 1.

The phase composition of desulfurization ash was analyzed by X-ray diffractometer, and the results are shown in Fig. 2. As shown in Fig. 2, the main components of the semi-dry desulfurization ash were semi-hydrated calcium sulfite ($CaSO_3 \cdot 1/2H_2O$) and calcium carbonate ($CaCO_3$).

Combined with XRF detection and analysis, it could be concluded that the main phase of desulfurization ash was $CaSO_3 \cdot 1/2H_2O$, $CaCO_3$, $CaSO_4$, and $Ca(OH)_2$. The main phase is basically consistent with the semi-dry sintering flue gas desulfurization ash in reference [29]. However, due to different raw materials used in sintering, the phase of the final desulfurization product may be different. Based on the above analysis and test results, the phase composition of desulfurization ash is shown in Table 2; the $CaSO_3$ content in the semi-dry desulfurization ash of sintered flue gas is relatively high, which is determined by the semi-dry circulating fluidized bed desulfurization process.

The results of thermogravimetric analysis of raw materials are shown in Fig. 3. The mass of the experimental sample is 10.0 mg, the heating rate is 10 °C/min, and the test temperature range is 10 ~ 1000 °C. It can be seen from Fig. 3 (solid line) that the TG curve can be roughly divided into three characteristic stages: the first weight

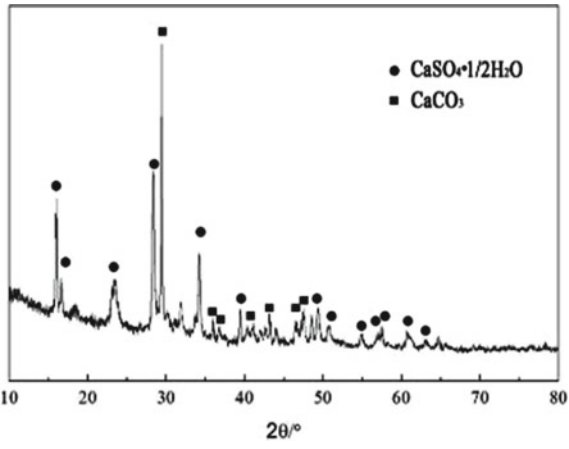

Fig. 2 XRD patterns of semi-dry desulfurization ash

Table 2 Phase composition of desulfurized ash W_B/%

$CaSO_3 \cdot 1/2H_2O$	$CaSO_4 \cdot 2H_2O$	$CaCO_3$	$Ca(OH)_2$	$CaCl_2$	$SiO_2 + Al_2O_3 + Fe_2O_3$
~60	<2	~30	~5	1.7	0.86

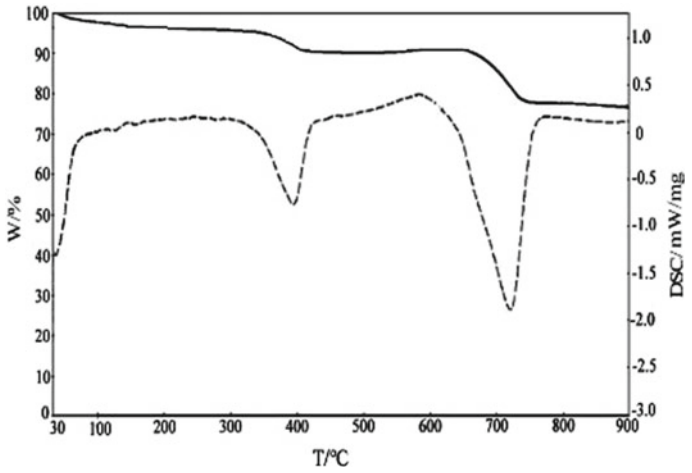

Fig. 3 Differential thermogravimetric analysis of desulfurized ash

loss step is between 30 and 300 °C, with a weight loss rate of about 3.398%, mainly due to the desulfurization ash was heated to lose physical water. The second weight loss step is about 330 ~ 430 °C, and the weight loss rate is about 4.860%. The reason is that $CaSO_3 \cdot \frac{1}{2} H_2O$ loses crystal water, and the chemical reaction is $CaSO_3 \cdot \frac{1}{2} H_2O \rightarrow CaSO_3 + \frac{1}{2} H_2O$, which is endothermic reaction. The third weight loss step is about 700 °C, with a weight loss rate of approximately 13.828%. Within this temperature range, $CaSO_3$ begins to decompose at 650 °C, resulting in the production of SO_2.

Oxidation Mechanism

The traditional low-temperature catalytic chemical reaction is as follows:

$$2CaSO_3 + O_2 \rightarrow^{\text{catalyst}} 2CaSO_4 \tag{1}$$

$$Ca(OH)_2 + H_2SO_4 \rightarrow CaSO_4 + 2H_2O. \tag{2}$$

The principle of the semi-dry desulfurization ash oxidation test in this article is to adjust the pH value, convert the extremely soluble $CaSO_3$ (0.04 g/L) into soluble

$CaHSO_3$ under suitable acidic conditions, and then introduce air for oxidation. The prominent advantage of this method is that it belongs to liquid phase reaction, with high efficiency and low temperature and pressure requirements.

The $CaSO_3$ oxidation reaction in this article is as follows:

$$CaSO_3\frac{1}{2}H_2O \rightarrow CaSO_3 + \frac{1}{2}H_2O \tag{3}$$

$$CaSO_3 \rightarrow Ca^{2+} + SO_3^{2-} \tag{4}$$

$$H^+ + SO_3^{2-} \rightarrow HSO_3^{2-} \tag{5}$$

$$HSO_3^{2-} + \frac{1}{2}O_2 \rightarrow H^+ + SO_4^{2-} \tag{6}$$

$$Ca^{2+} + SO_4^{2-} \rightarrow CaSO_4 \tag{7}$$

$$CaSO_4 + H_2OCaSO_4 \cdot H_2SO_4 \tag{8}$$

$$Ca(OH)_2 + H_2SO_4 \rightarrow CaSO_4 + 2H_2O. \tag{9}$$

Oxidation Experimental Result and Analysis

In this paper, the oxidation experiment of desulfurization ash was carried out; the effects of different oxidant types, oxidant dosage, reaction time, and other conditions on the conversion rate of $CaSO_3$ were analyzed. The effects of H_2O_2 and air as oxidants on the conversion of $CaSO_3$ were studied. In the air oxidation experiment, the effect of adding $MnSO_4$ catalyst on the air oxidation modification experiment was studied. The experimental design was all single response variable.

H_2O_2 Oxidation Modification Test

In the H_2O_2 oxidation modification experiment of desulfurization ash, the addition amount of H_2O_2, the solidification rate of slurry, pH value, and reaction time will affect the conversion rate of $CaSO_3$.

When the reaction time was 1.5 h and the solid content in the $CaSO_3$ slurry was 10%, the effect of the molar ratio of H_2O_2 to $CaSO_3$ on the $CaSO_3$ conversion rate is shown in Fig. 4. As shown in Fig. 4, without the addition of sulfuric acid, the

conversion rate of $CaSO_3$ first increased and then decreased with the increase of H_2O_2 dosage. The results of the two experiments are similar, but the conversion rate of calcium sulfite increased significantly under acidic conditions. When pH = 5.5, the molar ratio of H_2O_2 to $CaSO_3$ reaches 1:1, and the conversion rate is up to 96%.

The effect of solid content in $CaSO_3$ slurry on its conversion rate was studied under the optimal conditions of pH = 5.5, the molar ratio of H_2O_2 to CaSO3 was 1:1, and the reaction time was 1.5 h. The results are shown in Fig. 5. Under the condition of constant pH, the conversion rate of calcium sulfite continues to decrease with the increase of the solid content of the slurry. When the solid content was 10%, the conversion rate was the highest.

Under the optimal experimental conditions in Fig. 5 (pH = 5.5, molar ratio of H_2O_2 to $CaSO_3$ 1:1, solid content of 10%), the effect of pH on conversion rate was studied at a reaction time of 1.5 h. It can be seen from Fig. 6 that low pH was

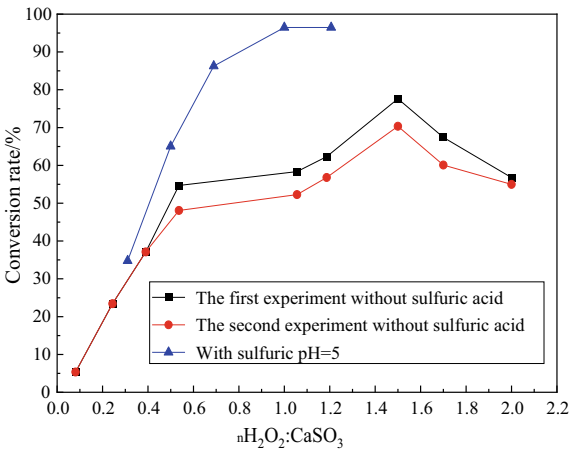

Fig. 4 Effect of H_2O_2 addition on conversion of $CaSO_3$

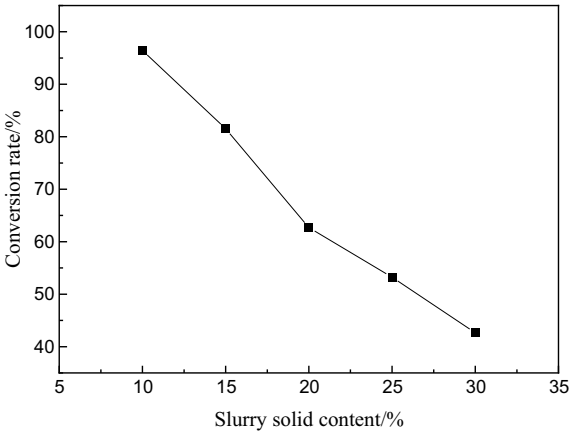

Fig. 5 Effect of slurry solid content on conversion of $CaSO_3$

conducive to the conversion of $CaSO_3$. According to the actual application of the enterprise, the pH value was 5.5.

Using the optimal experimental conditions in Fig. 6, the effect of reaction time on conversion rate was studied, and the results are shown in Fig. 7. When the reaction time was 0.5 h, the conversion rate was 90%, and when the reaction time was 2 h, the conversion rate was 98%. Further increasing the reaction time, the conversion rate did not increase significantly.

According to the above experimental results, the optimal industrial experimental conditions for H_2O_2 oxidation modification experiment were pH 5.5, molar ratio of H_2O_2 to calcium sulfite was 1:1, slurry solid content was 10%, and reaction time was 1.5 h.

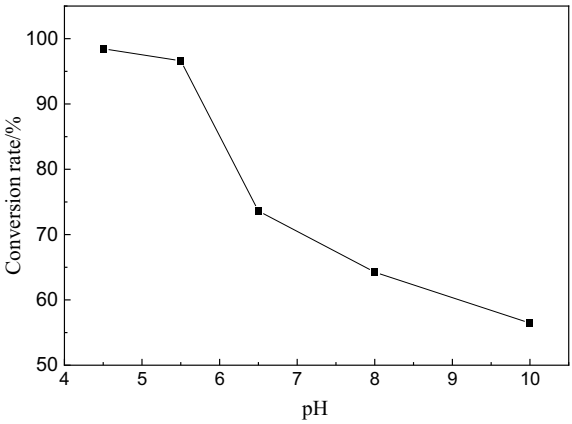

Fig. 6 Effect of pH on conversion of $CaSO_3$

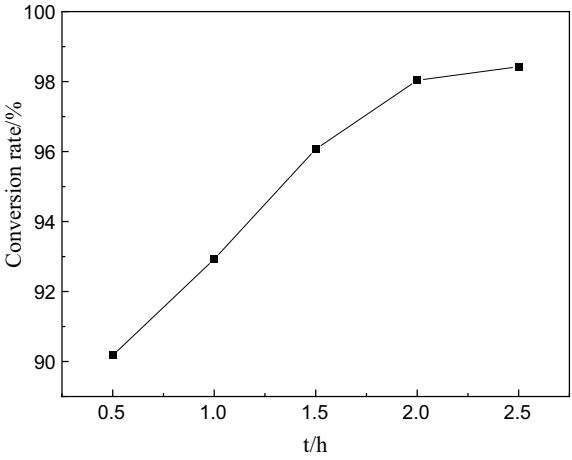

Fig. 7 Effect of reaction time on conversion of $CaSO_3$

Air Catalytic Modification Experiment

In the air catalytic modification experiment, the effects of $MnSO_4$ addition and reaction time on the $CaSO_3$ conversion rate were investigated. Under the condition of pH 5.7 and slurry solid content of 10%, the effect of $MnSO_4$ addition on $CaSO_3$ conversion is shown in Fig. 8. It could be seen that the addition of $MnSO_4$ catalyst in both the bubbling reactor and the countercurrent reaction tower can significantly improve the conversion rate of $CaSO_3$. The increase in $CaSO_3$ conversion rate by $MnSO_4$ in the two is not much different, but the conversion rate of $CaSO_3$ in the countercurrent reaction tower is significantly higher than that in the bubbling reactor. This is because the gas–liquid–solid three-phase contact in the countercurrent reaction tower is more sufficient, and the mass and heat transfer conditions are better.

When the pH and solid content of the slurry remained unchanged and the amount of $MnSO_4$ added was 1%, the effect of reaction time on the $CaSO_3$ conversion rate in a countercurrent reaction tower was studied, and the results are shown in Fig. 9. When the pH was 5.7, the solid content of the slurry was 10%, and the amount of $MnSO_4$ added remained constant, and the conversion rate increases with the increase of reaction time. When the reaction time reached 4 h, the conversion rate was the highest, which is similar to the $CaSO_3$ conversion rate in the modification experiment using MnO_2 as catalyst by Zhou Chenhui et al. [30].

In order to study the residual amount of $MnSO_4$, ICP test was carried out on the filtrate after catalytic reaction. The filtrate with 1% $MnSO_4$ (the actual amount of $MnSO_4$ addition was 100 mg) was taken as the sample, and the content of $MnSO_4$ was 37.4 mg. The results indicated that the residual amount of $MnSO_4$ after the reaction was too large, and more than half of it entered the final reaction product, which was not conducive to the resource utilization of calcium sulfate resources after the reaction. Therefore, $MnSO_4$ was not considered as a catalyst in subsequent experiments.

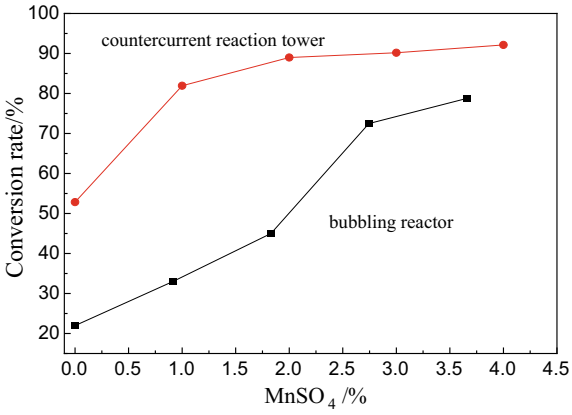

Fig. 8 Effect of $MnSO_4$ addition on conversion of $CaSO_3$

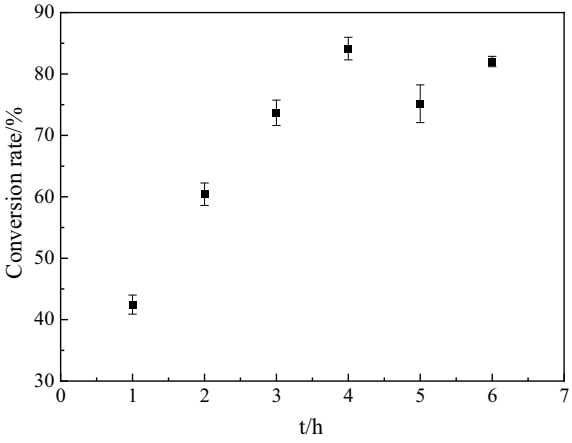

Fig. 9 Effect of reaction time on conversion of $CaSO_3$

Air Oxidation Modification Experiment

In order to reduce the conversion cost of $CaSO_3$, the air oxidation modification experiments were carried out in this paper. The effects of pH value, blowing rate, stirring rate, and oxidation reaction time on the conversion rate of calcium sulfite were investigated. The results are shown in Figs. 10, 11, 12, and 13.

When the air is used as oxidant, the slurry solid content is 10%, the reaction time is 2 h, the air blowing rate is 59 ml/min, and the stirring rate is 50 r/min; the effect of pH on the conversion rate is shown in Fig. 10, the conversion rate of $CaSO_3$ increases significantly with the decrease of pH, and when pH = 4.3, the conversion rate of calcium sulfite can reach more than 92%. When the pH value remains 4.3 constant, it can be seen from Figs. 11, 12, and 13 that blowing rate, reaction time, and stirring

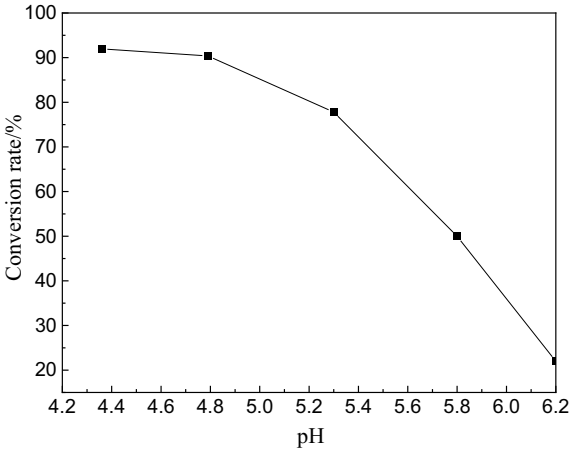

Fig. 10 Effect of Ph on conversion of $CaSO_3$

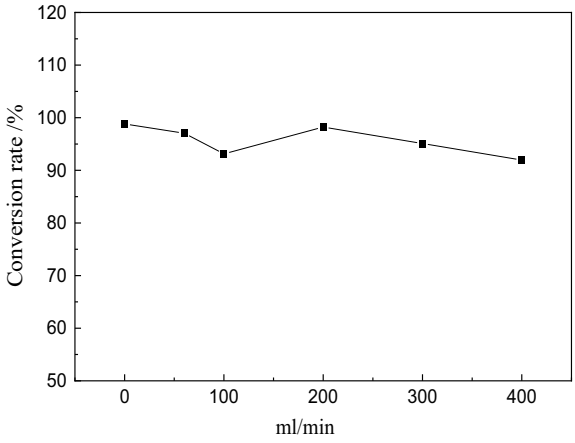

Fig. 11 Effect of air blowing rate on conversion of $CaSO_3$

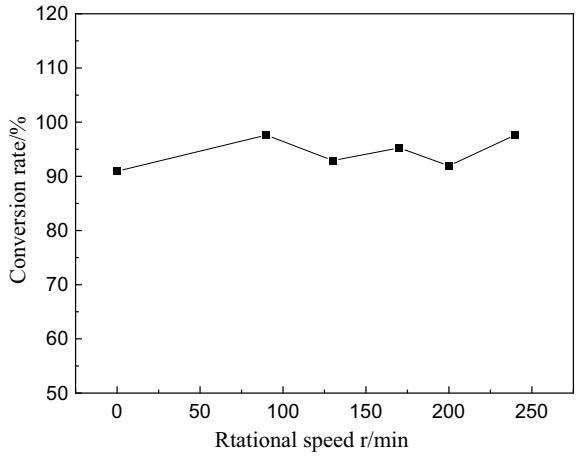

Fig. 12 Effect of rotational speed on conversion of $CaSO_3$

speed have little effect on the conversion rate of $CaSO_3$. This may be because, during the stirring process, the slurry is in contact with the air, which provides the oxygen required for the reaction. In the early stage of the reaction, most of $CaSO_3$ has already undergone oxidation reaction with O_2. According to the conclusion of Linek V. et al. [31], the concentration of sulfite in the initial stage of the reaction is the highest, and the oxidation rate is also the highest. After sulfite is oxidized, sulfate ions are generated and accumulated near the phase interface, which hinders the dissolution and diffusion of oxygen, leading to a rapid decrease in the chemical reaction rate.

Therefore, two groups of comparative experiments were carried out to investigate the effects of air blowing rate and reaction time on the oxidation rate of calcium sulfite under low pH value (4.3) in this paper. The comparative experiments were as follows: (1) Sulfuric acid was added to a sealed conical flask without air blowing; (2) after adding sulfuric acid into the sealed conical flask, the air was blown at 100 ml/min,

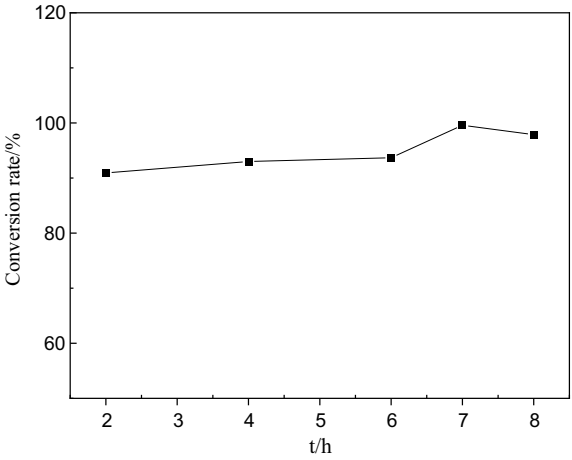

Fig. 13 Effect of reaction time on conversion of $CaSO_3$

and the results are shown in Fig. 14. It could be seen that there was no obvious pattern in the conversion rate of calcium sulfite during different reaction time periods, and the effect of blowing air on the conversion rate of calcium sulfite is not significant. The results in Fig. 14 further demonstrate that under lower pH conditions, as sulfuric acid has reacted with most of the calcium sulfite, the effect of air blowing on the conversion rate is not significant.

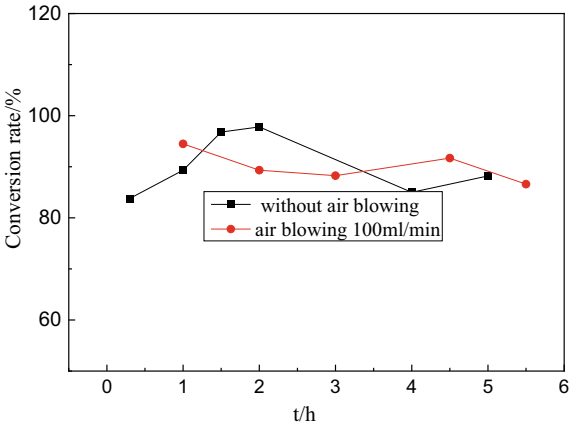

Fig. 14 Effect of air blowing rate on conversion of $CaSO_3$

Conclusion

The physicochemical properties of sintering flue gas desulfurization ash were analyzed in this paper. On this basis, the effects of different process conditions on $CaSO_3$ conversion rate in H_2O_2 oxidation modification, $MnSO_4$ catalytic modification and air oxidation modification were studied, respectively. The optimal conditions for desulfurization ash oxidation conversion under different oxidation methods were explored, and the optimal oxidation method was selected. The research results are as follows:

The by-products of semi-dry desulfurization contain $CaSO_3 \cdot 1/2H_2O$, $CaCO_3$, $CaSO_4$ and $Ca(OH)_2$. When hydrogen peroxide was used as the oxidant, the highest conversion rate of $CaSO_3$ was up to 98%. The optimal process conditions were as follows: pH value 5.5, molar ratio of H_2O_2 to $CaSO_3$ addition 1:1, slurry solid content 10%, and reaction time 1.5 h. In the $MnSO_4$ catalytic modification experiment, part of the catalyst $MnSO_4$ remains in the final reaction product, which was not conducive to the industrial application of the oxidation product $CaSO_4$. In the air oxidation modification experiment, when air was used as the oxidant, the solid content of the slurry was 10%, the reaction time was 2 h, the air blowing amount was 59 ml/min, and the stirring rate was 50 r/min, and the conversion rate of calcium sulfite increased significantly with the decrease of pH. When the pH was around 4.3, the conversion rate of $CaSO_3$ was up to 92%. Under this condition, the air blowing rate, reaction time, and stirring speed have no significant effect on the conversion rate of calcium sulfite.

Acknowledgements This work was financially supported by the Key Laboratory for Ecological Metallurgy of Multimetallic Mineral (Ministry of Education).

References

1. Zhang Y, Ren Y, Liu BL et al (2015) Comprehensive utilization status of sintering flue gas desulfurization gypsum. Bull Chin Ceram Soc 34(12):3563–3570
2. Bian Y, Wang B, Shen BX et al (2022) Research progress on collaborative control of multi pollutants in sintering flue gas in iron and steel industry. Mod Chem Ind 42:24–29
3. Zhu TY (ed) (2008) Sintering flue gas purification technology. Chemical Industry Press, Beijing
4. Stieler F, Magedanz N, Gerlach W et al (1995) Process for sintering iron oxide-containing materials on a sintering machine. US. Patent 05476533:19
5. Zhang MZ, Zhu X, Zhang LQ et al (2021) Intensification of NOx conversion over activated coke by ozone oxidation for sintering flue gas at low temperatures. ACS Omega 6(20):13484–13495
6. Zhu TY, Liu Q, Li YR et al (2014) Emission characteristics of multiple pollutants from iron-steel sintering flue gas and review of control technologies. Sci Technol Rev 32(33):51–56
7. Wei SJ, Wang S, Zhou R (2014) Research on present situation of desulfurization and denitrification technology for sintering flue gas. Air Pollut Control 32(2):95–97
8. Hu J (2022) Discussion of multi-pollutant reduction technology for sintered flue gas in steel industry 4:124–129

9. Bigham JM, Kost DA, Stehouwer RC et al (2005) Mineralogical and engineering characteristics of dry flue gas desulfurization products. Fuel 84(14–15):1839–1848
10. Bian JF, Guo B (2009) Comprehensive utilization of semi-dry desulfurization by-products from circulating fluidized bed. Hebei J Ind Sci Technol 26(01):40–43
11. Su DG, Chen K, Han X et al (2006) Application of desulfurization ash in cement industry. Multipurpose Utilization Mineral Resour 5:39–43
12. Xue YJ, Li XH, Han X et al (2009) Application status quo and development for resource utilization of flue gas desulfurization byproduct. Electricity Power Environ Prot 25(4):47–49
13. Xiao BQ, Song CY (2007) Analysis of the factors influencing desulfurization of the desulfurizing agent with calcium under high temperature. Pollut Control Technol 20(1):3–7
14. Tian Y, Jing YN, Wang Y (2014) Discussions on approaches for comprehensive utilization of by-products for flue gas desulfurization of sintering. Sci Technol Baotou Steel 40(2):72–75
15. Long HM, Wang YF, Lu NN et al (2017) Research development of resource utilization of sintering flue gas calcium based desulfurization byproduct. J Eng Stud 9(1):78–84
16. Wang CQ, Tan KF, Xu XX et al (2014) Effect of activators, admixtures and temperature on the early hydration performance of desulfurization ash. Constr Build Mater 70(15):322–331
17. Mao YL, Zhang DL, Qu YL (2011) Recycling of semidry sintering FGD residues. Angang Technol 4:6–10
18. Lancia A, Pepe F, Musmarra D (1996) Uncatalyzed heterogeneous oxidation of calcium bisulfite. Chem Eng Sci 51(16):3889–3896
19. Ermakov AN, Purmal AP (2002) Catalysis of $HSO^{3-}/SO_3{}^{2-}$ oxidation by manganese ions. Kinet Catal 43(2):249–260
20. Li Y, Sadakata M (1999) Study of gypsum formation for appropriate dry desulfurization process of flue gas. Fuel 78(9):1089–1095
21. Yang LS, Wang X, Zhu XF et al (2012) Preparation of calcium sulfate whisker by hydrothermal method from flue gas desulfurization (FGD) gypsum. Appl Mech Mater 268:823–826
22. Luo YF, Qian LX, Long HM et al (2019) Effect of pretreatment sintering desulfurization ash addition on basic sintering characteristics of iron ore. Iron Steel 12(54):117–124
23. Wei RF, Zhu YL, Zhou D et al (2021) Impurity removal and hydrothermal heterogeneous cryogenic rapid oxidation of semi-dry desulfurization ash from iron ore sintering flue gas. Chin J Process Eng 21(8):951–958
24. CN-GB (1987) General rules for the sampling and sample preparation of minerals in bulk—sampling by manual method. Standard GB/T 2007.1–1987. 15 December 1987
25. CN-JG (2006) Standard for technical requirements and test method of sand and crushed stone (or gravel) for ordinary concrete. Standard JGJ 52–2006. 19 December 2006
26. CN-GB (2012) Methods for chemical analysis of gypsum. Standard GB/T 5484–2012.31 December 2012
27. CN-GB (2014) Analytic method for calcium carbonate. Standard GB/T 19281–2014.8 July 2014
28. Ji XK (2007) Utilization and some properties of circulating fluidized bed combustion ashes. M.D. thesis, Chongqing University
29. Zhou CH, Zhou XP, Rao L et al (2009) Research on comprehensive utilization technology of calcium-based semi-dry sintering flue gas desulfurization by-products paper presented at the Chinese society for metals seminar on energy saving and emission reduction technology of sintering process, Shan Ming, Fujian, 11–12 October 2009
30. Zhou CH, Zhou XP, Rao L et al (2011) Masteel sintering flue gas desulfurization and by-products comprehensive utilization research. Paper presented at the 8th China iron and steel annual conference, Beijing, 26–28 October 2011
31. Linek V, Vacek V (1981) Chemical engineering use of catalyzed sulfite oxidation kinetics for the determination of mass transfer characteristics of gas-liquid contactors. Chem Eng Sci 36(11):1747–1768

Study on the Influence of Low-Frequency Electromagnetic Field on the Absorption Rate of Al_2O_3 Inclusion in Low Reactivity Mold Flux

Bo Bai, Yu Wang, Fushen Li, Hongpo Wang, and Zhaolin Ding

Abstract With the wide application of electromagnetic stirring in continuous casting and the rapid development of low reactive mold flux, the effect of low-frequency electromagnetic field on the assimilation and absorption rate of Al_2O_3 inclusion in the low reactive mold flux was studied by using the rotating cylinder method, and the relationship between electromagnetic field parameters and the dissolution rate of Al_2O_3 inclusion was also studied. The results show that the low-frequency electromagnetic field can obviously promote the assimilation and absorption of Al_2O_3 inclusion in low reactivity mold flux. When the magnetic field intensity (MFI) is 30 mT and the magnetic field frequency (MFF) is 12 Hz, the maximum dissolution rate of Al_2O_3 inclusion is 2.66×10^{-4} g $mm^{-2}min^{-1}$, which is 10.64 times higher than in the absence of magnetic field. Furthermore, the higher the MFI and MFF, the faster the dissolution rate of Al_2O_3 inclusion.

Keywords Low-frequency electromagnetic field · Low reactivity mold flux · Al_2O_3 inclusion

Introduction

Assimilation and absorption of inclusion is an important function of continuous casting mold flux. The increase of Al_2O_3 inclusions in molten steel is easy to cause defects such as subcutaneous inclusions, surface cracks, and peeling, which seriously affects the quality of products [1]. As the main inclusions in high Mn and high Al steel, Al_2O_3 inclusions are the research object of many scholars. Xu [2] used SEM–EDS to observe the radial cross-section of Al_2O_3 sample dissolved in different mold fluxes, different relative motion speeds, and different temperatures. It was found that there was a clear boundary between Al_2O_3 inclusion and the mold flux, and there was a similar transition layer area. Bui [3] studied the mold flux based

B. Bai · Y. Wang (✉) · F. Li · H. Wang · Z. Ding
College of Materials Science and Engineering, Chongqing University, Chongqing 400045, China
e-mail: wangyu@cqu.edu.cn

S. Wagstaff et al. (eds.), *Materials Processing Fundamentals 2024*, The Minerals, Metals & Materials Series, https://doi.org/10.1007/978-3-031-50184-5_29

on $CaO–SiO_2–Al_2O_3$ by rotating cylinder method and found that the dissolution of Al_2O_3 is not only controlled by the mass transfer in the melt but also by the formation of intermediates on the interface. Li [4] also found the existence of a transition product layer by studying the dissolution of Al_2O_3 inclusion in low SiO_2 content mold flux, and it is mainly $BaO·6Al_2O_3$ and $BaO·2CaO·4Al_2O_3$. At the same time, Li [5] also found an intermediate product layer composed of $CaO·2Al_2O_3$ and $CaO·6Al_2O_3$ when studying the interaction between $CaO–Al_2O_3–CaF_2$ flux and Al_2O_3 inclusions. In addition, Ren [6] studied the factors affecting the dissolution of Al_2O_3 inclusions in $CaO–Al_2O_3–SiO_2$ system by high temperature confocal method (CSLM) and established the relationship between dissolution rate and driving force, which provided ideas for subsequent research. At present, many studies mainly focus on the interaction between $CaO–SiO_2$ mold flux and Al_2O_3 inclusion, while a few studies on the interaction between $CaO–Al_2O_3$ low reactivity mold fluxes and Al_2O_3 inclusions, especially on the assimilation and absorption of Al_2O_3 inclusions by low reactivity mold flux under electromagnetic fields.

In this paper, the influence of electromagnetic field environment (magnetic field intensity (MFI) and magnetic field frequency (MFF)) on the assimilation and absorption of Al_2O_3 inclusions by low reactivity mold flux was investigated by rotating cylinder method, which provided theoretical guidance for the design and practical application of low reactivity mold flux.

Experiments

In this paper, the low reactivity mold flux proposed by Zhang [7] was selected as the research object, and its chemical composition, basic physical, and chemical properties are shown in Table 1. CaO, BaO, Li_2O, and Na_2O were introduced by $CaCO_3$, $BaCO_3$, Li_2CO_3, and anhydrous Na_2CO_3, respectively.

Table 1 Composition and content of the low reactivity mold flux

Composition and mass fraction (wt%)									Viscosity(Pa·s)	Melting point (°C)	Ca/Al
CaO	BaO	MgO	Al_2O_3	SiO_2	B_2O_3	F^-	Li_2O	Na_2O			
37	5.2	2	29.8	7.7	4	4.4	1.4	8.5	0.23	1065	1.24

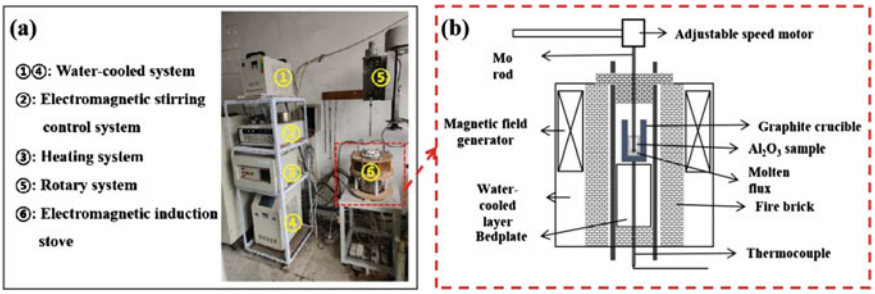

Fig. 1 Diagram of experimental equipment. **a** Physical figures; **b** chematic diagram

Experimental Method

Experimental Equipment

In this paper, the effect of electromagnetic field environment on the absorption of Al_2O_3 inclusions by the low reactivity mold flux was investigated by rotating cylinder method. The main experimental equipment is shown in Fig. 1.

Experimental Process

The effects of different magnetic field environments on the absorption of Al_2O_3 inclusions by the low reactivity mold flux were investigated by adjusting the magnetic field parameters under experimental conditions of 1300 °C, rotation speed of 100 r/min, and time of 5 min. The experimental parameters are shown in Table 2, where A0 is the control group in the non-magnetic field environment, while the other experimental groups are carried out in the electromagnetic field environment.

Each set of mold flux was weighed in proportion and placed in a mortar to be thoroughly ground and mixed. The material was then placed in a graphite crucible and pre-melted in a Si–Mo furnace (1300 °C). The Mo rod was used to stir the flux for mix composition and remove all the volatiles and then poured out after cooling and crushed for use. Figure 2 depicts the rotation experiment process.

By comparing the size changes of Al_2O_3 probes before and after the experiment, and combining with SEM–EDS and XRD patterns, the effect and mechanism of low frequency electromagnetic field on the rate of absorption of Al_2O_3 inclusion by the low reactivity mold flux were analyzed.

Table 2 Experimental parameter setting table

No	MFI (mT)	MFF (Hz)	Temperature (°C)	Rotational speed (rpm)	Time (min)
A0	0	0	1300	100	5
A1.1	10	3	1300	100	5
A1.2	10	6	1300	100	5
A1.3	10	9	1300	100	5
A1.4	10	12	1300	100	5
A2.1	20	3	1300	100	5
A2.2	20	6	1300	100	5
A2.3	20	9	1300	100	5
A2.4	20	12	1300	100	5
A3.1	30	3	1300	100	5
A3.2	30	6	1300	100	5
A3.3	30	9	1300	100	5
A3.4	30	12	1300	100	5

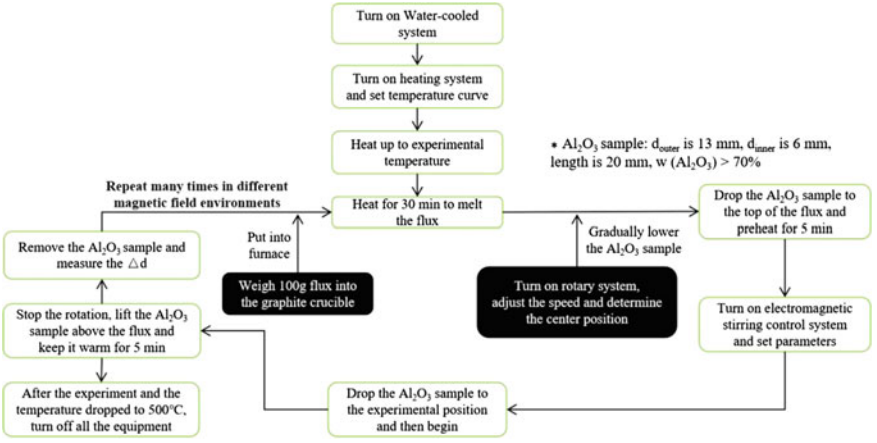

Fig. 2 Experimental process

Experimental Parameter Setting

In this paper, the experiment is carried out based on the self-built mold flux performance test system under the action of electromagnetic field [8]. The electromagnetic parameters are set as follows:

(1) The magnetic field coil currents are 0 A, 2.2 A, 4.4 A, and 6.6 A, respectively, and the corresponding MFI are 0 mT, 10 mT, 20 mT, and 30 mT, respectively.
(2) The MFF were 3 Hz, 6 Hz, 9 Hz, and 12 Hz, respectively.

Results and Discussion

Kinetic Characterization of Mold Flux Absorbing Al_2O_3 Inclusions

The dissolution rate (R_d) of Al_2O_3 in mold flux can be expressed as [9]:

$$R_d = \frac{\Delta m}{S \times t}. \tag{3.1}$$

Among them, Δm is the mass change of Al_2O_3 inclusions (g), t is the dissolution time (min), and the average contact area S of the mold flux and Al_2O_3 inclusions is:

$$S = \pi \times h \times \frac{(d_1 + d_2)}{2}, \tag{3.2}$$

where d_1, d_2 are the average diameter of Al_2O_3 before and after the experiment (mm), h is the length of Al_2O_3 sample (mm). Assuming that the composition of Al_2O_3 inclusion is uniform and the density of each part is the same, the following formula can be obtained:

$$\Delta m = \rho_{Al_2O_3} \times \pi \times h \times \frac{\left(d_1^2 - d_2^2\right)}{4}. \tag{3.3}$$

Combined formula (3.1) and formula (3.2), the absorption rate of Al_2O_3 inclusion by mold flux can be obtained as follows:

$$R_d = \rho_{Al_2O_3} \frac{(d_1 - d_2)}{2 \times t}. \tag{3.4}$$

In this paper, $\rho_{Al_2O_3}$ is 2.6 g cm^{-3}, the following formula is obtained:

$$R_d = 1.3 \times \frac{\Delta d}{t} \times 10^{-3}, \tag{3.5}$$

where R_d is the dissolution rate (g mm^{-2} min^{-1}), Δd is the diameter change (mm).

The specific dissolution amount of mold flux is expressed as:

$$R_m = \Delta d / m_{mf}. \tag{3.6}$$

In the formula (3.6), R_m is the ratio of the mass change of Al_2O_3 sample before and after the experiment to the mass of mold flux (mm g^{-1}), m_{mf} is the mass of mold flux (g).

The Effect of Magnetic Field Environment on the Absorption of Al_2O_3 Inclusion by Mold Flux

In different magnetic field environments, the change of diameter of Al_2O_3 sample before and after the experiment is shown in Table 3.

The Effect of MFF on the Absorption of Al_2O_3 Inclusion by Mold Flux

Combined with the experimental data, the relationship between the MFF and the dissolution rate of Al_2O_3 inclusions and the specific dissolution amount of mold flux under different MFI can be obtained, as shown in Fig. 3. Under the experimental conditions, with the increase of MFF, the dissolution rate of Al_2O_3 inclusions and the specific dissolution amount of mold flux increased gradually. At the same time, under the MFI of 10 mT, 20 mT and 30 mT, the growth rate of Al_2O_3 inclusion dissolution rate with the MFF is 1.35×10^{-5}, 1.50×10^{-5} and 1.61×10^{-5} g mm^{-2} min^{-1} Hz^{-1}, respectively. The specific dissolution amount of mold flux increases with the increase of MFF by 5×10^{-4}, 5.7×10^{-4} and 6.2×10^{-4} mm g^{-1} Hz^{-1}, respectively.

The Effect of MFI on the Absorption of Al_2O_3 Inclusion by Mold Flux

Combined with the experimental data, the relationship between the MFI and the dissolution rate of Al_2O_3 inclusion and the specific dissolution amount of mold flux at different MFF can be obtained, as shown in Fig. 4. Under the experimental

Table 3 Experimental data of diameter change of Al_2O_3 under different magnetic fields

No	d_1/mm	d_2/mm	h/mm	Δd/mm
A0	13.230	13.133	21.30	0.097
A1.1	13.237	13.130	19.37	0.107
A1.2	13.200	12.847	19.58	0.353
A1.3	13.227	12.780	21.18	0.447
A1.4	13.223	12.647	19.91	0.577
A2.1	13.217	12.883	18.94	0.333
A2.2	13.197	12.753	20.91	0.443
A2.3	13.193	12.477	21.92	0.717
A2.4	13.227	12.410	21.97	0.817
A3.1	13.240	12.747	21.21	0.493
A3.2	13.197	12.650	21.03	0.547
A3.3	13.293	12.477	19.36	0.817
A3.4	13.217	12.193	21.13	1.023

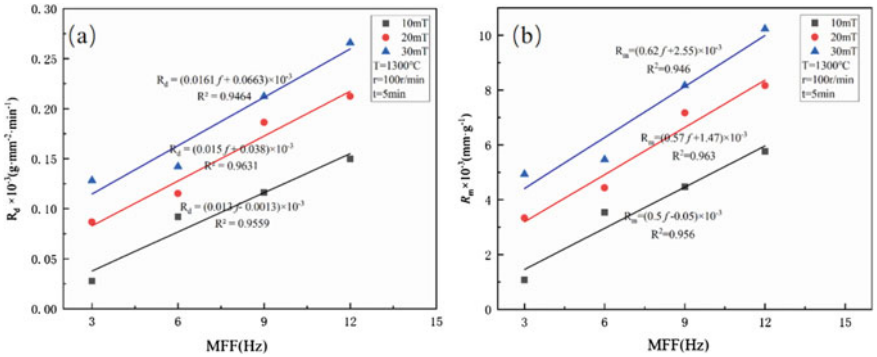

Fig. 3 **a** MFF and rate of absorption of Al_2O_3 by the mold flux **b** MFF and the specific dissolution amount of mold flux

conditions, with the increase of MFI, the dissolution rate of Al_2O_3 inclusion and the specific dissolution amount of mold flux also increased gradually. When the MFI is 30 mT and the MFF is 12 Hz, the maximum dissolution rate of Al_2O_3 inclusion is 2.66×10^{-4} g mm^{-2} min^{-1}, which is 10.64 times higher than that without magnetic field. At the same time, under the MFF of 3 Hz, 6 Hz, 9 Hz and 12 Hz, the growth rate of the dissolution rate of Al_2O_3 inclusions with the MFI is 5.031×10^{-6}, 2.509×10^{-6}, 4.81×10^{-6}, and 5.811×10^{-6} g mm^{-2} min^{-1} mT^{-1}, respectively. The growth rates of the specific dissolution of the mold flux with the MFI were 1.93×10^{-4}, 9.67×10^{-5}, 1.85×10^{-4}, and 2.23×10^{-4} mm g^{-1} mT^{-1}, respectively.

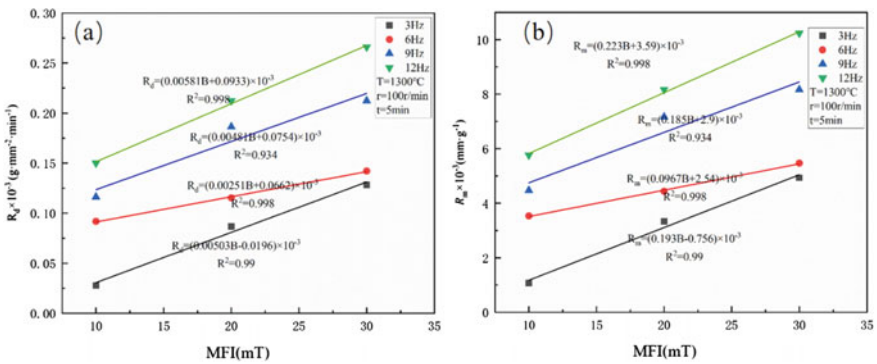

Fig. 4 **a** MFI and rate of absorption of Al_2O_3 by the mold flux **b** MFI and the specific dissolution amount of mold flux

The Relationship Between Magnetic Field Parameters and Absorption of Al_2O_3 Inclusion by Mold Flux

The binary nonlinear regression of the dissolution rate of Al_2O_3 inclusion with respect to the MFI and the MFF was performed, and the regression Eq. (3.7) was obtained:

$$\begin{aligned} R_d^* = &\left(-58.197 + 6.708B + 10.68f - 0.083B^2 + 0.063f^2\right. \\ &\left.+0.154Bf \times 10^{-5}\right)\left(R^2 = 0.97\right) \end{aligned} \tag{3.7}$$

The regression calculation was carried out under the magnetic field condition of 20 mT and 3 Hz. The deviation between the calculated results and the experimental results was 2.28%, indicating that the regression equation can better reflect the relationship between the absorption rate of the mold flux to the Al_2O_3 inclusion and the MFI and MFF.

At the same time, the binary nonlinear regression of the specific dissolution amount of the mold flux with respect to the MFI and MFF is obtained, and the regression Eq. (3.8) is obtained:

$$\begin{aligned} R_m^* = &\left(-22.383 + 2.5B + 4.108f - 0.032B^2\right. \\ &\left.-0.024f^2 + 0.059Bf\right) \times 10^{-4}\left(R^2 = 0.97\right) \end{aligned} \tag{3.8}$$

The regression calculation was carried out under the magnetic field of 20 mT and 3 Hz. The deviation between the calculation results and the experimental results was 3.85%, indicating that the regression equation can reflect the relationship between the specific dissolution of the low reactivity mold flux and the MFI and MFF to a certain extent.

Mechanism Analysis

Test Analysis Results

The interface between the flux and the Al_2O_3 sample after the experiment was analyzed by SEM–EDS, and the results of A0 and A2.4 are shown in Fig. 5. It can be found that Ca, Al, and other elements have a certain gradient transition layer near the interface between the flux and the Al_2O_3 sample, while the flux elements such as Na, F, and Mg are basically evenly distributed in the mold flux and the Al_2O_3 sample, indicating that the above elements migrate during the reaction process. In addition, the thickness of the interface transition layer under different magnetic field environments is not consistent. The transition layer in experiment A0 is about 23 μm, while the transition layer in experiment A2.4 is about 42 μm, indicating that the electromagnetic field can promote the absorption of Al_2O_3 inclusion by flux, and

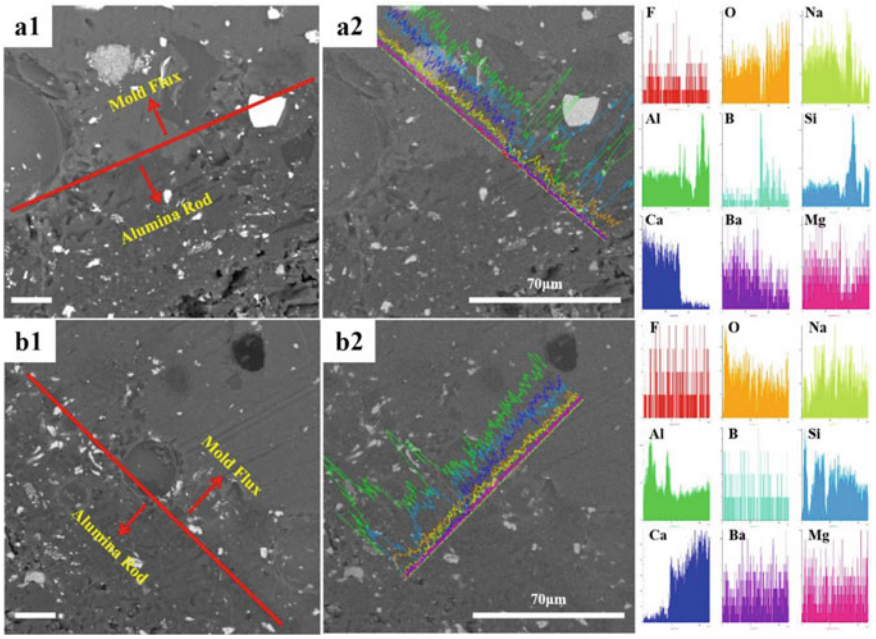

Fig. 5 SEM–EDS of inclusion-flux interface **a** A0 **b** A2.4

the absorption rate and the specific dissolution of Al_2O_3 inclusions increase with the increase of MFI and MFF, which is consistent with the experimental results.

In addition, samples were taken before and after the experiment (A0 group, A1.1 group, and A3.4 group were taken after the experiment) for XRD detection, and the results are shown in Fig. 6. From the (a) diagram, it can be obtained that there are three phases of CaF_2, $12CaO{\bullet}7Al_2O_3$, and $BaMgSiO_4$ in the primary flux. Under the action of magnetic field and no magnetic field, the phase $BaAl_2O_4$ is formed after the mold flux absorbs Al_2O_3 inclusions. However, under the action of electromagnetic field, the phase formed after the mold flux absorbs Al_2O_3 inclusions is $5CaO{\bullet}3Al_2O_3$, while it's $Ba_2MgSi_2O_7$ without magnetic field.

Mechanism Analysis

Based on the above analysis and test results, we proposed the absorption mechanism of Al_2O_3 inclusion by low reactivity mold flux under low-frequency electromagnetic field, as shown in Fig. 7.

According to the flux ion theory, after the action of electromagnetic field, the molten mold flux ion will be affected by the electromagnetic force, which increases the ion migration rate between the flux and the Al_2O_3 inclusion, and then changes

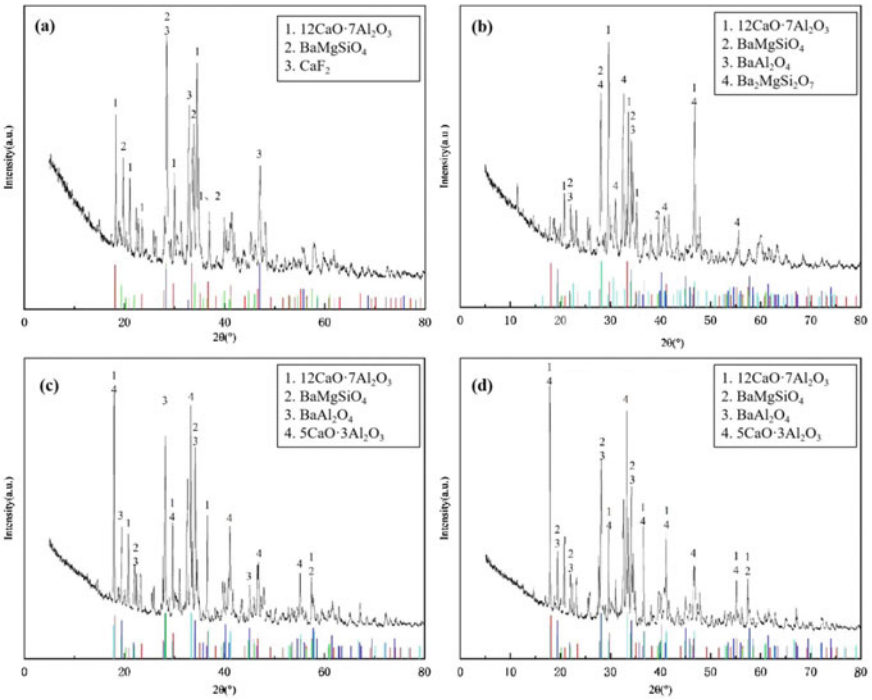

Fig. 6 XRD pattern. **a** Initial flux **b** A0 **c** A1.1 **d** A3.4

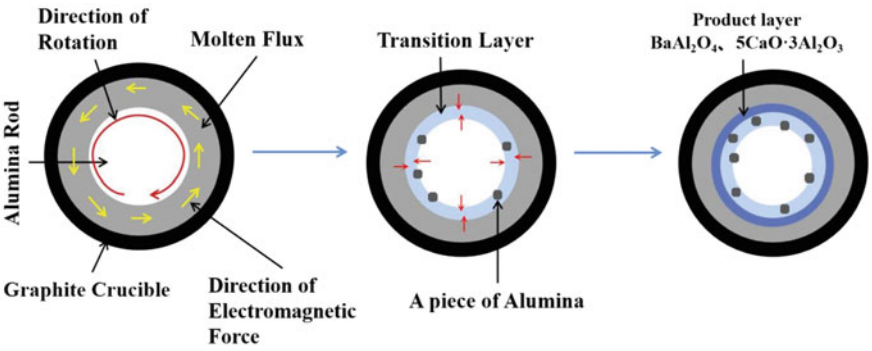

Fig. 7 Absorption mechanism of Al_2O_3 inclusion by low reactivity mold flux under low-frequency electromagnetic field

the interface in the molten flux. The renewal rate of the reactants increases the concentration driving force of the dissolution reaction and affects the rate of the flux to absorb the Al_2O_3 inclusions. Through ion migration, $BaAl_2O_4$, $5CaO{\bullet}3Al_2O_3$, and other phases were formed at the interface and finally integrated into the mold

flux. At the same time, with the increase of MFI and MFF, the electromagnetic force increases gradually, and the influence on the dissolution rate of Al_2O_3 inclusion and the specific dissolution amount of mold flux increases further.

In addition, Zhai [10] studied the distribution of electromagnetic field in the crystallizer under the action of electromagnetic stirring by numerical simulation. It was found that the distribution of electromagnetic force in the crystallizer was small in the middle and large around. Under the condition of the same radial distance, the electromagnetic force was equal in size and opposite in direction, forming a rotating torque. According to the actual situation of this experiment, the flux will also generate a rotating torque under the action of electromagnetic field, which will cause physical erosion to the Al_2O_3 inclusion. Combined with the dual effect of the rotating cylinder method, the outer layer of the Al_2O_3 inclusion gradually falls off, so that the contact area between the Al_2O_3 inclusions and the flux increases, which in turn promotes the dissolution of the Al_2O_3 inclusion in the flux.

At the same time, according to the Joule heat effect, when the current passes through a solid or liquid with limited conductivity, the resistance loss in the material will convert electrical energy into heat energy. When the conduction electrons transfer energy to the atoms of the conductor by means of collision, heat will be generated on a small scale. Wang [11] found that induced current will be generated in the flux under the action of electromagnetic field, and then Joule heat will be generated. With the increase of MFI and MFF, the magnetic induction Joule heat will also increase. Therefore, under the action of electromagnetic field, Joule heat increases the melt temperature, which increases the ion migration rate between the mold flux and the Al_2O_3 inclusion, thus affecting the dissolution rate of the Al_2O_3 inclusions and the specific dissolution amount of the mold flux.

Conclusions

In this paper, the effect of MFI and MFF on the rate of interaction between low reactivity mold flux and Al_2O_3 inclusions and its mechanism was studied by the dynamic rotating cylinder method. The conclusions are as follows:

(1) Low-frequency electromagnetic field can promote the absorption of Al_2O_3 inclusions by low reactivity mold fluxes. With the increase of MFI and MFF, the absorption rate of Al_2O_3 inclusions by flux increases. Based on the experimental data, the binary nonlinear regression equation of the influence of MFI and MFF on the dissolution rate of Al_2O_3 inclusion in molten flux was established:

$$R_d^* = \left(-58.197 + 6.708B + 10.68f - 0.083B^2 + 0.063f^2 + 0.154Bf\right) \times 10^{-5} \left(g \cdot mm^{-2} \cdot \overset{-1}{min}\right)$$

The binary nonlinear regression equation of the relationship between the specific dissolution amount of the mold flux and the MFI and MFF:

$$R_m^* = \left(-22.383 + 2.5B + 4.108f - 0.032B^2 - 0.024f^2 + 0.059Bf\right) \times 10^{-4}\left(mm \cdot g^{-1}\right)$$

(2) Through SEM–EDS, it is observed that there is obvious element migration in the process of flux absorbing Al_2O_3 inclusions, and there is a transition layer in the element distribution, and the thickness of the transition layer is greater than that without magnetic field under the condition of magnetic field. At the same time, in the electromagnetic field environment, $BaAl_2O_4$ and $5CaO{\bullet}3Al_2O_3$ phases were formed after the mold flux absorbed Al_2O_3 inclusion.

(3) Under the action of electromagnetic field, the flux ions are affected by the combined action of electromagnetic force and Joule heat, which increases the ion migration rate between the mold flux and Al_2O_3 inclusion, and then changes the renewal rate of the interface reactants in the molten mold flux, thereby increasing the concentration driving force of the dissolution reaction, and finally affecting the absorption rate of Al_2O_3 inclusions by the mold flux.

References

1. Holappa L, Wijk O (2014) Inclusion engineering. Treatise Process Metall 347–372
2. Xu KP (2018) Study on absorption of Al_2O_3 inclusion by mold flux of high-Mn and high-Al steels. Master's thesis, Chongqing University
3. Bui AH, Hyun-Mo HA, Chung IS (2005) Dissolution kinetics of alumina into mold fluxes for continuous steel casting. ISIJ Int 45(12):1856–1863
4. Li Z, Jia B, Zhang Y, He S, Wang Q, Wang Q (2019) Dissolution behaviour of Al_2O_3 in mould fluxes with low SiO_2 content. Ceram Int 45(3):4035–4042
5. Li JL, Shu QF, Liu YA, Chou KC (2014) Dissolution rate of Al_2O_3 into molten CaO–Al_2O_3–CaF_2 flux. Ironmaking Steelmaking 41(10):732–737
6. Ren C, Zhang L, Zhang J, Wu S, Zhu P, Ren Y (2021) In situ observation of the dissolution of Al_2O_3 particles in CaO–Al_2O_3–SiO_2 slags. Metall Mater Trans B 52(5):3288–3301
7. Zhang C, Cai DX, Zong ZY, Zhi JJ (2018) Low reactive mold flux and preparation method. CN. Patent CN106270429B. 2 October 2018
8. Zhao L, Wang Y, Zhao LM (2017) Design and construction of a testing system for the performance of mold flux under electromagnetic field. Paper presented at the 11th China Iron and Steel Annual, Beijing, 21–22 November 2017
9. Shi GY, Zhang TA, Dou ZH, Niu LP (2020) Dissolution behavior of Al_2O_3 inclusions in CaO–Al_2O_3 based slag representing aluminothermic reduction flux. Crystals 10(11):1–12
10. Zhai MJ (2015) Numerical simulation of multi-physical field coupling in mold under electromagnetic agitation. Master's thesis, Yanshan University
11. Wang YJ, Bai B, Wang Y, Wang HP, Wang MX, Li FS (2023) Study on the magnetocaloric effect of molten mold flux under low-frequency electromagnetic field. Paper presented at the TMS annual meeting, San Diego, California, 19–23 March 2023

Author Index

S. Wagstaff et al. (eds.), *Materials Processing Fundamentals 2024*, The Minerals, Metals & Materials Series, https://doi.org/10.1007/978-3-031-50184-5

Subject Index

S. Wagstaff et al. (eds.), *Materials Processing Fundamentals 2024*, The Minerals, Metals & Materials Series, https://doi.org/10.1007/978-3-031-50184-5